Field Aligned Electron Distributions in the Inner Magnetosphere

Gary Alexander Abel

Mullard Space Science Laboratory

Department of Space and Climate Physics

University College London

A thesis submitted to the University of London

for the degree of Doctor of Philosophy

September 1999

ProQuest Number: 10609076

All rights reserved

INFORMATION TO ALL USERS
The quality of this reproduction is dependent upon the quality of the copy submitted.

In the unlikely event that the author did not send a complete manuscript
and there are missing pages, these will be noted. Also, if material had to be removed,
a note will indicate the deletion.

ProQuest 10609076

Published by ProQuest LLC (2017). Copyright of the Dissertation is held by the Author.

All rights reserved.
This work is protected against unauthorized copying under Title 17, United States Code
Microform Edition © ProQuest LLC.

ProQuest LLC.
789 East Eisenhower Parkway
P.O. Box 1346
Ann Arbor, MI 48106 – 1346

Abstract

Low energy ($\leq$ 100 eV - 10 keV) field aligned electrons are often observed by the Low Energy Plasma Analyzer (LEPA) on the CRRES satellite. These electrons usually occur in bursts of less than 10 minutes duration and are mostly bi-directional though not always equally. The events can be seen from L-values of 5 outwards (to at least L=7) and over most of the MLT range covered by CRRES. Most events are seen at the outer edge of CRRES' coverage and in the evening and early morning sectors, when the apogee of CRRES was at higher latitudes. The bursts normally occur within 20 minutes of substorm onset.

The counterstreaming electrons usually appear to be scattered out of the loss cone while gaining energy. The total increase in energy may be more than an order of magnitude while the pitch angle increases to about 60 degrees. Theoretical diffusion curves for the resonant interaction between electrons and parallel propagating whistler mode waves have been suggested by *Summers et al.*, 1998. These curves are distinctly different from the scattering paths seen in the LEPA data. The diffusion paths suggested by *Summers et al.*, 1998, assume that the dispersion relation of the plasma is dominated by the cold plasma. We show that in the case of counterstreaming beams the dispersion relation is markedly different from the isotropic cold plasma approximation, and that the diffusion curves may well be different under this regime.

High latitude spacecraft often observe upgoing field aligned electron beams. We believe these to be the source of the field aligned electron beams seen by CRRES. We see magnetic field perturbations, around the time of the counterstreaming beams, consistent with field aligned currents. We suggest that the electrons populating the counterstreaming beams may be the current carriers.

The Answer *(Sambora/Foster)*

The lightning flashed as angels
Rode fiery chargers through the clouds
That answer scared me into tears
And all the grownups laughed out loud

Now the years hold on, tired voices have all gone
Now they ride their thunder through the heavens

There's a world in every drop of rain
Embracing oceans sweep us home again
Come along with me, come along with me
Seek the truth, you shall not find another lie

They say for every living thing
There's a guide up in the sky
That helps you pass from world to world
So you never really die

Then with scythe and cloak
Death comes waltzing to your side
As the vision pass you ask
If there was meaning to your life
As you strain to hear the answer, spirits sing, and devils fiddle
As he bends to whisper in your ear, he leaves you one more riddle

Oh, the answer lies beyond the pain
All the questions in our minds, we surely ask in vain
Come along with me, come along with me
Seek the truth, and you shall find another life

Taken from the Richie Sambora Album *Stranger in this town*

Contents

Abstract **2**

1 Introduction **15**

1.1 The Birth of Solar Terrestrial Physics 15

1.2 Thesis Outline 19

2 The Earth's Magnetosphere **21**

2.1 The Structure of the Magnetosphere 21

2.1.1 The Closed Magnetosphere 21

2.1.2 The Open Magnetosphere 22

2.1.3 Plasma Populations in the Magnetosphere 25

2.2 Trapped Particle Motion in the Magnetosphere 28

2.3 The Aurora 32

2.4 Magnetospheric Current Systems 34

2.5 Substorms 39

2.5.1 Phases of a Substorm 39

2.5.2 Substorm Current Wedge 44

2.6 Waves 45

2.6.1 Plasma Oscillations 45

2.6.2 Wave Modes Found in the Magnetosphere 46

2.7 Coordinate System 47

3 The CRRES Spacecraft **50**

3.1 Mission Objectives 50

3.2 Orbit 53

3.3 CRRES Instrumentation 56

3.4 Low Energy Plasma Analyzer (LEPA) 58

3.4.1 Instrument Description 58

3.4.2 Problems with the LEPA data 66

3.5 Fluxgate Magnetometer 73

3.5.1 Instrument Description 73

3.5.2 Coordinate System 75

3.6 Plasma Wave Experiment 77

4 Field Aligned Electron Events **79**

4.1 What is a Field Aligned Electron Event? 79

4.1.1 Previous Observations of Field Aligned Electrons 79

4.1.2 Preliminary Studies of FAEs Using CRRES/LEPA, *Johnstone et al.*, 1994. 82

4.2 Distribution of FAEs 90

4.2.1 Lifetimes of FAEs 90

4.2.2 Spatial Distribution of FAEs 96

4.3 Association of FAEs with Substorms 102

4.4 AMPTE/CCE Observations [*Klumpar*, 1993]. 114

4.5 Summary 118

5 Acceleration of Field Aligned Electrons Part 1 - Electron Observations **120**

5.1 Previous Observations of the Acceleration of Field Aligned Electrons - *Lin et al.*, 1979 121

5.2 LEPA Observations of the Acceleration of Field Aligned Electrons . . 122
5.2.1 Examples 122
5.2.2 Acceleration Characteristics 137
5.3 Summary 149

6 Acceleration of Field Aligned Electrons Part 2 - Investigation of Diffusion Process 151

6.1 Observational Study of Plasma Waves and the Acceleration of Field Aligned Electrons 152
6.1.1 Introduction to Plasma Wave Observations 152
6.1.2 Plasma Wave Observations Around the Time of FAEs 155
6.1.3 Comparison Between the Acceleration of Field Aligned Electrons and Wave Power 157
6.2 Theoretical Study of Plasma Waves and the Acceleration of Field Aligned Electrons Using the Cold Plasma Approximation 160
6.2.1 Theoretical Diffusion Curves [*Summers et al.*, 1998] 161
6.2.2 Post-FAE Diffusion Into the Loss Cone 163
6.2.3 Scattering Without Acceleration During FAEs 164
6.2.4 Acceleration Region Location 164
6.3 Consequences of the Electron Beams on Resonant Diffusion 168
6.3.1 'Ingredients' of *Summers et al.*, 1998, Diffusion Curves 168
6.3.2 Dispersion Relations 170
6.4 Summary 178

7 The Source of FAEs and The Relation of FAEs to FACs 181

7.1 Introduction 181
7.2 High Latitude Observations of Field Aligned Electron Beams 183

7.2.1 Older Studies 183
7.2.2 FAST Observations of Field Aligned Electron Beams 186
7.2.3 Comparison of FAST and CRRES Observations 191
7.2.4 Distribution of High Latitude Observations of Electron Beams 193
7.3 FAEs and FACs 195
7.3.1 AE index 195
7.3.2 Distribution of Nightside FACs 198
7.4 Magnetic Field Measurements 200
7.5 Estimating FAC Densities from LEPA data 201
7.6 Estimated FACs at the time of FAEs 210
7.7 Summary 214

8 Conclusions and Future Work **216**
8.1 Conclusions 216
8.2 Future Work 219
8.3 Final Word 220

A LEPA energy channels **221**

B List of FAEs **223**

C Dispersion Relation for a Cold Plasma **237**

D Dispersion Relation for a Cold Plasma with Counterstreaming Beams **241**

Acknowledgements **242**

References **243**

List of Figures

1.1 A photograph of the aurora. 16

2.1 The magnetosphere under the frozen-in flow conditions. 23

2.2 X-type magnetic field configuration at the magnetopause. 24

2.3 Dungey's 'open' magnetosphere. 26

2.4 Flow of plasma within a reconnection driven convective magnetosphere. 27

2.5 Plasma regions of the Earth's magnetosphere. 28

2.6 Motion of a charged particle in the geomagnetic field. 29

2.7 The three basic types of motion associated with charged particles in the magnetosphere. 30

2.8 DMSP satellite picture of the aurora over western Europe taken at a geomagnetically active time. 35

2.9 Schematic representation of the currents flowing in the Earth's magnetosphere. 36

2.10 Synopsis of the ingredients of the auroral electrojet system. 38

2.11 A summary of the distribution and direction of the Region-1 and Region-2 currents during weakly disturbed conditions. 40

2.12 Schematic representation of six stages in the development of an auroral substorm. 41

2.13 Reconfiguration of the magnetotail during a substorm. 43

2.14 Schematic of the substorm current wedge. 45

2.15 The solar-magnetic coordinate system. 48

3.1 The CRRES spacecraft. 51
3.2 Initial CRRES Orbit. 54
3.3 Precession of CRRES orbit in local time coordinates. 55
3.4 Schematic diagram of the LEPA Detector. 61
3.5 Schematic diagram of the LEPA discrete anode structure. 62
3.6 Illustration of the symmetry plane, loss cone and the 90° distributions. 64
3.7 Data returned from the LEPA electron sensor during Orbit 445 prior to the magnetic byte swapping correction. 67
3.8 Illustration of the apparent magnetic field direction used by LEPA as a result of the magnetic byte swapping error. 69
3.9 The effect of the LEPA onboard possessing error. 70
3.10 Data returned from the LEPA electron sensor during Orbit 445 following the magnetic byte swapping correction. 72
3.11 Astromast boom and magnetometer sensor orientation. 74
3.12 The VDH coordinate system. 76

4.1 An example of an FAE of the dropout type. 84
4.2 An example of an FAE of the sharp onset type. 85
4.3 An example of two FAEs of the substorm type. 86
4.4 A schematic illustration of the collection directions of the data shown in the LEPA survey plots. 87
4.5 The distribution of durations of FAEs. 91
4.6 The distribution of durations of FAEs against radial distance. 93
4.7 The effect of feature structure on the perceived lifetime of an associated event observed by CRRES. 95

4.8 Operational time spent by CRRES, with LEPA operating, in each 0.25L × 30 minutes MLT bin summed over all magnetic latitudes. . . 97

4.9 Operational time spent by CRRES, with LEPA operating, in each 0.25L × 4° magnetic latitude bin summed over 2 hours MLT. 98

4.10 Number of FAEs seen normalised to the observation time in each 0.25L × 30 minutes MLT bin summed over all magnetic latitudes. 100

4.11 Number of FAEs seen normalised to the observation time in each 0.25L × 4° magnetic latitude bin summed over 2 hours MLT. 101

4.12 Number of FAEs of the 'dropout' type seen normalised to the observation time in each 0.25L × 30 minutes MLT bin summed over all magnetic latitudes. 103

4.13 Number of FAEs of the 'sharp onset' type seen normalised to the observation time in each 0.25L × 30 minutes MLT bin summed over all magnetic latitudes. 104

4.14 Number of FAEs of the 'substorm' type seen normalised to the observation time in each 0.25L ×30 minutes MLT bin summed over all magnetic latitudes. 105

4.15 The distribution of times between substorm onset and the observation of an FAE. 107

4.16 The distribution of times between substorm onset and the observation of FAEs of the different types. 109

4.17 The probability of observing an FAE within 1 hour of substorm onset. 110

4.18 The number of FAEs seen per hour of observation in each 2 hour MLT bin 111

4.19 The ratio between the probability of observing an FAE within 1 hour of substorm onset and the number of FAEs CRRES seen per hour as a function of MLT. 111

4.20 Average AE index development during substorms. 113

4.21 The distribution of the maximum AE index in the hour following an FAE. 114

4.22 The probability of occurrence of the 6.4 minute average anisotropy index exceeding 1.5 in any two energy channels of the HPCE on the AMPTE/CCE. 116

5.1 LEPA survey plot illustrating two FAEs on Orbit 77. 124

5.2 A series of pitch angle energy spectrograms illustrating an FAE on Orbit 77. 126

5.3 The axes used by spectrograms in Figures 5.2, 5.5, and 5.7. 127

5.4 LEPA survey plot illustrating three FAEs on Orbit 264. 129

5.5 A series of pitch angle energy spectrograms illustrating two FAEs on Orbit 264. 130

5.6 LEPA survey plot illustrating a five of FAEs on Orbit 69. 132

5.7 A series of pitch angle energy spectrograms illustrating three FAEs on Orbit 69. 134

5.8 The characteristic diffusion curves for whistler mode waves. 135

5.9 The general ordering of the process of acceleration/scattering of FAEs seen by CRRES. 137

5.10 A schematic view of the scattering path followed by electrons during FAEs. 138

5.11 A sequence of plots in velocity space illustrating the 15:44 - 15:55 UT FAE in Orbit 77 in differential energy flux. 140

5.12 A sequence of plots in velocity space illustrating the 15:44 - 15:55 UT FAE in Orbit 77 in phase space density. 141

5.13 A sequence of plots of the phase space density as a function of pitch angle for each energy channel. 143

5.14 A sequence of plots of the phase space density as a function of energy averaged over 30° pitch angle bins. 145
5.15 Definition of the angle θ. 147
5.16 The change in θ as a function of magnetic latitude. 148

6.1 LEPA survey plot for Orbit 438. 153
6.2 PWE survey plot for Orbit 438. 154
6.3 PWE survey plot for Orbit 77. 156
6.4 Wave intensity as a function of time in three different wave modes around the time of six FAEs. 159
6.5 Resonant diffusion paths of electrons scattered by whistler mode waves, in velocity space. 162
6.6 A sequence of plots in velocity space illustrating the period 10:49 - 10:51 UT following an FAE in Orbit 69 in differential energy flux. . . 165
6.7 Resonant diffusion paths of electrons scattered by whistler mode waves, in velocity space. 166
6.8 The appearance of a *Summers et al.*, 1998, type diffusion curve formed at 28° magnetic latitude seen at varying magnetic latitudes. 169
6.9 Dispersion diagram for parallel-propagating electromagnetic waves in a magnetised plasma for the case when $\omega_L > \Omega_e$. The lowest frequency branch (labeled R) corresponds to whistler mode waves and is the basis of the analysis in Section 6.2. 172
6.10 Dispersion diagram for parallel-propagating electromagnetic waves in a cold magnetised plasma with cold counterstreaming beams. 174
6.11 Dispersion diagram for parallel-propagating electromagnetic waves in a cold magnetised plasma with counterstreaming beams shown in terms of the order of cyclotron resonance with $v_{||} = v_b$. 175

6.12 Dispersion diagram for parallel-propagating electromagnetic waves in a cold magnetised plasma with counterstreaming beams with $\omega_{pb} = 0$ 178

7.1 FAST observations of an auroral crossing near magnetic midnight. . . 189

7.2 The frequency of occurrence of an electron beam observed with the S3-3 satellite as a function of (a) invariant latitude and (b) MLT. . . 194

7.3 The frequency of occurrence of an electron beam observed with the S3-3 satellite as a function of invariant latitude and MLT. 196

7.4 The distribution of AE index at the time of FAEs normalised to the distribution of the AE index throughout the lifetime of CRRES. . . . 197

7.5 The vector diagram of field aligned currents for disturbed periods in the post midnight sector. 199

7.6 The magnetic field variations around the time of six FAEs. 202

7.7 Root mean squared ΔB_D averaged over FAE lifetimes, plotted against magnetic latitude. 203

7.8 LEPA survey plot illustrating an electron pancake distribution on Orbit 426. 206

7.9 The field aligned current density for an equatorial crossing on Orbit 426. 207

7.10 The field aligned current density, smoothed using a 9 point boxcar average, for an equatorial crossing on Orbit 426. 208

7.11 FAC densities around the time of six FAEs. 211

7.12 Current density estimated from LEPA data averaged over FAE lifetimes, and plotted against magnetic latitude. 213

List of Tables

7.1 Summary of observations made by *Maynard et al.*, 1996. 182

7.2 Classification Scheme for Beams and Conics. 185

7.3 Signatures of regions of diverging and converging electrostatic shocks, after *Carlson et al.* 1997. 187

A.1 LEPA energy channels when operated over the unattenuated range. . 221

A.2 LEPA energy channels when operated over the attenuated range. . . . 222

B.1 List of FAEs as observed by the LEPA on CRRES. 223

Chapter 1

Introduction

The aurora borealis, Figure 1.1, and it's southern hemisphere counterpart the aurora australis, are the most obvious and visually stunning signs of continual interaction between the Earth's atmosphere, its magnetic field, and the endless stream of particles flowing away from the sun, known as the solar wind. The term aurora borealis is latinised Greek meaning 'northern dawn' and was first published by Gassendi in 1649, though it may be that the term was introduced by Galileo some years earlier.

1.1 The Birth of Solar Terrestrial Physics

Once thought to be signs from the gods, it was not until this century that the true nature of the aurora, and consequently the Sun-Earth system, was realised. Even now many aspects of auroral phenomena cannot be explained. Along the way many theories have been suggested to explain the aurora, such as Galileo's proposal that the aurora was caused by air rising out of the Earths shadow to be illuminated by the sun, or that of Descartes that the aurora was caused by sunlight reflected from ice crystals in high altitude cirrus clouds. It took two separate technological advances before the connection between the aurora and the Sun could be made.

The first of these was the invention of the magnetic compass, which led to the field

Figure 1.1: A photograph of the aurora taken near Sondrestrom, Greenland (Courtesy of N. P. Meredith, MSSL).

of geomagnetism being established. The connection between the Earth's magnetic field and the aurora was made following the discovery, by George Graham in 1722, that the compass is always in motion. O. Hiorter made observations of the temporal changes in the magnetic field direction, which lead to the discovery of the diurnal variation of the geomagnetic field. The diurnal effect arises as the Earth rotates within the current systems flowing in the upper atmosphere, which stay fixed with respect to the Earth-Sun direction. Perhaps more significant was the discovery by Hiorter in 1741, that geomagnetic activity and the occurrence of aurora were correlated.

The second invention was that of the telescope, which led, amongst other things, to sunspot observations. The study of sunspots started slowly, perhaps due to the unfortunate timing of the Maunder minimum (1645 to 1700), an interval during which very few sunspots were seen. It was not until 1851 that the 11 year sunspot cycle was discovered by Heinrich Schwabe.

In the early nineteenth century a widespread network of magnetometers was established. Using data from four geomagnetic observatories Edward Sabine was able to show that the geomagnetic disturbances varied with the solar cycle. The link between geomagnetic and solar activity was furthered by the sighting of a great solar flare by Richard Carrington, which caused an almost immediate response in the geomagnetic field observed at the Kew Observatory in London (which we now know to be due to the increased conductivity in the ionosphere caused by UV and x-ray radiation). A mere 18 hours later one of the strongest magnetic disturbances on record broke out, with aurora being seen as far south as Puerto Rico.

Around the turn of the century, great advances were made in the understanding of the aurora. Kristian Birkeland suggested that electrons, newly discovered by J. J. Thomson, caused the lights in the sky by interacting with the atmosphere. Measurements of the magnetic field in northern Norway (1902-1903) led Birkeland to the discovery of electric currents flowing in the region we now call the ionosphere.

However, the question still remained as to how the auroral process was linked to the behavior of the Sun. In 1918, Sydney Chapman returned to an idea previously criticised by A. Schuster. His idea was that a beam of electrons could stream out from the sun, and cause worldwide magnetic disturbances. Frederick Lindemann was soon to echo the argument of Schuster that such a beam would destroy itself due to electrostatic repulsion. Lindemann suggested that rather than a beam of electrons, there was a beam containing both electrons and singly charged ions in equal number, known now as a plasma. The idea of a plasma proved to be a breakthrough, signaling the start of the work by Chapman and his co-workers, which would form the foundations for the modern understanding the solar wind and the magnetosphere. Over the next few decades ideas concerning the structure of the magnetosphere and solar wind were developed, but experimental confirmation had to wait for a technological advance which would allow scientific instruments to be sent into space.

In 1958 the first artificial satellite, Sputnik 1, was launched. The following year, Explorer 1 was launched carrying a Geiger counter. It was the data collected by this experiment which lead to James Van Allen's discovery of the trapped radiation belts which bear his name. Following Explorer 1 there has been a continuing programme of missions to study the magnetosphere, solar wind and the Sun itself. As improvements have been made in spacecraft and instrumentation technology, so our understanding of the solar terrestrial system and the processes which give rise to the aurora has also improved. The exact nature of the magnetosphere and all the processes within it are far from understood, and as with many studies, the more we find out, the more there is to explain.

1.2 Thesis Outline

The work contained within this thesis has been based on the analysis of data collected from the CRRES mission. The spacecraft is reviewed, with details of its mission, orbit, and instrumentation in Chapter 3. The instruments which provided the data presented here are discussed, particularly the Low Energy Plasma Analyzer (LEPA), but also the Plasma Wave Experiment (PWE) and the onboard magnetometer.

The thesis is concerned with investigating a type of event occurring on auroral field lines, first identified within the LEPA data set by *Johnstone et al.*, 1994, and known as a 'Field Aligned electron Event' or FAE. These events are investigated with respect to their global distribution and their role in the magnetospheric system, and with respect to the microphysics associated with their development. In Chapter 4 the characteristics of these events are reviewed. The location of the events within the magnetosphere is studied, as is the temporal relationship with substorm onset.

A feature seen in many of the FAEs is the apparent acceleration of particles as they are scattered out of the loss cone. In Chapter 5 the observations of this acceleration are reviewed, and in Chapter 6 their relation to the wave activity seen by the PWE is studied. The theoretical diffusion curves due to whistler mode waves suggested by *Summers et al.*, 1998, (which are based on the isotropic cold plasma dispersion relation) cannot explain the scattering paths seen in the LEPA data. We have examined the theoretical diffusion curves in the context of a field aligned electron distribution and have suggested a more realistic dispersion relation, which may radically change the theoretical diffusion curves.

The role of the FAEs is examined in Chapter 7. High latitude observations of electron beams made with a number of spacecraft are reviewed, particularly those made with the FAST satellite. The electron beams seen at high latitudes are thought to be carriers of field aligned currents, and we suggest that they are the source of the FAEs seen with CRRES. The CRRES LEPA and magnetometer FAE observations

are further discussed in the context of field aligned currents.

Before the discussion of the FAEs, the Earth's magnetosphere and some of the processes at work within it are introduced in Chapter 2.

Chapter 2

The Earth's Magnetosphere

2.1 The Structure of the Magnetosphere

2.1.1 The Closed Magnetosphere

A great deal of the magnetospheric system can be explained using the ideal magneto-hydrodynamics (MHD) approximation to describe the plasma behavior. Under ideal MHD we can employ the frozen-in flux condition, which essentially implies that the plasma is frozen, or tied, to the magnetic field. The frozen-in flux condition means that the magnetic flux threading a surface will remain constant as the plasma moves through a system. Practically, this means that a population of plasma occupying a particular field line, will always occupy that field line. It is the fact that the plasma is 'frozen' into the magnetosphere which allows the geomagnetic field to protect the Earth from the solar wind, as the frozen-in flux condition inhibits the mixing of plasma populations.

Figure 2.1 shows the structure of the magnetosphere assuming ideal frozen-in flow conditions. Under these conditions the solar wind plasma is separated entirely from that of the magnetosphere. The boundary which separates the two populations is known as the magnetopause. The Earth's dipole field is compressed on the dayside

and dragged out on the night side by the solar wind. As the Earth's magnetosphere is impeding the solar wind flow, which is supersonic, a collisionless bow shock forms upstream of the magnetosphere. As it crosses the bow shock, the solar wind plasma is slowed, compressed and heated. The magnetopause on the dayside will lie at the point where the magnetic pressure of the magnetospheric plasma equals the dynamic pressure in the solar wind plasma. The magnetopause boundary constitutes a current sheet as the magnetic field changes abruptly across it, in both magnitude and direction. Similarly, the stretched magnetotail's magnetic field geometry gives rise to a cross-tail current sheet flowing east to west. Inside the magnetosphere, trapped plasma co-rotates with the earth, due to atmospheric drag. In reality the frozen-in flux condition does not always hold, and the closed magnetosphere model illustrated above does not tell the full story.

2.1.2 The Open Magnetosphere

Ideal MHD only holds while the magnetic field changes slowly on the length and time scales of the motion of individual charged particles (see Section 2.2). When the direction of the magnetic field in the magnetosheath differs greatly from that inside the magnetopause there is a large magnetic shear across the magnetopause current sheet, leading to the possibility of magnetic reconnection (a violation of frozen-in flux). The extreme example of the situation outlined above occurs when the Interplanetary Magnetic Field (IMF) has only a southward component (where north is defined as lying along the Earth's dipole axis) as illustrated in Figure 2.2. It is the breakdown of the frozen-in flux condition which allows energy and matter to be transferred between the solar wind and the magnetosphere.

In the case shown in Figure 2.2, the magnetic fields on either side of the boundary diffuse into the current sheet forming an x-type geometry, at the centre of which there is a null point in the field. Following reconnection, a field line will be occupied by

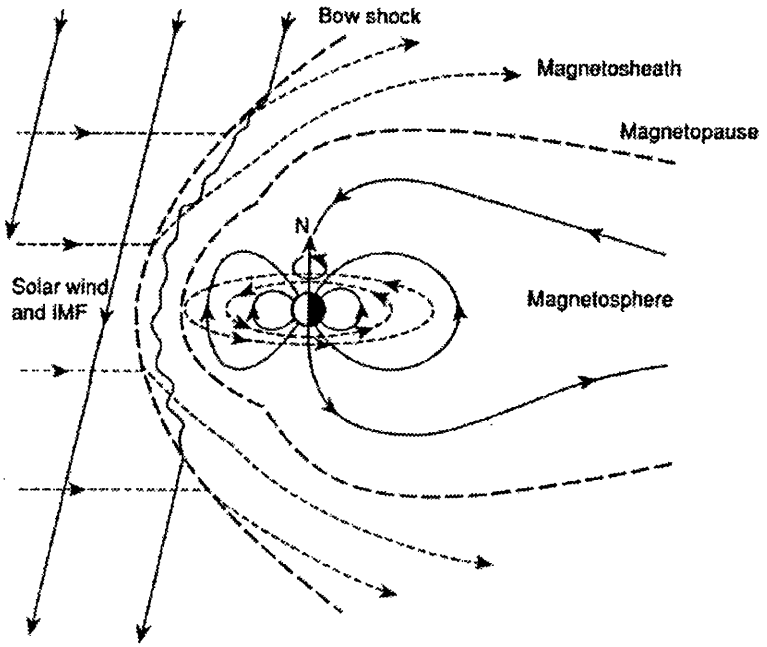

Figure 2.1: A sketch of the magnetosphere under the frozen-in flow conditions (in the noon-midnight meridian plane). The solid lines indicate magnetic field lines, and the arrowed dashed lines indicate the plasma stream lines. The heavy dashed lines indicate the principal boundaries (bow shock and magnetopause). [*Cowley*, 1993].

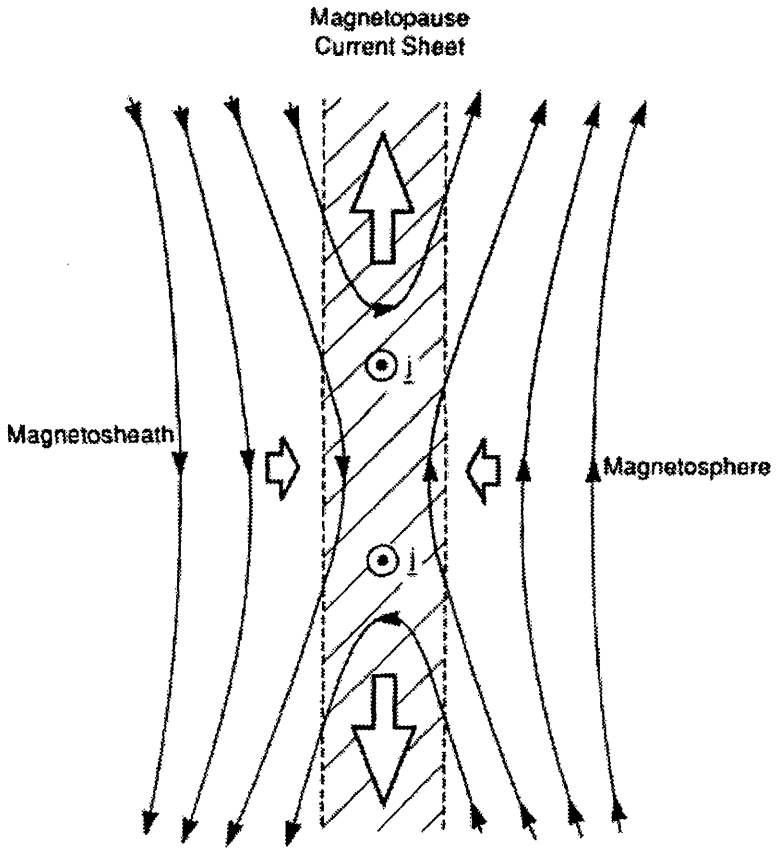

Figure 2.2: A sketch showing the x-type magnetic field configuration at the magnetopause leading to reconnection [*Cowley*, 1993].

both magnetospheric and magnetosheath plasma, with one end reaching the Earth and the other open to the solar wind. The magnetic tension effect will cause these newly reconnected field lines to move away from the reconnection site.

Once reconnected, in addition to the motion in response to the tension force the plasma on open field lines is dragged anti-sunward with the solar wind flow, forming the long magnetotail. A situation arises where a second x-type field configuration can exist in the tail. Here field lines are reconnected, with those tailward of the reconnection site disconnected from the magnetosphere and free to flow with the solar wind, and those earthward becoming closed (illustrated in Figure 2.3). The closed field lines then flow back around the Earth, towards the dayside. The overall process resulting in a large scale cyclic plasma convection system, in which open field lines flow anti-sunward over the poles and closed field lines move sunward through the central magnetosphere. The convective cycle is shown in Figure 2.4.

2.1.3 Plasma Populations in the Magnetosphere

Figure 2.5 shows schematically the different plasma populations that exist within the Earth's magnetosphere. These populations are not necessarily mutually exclusive and may occupy the same regions of space. It will be shown later (in Section 2.5) that the magnetosphere is a highly dynamic system and as such the boundaries described below are not fixed. Closest to the planet (at the equator) exists the plasmasphere, the region of corotating cold ($\sim$ 1 eV), dense plasma, extending out to 4 or $5R_E$. The outer edge of the plasmasphere, the plasmapause, is usually characterised by a sharp drop in density. Hot ($\sim$ 100 keV) trapped particles make up the trapped radiation belts. The radiation belt particles extend from equatorial altitudes of 1000 km out to around $6R_E$ following field lines. The plasma sheet lies tailward of the Earth and consists of hot (keV) particles on newly reconnected field lines. Between the plasma sheet and the low density tail lobes lies the plasma sheet boundary layer. The plasma

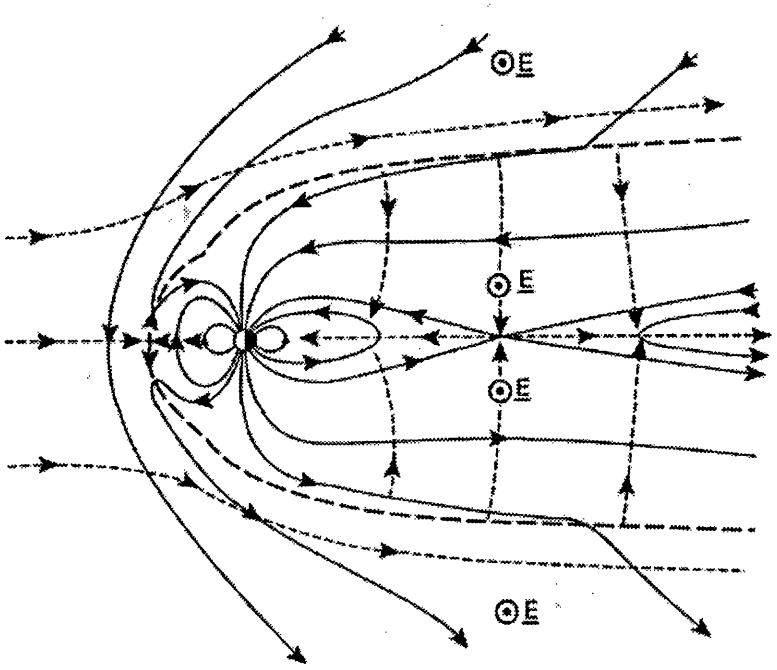

Figure 2.3: A sketch of the 'open' magnetosphere in the noon-midnight meridian plane as suggested by *Dungey*, 1961. The solid lines indicate magnetic field lines, and the arrowed dashed lines indicate the plasma stream lines. The heavy dashed lines indicate the principal boundaries (bow shock and magnetopause). [*Cowley*, 1993].

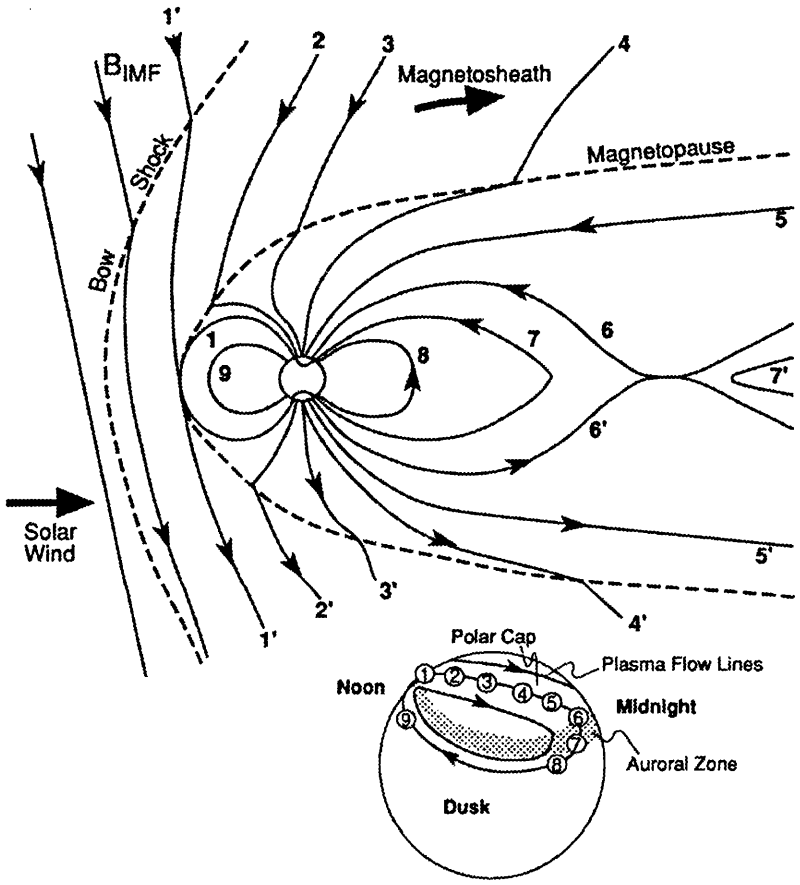

Figure 2.4: Flow of plasma within a reconnection driven convective magnetosphere. The closed magnetic field line 1 reconnects with the solar wind field line 1′ forming two open field lines, 2 and 2′. Field lines 2-5 (and 2′-5′) show the progression as the field line is dragged back by the solar wind forming the magnetotail. Field lines 6 and 6′ reconnect in the tail, after which the newly closed field line returns to the dayside at lower latitudes (7-9). Tailward of the reconnection site the field line open to the solar wind moves downtail (7′). The inset illustrates the movement of the field line footpoints in the ionosphere, giving rise to a two cell convection pattern. [*Hughes*, 1995].

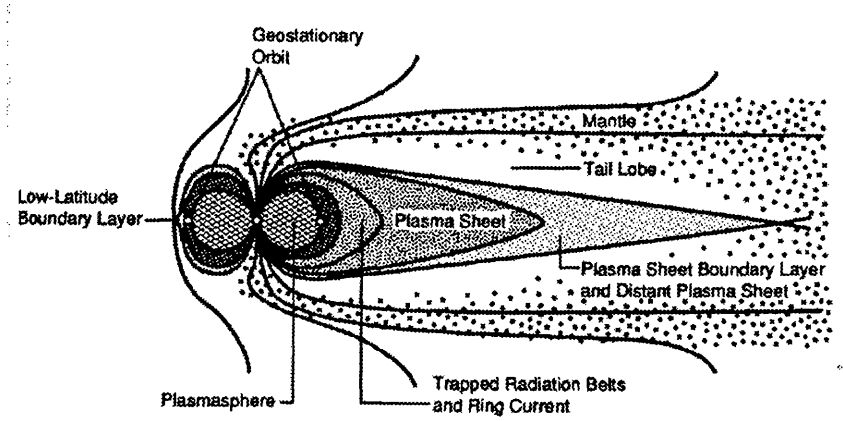

Figure 2.5: Schematic view of the plasma regions of the Earth's magnetosphere viewed in the noon-midnight meridian. [*Wolf*, 1995].

in this region is hotter than that in the central plasma sheet, has densities between that of the central plasma sheet and that of the tail lobes, and probably lies on closed field lines. Further details of the magnetospheric configuration can be found in *Wolf*, 1995.

2.2 Trapped Particle Motion in the Magnetosphere

While the MHD approximation (along with reconnection) can explain much of the large scale structure and behavior of the magnetospheric system we need to study the motion of individual particles to explain many further features.

It is well known that energetic charged particles are trapped in the magnetic bottle geometry of the Earth's magnetic field (see Figure 2.6). These particles undertake three basic types of motion, Firstly they gyrate about the magnetic field, in a variable pitch helix, with a gyrofrequency, Ω_e, given by

$$\Omega_e = eB/m_e. \tag{2.1}$$

The particle's magnetic moment, μ, also known as the first adiabatic invariant, is

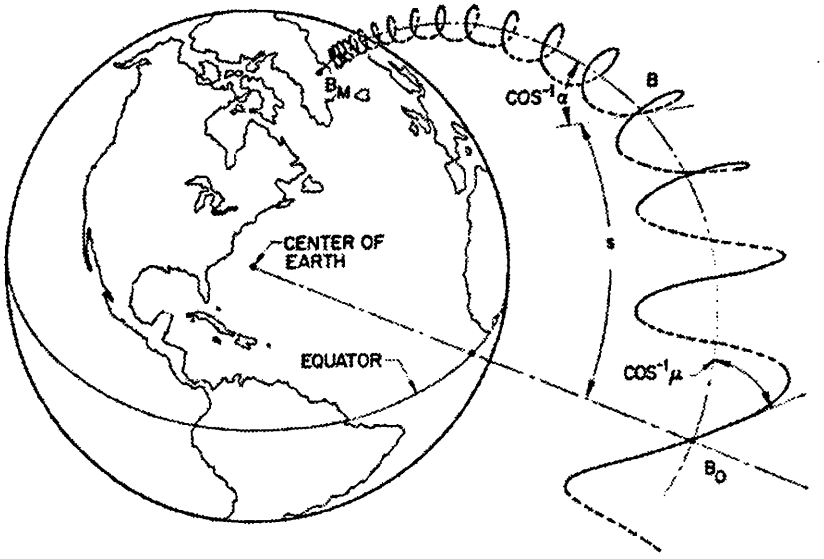

Figure 2.6: Motion of a charged particle in the geomagnetic field [*Walt and MacDonald*, 1964].

associated with the particle's gyromotion. This quantity remains constant as long as any changes to the magnetic field occur gradually over timescales of the gyroperiod and lengthscales of the gyroradius. Assuming that the electric field parallel to the magnetic field is zero, motions along the field line do not change the kinetic energy of the particle, i.e. the total velocity, v, of a non-relativistic particle, remains constant though the magnetic field strength may change. Combining this fact with Equation 2.1 implies that a particle's pitch angle, α, defined as the angle between the particle's velocity and the magnetic field direction, i.e.

$$\alpha = \tan^{-1}(v_{\perp}/v_{\parallel}), \tag{2.2}$$

where $\parallel$ and $\perp$ refer to the magnetic field direction, will increase with increasing field strength, until it reaches 90°. When a particle's pitch angle equals 90° the gradient in magnetic field strength will force the particle to reverse its direction of travel along the field line (while still gyrating in the same sense), a process is known as magnetic

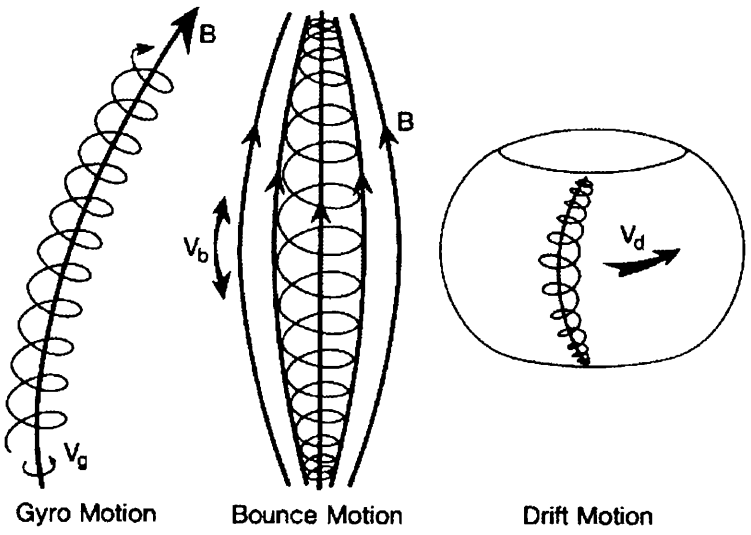

Figure 2.7: The three basic types of motion associated with charged particles in the magnetosphere [*Kivelson*, 1995].

mirroring. A particle will mirror when the field strength reaches B_M, given by

$$B_m = \frac{1}{2}\frac{mv^2}{\mu}. \tag{2.3}$$

If the idea of magnetic mirroring is extended to the geometry of a flux tube as in Figure 2.7, it is easy to see that a charged particle will perform bounce motion, between two mirror points, as indicated. Following a magnetic field line of the Earth's magnetic field, with an equatorial field strength, B_0, an electron with an equatorial pitch angle, α_0, will mirror when the magnetic field reaches B_m, given by

$$B_m = \frac{B_0}{\sin^2 \alpha_0}. \tag{2.4}$$

In the dipole-like geometry of the geomagnetic field, particles with small equatorial pitch angles mirror closer to the Earth than those with large equatorial pitch angles, which mirror near the equator. The second adiabatic invariant, J, is associated with the bounce motion and is defined as;

$$J = \oint mv_{\|} ds, \tag{2.5}$$

where m is the particle's mass, and s is the bounce path (from mirror point m to the conjugate mirror point m' to mirror point m). J will remain constant if changes in the magnetic field take place on timescales long compared to the bounce period (or if motion of the particle around the Earth is such that the field seen by the particle is gradually changing).

The third type of motion is drift motion, where the particles drift azimuthally around the Earth. The third adiabatic invariant, Φ, which is equal to the magnetic flux enclosed by the drift shell of a particle, is associated with the drift motion. Φ remains constant while the magnetic field changes on timescales small compared to the drift period.

The drift velocity of a charged particle in a time stationary field is given by

$$\mathbf{v}_D = \frac{W_\perp \mathbf{B} \times \nabla B}{qB^3} + \frac{2W_{||}\hat{\mathbf{r}}_c \times \mathbf{B}}{qR_c B^2} + \frac{\mathbf{E} \times \mathbf{B}}{B^2} + \frac{\mathbf{F}_{ext} \times \mathbf{B}}{qB^2}, \tag{2.6}$$

where $W_\perp$ and $W_{||}$ are the particle's kinetic energy perpendicular and parallel to the magnetic field respectively (i.e. $W_\perp = mv_\perp^2/2$ and $W_{||} = mv_{||}^2/2$), R_c is the radius of curvature of the magnetic field line and $\hat{\mathbf{r}}_c$ is a unit vector radially outward from the center of curvature.

The first term of Equation 2.6 describes what is known as gradient drift, which arises as a result of the gradient in magnetic field strength. The second term in Equation 2.6 describes the curvature drift, which arises as a result of motion along a curved magnetic field line. The third term in Equation 2.6 is the $\mathbf{E} \times \mathbf{B}$ drift, and describes the drift motion caused by the presence of an electric field. The final term in Equation 2.6 represents the drift experienced due to external (non-electromagnetic forces). In the case of the magnetosphere, gravity is usually the only external force acting and the drift produced is small and thus ignored.

Which of the drift terms is dominant varies with the energy of a particle and the radial distance from Earth. Near the Earth the gradient drift dominates. Moving further away from the Earth The $\mathbf{E} \times \mathbf{B}$ drift becomes increasingly important, initially

for the highest energy particles, then becoming dominant for lower energy particles as radial distance from the Earth increasese. In the case of the electrons which are looked at within this study (6 eV - 30 keV at 5 - 6 R_E) the situation is not clear. Normally the lower energy electrons (< 1 keV) will be dominated by the $\mathbf{E} \times \mathbf{B}$ drift, and the gradient-curvature drifts will have increasing effect at higher energies. However, the electromagnetic field properties in the region of the magnetosphere we are studying can vary a great deal; the electric field strength, the magnetic field strength, curvature, and gradient, can vary, all of which will affect the various drift velocities. The FAEs are generally seen as covering a limited energy range, and fairly short lived, which means that drift motions will play little role in shaping the electron distributions in question.

All of the drifts detailed in Equation 2.6 are charge dependent, with the exception of the $\mathbf{E} \times \mathbf{B}$ drift. It is the gradient and curvature drifts, sending electrons eastwards and ions westwards, which gives rise to the ring current.

2.3 The Aurora

The aurora is a visible manifestation of the interaction between the solar wind and the magnetosphere. The aurora is caused by particles from the magnetosphere which reach the atmosphere, ionising and exciting atmospheric atoms. As the atmospheric atoms recombine and return to their ground state they release energy in the form of visible light. The colour of the auroral light depends on the energy and species (i.e. electron, protons, and various other ions) of the incident particles, the species of atom they interact with, and the excitation they cause. Predominantly, auroral light is seen as red and green, though it extends into both the ultraviolet and infrared. A related X-ray aurora is caused due to the incident particle releasing some of its energy as bremsstrahlung radiation.

In the case of most magnetospheric particles the magnetic mirror point is well above the Earth's atmosphere (which reaches out to about 200 km) and the particles continually mirror back and forth. If, however, the mirror point is located within the atmosphere, the particle will interact with the atmosphere as described above and will be removed from the magnetic bottle, in a process known as precipitation. This idea leads to the concept of a loss cone, i.e. any particle with a pitch angle less than the half angle of the loss cone will be lost through precipitation. The size of the loss cone is often given in terms of equatorial pitch angle. The size of the loss cone will increase with B, along a field line moving away from the equator, and will reach 90° at the edge of the atmosphere. This analysis assumes that the atmosphere has a distinct boundary, which is of course not the case. In reality the atmospheric density decreases with increasing altitude and so does the probability of a particle being scattered by the atmosphere. The size of the loss cone at the equator at 5 - 6 R_E is around a few degrees.

The aurorae generally lie on an oval around each pole between 60° and 70° magnetic latitude (see Section 2.7), with the oval on the sunward side lying at higher magnetic latitudes than the anti-sunward side. The precipitation process causes the conductivity of the ionosphere to increase in the auroral oval, enhancing the eastward and westward electrojet currents described in Section 2.4.

The aurora is often classified into two types according to morphology; the diffuse and the discrete aurora. The diffuse aurora is so-called due to its apparent lack of structure. In fact there are structures within the diffuse aurora, but they are weak and difficult to observe. The diffuse aurora is thought to be caused by the slow pitch angle diffusion of trapped particles into the loss cone and is present almost continually. Diffuse aurora is seen in the equatorward part of the auroral oval with the strongest emissions occurring in the post-midnight sector, mainly caused by electrons.

The discrete aurora is what is classically known as aurora, taking its name from

the fact that it a highly structured phenomenon. The term discrete aurora covers a range of auroral forms including quiet auroral arcs, spirals, curls, folds, the auroral bulge, omega bands, sun-aligned arcs, and afternoon auroral spots. A number of spatial scales can be associated with the discrete aurora (taken in the north-south direction), (1) the thickness of fine scale auroral arcs $\sim$ 0.1 km, (2) the thickness of dynamic arc systems $\sim$ 1 km, (3) the thickness of the region of diffuse glow around arcs $\sim$ 10 km, (4) the separation of auroral arcs $\sim$ 10 km, and (5) the thickness of the auroral zone $\sim$ 100 km [e.g. *Borovsky*, 1993b]. During active times it is normal for many east-west aligned arc forms to fill the auroral region. Some of the different auroral forms covering a range of scales can be seen in Figure 2.8. Field aligned acceleration plays an important part in the formation of discrete auroral arcs, producing inverted-V precipitation. The discrete aurora are seen in the poleward part of the auroral oval, and are more pronounced in the pre-midnight sector, reflecting the dynamics of the magnetotail (i.e. the occurence of discrete aurora is much more during geomagnetically active times).

The shape of the auroral oval, and the amount of light produced can vary a great deal depending on geomagnetic conditions (especially true of the discrete aurora).

2.4 Magnetospheric Current Systems

Figure 2.9 shows schematically the main currents flowing in the magnetosphere. We have already discussed, in Section 2.1.1, the magnetopause current, and the neutral sheet or cross-tail current. Note that in Figure 2.9 the neutral sheet (cross tail) current flow merges with the magnetopause current in the tail, closing the system. The other two magnetospheric currents shown in Figure 2.9 are the ring current and field aligned currents (FACs). It was noted in Section 2.2, that the ring current arises as a result of particle motion under the influence of the gradient and curvature of

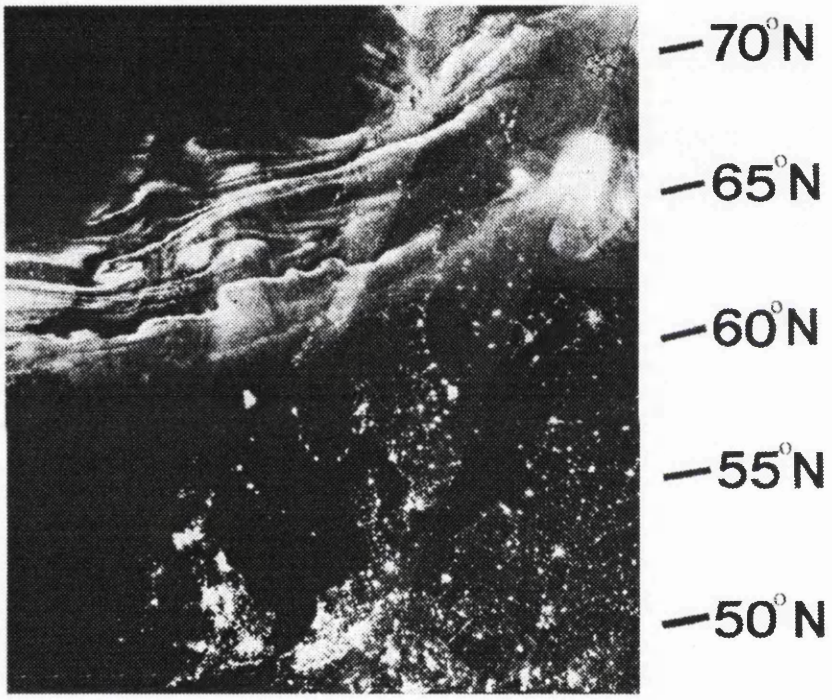

Figure 2.8: DMSP satellite picture of the aurora over western Europe taken at a geomagnetically active time. Within the auroral region a number of arcs and curls can be seen, over different spatial scales. Note that the British Isles (illuminated by street lights) can be seen in the lower left part of the picture, with Scandinavia and mainland Europe to the right. [*Eather*, 1980]

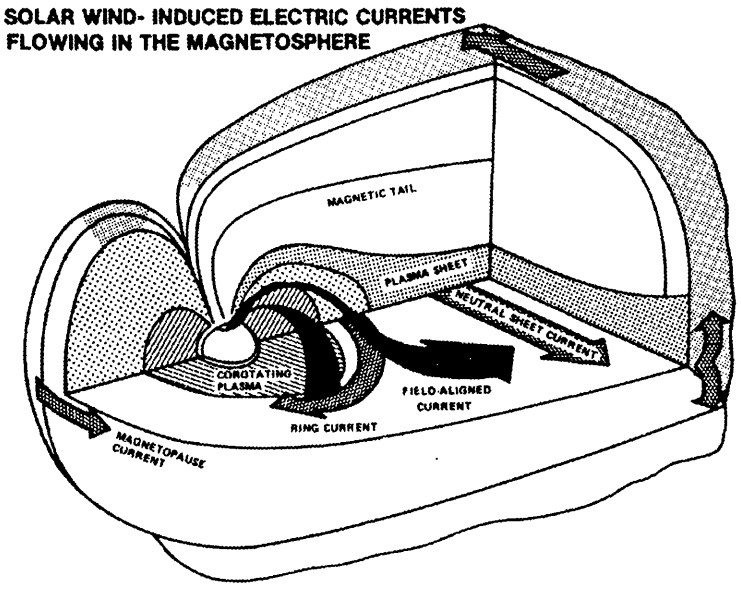

Figure 2.9: Schematic representation of the currents flowing in the Earth's magnetosphere [*Parks*, 1991].

the Earth's magnetic field. The FACs flow into, or out of the ionosphere (connecting via ionospheric currents), along the magnetic field, and merge in equatorial regions with the other current systems. It is these FACs which provide a link between the ionosphere and the distant magnetospheric regions. The FACs can more clearly be understood if we look at the ionospheric current system.

Above around 75 km the electron gyrofrequency is greater than the electron neutral collision frequency, and the electron guiding center motion is controlled by the $\mathbf{E} \times \mathbf{B}$ drift. The ion neutral collision frequency, below about 125 km, is greater than the ion cyclotron frequency, so collisions interrupt the ion's gyromotion and their net movement is in the direction of $\mathbf{E}$. The result of the electron and ion motion in the 'dynamo layer' ($\sim$ 75-125 km altitude) is a current flowing along $-\mathbf{E} \times \mathbf{B}$ (Hall current) carried by the electrons, and a current flowing perpendicular to $\mathbf{B}$ and parallel to $\mathbf{E}$ (Pedersen current) carried by the ions.

Figure 2.10 shows the various ingredients of the auroral electrojet system. Due to the particle precipitation which causes the aurora (see Section 2.3) there is enhanced conductivity within the auroral oval, Figure 2.10 (a). The enhanced conductivity combined with the electric field pattern, Figure 2.10 (b), set up as a result of the two cell convection pattern (Figure 2.4) gives rise to the Hall and Pedersen Currents shown in Figure 2.10 (c and d). There is a flow reversal region near midnight, known as the Harang discontinuity, where field lines which have convected over the polar cap either flow east or west (and thus giving a peculiar electric field pattern).

The Hall currents originate around noon, and are fed by downward FACs. The eastward electrojet flows in the afternoon sector, terminating in the region of the Harang discontinuity. Here the current partially flows out of the ionosphere along magnetic field lines, and partially flows polewards to join the westward electrojet. The westward electrojet flows in the morning sector, and extends into the evening sector where it then leaves the ionosphere via FACs.

The Pedersen currents flow poleward in the region of the eastward electrojet, connecting regions of downward FAC in the equatorward half of the auroral oval, to upward FAC in the poleward half of the auroral oval. In the region of the westward electrojet the situation is reversed with equatorward flow connecting regions of downward FAC in the poleward half of the auroral oval, to upward FAC in the equatorward half of the auroral oval. In the region of the Harang discontinuity the situation is less clear with the two Pedersen current systems overlapping and giving rise to three current sheets. The FAC sheets seen nearest the poles are named Region-1 currents and the FAC sheets seen in the equatorward half of the auroral oval are named Region-2 currents. The measured distribution and direction of the Region-1 and Region-2 currents is shown in Figure 2.11. The Region-1 currents lie along the boundary between the anti-sunward convection over the poles and the return flow at lower latitudes, and the Region-2 currents lie along the boundary between the return convective flow and

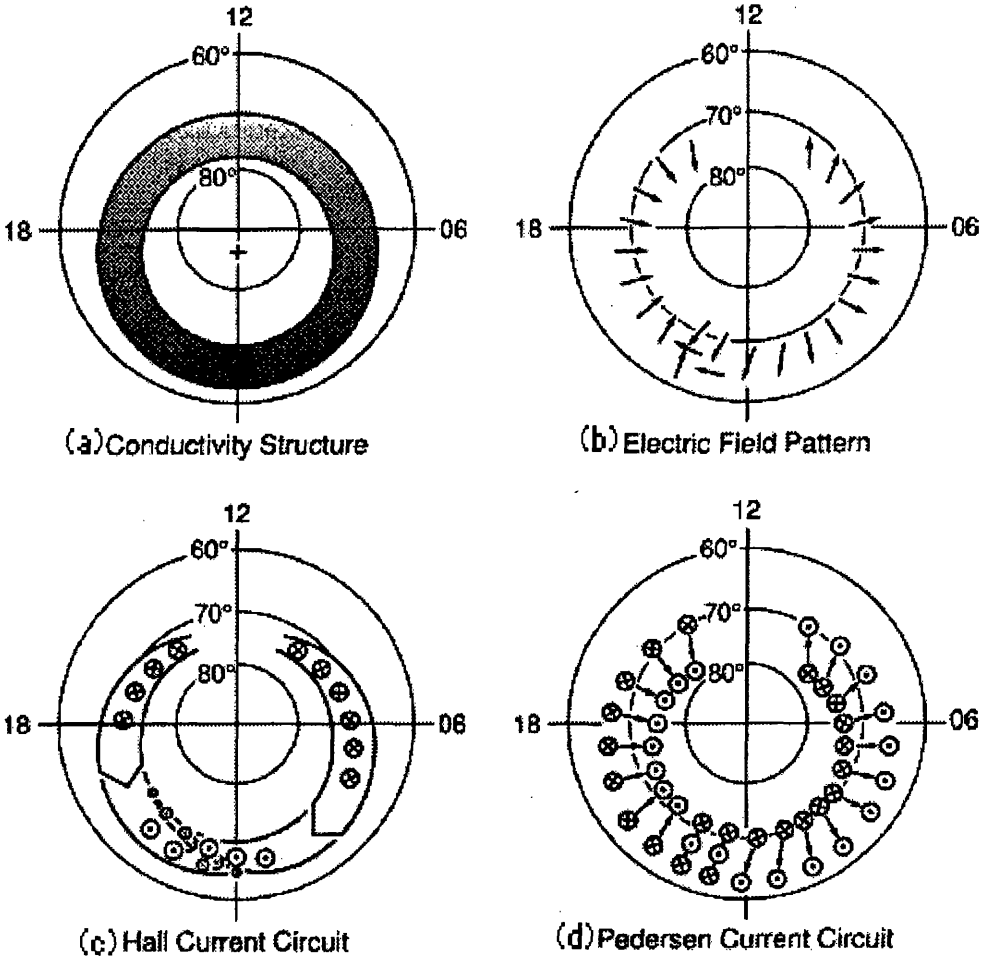

Figure 2.10: Synopsis of the ingredients of the auroral electrojet system [*Baumjohan and Treumann*, 1996].

the corotating region of the magnetosphere.

2.5 Substorms

The solar wind flow is far from uniform. There are continual changes in velocity, and density, as well changes in both the magnetic field strength and direction. These changes affect the dayside reconnection rate so that the convection within the magnetospheric system described in Section 2.1.2 is far from steady. Even if the reconnection taking place on the dayside were steady it seems that the nightside reconnection is an inherently non-steady process. The response of the magnetosphere to the changing dayside and nightside reconnection rates takes the form of magnetospheric substorms.

The nature and triggering mechanisms of substorms are areas of controversy, with many models proposed to explain the phenomena. While this thesis is concerned with substorm related phenomenon it is not directly concerned with the workings of the substorm process, and as such it neither subscribes to any particular model nor aims to support one over another. A review of the various proposed substorm models can be found in *McPherron*, 1995.

2.5.1 Phases of a Substorm

The magnetospheric substorm is normally described in terms of three phases; the growth phase, the expansion phase, and the recovery phase. Associated with each of these phases are auroral responses, shown in Figure 2.12.

Growth Phase

During the growth phase the IMF has a predominantly southward component allowing reconnection to take place on the dayside. The dayside reconnection rate exceeds that on the nightside, such that the geomagnetic field lines on the dayside are eroded and

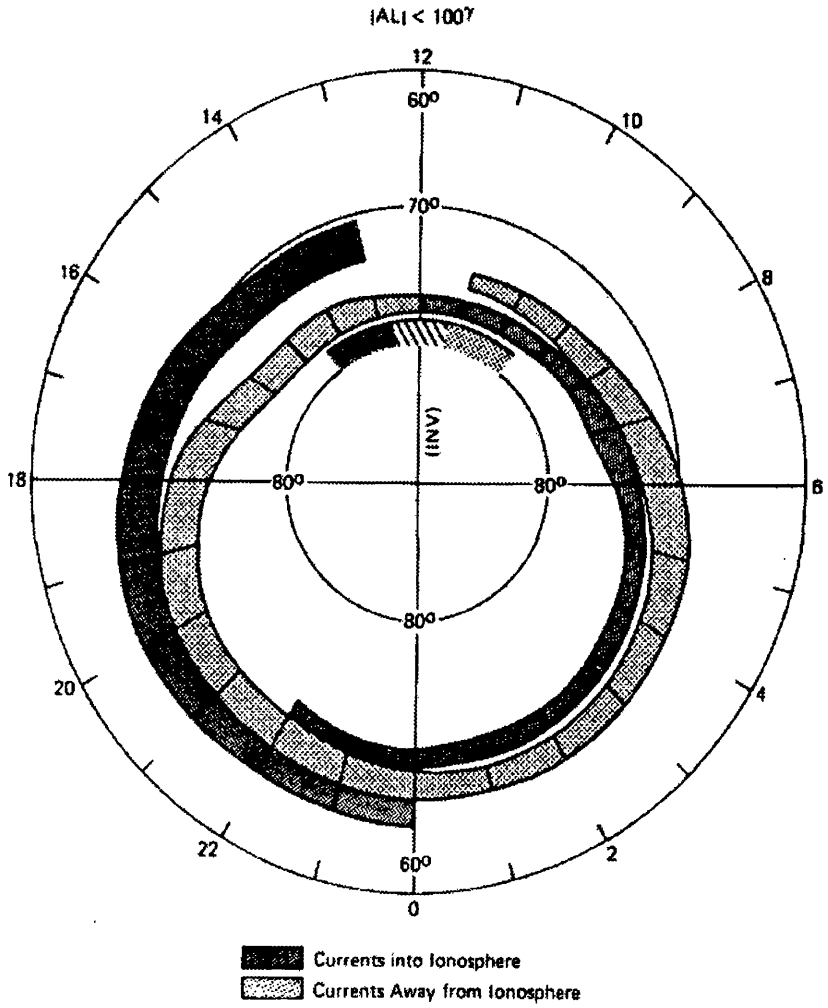

Figure 2.11: A summary of the distribution and direction of the Region-1 and Region-2 currents during weakly disturbed conditions. The distribution is based on data obtained by the Triad mission. [*Iijima and Potermra*, 1976].

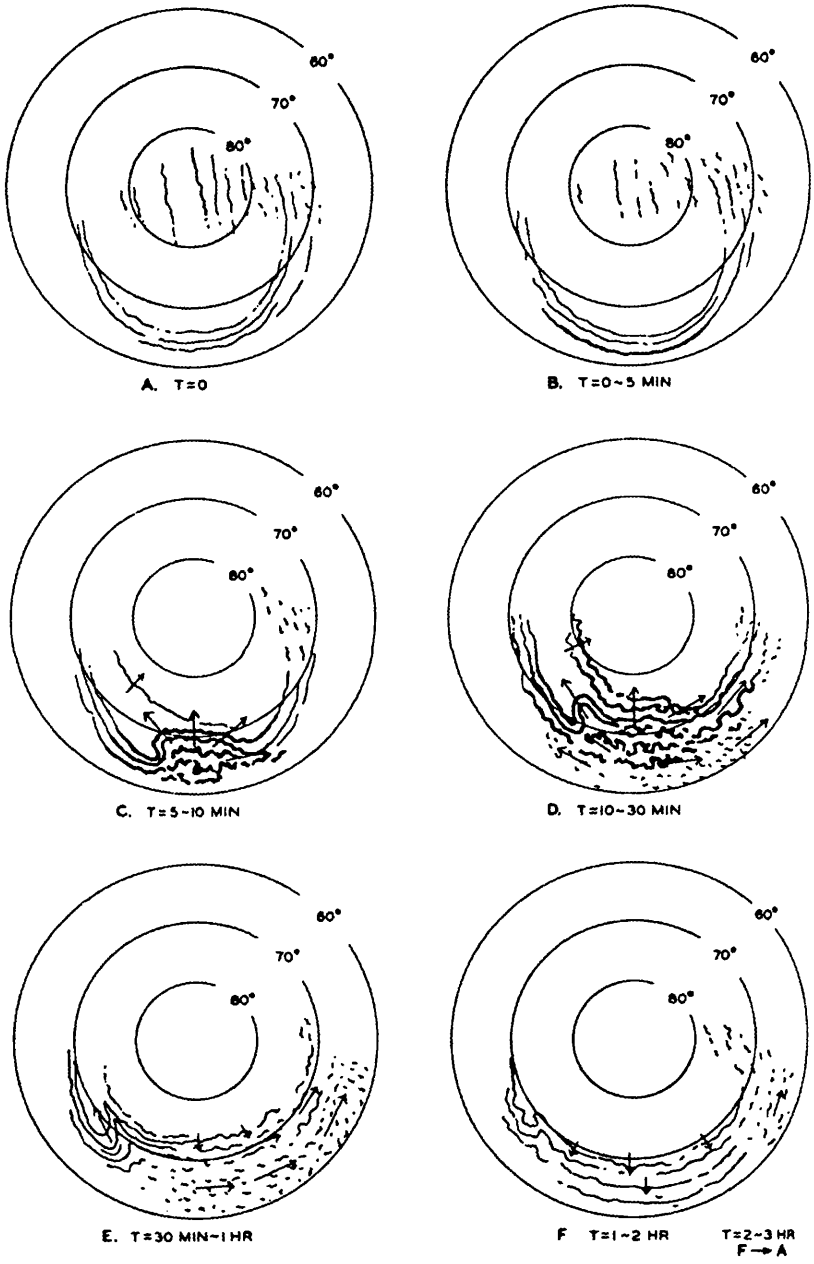

Figure 2.12: Schematic representation of six stages in the development of an auroral substorm, as determined from all-sky camera data during the International Geophysical Year (1957) [*Akasofu*, 1964].

energy is stored in the magnetotail. The field lines on the nightside become stretched and more tail like, supported by an enhanced cross-tail current. There is strong convection from the dayside to the nightside and thus the convection related currents are enhanced. The auroral response to the growth phase is shown in Figure 2.12 (a), where multiple arc systems drifts slowly equatorward. As more field lines become open, so the polar cap expands.

The growth phase typically lasts for around an hour.

Expansion Phase

The expansion phase starts with substorm onset. In terms of the auroral substorm, onset is signified by a sudden brightening of a portion of the most equatorial arc somewhere in the pre-midnight sector, Figure 2.12 (b). The brightening then rapidly expands westward and poleward, Figure 2.12 (c). This expansion continues, and within a short period of time (5-10 minutes) the enhanced auroral activity covers a broad region spanning the midnight sector. The auroral bulge develops a sharp kink at its westward edge, which often appears to move westward. This feature is known as the westward traveling surge, Figure 2.12 (d). At the eastern edge of the bulge eastward drifting omega bands appear, Figure 2.12 (d). Omega bands are torch-like auroral forms extending poleward from the diffuse aurora. At the equatorwards edge of the eastern region, dim patches of pulsating aurora are often seen. Towards the end of the expansion phase the auroral activity begins to dim, quiet arcs reappear, and the westward traveling surge is replaced by a westward traveling loop, Figure 2.12 (e). Pulsating aurora can persist in the morning sector for some time.

In terms of the magnetospheric substorm the expansion phase covers the period of time when the energy stored within the magnetotail is released. Onset is characterised by a surge of tail plasma earthward, as the nightside field lines become rapidly more dipolar (dipolarisation). Injections of energetic (tens to hundreds of keV) particles are

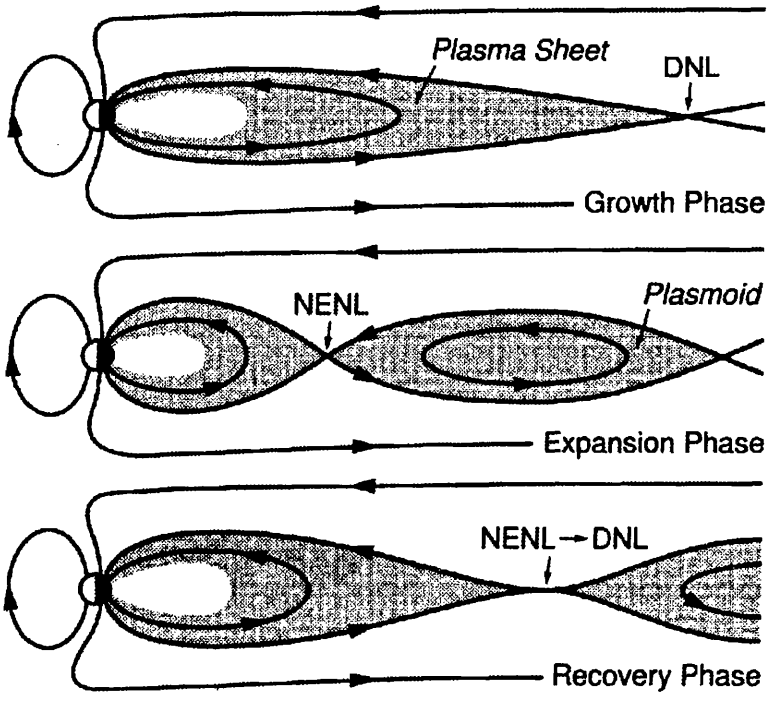

Figure 2.13: Reconfiguration of the magnetotail during a substorm [*Baumjohan and Treumann*, 1996].

seen close to geosynchronous orbit (and closer to the Earth). Pi2 pulsations (irregular pulsations with periods 40-150 s) are normally seen in ground based magnetometer data around the time of onset.

Many observations and substorm models suggest that a second reconnection site forms earthward of the initial Distant Neutral Line (DNL) (shown in Figure 2.13). The second reconnection site is called the Near Earth Neutral Line (NENL) and occurs between 15 and 30 R_E from the earth. Reconnection at the NENL is very rapid, occuring around the same time as the onset phenomenon. The field lines earthward of the NENL become closed, contract and become more dipolar. Tailward of the NENL, field lines become closed and hence disconnected from the Earth, forming a 'plasmoid' between the NENL and the DNL, which later convects downstream into the solar wind.

The expansion phase typically lasts for 30 minutes to an hour.

Recovery Phase

The recovery phase covers the time when the magnetosphere returns to its quiet state. The NENL moves slowly down tail to replace the old distant reconnection site, with nightside field lines becoming stretched back into a tail-like geometry. In the aurora, the active bulge disappears, and quiet arcs may reappear, Figure 2.12 (f). In the case when the IMF remains southward the recovery phase may be interrupted by the start of a new growth phase, and the substorm process may continue in a cyclic fashion. Otherwise a substorm may be seen as an isolated event.

The recovery phase can last between 1 and 2 hours, though it may be shorter if interrupted by the start of a new growth phase.

2.5.2 Substorm Current Wedge

Associated with the brightening in the auroral bulge during the expansion phase is the enhancement of westward current flow, within the bulge region, know as the auroral electrojet. The auroral electrojet arises as a result of the increased conductivity in the region of strong precipitation. This electrojet forms part of a current system which arises only at substorm times, known as the substorm current wedge (illustrated schematically in Figure 2.14). It is thought that part of the cross-tail current is diverted, along field lines, into the ionosphere, passing through the auroral electrojet, before rejoining the cross-tail current.

The decreased cross-tail current is associated with the field becoming less stretched, i.e. dipolarisation. As the expansion phase continues the auroral electrojet grows in east-west extent, and as this happens the substorm current wedge widens. Along with the widening of the substorm current wedge the magnetic signatures of dipolarisation also spread away from midnight.

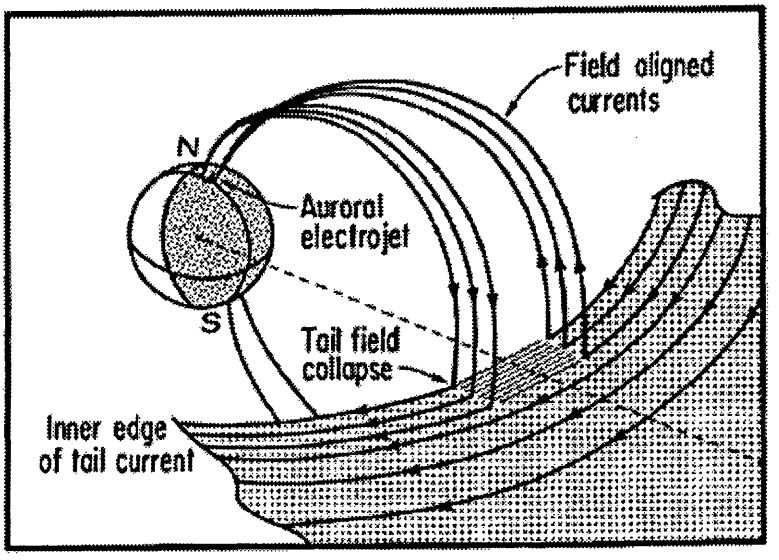

Figure 2.14: Schematic of the substorm current wedge [*McPherron et al.*, 1973].

2.6 Waves

The nature of a plasma, where electrons and ions respond to the magnetic and electric field perturbations, results in a range of wave modes which are able to propagate. Very low frequency waves ($\omega \ll \Omega_i$) can be explained using ideal MHD, as the electron inertia has little effect. At higher frequencies the charged particle dynamics become important and MHD is no longer valid. There are a number of wave modes, not described by MHD, which propagate in the Earth's magnetosphere.

2.6.1 Plasma Oscillations

If the electrons in an unmagnetised plasma were displaced from a uniform background by a small distance, an electric field would exist in a direction so as to restore the electrons to their original position. Due to their inertia, the electrons will move back and forth around the equilibrium position oscillating with the 'plasma frequency' ω_{pe},

given by

$$\omega_{pe} = \left(\frac{n_e e^2}{m_e \epsilon_0}\right)^{\frac{1}{2}}, \tag{2.7}$$

where m_e is the electron mass. ω_{pe} is the natural frequency with which waves will propagate in an unmagnetised plasma in response to small displacements.

In a magnetised plasma the situation changes slightly as electron gyromotion comes into play. If the displacement of electrons occurs perpendicular to the magnetic field there is a resonance at Ω_{UHR}, which is given by

$$\Omega_{UHR}^2 = \Omega_e^2 + \omega_{pe}^2. \tag{2.8}$$

Ω_{UHR} is known as the Upper Hybrid Resonance (UHR) frequency, and occurs when the gyromotion and restoring motion combine in phase. Displacement of electrons parallel to the magnetic field results in plasma oscillations with frequency ω_{pe} as described above for an unmagnetised plasma.

2.6.2 Wave Modes Found in the Magnetosphere

In this section we review a number of the different wave emissions found in the magnetosphere. This discussion is far from complete, and is not concerned with MHD waves (e.g. Pi2s).

Whistler Mode Waves

Whistler mode emissions are seen propagating at frequencies $\omega < \Omega_e$ inside the plasmasphere as plasmaspheric hiss, and on auroral field lines as chorus. The terms hiss and chorus date back to when measurements of geomagnetic radio emissions were recorded on the ground and played as audio signals. Whistler mode waves are normally right hand circularly polarised waves propagating along or close to the magnetic field direction. Whistler mode waves may interact with energetic gyrating electrons via cyclotron resonance.

Electromagnetic Ion Cyclotron (EMIC) Waves

EMIC emissions are occur at frequencies $\omega \sim \Omega_i$. EMIC waves are mainly seen in the outer magnetosphere ($>7R_E$), though they are also seen near the plasmapause. Near the magnetic equator EMIC waves are left hand polarised, but away from the magnetic equator they are linearly polarised.

Electrostatic Electron Cyclotron Harmonic (ECH) Waves

ECH waves, also known as Bernstein Waves, propagate between the harmonics of Ω_e with the strongest emissions often seen near Ω_{UHR}. The waves are electrostatic, which means that the wave vector $\mathbf{k}$ is parallel to $\mathbf{E}$, and thus the induced magnetic field is small such that it can be neglected. ECH waves propagate at large angles to the magnetic field direction ($\sim 89°$) and are undamped for perpendicular propagation. ECH waves can interact with energetic gyrating electrons as described by *Horne et al.*, 1987.

Auroral Kilometric Radiation (AKR)

AKR is electromagnetic radiation emitted from the auroral regions (10000 km altitude) with frequencies in the range 30-700 kHz. The corresponding wavelengths are the order of kilometers, hence the use of the term kilometric. The generation of AKR is strongly dependent on auroral activity. AKR propagates roughly perpendicular to the magnetic field direction both as right hand (in the extraordinary mode) and left hand mode waves, though the right hand emission is normally dominant.

2.7 Coordinate System

The observations in this thesis are presented in terms of their location within the magnetosphere, and in order to do this we require a coordinate system aligned with the

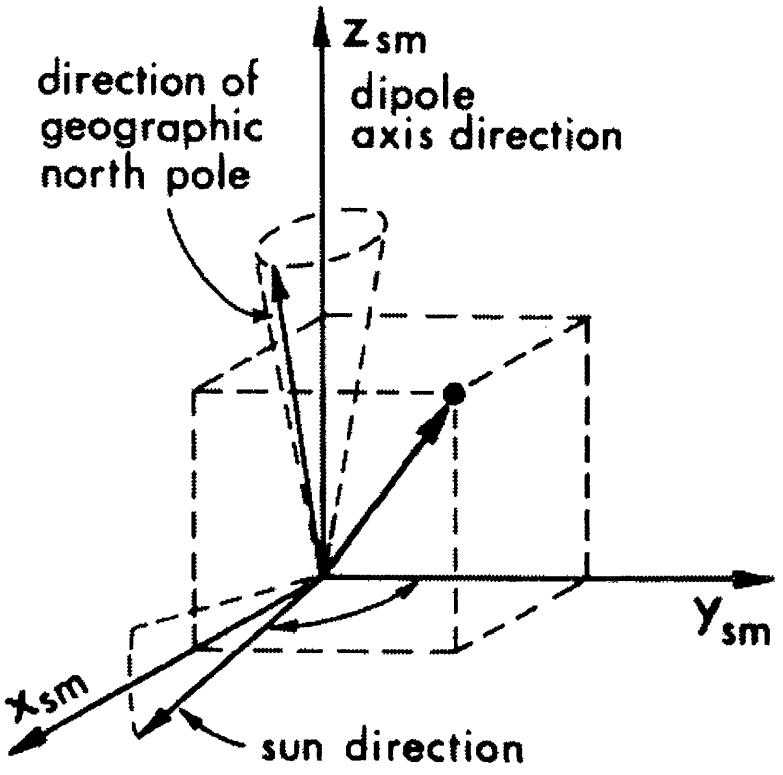

Figure 2.15: The solar-magnetic coordinate system [*Knecht and Shuman*, 1985].

geomagnetic field. The coordinates used are Magnetic Local Time (MLT), magnetic latitude (λ) and L-value.

MLT and magnetic latitude are defined in terms of the solar-magnetic coordinate system (Figure 2.15). In the solar-magnetic coordinate system the z-axis is parallel to the Earth's dipole, and the Sun direction is in the z, x plane. Magnetic latitude is defined relative to the z-axis similarly to the way in which latitude is defined in geographic coordinates. MLT is defined in the x, y plane relative to the x-axis at 0 hours MLT, with 24 hours covering 360°.

In a perfect dipole field the L-value is defined as the distance, in R_E, from the origin to the point where the field line crosses the magnetic equator. In a non-dipole

field geometry the definition is less clear. We want to use the L-value to identify a population of particles occupying a field line. In Section 2.2 we described how particles perform bounce motion along field lines, and have azimuthal drift motions perpendicular to them. Due to the distortions of the Earth's dipole field a particle population on a field line at 12:00 MLT will not cross the equator at the same distance after drifting to 06:00 MLT. The coordinate we need to define is a drift shell, or L-shell.

McIlwain, 1961, introduced the L parameter as a function of B and I, which, in a dipole field satisfies the dipole field definition given above. I is the integral invariant, and is related to the second adiabatic invariant and given by

$$I = \oint_m^{m'} \left(1 - \frac{B}{B_m}\right)^{\frac{1}{2}} ds, \tag{2.9}$$

where B_m is the magnetic field strength at the mirror point, m, and the conjugate mirror point m'. In fact the L-shell for a given point in space is only valid for particles that mirror at that point, and L-values should be defined at the mirror point of a particle population. The reason for the L-shell dependence on pitch angle is that the drift motion is also dependent on pitch angle (note the terms in Equation 2.6 are given in terms of energy parallel and perpendicular to the field). We have found that in the region of space under study in this thesis, the field is such that the dependence of L-shell on pitch angle is small, and thus will be ignored. All L-values are calculated, from the Olson Pfitzer 85 model field [*Pfitzer et al.*, 1988], for particles mirroring at the spacecraft.

One further coordinate that is used is invariant latitude (Λ). Invariant latitude is defined as the magnetic latitude at which a field line crosses the surface of the Earth. In a perfect dipole field invariant latitude is related to L by

$$\Lambda = \cos^{-1}\left(\frac{1}{L}\right)^{\frac{1}{2}}. \tag{2.10}$$

Chapter 3

The CRRES Spacecraft

3.1 Mission Objectives

The Combined Release and Radiation Effects Satellite (Figure 3.1) was launched on July 25, 1990, as a joint NASA and U.S. Department of Defense (DoD) mission, details of which can be found in *Johnson and Ball*, 1992, and references therein. The specified DoD mission lifetime was 1 year with a goal of extension to 3 years. During the first 3 years of operation the mission was to be under the management of the U.S. Air Force Space Systems Division, after which it was to pass over to NASA and to join a constellation of spacecraft as part of the Global Geospace Science Programme. In October 1991 the spacecraft suffered a critical power subsystem failure, ending the mission after less than 15 months of operation.

There were 3 main areas of interest on which the CRRES mission was focussed;

- DoD Studies of the Radiation Environment,
- NASA Chemical Release Experiments,
- DoD Low Altitude Scientific Studies of Ionospheric Irregularities (LASSII).

The main aims of the radiation environment studies were the investigation of

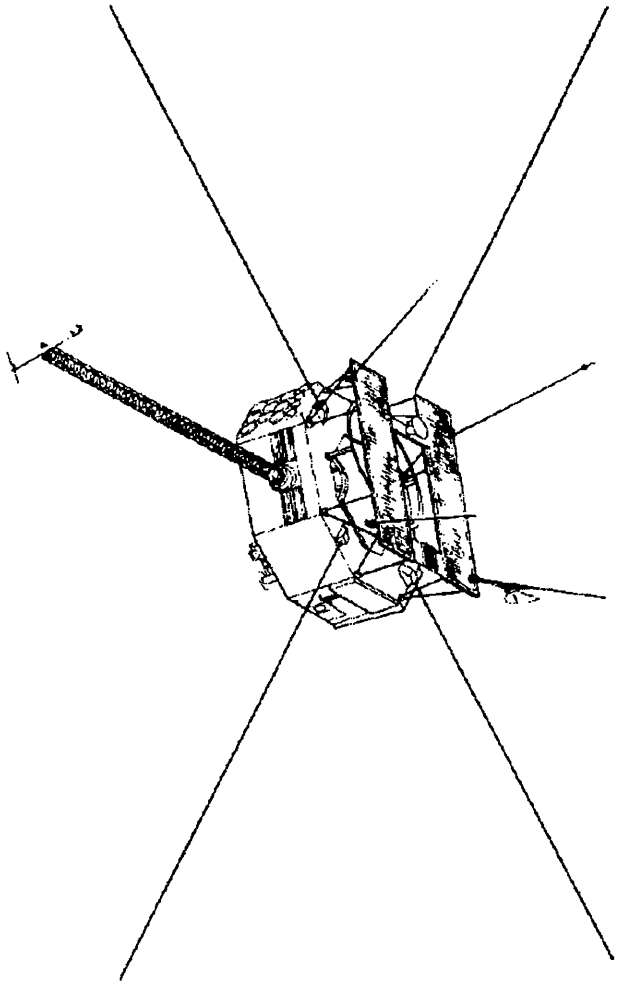

Figure 3.1: The CRRES spacecraft.

the natural radiation environment and its effect on microelectronic components. By studying the performance of components exposed to the radiation belts, their suitability for future space missions was to be assessed. It was desirable to have the ability to correlate the performance of the components with the conditions within the radiation belts, and so CRRES was equipped with instrumentation capable of measuring this environment and hence characterising of the radiation belts.

The chemical release experiments were carried out during three campaigns in which a total of 24 chemical canisters were released. These campaigns took place over the first 13 months of operation at various altitudes. The gas clouds produced from the releases and their effect on the magnetosphere and ionosphere were measured using a variety of optical, radar, and in-situ observations made from ground-based facilities, aircraft, and onboard CRRES. The campaigns were;

- low-altitude releases over the South Pacific in September 1990,
- high-altitude releases over North America in January and February 1991,
- low-altitude releases over the Caribbean in July and August 1991.

One of the aims of the high altitude releases was to try to artificially induce auroral precipitation by increasing N and hence lowering the characteristic energy, E_c, of the plasma. E_c is the magnetic energy per particle and is given by,

$$E_c = \frac{B^2}{2\mu_0 N} = \frac{m_e c^2}{2}\left(\frac{\Omega_e}{\omega_{pe}}\right)^2. \tag{3.1}$$

The theory accepted at the time predicted that a lower E_c would increase wave-particle interactions scattering particles into the loss cone and hence increase precipitation [*Kennel et al.*, 1970, *Kennel and Ashour-Abdalla*, 1982, *Lyons and Williams*, 1984.] This did not happen and an alternative hypothesis has subsequently been proposed [*Johnstone*, 1996].

The LASSII experiment investigated both naturally occurring and artificially created ionospheric irregularities. Particular studies included the equatorial Spread-F region, the chemical releases, ionospheric heating, and wave-particle interactions. The effect of these irregularities on radio communications was also investigated. The LASSII instrumentation was composed of the Pulsed Plasma Probes (P3), the Very Low Frequency Wave Analyzer (VLFWA), and the Quadrupole Ion Mass Spectrometer (QIMS). When perigee was between 17:30 LT and 02:30 LT LASSII would operate below 1000 km every fourth orbit. When perigee occurred at other local times LASSII would operate below 3000 km every other orbit. The telemetry system did not allow LASSI and the space radiation effects experiments to operate simultaneously. The space radiation effects experiments are described in Section 3.3.

3.2 Orbit

The CRRES spacecraft was launched into a 350×33584 km orbit with an inclination of 18.1° and period of 9 hours and 52 minutes. The initial apogee altitude was 2202 km lower than the targeted geosynchronous altitude. The chosen orbit was a compromise between the ideal orbits for the low altitude and high altitude studies. Further details of the initial orbit are given in Figure 3.2. In June 1991 the apogee of CRRES was raised by 1450 km (increasing the orbital period to 10 hours and 17 minutes) in order for the low-altitude releases over the Caribbean to take place in appropriate conditions. The apogee of CRRES precessed from southern latitudes (-18°) near 19:00 LT, to equatorial regions around 23:00 LT, and then to northern latitudes (18°) near 04:00 LT. The precession of the CRRES orbit, through its lifetime, can be seen in Figure 3.3, along with the location of the chemical release experiments.

The CRRES spacecraft was orientated with its spin axis in the ecliptic and pointed 12° ahead of the Sun's apparent motion. The spacecraft nominal operational spin rate

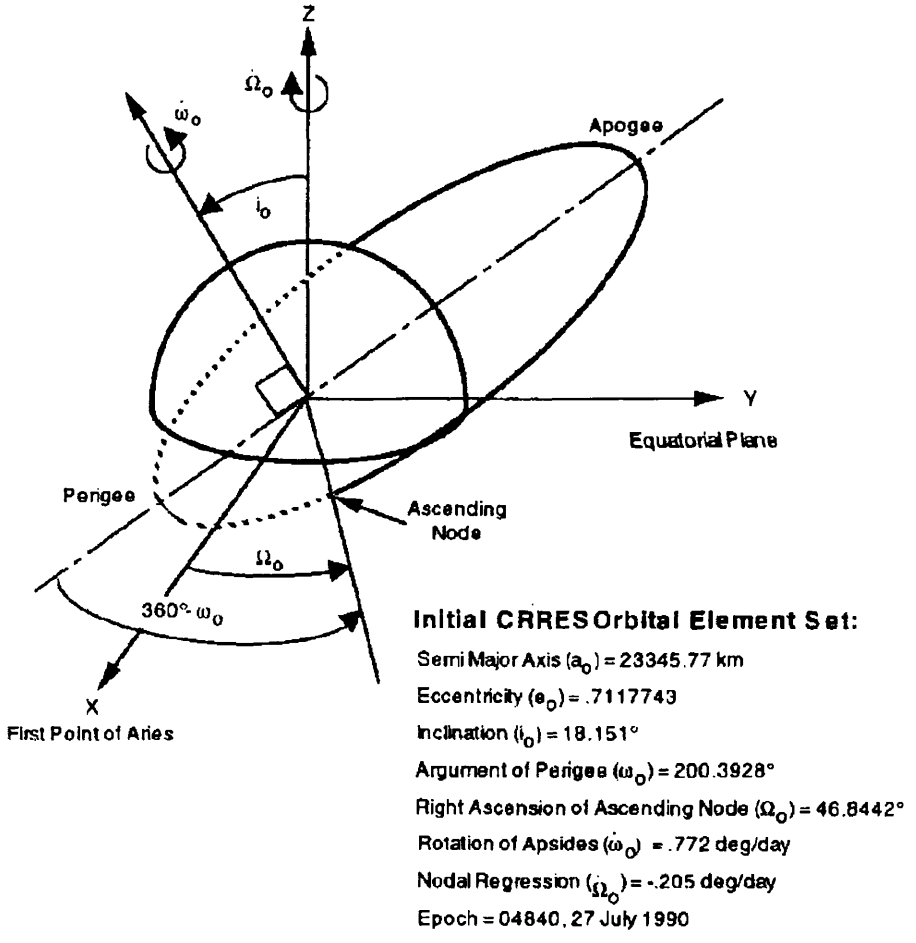

Figure 3.2: Initial CRRES Orbit (not to scale).

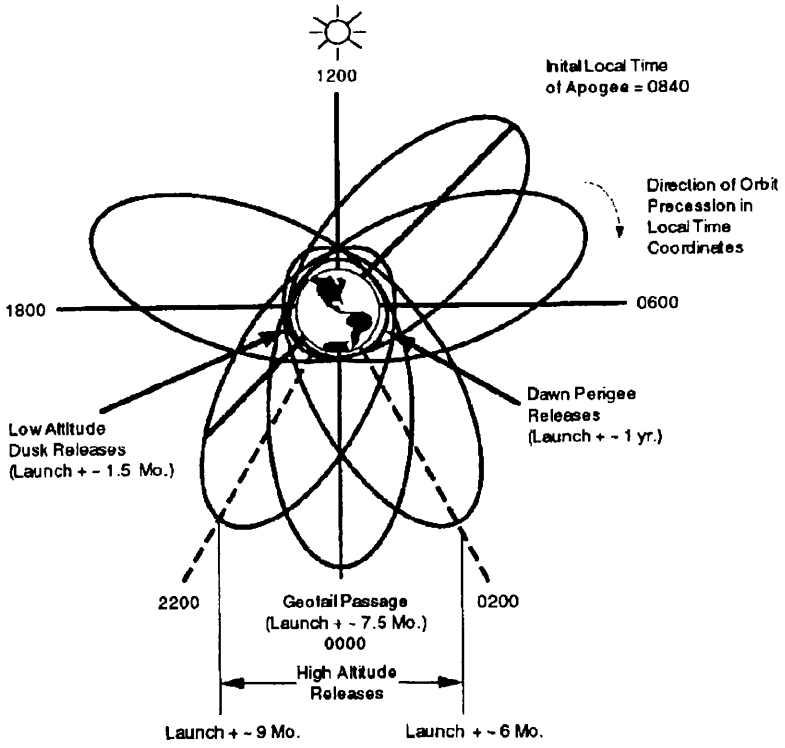

Figure 3.3: Precession of CRRES orbit in local time coordinates.

was 2 rpm.

3.3 CRRES Instrumentation

A brief description of the instrumentation flown on the CRRES spacecraft is given below. Further information can be obtained from the U.S.A.'s National Space Science Data Center (NSSDC).

- **Experiment for High Energy Heavy Nuclei Composition.** This instrument consisted of a stack of lithium-drifted silicon detectors, and measured elemental composition along with an energy spectrum (20-500 MeV/amu) for each element (H - Fe).

- **Spectrometer for Electrons and Protons.** This instrument consisted of 3 identical particle telescopes mounted at 40°, 60°, and 80° to the spacecraft spin axis. These telescopes could measure electrons from 20 keV to 5 MeV, and protons from 0.5 - 100 MeV.

- **High-Energy Electron Fluxmeter (HEEF).** A 3 element electron telescope with an anticoincidence element which measured the differential energy spectrum of electrons in the 1-10 MeV range.

- **Medium Electron Sensor.** This was sensor A of the Medium Energy Electron spectrometer, and was also known as MEA. It consisted of 18 lithium-drifted solid-state detectors placed in the focal plane of a 180° focussing magnet. It measured the temporal, spectral, and directional variations in electron fluxes in the 0.1-2 MeV range.

- **Electron-Proton-Angle-Spectrometer (EPAS).** This was sensor B of the Medium Energy Electron spectrometer, and was also known as MEB. It consisted of 2 identical units, each with 5 solid-state detectors in the focal plane

of a focussing magnet for detection of electrons in the range 16-300 keV, and 2 2-element solid-state telescopes for ion detection.

- **Low Energy Plasma Analyzer (LEPA).** A description of LEPA is given in Section 3.4.

- **Relativistic Proton Detector.** This experiment consisted of a group of Cerenkov and solid-state silicon based sensors designed to measure electrons above 200 keV and higher energy electrons (>35 MeV) and protons (>80 MeV) trapped in the radiation belts.

- **Proton Switch.** This instrument measured the omnidirectional flux of protons in the energy range 20-80 MeV using 2 lithium-drifted silicon detectors, each centered under a hemispherical aluminum dome.

- **Proton Telescope** This instrument consisted of 2 sensor units, one measuring 1-9 MeV protons in 8 contiguous energy channels, and the other measuring 6-100 MeV in 16 channels.

- **Magnetospheric Ion Composition Sensor (MICS).** This instrument consisted of a conically shaped electrostatic analyser and a time of flight analyser, measuring the mass and E/q spectra of ions in the range 30-400 keV.

- **Heavy Ion Telescope (HIT).** The HIT used a 3 element solid state detector to uniquely determine the ion mass, elemental identification, and incident energy, for ions in the range 0.1-15 MeV for H-Ar.

- **Low Energy Magnetospheric Ion Composition Sensor (LOMICS).** LOMICS used a 90° spherical section electrostatic analyser followed by a time of flight analyser to determine E/q and mass for ions up to 56 AMU in the energy range 40 eV - 40 keV. This was done for the 3 incident angles; 60°, 90°, and 120° to the spin axis.

- **Fluxgate Magnetometer.** Details of the fluxgate magnetometer are given in Section 3.5.

- **Plasma Wave Experiment (PWE).** Details of the PWE are given in Section 3.6.

- **Electric Field/Langmuir Probe Instrument (EF/LP).** This instrument consisted of 2 pairs of orthogonal booms with a tip-to-tip separation of 100 m. It was used to measure the temperature and density of cold electrons, and electric fields.

- **Low Energy Ion Mass Spectrometer (IMS-LO).** This experiment consisted of 2 identical instruments, with a 5° conical field of view, mounted with look directions at 45° and 75° to the spin axis. Each sensor was made up of a Wein velocity filter, followed by an electrostatic analyser and then a channel multiplier, and covered the E/q range of 0.1-32 keV/Q.

- **Medium Energy Ion Mass Spectrometer (IMS-HI).** IMS-HI was designed to measure ring current ions in the E/q range 20 keV/Q - 8MeV/Q. A narrowly collimated beam of incident ions passed into a cross-magnetic field chamber, and then depending on the incident energy of the ions, would collide with 1 of 6 cooled solid state detectors.

3.4 Low Energy Plasma Analyzer (LEPA)

3.4.1 Instrument Description

The work contained in this thesis is concentrated on and driven by the electron observations obtained from the LEPA instrument, full details of which can be found in *Hardy et al.*, 1993. LEPA consists of two tri-quadrispherical electrostatic analysers

each backed by a single arc-segment microchannel plate chevron pair. The design of the sensors is based on those of instruments previously flown on the AMPTE and Giotto spacecraft [*Coates et al.*, 1985, *Johnstone et al.*, 1987]. One sensor is configured to measure electrons and the other, ions.

The field of view and angular dispersion of LEPA could have been achieved with a single quadrispherical analyser, but such instruments have the disadvantage that the energy of particles measured varies with arrival angle for a given voltage setting. The LEPA hemispherical analyser section acts as an incident angle independent E/q selector. The LEPA quadrisphere then acts simply to disperse the particles (having been E/q selected) according to their incident angle, hence giving better performance than a single quadrisphere [*Hardy et al.*, 1993, *Coates et al.*, 1984, *Johnstone et al.*, 1987].

The LEPA analysers are shown schematically in Figure 3.4. Particles enter the detector through the aperture into the hemispherical electrostatic analyser. The electrostatic analyser consists of two concentric hemispherical plates, to which a variable voltage is applied at a fixed ratio of $V_{inner}/V_{outer} = -1.18$. The outer plate is negatively charged and the inner plate positively charged for the electron sensor, and vice versa for the ion sensor. In both cases there is a zero potential surface midway between the plates. By controlling the voltage applied to the plates, particles of the desired E/q are forced to follow part of a great circle path around the hemisphere. Particles with a higher E/q collide with the outer plate, and those with a lower E/q collide with the inner plate (in both cases they are usually absorbed). In fact particles with an E/q near to the desired value also pass through the analyser. For a given voltage setting, the range of accepted E/q values is defined by the analyser characteristics, such as plate spacing and the aperture size. For LEPA this 'energy pass band width' is approximately 3% of the central 'energy'. In normal operation the voltage applied to the plates is varied systematically in order to sample a wide range of E/q,

collecting a particle energy spectrum.

As the particles pass through the hemisphere they follow different great circle paths according to their incident direction on entering the detector, e.g. compare the upper and lower figures in Figure 3.4. After passing through 180°, the particles within the energy pass band which entered at the same point within the aperture reconverge irrespective of their incident angle. As we need to know the incident direction of the particles they are then passed through an 80° (near quadrispherical) electrostatic analyser of the same plate separation and voltages as the hemispherical analyser. A full quadrisphere is not used so as not to obstruct the field of view of the entrance aperture.

After passing through the final quadrisphere the particles have spread out according to their incident angle and strike a microchannel plate chevron pair (MCP). Each incident particle generates a cloud of electrons at the far side of the MCP. Each electron cloud is are then collected on an array of discrete anodes. Signals from these anodes thus reveal the incident direction of the detected particles.

A tri-quadrispherical detector is capable of a 180° fan field of view, but with degraded performance at the extremes of the field of view. The 'edge effects' are caused firstly by particles near the edge of the field of view (0° and 180°) whose trajectories are distorted by traveling near the housing of the detector, both before and after passing through the entrance aperture. Secondly the small apparent size of the aperture as seen by particles near the edge of the field of view results in very low counts and high Poisson noise. Thus on LEPA the field of view has been restricted, by deliberate reduction of the aperture size, to 128°, centered around 90°, where the edge effects are not seen.

LEPA is mounted in such a way that the 128° field of view fan is in a meridian plane relative to the spacecraft spin axis and centered on the spacecraft equator. The field of view in the spin plane is limited due to the spacing of the analyser plates and

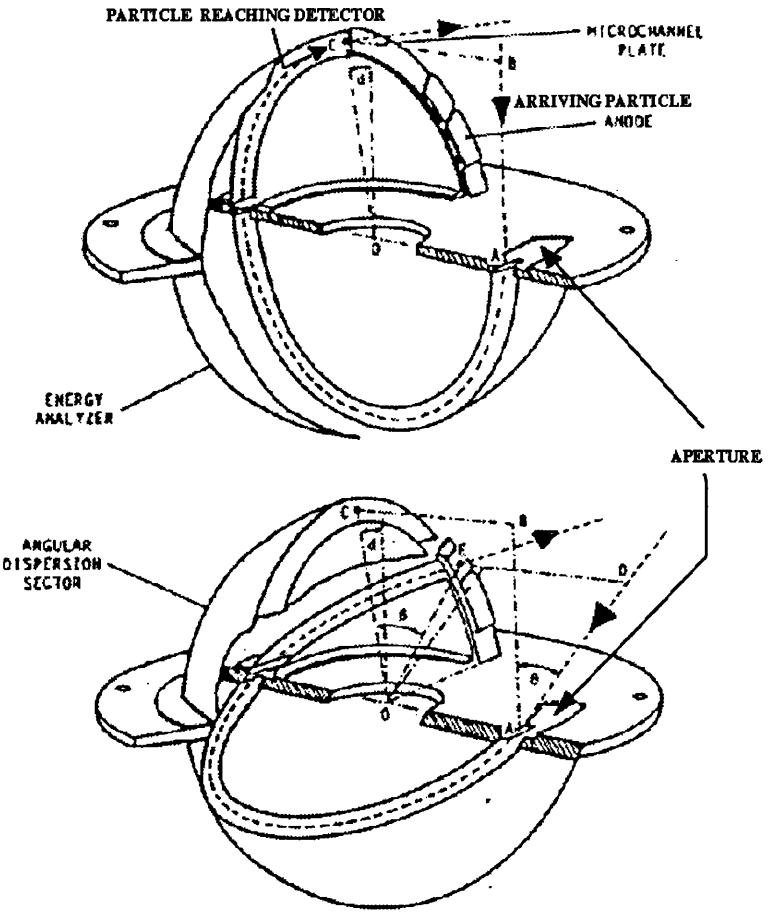

Figure 3.4: Schematic diagram of the LEPA Detector.

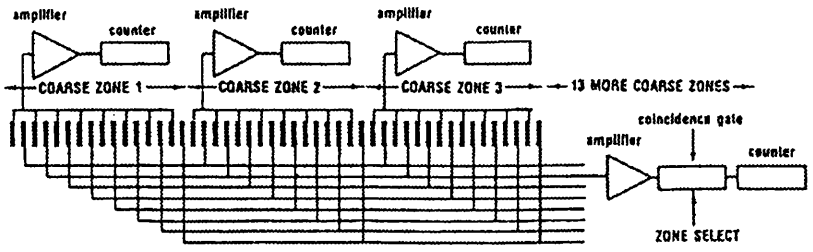

Figure 3.5: Schematic diagram of the LEPA discrete anode structure.

by a collimator in front of the entrance aperture, which forms part of the instrument's radiation shielding. Hence the variation with angle in the spin plane of the instrument response is roughly bell shaped with a FWHM=5.6°.

In order to achieve a scientifically desireable resolution of 1° along the field of view fan the array of discrete anodes would have to number 128. As each anode requires a separate amplifier and counting chain, the instrument would require more amplifiers and counters than could be accommodated within the resource constraints. Instead the anode array was divided into 16 coarse zones, numbered 0 to 15, each connected to its own amplifier and counter. Each coarse zone receives signals corresponding to electrons arriving from an 8° wide field of view. These 16 coarse zones then cover the entire 128° field of view. Coarse zone 15 is masked off to provide a background channel (i.e. it only responds to penetrating radiation), and thus the field of view is reduced to 120°. Each of the coarse zone anodes is effectively further subdivided into 8 fine zones, each 1° wide (in fact the uses interleaved fingers of 75μm width). Each fine zone is then connected in parallel with the corresponding fine zones from each of the other coarse zones, and to an amplifier and counter. By looking for coincidence pulses between a nominated coarse zone and the fine zone anodes, 1° resolution can be obtained in the nominated coarse zone. (The anode structure is illustrated in Figure 3.5.)

The anode structure with coincidence logic allows complete coverage of the field of view at 8° resolution, and at 1° resolution within a single chosen coarse zone. High angular resolution measurements are most important near the magnetic field direction (e.g. to make detailed studies of field aligned phenomenon or loss cone features). Thus fine zone data was usually collected from the coarse zone containing the magnetic field direction, as determined in real time from the onboard magnetometer. It must be remembered that the 1° resolution is in the spin meridian plane, and the resolution is still 5.6° in the spin plane. (At this time the LEPA fine zone data has yet to be used.)

LEPA could be programmed to operate such that each voltage sweep could contain any number of energy steps between 1 and 128. These energy sweeps would be spin synchronized so that there were an integral number of sweeps per spin. The spin rate is determined in real time from the time difference between two consecutive Sun pulses. The experiment would normally operate so that either a 30 point spectrum would be measured 64 times a spin (each time sampling a given E/q at a different spin plane angle so as to give 5.625° resolution in the spin plane) or a 120 point spectrum 16 times a spin (22.5° resolution in the spin plane). A sweep would cover either the full energy range of 10 eV to 30 keV, or an attenuated range of 6 eV to 21 keV. LEPA made measurements using the attenuated energy range for all orbits up to and including 209 (19/10/1990), and the unattenuated energy range for all subsequent orbits. The boundary energies for the 30 point spectra when LEPA operated in the attenuated and unattenuated voltage modes are given in Appendix A. Whether LEPA was operated in the attenuated mode or not has had little effect on the analysis presented in this thesis, and the data which has been used contains examples from before and after Orbit 209.

The data generation rateof LEPA was much greater than the 2.6 kbit/sec telemetry rate available for transmission to Earth. Thus LEPA was designed to operate

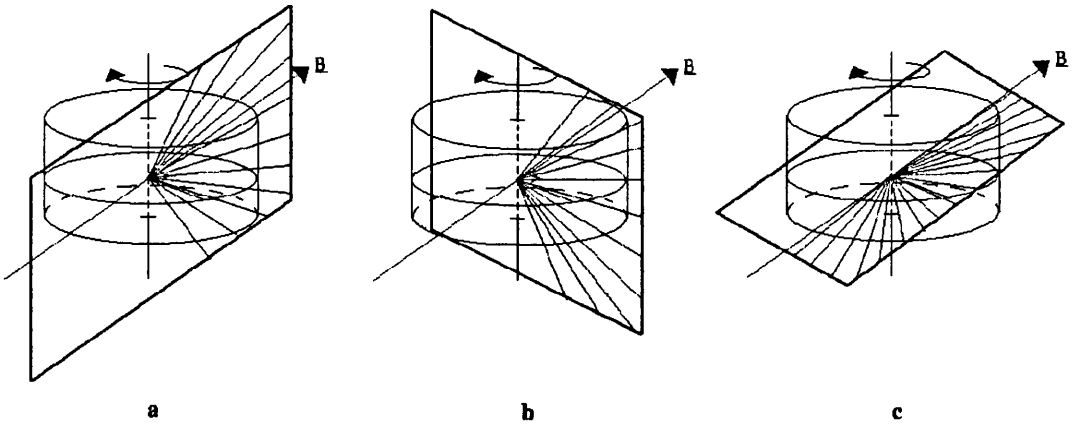

Figure 3.6: Illustration of a) the loss cone distribution, b) the 90° distribution and c) the symmetry plane distribution, as described in the text. Note that the loss cone distribution is returned looking both up and down the field. Also diagrams a and b show only 10 coarse zones for clarity (in fact there are 16) but the angular range is correct, similarly the symmetry plane shows only 17 azimuths (and not 36).

in different data transmission modes, in which it returned different portions of the available information.

As part of the data selection four distributions were defined; three slices through the 3D distribution and one distribution covering all angles sampled by LEPA. The three planar distributions are illustrated in Figure 3.6.

The distributions were defined as follows (note that the magnetic field direction was usually near the spin equator, and at nearly all times within 60° i.e. within LEPAs field of view);

- **Loss cone distribution.** A 30 point spectrum was collected from all coarse zones from the spin azimuths in which the plane of the field of view contained the magnetic field direction. This 'snapshot' distribution is collected twice per spin when the detector field of view looks parallel and then anti-parallel to the field direction. The loss cone distribution could cover a pitch angle range as large as 0° to 120° (when the magnetic field direction lies at the edge of the

120° field of view of the detector) and always covers at least 0° to 60°(when the magnetic field direction lies at the center of the 120° field of view of the detector).

- **90° distribution.** A 30 point spectrum was collected from all coarse zones for the spin azimuth when the plane of the field of view contained the 90° pitch angle in the symmetry plane (see below). This 'snapshot' distribution is collected twice per spin, $\frac{1}{4}$ spin after the loss cone distribution is collected. Unless the magnetic field direction is perpendicular to the spin axis, only one coarse zone (per distribution) will observe 90° pitch angle particles. The remainder see particles with pitch angles close to 90°.

- **Symmetry plane distribution.** The 'symmetry plane' was defined as the plane which contained both the magnetic field direction and the direction where the 90° pitch angle circle and spacecraft equator crossed. Every $\frac{1}{64}$ of a spin, a 30 point spectrum was collected from the particular coarse zone which was determined to lie at that time in the symmetry plane (note that the coarse zone lying in the symmetry plane will usually change as the spacecraft rotates). In half a spin data is collected from all pitch angles from 0° to 180°, making up a complete symetry plane distribution.

- **Full angular coverage distribution.** A 30 point spectrum is returned, averaged over adjacent coarse zones and four energy sweeps, every 22.5° of satellite spin (i.e. 16°× 22.5° resolution) covering all look directions every 1 spin.

LEPA spent 90% of the time operating in one of two data selection modes. In the first of these the three planar distributions were returned for the electrons, and the full angular coverage distribution for the ions. In the second mode the full angular coverage distribution was returned for both electrons and ions. LEPA spent a total

of 4655 hours returning data in the first mode, and 2892 hours returning data in the second mode.

The data analysis presented in Chapters 5, 6 and 7 uses electron pitch angle distributions. Pitch angle distribution are constructed using data acquired during half a spin, and thus information at a time resolution better than 15 seconds is lost. Pitch angle distributions are constructed by calculating the pitch angle range covered by each returned measurement (by using the magnetic field information returned by LEPA which was collected onboard from the magnetometer), and performing a weighted average of those measurements which form part of the designated pitch angle bin.

For the purposes of analysing the data, the returned distributions, either the symmetry plane, 90° and loss cone; or the full angular coverage distribution, are combinned to form a pitch angle distribution with 33 bins, 5.625° wide, covering the range -2.8125° to 182.8125°.

3.4.2 Problems with the LEPA data

Some problems have been found with the LEPA data, most of which were solved or corrected for, in the early stages of the mission. For example the boom on which the magnetometer was mounted failed to reach full deployment, so that it measured components of the magnetic field in different directions than intended. As mentioned in Section 3.4.1, information is fed directly from the magnetometer to LEPA and used onboard to create the data products. This problem was corrected, by uploading new software early in the mission to account for the true magnetometer sensor orientation. It was also found that the LEPA instrument was not sensitive to energies less than 150 eV, although the reason for this is still not known.

A problem which only came to light during the preliminary stages of the work contained within this thesis, is illustrated in Figure 3.7. The three spectrograms

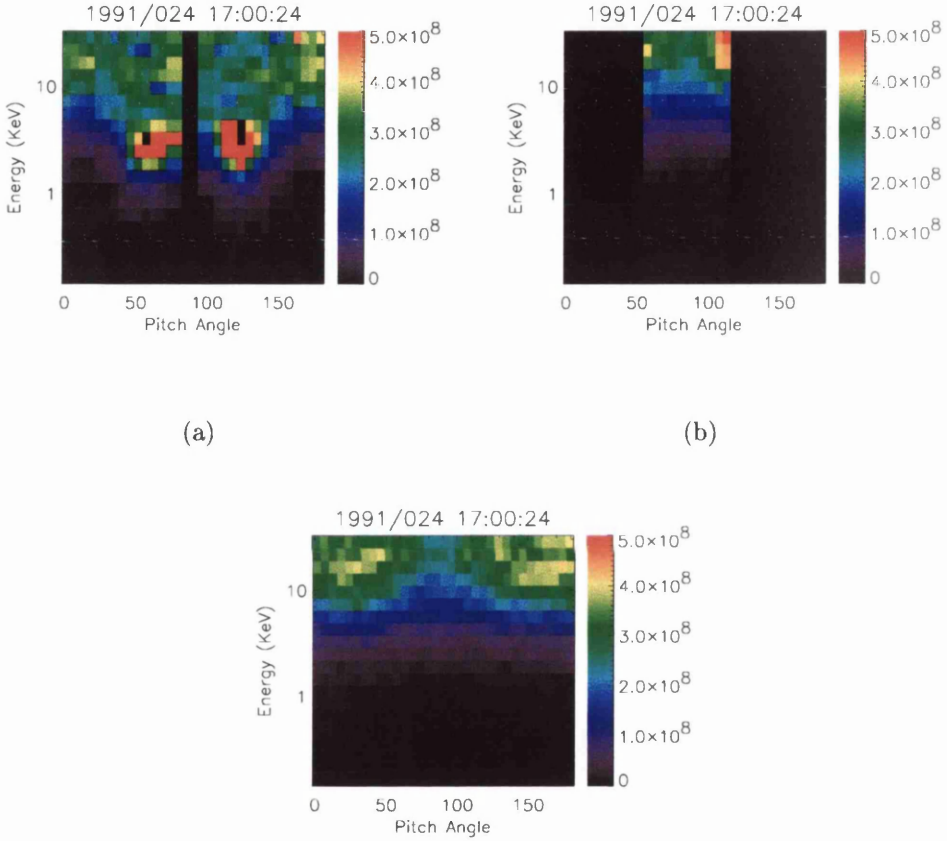

Figure 3.7: Three pitch angle vs energy spectrograms showing data returned from the LEPA electron sensor during Orbit 445, with pitch angles calculated prior to magnetic byte swapping correction. The colour scale indicates the differential energy flux in $cm^{-2}s^{-1}ster^{-1}$. (a) shows the data from the loss cone distribution, (b) shows the data from the 90° distribution, and (c) shows the data from the symmetry plane distribution.

show the data returned for the three planar distributions averaged over one spin (i.e. both the loss cone distribution looking up and down the field lines are shown, and the 90° and symmetry plane data are averages over two sequential distributions). Assuming that there is no gyrophase anisotropy we would expect the distributions shown in the three plots in Figure 3.7 to be roughly the same (with any differences arising from changes in the measured electron distributions within a spin period). Clearly, there are distinct differences between the distributions shown in Figure 3.7. The most marked difference is the presence the two high flux populations of electrons at pitch angles around 60° and 120°, and energies around 2 keV, seen in the loss cone distributions, but completely absent in the symmetry plane and 90° distributions. After much investigation, an explanation of the observed discrepancies between the three planar distributions has been found, and appropriate corrections made.

The problem described above arose as the result of an error contained within the byte of information passed from the magnetometer to LEPA regarding the magnetic field direction. This appears to have been byte swapped resulting in the apparent field direction being mirrored around the spin plane (illustrated in Figure 3.8).

One effect of the magnetic byte swapping concerns the selection of coarse zones which constitute the symmetry plane distribution. The coarse zone selected for each spin azimuth as part of the symmetry plane has, in fact, been mirrored around the spacecraft equator compared to the required zone (e.g. the magnetic field direction as provided to LEPA would appear to be at +30° to the spacecraft equator if it was in fact at -30° to the spacecraft equator). The result is that the data returned is not in the symmetry plane and that under certain conditions (such as those in the example above) there can be a severe reduction in the range of pitch angles covered. The effect of the magnetic byte swapping on the selection of coarse zones in the symmetry plane is illustrated in Figure 3.9. The difference between the returned and the required coarse zones is small when the magnetic field direction is close to the equator of the

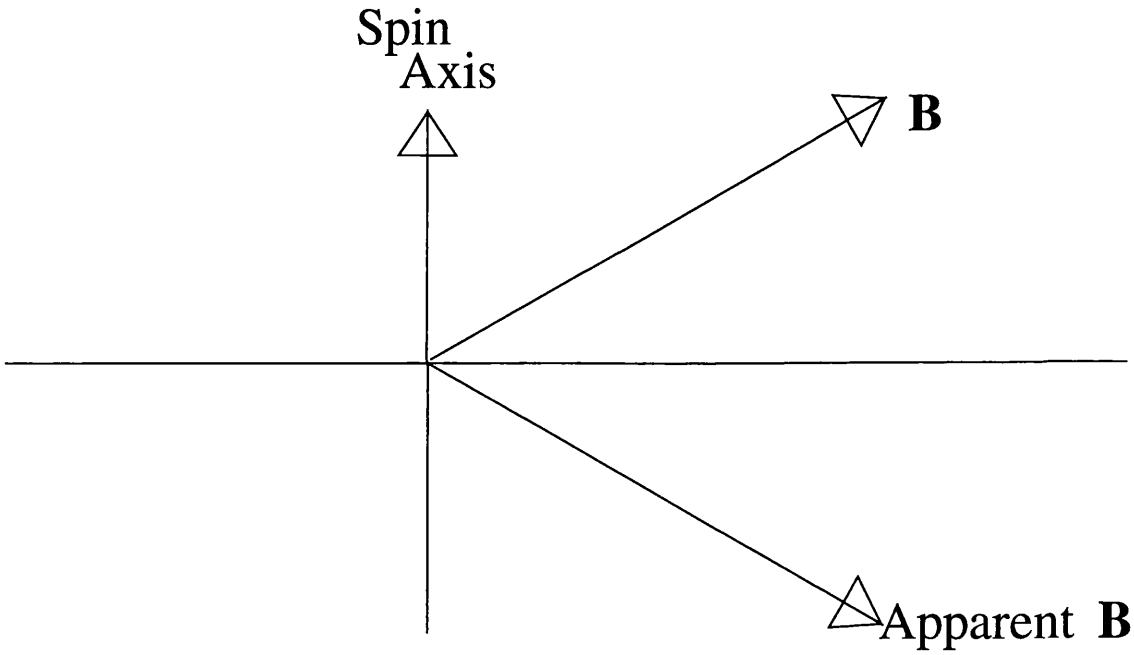

Figure 3.8: Illustration of the apparent magnetic field direction used by LEPA as a result of the magnetic byte swapping error (with respect to the spacecraft spin axis and equator), and the true magnetic field direction shown.

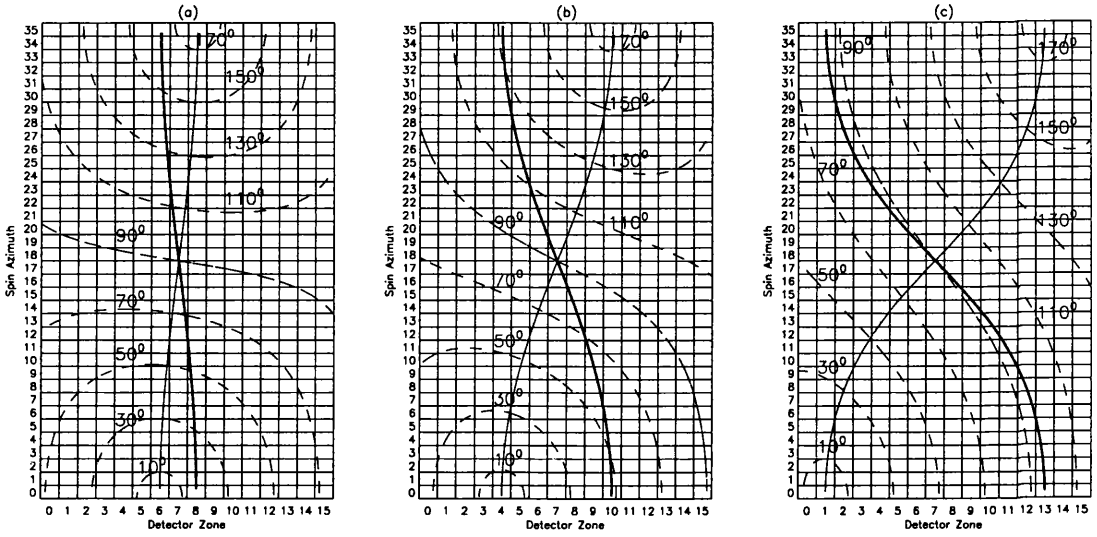

Figure 3.9: Three examples of the effect of byte swapping the magnetic field information to LEPA on the selection of the coarse zone lying in the symmetry plane for times when (a) the magnetic field direction is close to (8° from) the spacecraft equator, (b) the magnetic field direction is 24° from the spacecraft equator, and (c) near the edge of LEPA's field of view. Each plot is a grid of detector zones and spin azimuth for half a spin. The dashed lines show contours in pitch angle. The thin solid line shows the location of the true symmetry plane while the thick solid line shows the detector zones actually sampled.

spacecraft, Figure 3.9 (a) (the conditions expected when CRRES is near the magnetic equator on dipole field lines). However, the difference becomes significant when the magnetic field direction is far away from the spacecraft equator, Figure 3.9 (b), and in extreme cases can result in only pitch angles close to 90° being sampled, Figure 3.9 (c). In the example shown in Figure 3.7 the magnetic field is approximately 25° from the spacecraft equator (similar to Figure 3.9 (b)).

The effect of the magnetic byte swapping on the loss cone and 90° distributions is more subtle. The data selected for the loss cone and 90° distributions is that which was intended, however, the calculated pitch angles are wrong. The pitch angles for the LEPA data are calculated, on the ground, using the magnetic field information passed to LEPA on board. The fact that the magnetic field direction used is wrong,

means that the calculated pitch angles are also wrong. In the case of the loss cone distribution, where the magnetic field direction lies in the plane of the field of view, more than one coarse zone looks at the same pitch angle. For example, if the magnetic field direction is thought to lie between zones 4 and 5, then both zones 4 and 5 are thought to cover pitch angles 0° to 8°, zones 3 and 6 are thought to cover pitch angles 8° to 16°, zones 2 and 7 are thought to cover pitch angles 16° to 24°, etc. If the magnetic byte swap is then accounted for, and the magnetic field actually lies between zones 10 and 11, then, for example, zone 7 covers pitch angles 24° to 32° and zone 2 covers pitch angles 64° to 72°. When the pitch angle distributions are constructed, zones which are thought to cover the same pitch angle range are averaged together, when in fact they cover different pitch angles. The error leads to improper combination of measured data.

As the measured distributions are included in the telemetry, and the pitch angles are calculated on the ground, it is possible to make a correction to the magnetic field direction information, and to calculate the actual pitch angles of the data. As mentioned above, there is a reduction of coverage of the symmetry plane in pitch angle space, which at times can be significant. However, by combining all three planar distributions averaged over a spin it is nearly always possible to create a full 180° pitch angle distribution. The corrected pitch angle distributions for the data shown in Figure 3.7 is shown in Figure 3.10, along with a distribution containing data combined from all three distributions.

The magnetic byte swapping error has not been seen in the past, because of the type of studies previously carried out with the LEPA data. Earlier detailed studies of the LEPA data set have looked at fairly steady distributions, peaked near 90°, when the magnetic field direction was generally near the spacecraft equator. Under these conditions the effects of the magnetic byte swapping error are small, and not readily apparent. However, the studies presented here are concerned with rapidly varying

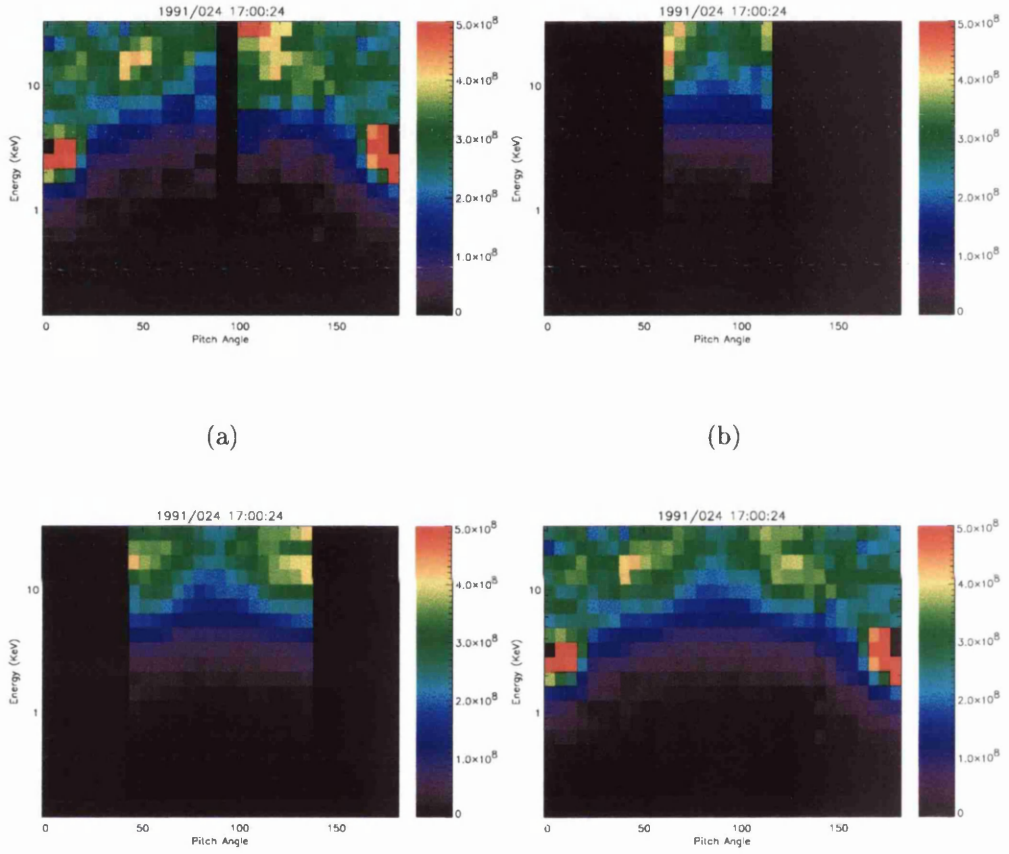

(a) (b)

(c) (d)

Figure 3.10: Four pitch angle vs energy spectrograms showing the data returned from the LEPA electron sensor during Orbit 445, with pitch angles calculated using the magnetic byte swapping correction. The colour scale indicates the differential energy flux in $cm^{-2}s^{-1}ster^{-1}$. (a) shows the data from the loss cone distribution, (b) shows the data from the 90° distribution, (c) shows the data from the symmetry plane distribution, and (d) shows data combined from the three distributions (a), (b), and (c).

distributions peaked at 0° and 180°, when the magnetic field direction is often away from the spacecraft equator, and the effects of the magnetic byte swapping error can be significant.

3.5 Fluxgate Magnetometer

As detailed above, the magnetic field as measured onboard is used to calculate the pitch angles of electrons detected by the LEPA instrument. Moreover, as the magnetic field is fundamental to the nature of the magnetosphere, the use of magnetic field measurements is not confined to calculation of pitch angles. The magnetic field strength affects the gyrofrequency of charged particles and in turn affects the properties of the wave-particle interactions discussed in Chapter 6. Also, the observed magnetic field behavior and its relation to FACs is presented in Chapter 7 and on the nightside it is an indicator of substorm activity. It is for these reasons that a more detailed description of the fluxgate magnetometer is given below.

3.5.1 Instrument Description

CRRES carried a triaxial fluxgate magnetometer (model SAM-63B-15) [*Singer et al.*, 1992], which was developed and built by Schonsted Instrument Company. The sensors were mounted on a rigid, 6.1 m Astromast boom, built by Astro Aerospace, while the analog electronics were mounted within the spacecraft itself. At the end of the boom was a T-bar (see Figure 3.11), at one end of which the fluxgate magnetometer was mounted. A search coil magnetometer, which was part of the PWE, was mounted at the other end of the T-bar. The deployed boom and T-bar placed the fluxgate magnetometer ~7.5 m from the center of the spacecraft, where there was less than a few nT of residual spacecraft-generated magnetic field (small compared to the typical measured field).

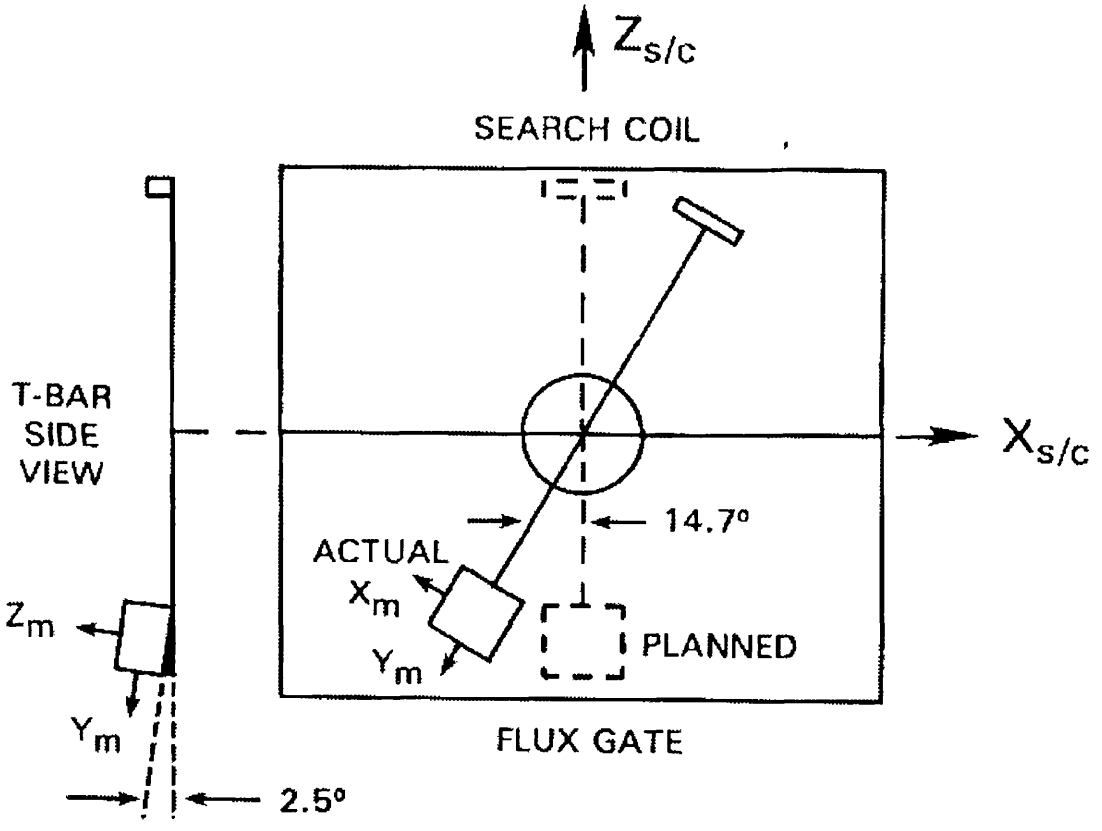

Figure 3.11: Astromast boom and magnetometer sensor orientation in the approximate deployed position. The spacecraft spin axis is along $Z_{s/c}$. (Dimensions are not to scale).

There was a deliberate 2.5° rotation of the fluxgate magnetometer axes relative to the T-bar in the Z-Y spacecraft plane, illustrated in Figure 3.11. The purpose of this rotation was to introduce a component in the spin plane to the magnetometer axis aligned with the spacecraft spin axis (the magnetometer Y-axis). In doing so all 3 axes would have a sine wave component coincident with the spacecraft spin, allowing the gain of the 3 sensors to be related.

A 3 axis signal is sampled by the 12-bit analogue to digital converter every 64 ms, with the 3 different axes sampled simultaneously to within ~150 μs. In the low gain mode the range covered is ~±45000 nT with a resolution of 22 nT. In the high gain mode the range is ~±850 nT and the resolution is 0.43 nT. Additional amplification can be applied to the magnetometer Y-axis sensor (for use in regions of low field strength) to give a resolution of 3.3 nT in the low gain mode, and 0.07 nT in the high gain mode. The magnetometer operates in the high gain mode ~75% of the time, i.e. when CRRES is beyond ~3.5R_e.

As mentioned in Section 3.4.2, the magnetometer failed to deploy as planned (Figure 3.11). Although the Astromast boom deployed nearly to its full length, the T-bar on which the magnetometer was mounted, was found to be rotated by 14.7° about the spacecraft y-axis compared to the intended position.

3.5.2 Coordinate System

The magnetometer data is presented in the VDH coordinate system (Figure 3.12). In this system H is anti-parallel to the Earth's dipole axis, V is radially outward in the Earth's spin plane and perpendicular to H, while D is eastward completing the orthogonal right handed coordinate system.

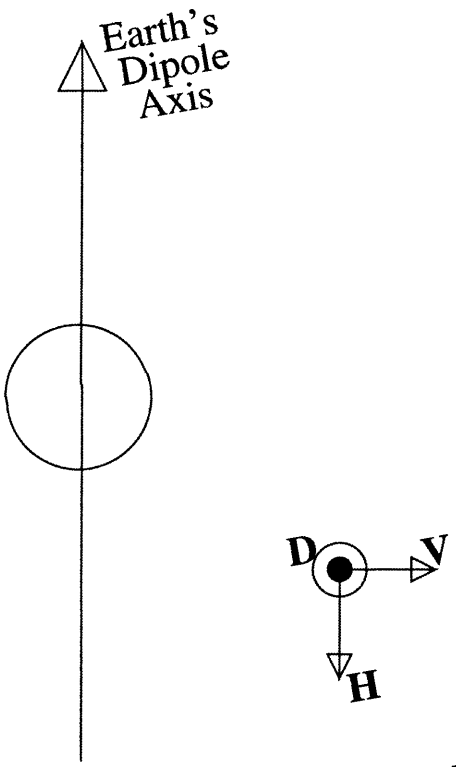

Figure 3.12: The VDH coordinate system as described in the text.

3.6 Plasma Wave Experiment

Data from the PWE onboard CRRES has been used in this study. Full details of the instrument can be found in *Anderson et al.*, 1992. The PWE consists of 3 sensors;

- a 100 m tip to tip extendable fine wire long electric dipole antenna designated WADA (Wire Antenna Deployment Assembly),
- a search coil magnetometer mounted on the same 6 m boom as the fluxgate magnetometer, but at the other end of the T-bar,
- a 94 m sphere to sphere double probe electric antenna designated SWDA (spherical-double-probe wire deployment assembly).

While the search coil magnetometer and the WADA (also known as the Passive Plasma Sounder (PPS)), were primarily part of the PWE, the SWDA was primarily part of the EF/LP (see Section 3.3) [*Wygant et al.*, 1992], with its use in the PWE being a secondary function.

The electric field sensors provide measurements of electric field variations in the frequency range from 5.6 Hz to 400 kHz with a dynamic range of at least 100 dB (a factor of 10^5 in amplitude), while the magnetic field sensors provide measurements with a dynamic range of at least 100 dB over the frequency range 5.6 Hz - 10 kHz. Magnetic field measurement are possible up to 400 kHz, but with a smaller dynamic range due to the roll-off of the search coil magnetometer response above 10 kHz. Signals from the sensors are fed through appropriate preamplifiers and differential amplifiers and then via 2 antenna selection switches to a multichannel spectrum analyser and a sweep frequency receiver. The dynamic range for both of the receivers is around 100 dB. Each receiver can be independently commanded either to cycle through all 3 sensors or to have their input locked to just 1. It is the data from the sweep frequency receiver which is used in the work contained within Chapters 5 and 6.

The multichannel spectrum analyser covers the frequency range 5.6 Hz - 10 kHz in 14 logarithmically spaced narrowband filters followed by 14 logarithmic compressors. The bandwidth of each narrow band filter is set at ± 15% of the center bandwidth, with the exception of the 2 highest frequency channels which are set at ± 7.5% of the centre bandwidth. The logarithmic compressors produce an output voltage roughly proportional to the logarithm of the input signal. The 14 outputs are sampled simultaneously 8 times every second.

The sweep frequency receiver covers the range 100 Hz - 400 kHz in 4 bands with 32 steps per band. With each step the frequency sampled increases by about 6.7%. Band 1 (100 - 800 Hz) is sampled at 1 step/s or 32 s/sweep, band 2 (800 Hz - 6.4 kHz) at 2 steps/s or 16 s/sweep, and bands 3 (6.4 - 50 kHz) and 4 (50 - 400 kHz) at 4 steps/s or 8 s/sweep. The nominal bandwidths of the 4 bands are 7 Hz, 56 Hz, 448 Hz, and 3.6 kHz, respectively. The signal from each band is fed into a logarithmic compressor, and sampled every step.

Chapter 4

Field Aligned Electron Events

4.1 What is a Field Aligned Electron Event?

Field aligned electron distributions are not uncommon in the Earth's magnetosphere, and are characterized by anisotropic fluxes which are largest parallel and antiparallel to the magnetic field direction. The Field Aligned Events (FAEs) are normally seen as counterstreaming (i.e. they are seen at both 0° and 180° simultaneously) bursts of electrons at low energies (~1 keV), with equatorial pitch angles < 15°. Sometimes there are differences in the energies and fluxes between the upgoing and downgoing beams, and occasionally they are seen in one direction only.

4.1.1 Previous Observations of Field Aligned Electrons

The first observations of field aligned electron distributions in the near equatorial regions of the magnetosphere were reported by *McIlwain*, 1975. The distributions were observed using the Auroral Particles Experiment on the ATS-6 satellite. The scientific package was mounted behind the 10 m parabolic antenna which was normally kept pointing at the Earth. The Auroral Particles Experiment consisted of five electrostatic analysers, four of which were normally scanned mechanically at $1.4°s^{-1}$,

and a fifth which was static. One pair of analysers scanned from the north, to radially outwards and on to the south, covering an azimuthal range of 220° before reversing, while the other pair scanned back and forth from east to radially outwards and on to west. The fifth sensor was fixed in the assembly, facing east. The 'north/south' scanning pair was not truly north/south scanning, but instead passed through 13° west of north to avoid a large solar panel. In geosysynchronous orbit (located at 94° west) the magnetic field direction was usually about 10° from the 'north/south' scanning plane and thus this instrumentation would not normally observe any field aligned electrons. However sometimes the geomagnetic field is distorted such that the north/south scanning detectors were able to observe electrons with small pitch angles. Within the first day of operation three events of intense field aligned electrons were seen. McIlwain identified these electrons as auroral in origin. All instrumentation prior to this mission either lacked the angular resolution needed to distinguish these distributions or did not observe the relevant pitch angles.

Parks et al., 1977, and *Moore and Arnoldy*, 1982, studied further examples of electron beams and their relation to substorm injections using the ATS-6 data. They mention indications of particles scattering from the beams to larger pitch angles. The temperature characteristics of typical electron distributions were studied using the ATS-6 data set, by *Lin et al.*, 1979, and it was shown that the distributions could be described by the superposition of two Maxwellians of different temperatures. The lower energy Maxwellian component ($\lesssim$ 1 keV) exists only when field aligned beams are seen. The low energy component appears initially only at small pitch angles, and later at larger pitch angles. *Lin et al.*, 1979, interpreted this behavior in terms of scattering of the electron beams to large pitch angles (i.e. a localised time evolution as opposed to a spatial effect). The scattering of field aligned electrons will be looked at further in Chapters 5 and 6, focusing on the CRRES/LEPA observations.

Field aligned electrons have also been observed in the equatorial regions of the

magnetosphere using the GEOS-1 [*Borg et al.*, 1978] and GEOS-2 spacecraft [*Kremser et al.*, 1988], and also the SCATHA (P78-2) satellite [*Richardson et al.*, 1981, *Arnoldy*, 1986]. However the most complete observations reported to date of counterstreaming electrons in the equatorial region have been made with the AMPTE/CCE satellite [*Klumpar et al.*, 1988, *Klumpar*, 1993]. *Klumpar*, 1993, made a statistical survey of counterstreaming electrons in terms of an anisotropy index (see Section 4.4). Occurrence probabilities of counterstreaming electrons $\geq$40% were observed from 21:00 - 02:00 MLT for radial distances of 8.75$\pm$0.25 R_e (and lower in other regions). The AMPTE/CCE observations will be discussed in further detail with reference to the CRRES observations described below, in Section 4.4.

There have also been many observations of field aligned electron beams made at high latitudes with a number of spacecraft, S3-3 [*Sharp et al.*, 1980, and *Collin et al.*, 1982], ISIS-2 [*Johnstone and Winningham*, 1982, and *Klumpar and Heikkila*, 1982], DE-1 [*Lin et al.*, 1982, and *Burch et al.*, 1983], VIKING [*Lundin et al.*, 1987, *Hultqvist and Lundin*, 1987, and *Hultqvist et al.*, 1988], and Freja [*Boehm et al.*, 1995]), and sounding rockets [*Raitt and Sojka*, 1979, and *Primdahl et al.* 1984]. These are discussed further in Chapter 7 with respect to the source of the FAEs seen by CRRES, along with some recent observations made by the FAST satellite [*Carlson et al.*, 1998b].

Bi-directional field aligned electron distributions have also been seen at similar energies in the geomagnetic tail. Observations have been made by IMP 6 [*Hada et al.*, 1981], ISEE 1 [*Fairfield and Scudder*, 1985], ISEE 3 [*Baker et al.*, 1986, and *Baker et al.*, 1987], and GEOTAIL [*Baker et al.*, 1997]. While these observations may be related in some aspects to those discussed here, it is clear that there are other processes involved, (e.g. polar rain) and so they shall be given no further consideration in this thesis.

4.1.2 Preliminary Studies of FAEs Using CRRES/LEPA, *Johnstone et al.*, 1994.

The LEPA on CRRES is an ideal instrument for finding and studying FAEs as the operational energy range covers that in which FAEs are most often seen, and the resolution and coverage in pitch angle is sufficient to reveal the details in the distribution. Throughout the operational life time of CRRES 532 FAEs were observed (listed in Appendix B. Preliminary studies of some of the events have been done by *Johnstone et al.*, 1994, and *Johnstone et al.*, 1996, though neither of these studies extended to the entire data set, and both were conducted prior to the discovery of the onboard processing error (see Section 3.4.2). The analysis by *Johnstone et al.*, 1996, concentrates on the acceleration of the field aligned electrons, which is further discussed in Chapter 5. The analysis by *Johnstone et al.*, 1994, is concerned with the general characteristics of the FAEs seen by CRRES and is reviewed below.

LEPA often observes enhancements in the field aligned electron fluxes at low energies (0.1 - 1 keV), simultaneous with increased injected[1] electron fluxes seen at higher energies, across all pitch angles, generally with minima in the field aligned directions. However, the enhanced field aligned electron fluxes are not always confined to low energies and have sometimes been seen across the entire energy range observed by LEPA. The electron beams are normally around 15° wide and are not confined to the loss cone though often it is within the loss cone that the greatest fluxes are seen. The events are generally short lived with durations typically less than 10 minutes.

Further generalizations can be made about the FAEs and the environment they appear within. *Johnstone et al.*, 1994, suggested grouping into three types i.e. 'Dropouts', 'Sharp Onsets' and 'Substorms'. The *Johnstone et al.*, 1994, catorgorisa-

[1]Note that the terms 'injected' and 'injection' within the scope of this thesis refer simply to the arrival of relatively long lived high fluxes of particles (in the LEPA energy range) in the region of the spacecraft, and suggests nothing of the cause, nature, or source of the particles.

tion is purely descriptive and is not intended to imply anything regarding the cause or nature of the events (including the use of the word substorm). Examples of the three types are shown in Figures 4.1, 4.2, and 4.3. These are shown using the standard survey plots for one orbit of LEPA data. The standard survey plot has six main panels; the top three panels show the data from the electron analyser, and the lower three, that from the ion analyser. The six main panels are all energy-time spectrograms shown in terms of differential energy flux units (keV cm^{-2} s^{-1} sr^{-1}) as indicated by the colours scales labeled Elec Flux and Ion Flux (note, the center colour scale is for the two minor panels indicating the counts s^{-1} in the background channels). For both the electrons and ions the top panels, labeled Perp, show the measured fluxes perpendicular to the local geomagnetic field direction. The lower two panels, labeled Equa and Erth, show the fluxes measured in the field aligned directions looking towards the magnetic equator, and towards the Earth respectively. Figure 4.4 shows schematically the data shown in the survey plots. The pitch angles covered by the data shown in the survey plots depends on the mode LEPA is operating in and the relative direction of the magnetic field to the spin axis, but essentially the highest resolution data available collected from the coarse zones is shown.

- **Dropouts.** In these events the fluxes of energetic electrons and ions drop below the sensitivity of the instrument, sometimes within a few seconds, for intervals of typically 1-2 minutes (though in some cases the very low fluxes last for up to an hour). At the edges of these dropouts, bursts of field aligned electrons are frequently found though not always. Figure 4.1 shows an example of an FAE of the dropout type. The event occurs at 08:34 UT and lasts for 5 minutes. For the 7 minutes immediately prior to, and the 8 minutes following the event, the electron flux seen in all three panels is below the sensitivity of the sensor. This event shows field aligned electrons covering most of the energy range of LEPA, though the distributions are more field aligned below 1 keV. There are

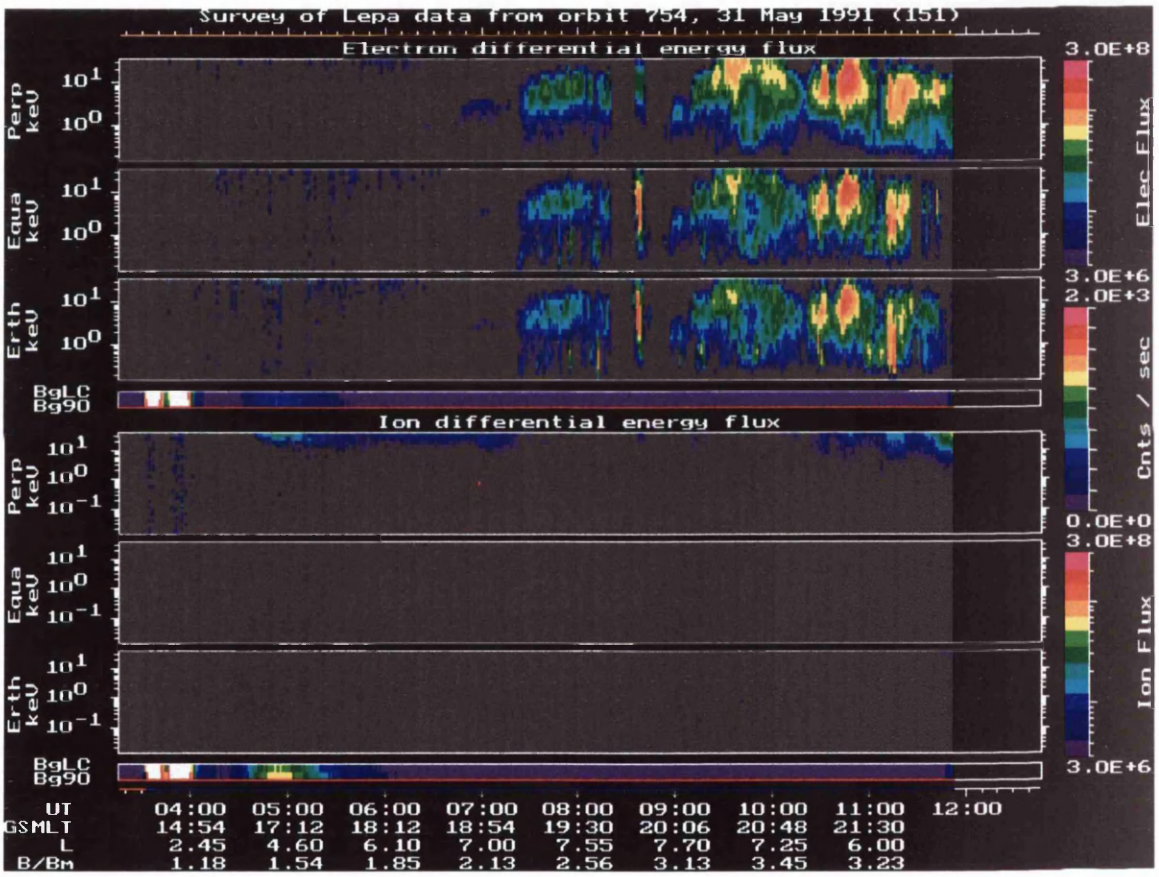

Figure 4.1: An example of an FAE of the dropout type. An explanation of the plot is given in the text.

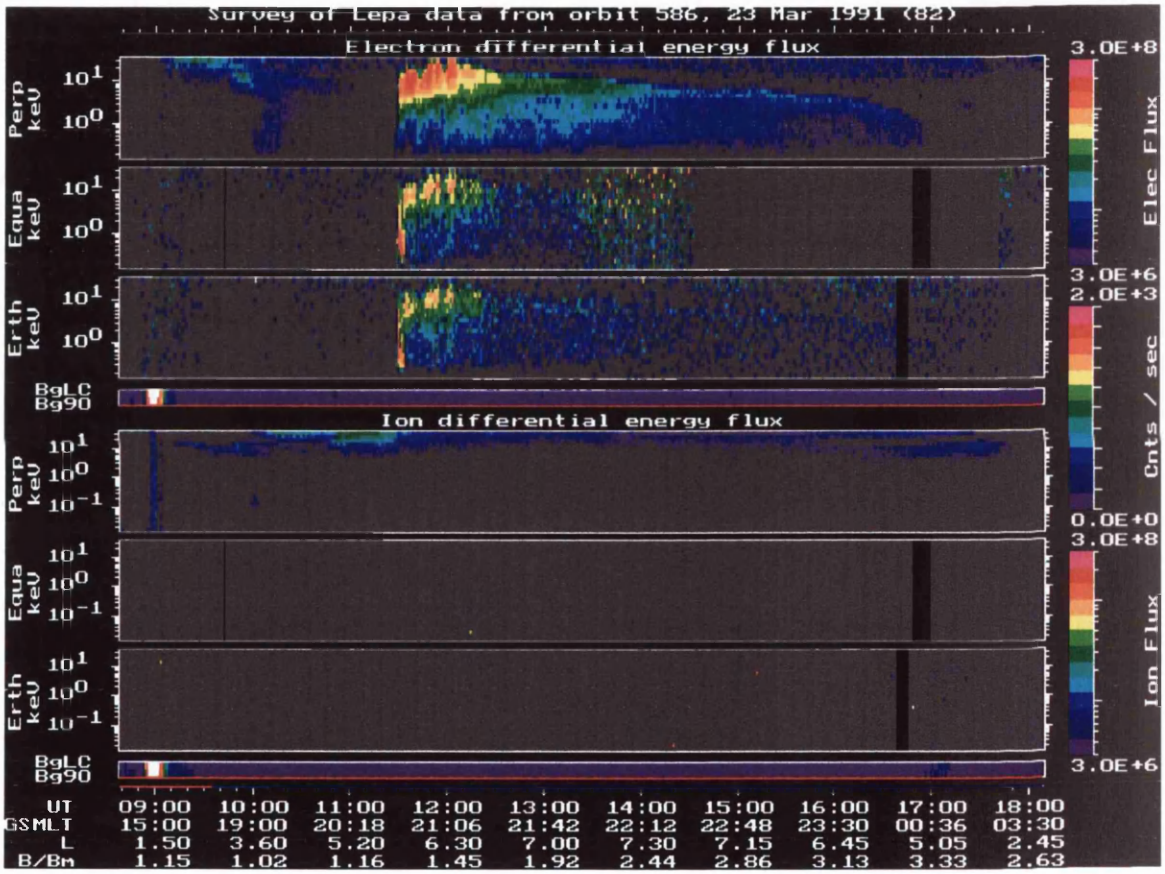

Figure 4.2: An example of an FAE of the sharp onset type. an explanation of the plot is given in the text.

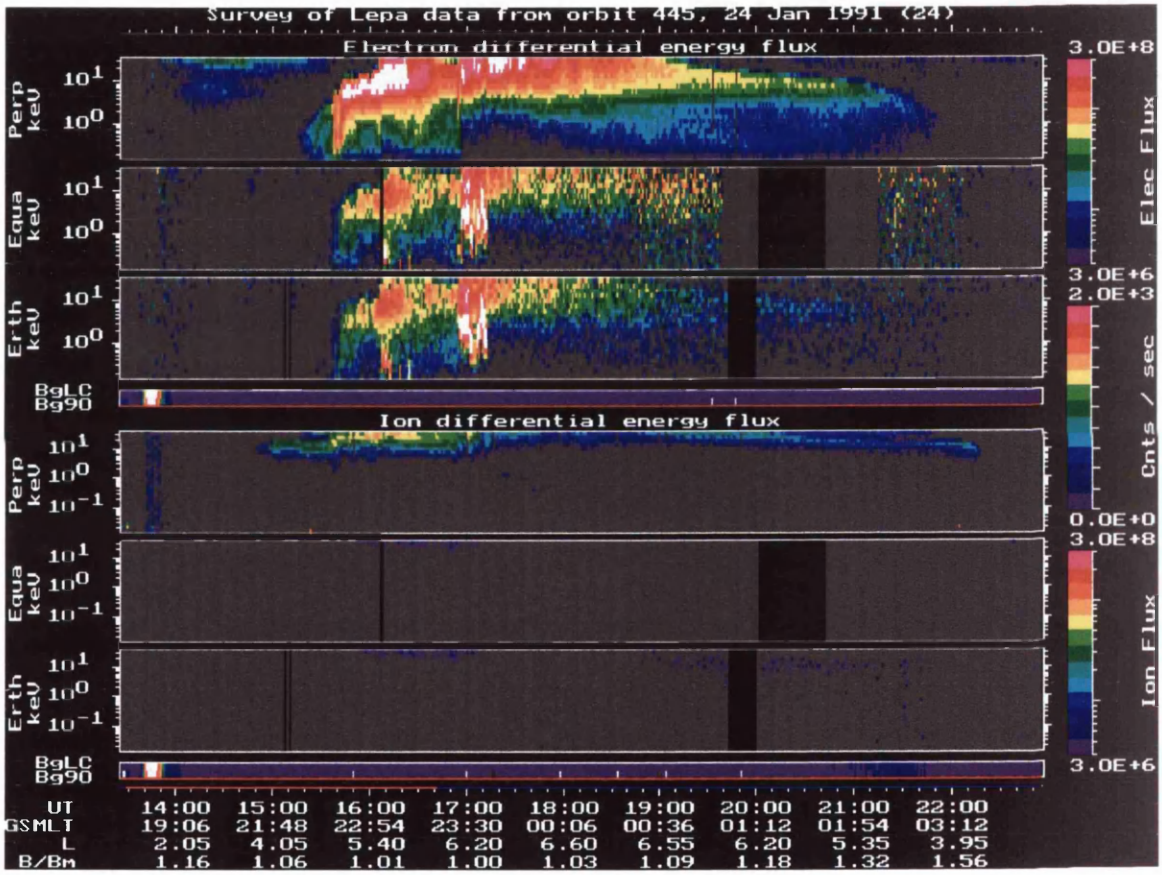

Figure 4.3: An example of two FAEs of the substorm type. An explanation of the plot is given in the text.

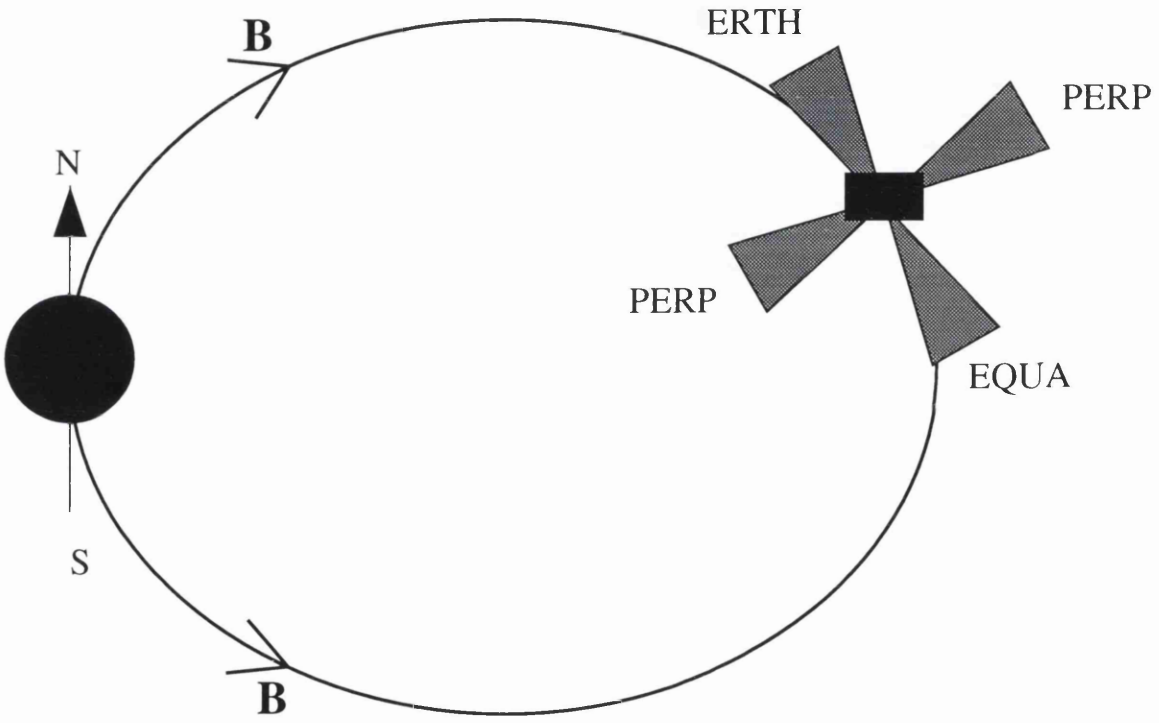

Figure 4.4: A schematic illustration of the collection directions of the data shown in the LEPA survey plots. The shaded triangles indicate the directions from which the electron fluxes shown in the LEPA survey plots are collected

a number of other FAEs present in this orbit which will be discussed further below. Sometimes low energy positive ions with a narrow energy spread and a generally field aligned distribution are found around the time of dropout events, though none are seen in the example in Figure 4.1.

- **Sharp Onsets.** Occasionally the intensity of the electrons increases by an order of magnitude within one half spin of the spacecraft i.e. 15s, at all energies from 10 eV up to 10 keV simultaneously across all pitch angles. When this happens field aligned electron distributions are often seen around 1 keV. The appearance of the 'Sharp Onset' events is quite distinctive and different from a more usual scenario for a substorm like injection where the increase is observed first at lower energies and then proceeds at higher energies (e.g. Figure 4.3). In the 'Sharp Onset' events the intensity decays over a period of 1 to 2 hours after which another event may occur. The fact that they are always seen as a sharp increase and a slow decay, whether on outbound or inbound orbits, and never the other way round, indicates that they are basically a time-dependent phenomena, although they could be caused by the propagation of a spatial structure, like a westward traveling surge, over the spacecraft. A distinctive feature of these events is that there is no visible related change in the positive ion distributions. Figure 4.2 shows an example of an FAE of the sharp onset type. The event occurs at 11:28 UT. Here the flux increases from a level below the sensitivity of LEPA to high values across the entire energy range simultaneously. The distribution, following the injection, is field aligned at low energies (<2 keV) and peaks at 90° at higher energies. The field aligned fluxes are seen for a comparatively short time (6 minutes) compared to the fluxes peaked at 90°, which remain for a number of hours. Following the FAE the electron fluxes with energies around 1 keV display a periodic like structure, which is common following 'sharp onsets'. In the events studied by *Johnstone et al.*, 1994, sharp

onsets are only seen in the pre-midnight sector prompting the suggestion that they may be connected with a westward traveling surge.

- **Substorms.** 'Substorm' events were picked out because they were associated with increases in the overall distributions, both electrons and ions, which looked like substorm particle injections. A second class, which initially seemed to be different, occurred during long-lasting injection events in what seem to be a steady decay phase. The feature that links these two types of events is that they generally occur following a reconfiguration of the geomagnetic field, such that it changes from a stretched tail-like direction to one more dipolar-like. Figure 4.3 shows an example of FAEs of the substorm type. The survey plot shows a typical substorm injection signature. Two FAEs, both classified as 'substorm' type, can be seen on this orbit. The first at 16:05 UT lasts for 9 minutes, and occurs at energies <1 keV and shows a distribution peak at 90° at higher energies. The second, occurs at 16:54 UT and lasts for 19 minutes, shows a field aligned distribution in the range 0.2 - 10 keV. Below 0.2 keV the electron flux is below the sensitivity of the instrument.

The three examples shown above show 'classic' examples of the three types of isolated FAEs. What is often seen is not an isolated event as shown above, but a number of events occurring in sequence around 10 minutes apart. Often the classification of events is not as clear as in the examples discussed above and there are a number of events which cannot clearly be placed into one of the three categories, sharing features of more than one type. It was mentioned above that Figure 4.1 contained a number of FAEs; these occur at 07:23 UT, 07:35 UT, 07:48 UT, 07:54 UT, 08:02 UT, 08:08 UT, 08:34 UT, 09:13 UT, 10:26 UT, 10:58 UT, 11:06 UT, and 11:11 UT. The events occurring prior to 08:30 UT have all been classed as dropout events. While in the events prior to 08:30 UT the flux does not fall below the sensitivity of the detector

across all energies, it does at the energies where the FAEs are seen (< 2 keV). The same is true of the event occurring at 09:13 UT. Similarly the last three events during this orbit have also been classified as dropout events. In these cases the electron flux seen either side of the FAEs drops considerably, though not to a level which cannot be detected. The 10:26 UT event has not been classified as one of the three types.

The classification of events between the sharp onset type and the substorm type is often hard. The requirement that substorm FAEs occur after a magnetic field reconfiguration does not uniquely define a substorm FAE. For example, the clear dropout event at 08:34 UT in Figure 4.1 occurs following a change in the magnetic field direction. In fact most events follow some change in the magnetic field direction regardless of their type. It is our conjecture that the different types of event are in fact the same phenomenon, whose appearance is affected by the position of CRRES within the dynamic magnetosphere and the background electron population at the time of the FAEs.

4.2 Distribution of FAEs

In this section the distribution of FAEs, firstly in terms of lifetime and secondly in terms of spatial occurrence, is investigated.

4.2.1 Lifetimes of FAEs

FAEs are generally short lived with durations lasting from 1 to 48 minutes though 92% lasted 10 minutes or less. Figure 4.5 shows the distribution of the durations of FAEs observed.

FAEs are seen throughout CRRES' operational lifetime, at most MLTs observed by CRRES, but only on L-shells > 4.5. Despite CRRES spending over 36% of its time inside an L-value of 4.5, only one FAE has been observed in this region. Clearly

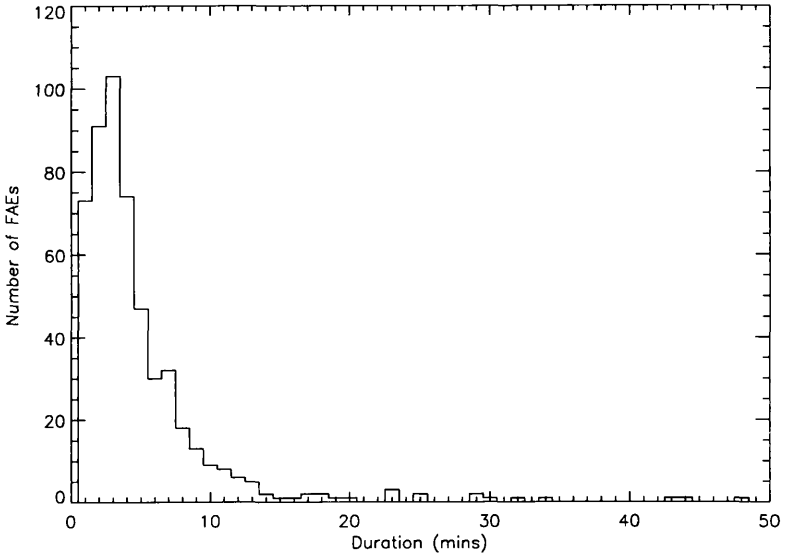

Figure 4.5: A histogram showing the distribution of durations of FAEs observed by LEPA onboard the CRRES satellite.

the closer a spacecraft is to the Earth the faster it travels in its orbit, and so one may expect that the spacecraft, when close to the Earth, may travel through these field aligned features faster than is detectable with the 30 second resolution available[2]. The inner boundary of observations coincides approximately with the position of the plasmapause. While this is far from a static boundary, we have found that FAEs are seen only outside of the plasmapause, as defined by the wave data from the PWE (see Section 6.1.1).

If it were the case that the lifetime of an FAE corresponded to CRRES moving through a static feature we would expect a general trend of shorter events with increasing spacecraft speed, and thus decreasing distance from the Earth. The speed,

[2]Although LEPA looks parallel to the field and then anti-parallel 15 seconds later the effective resolution is 30 seconds for two reasons. Firstly, these events are sometimes in one direction only, and secondly, we require that high fluxes parallel to the field are observed in consecutive field aligned bin in order to identify an event

v of a satellite in orbit around the Earth is given by,

$$v = \left(GM_E\left(\frac{2}{r} - \frac{1}{a}\right)\right)^{\frac{1}{2}}, \tag{4.1}$$

where G is the gravitational constant, M_E is the mass of the Earth, r is the distance from the Earth, and a is the semi-major axis of the ellipse describing the satellite's orbital path (given in Figure 3.2). If the features producing the FAEs all had the same linear size measured along the spacecraft track, then by approximating the spacecraft track through the feature to a straight line[3], the lifetime of an event would be proportional to $\frac{1}{v}$. A more likely scenario is that there is a distribution of feature sizes, in which case the distribution of FAE durations against the radial distance of observation site from Earth, will follow contours proportional to $\frac{1}{v}$. Figure 4.6 shows the distribution of FAE durations against the radial distance of observation site from earth. The red lines marked on the figure are proportional to $\frac{1}{v}$, and clearly do not follow contours of the distribution. Note that only events occurring prior to the orbit raising maneuvers (361 of a possible 532) have been used in this figure to avoid the complications associated with varying orbital parameters.

The above argument assumes that the dimensions of the features seen as FAEs are independent of the direction the spacecraft travels through them. Nearly all features in the magnetosphere are structured by the geomagnetic field, and have different dimensions in radial, azimuthal directions, and so the amount of time a feature may be observed will depend on the direction the spacecraft travels through it (see Figure 4.7). The green lines in Figure 4.6 are proportional to $\frac{1}{v\sin\phi}$, where ϕ is the angle between the satellite's velocity vector and the radial direction, and correspond to CRRES moving through a feature aligned similarly to that shown in Figure 4.7(b). The blue lines in Figure 4.6 are proportional to $\frac{1}{v\cos\phi}$, and correspond to CRRES moving through a feature aligned similarly to that shown in Figure 4.7(c).

[3]We can do this due to the fact that the events are short lived, over which the spacecraft's velocity remains fairly constant.

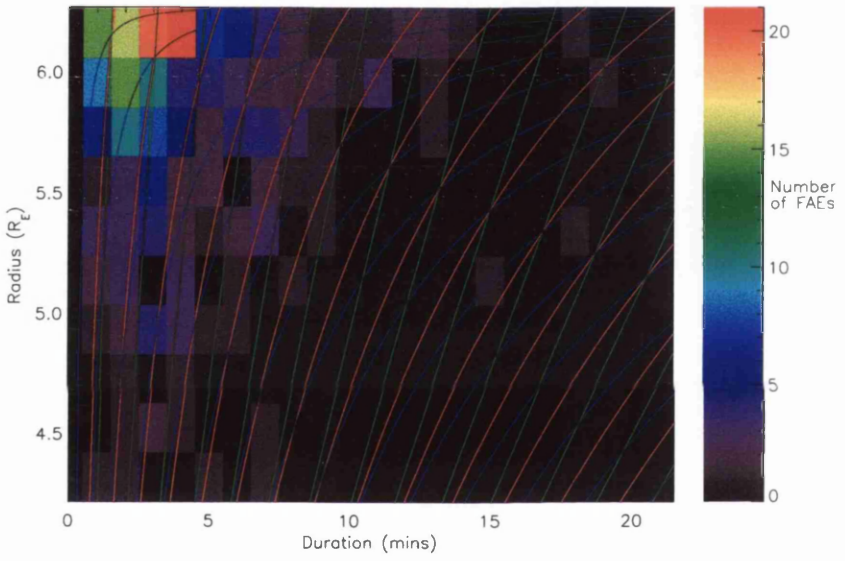

Figure 4.6: The distribution of durations of FAEs against radial distance of the observation site from Earth. The red lines represent the expected variation of duration if CRRES were to be passing through a feature of equal dimensions in all directions. The green lines represent the expected variation of duration if CRRES were to be passing through a radially aligned feature of limited azimuthal extent. The blue lines represent the expected variation of duration if CRRES were to be passing through an azimuthally aligned feature of limited radial extent.

The angle ϕ is defined by

$$\sin\phi = \left(\frac{a^2\,(1-e^2)}{r\,(2a-r)}\right)^{\frac{1}{2}} \tag{4.2}$$

where e is the eccentricity (given in Figure 3.2) of the ellipse describing the satellite's orbital path.

While it is clear that the red and green lines in Figure 4.6 do not follow contours of the distribution shown, the blue lines describe quite well the way the duration of events vary according to the distance of CRRES from the Earth. This suggests that the FAEs are caused by the radial motion of CRRES crossing spatial features roughly aligned azimuthally with respect to the Earth with a limited radial extent.

It is possible to make some estimate of the size of the events as each line in Figure 4.6 corresponds to CRRES moving through a feature of a particular size. From the range of blue lines fitting the distribution it appears that the radial dimensions of the features giving rise to FAEs are typically between 5×10^4 m and 5×10^5 m. It will be shown later in Chapter 7 that we believe that the field aligned electrons are related to the Earth's aurora, which lies in an oval (not strictly azimuthally aligned) around each of the Earth's poles. By approximating the Earth's field to a dipole we can estimate the size of the features crossed by CRRES, when mapped down to the Earth's surface at around 0.3 - 3 km, around the same size as an auroral arc system [e.g. *Borovsky*, 1993b].

This analysis suggests that the dominant effect on the observed lifetime of FAEs due to the spacecraft motion across a posibly long-lived a spatial feature. This is borne out by the fact that CRRES often observes a number of events in a sequence, which may be explained by CRRES moving through a number of features, possible related to a system of nested arcs (e.g. Figure 2.8).

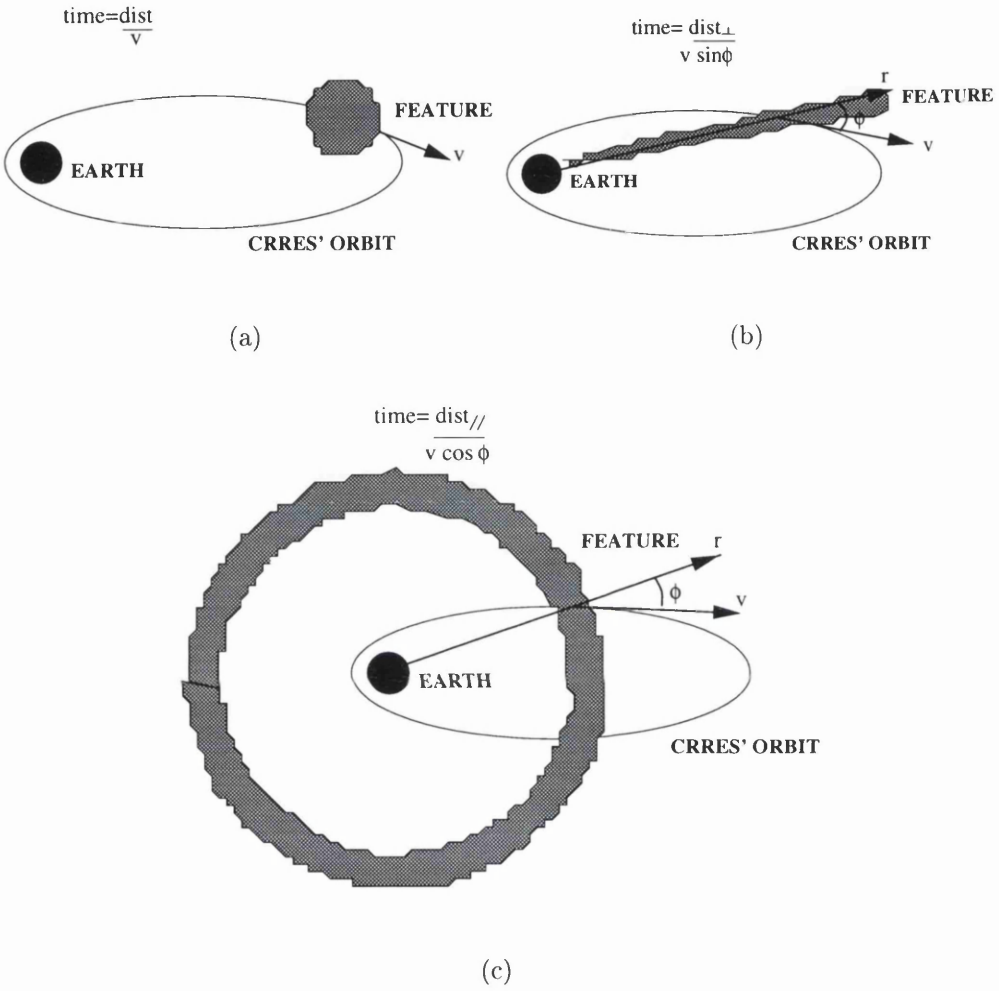

Figure 4.7: The effect of feature structure on the perceived lifetime of an associated event observed by CRRES. (a) shows a feature with dimensions roughly equal in all directions. An event associated with this feature will have a lifetime which is independent of the direction a spacecraft travels through it. (b) shows a radially aligned feature of limited azimuthal extent. The lifetime of an event associated with this feature will be dominated by the spacecraft velocity perpendicular to the radial vector and the structure thickness perpendicular to the radial vector. (c) shows an azimuthally aligned feature of limited radial extent. The lifetime of an event associated with this feature will be dominated by the spacecraft velocity along the radial vector and the structure thickness parallel to the radial vector.

4.2.2 Spatial Distribution of FAEs

The aim of the work in this section is to determine the FAE occurrence frequency as a function of MLT and L-shell. As the FAEs are relatively short lived events we can treat each event as the spacecraft making a single point measurement. The sampling coverage of CRRES is not uniform through the magnetosphere and so we must take into account how long the spacecraft spends in a given sampling region.

Figure 4.8 shows the coverage in terms of MLT and L-shell, summed over all magnetic latitudes, and Figure 4.9 includes the magnetic latitude coverage. Each plot in Figure 4.9 represents the distribution of coverage in terms of L-shell and magnetic latitude, shown in a dipolar field configuration, summed over 2 hours of magnetic local time. For both Figures 4.8 and 4.9 the colour scale indicates the amount of time CRRES spent in each bin. Bins coloured purple indicate those bins which were sampled by CRRES but for less time than the minimum value indicated by the colour scale. Areas coloured black were not visited at all. CRRES operations were suspended during certain intervals giving rise to the complex patterns seen in Figures 4.8 and 4.9.

Figure 4.9 only shows the coverage for 08:00 MLT through midnight to 16:00 MLT because coverage was sparse in the other MLT sectors, and as will be shown, very few FAEs were seen between 08:00 and 16:00 MLT. From Figures 4.8 and 4.9 it can be seen that its opperational lifetime CRRES covers all MLT, within L=5. The coverage is greatest between L-shells of 6 and 7, from 03:00 - 07:00 MLT and between midnight and 11:00 MLT. The coverage extends out to an L-value of 8.5, at higher latitudes, either side of midnight, where it reaches L=7. The magnetic latitude coverage is far from uniform with the morning observations limited to northern latitudes, and the observations in the evening to southerly latitudes. It is the deviation of CRRES' orbit from the geomagnetic equator, due to the combined effect of the orbit, dipole tilt and the spinning Earth, that allows LEPA to sample particles on the higher L-shells.

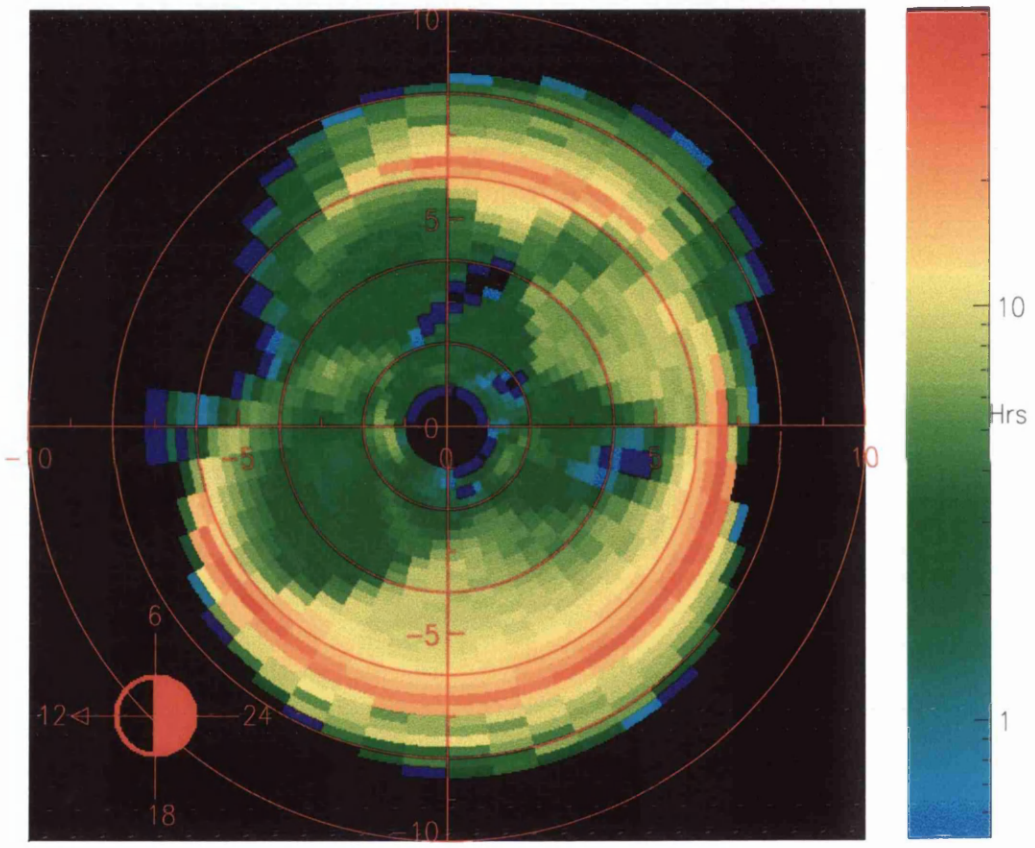

Figure 4.8: Operational time spent by CRRES over the full mission lifetime, in each 0.25L × 30 minutes MLT bin summed over all magnetic latitudes. Further explanation of the plot is given in the text.

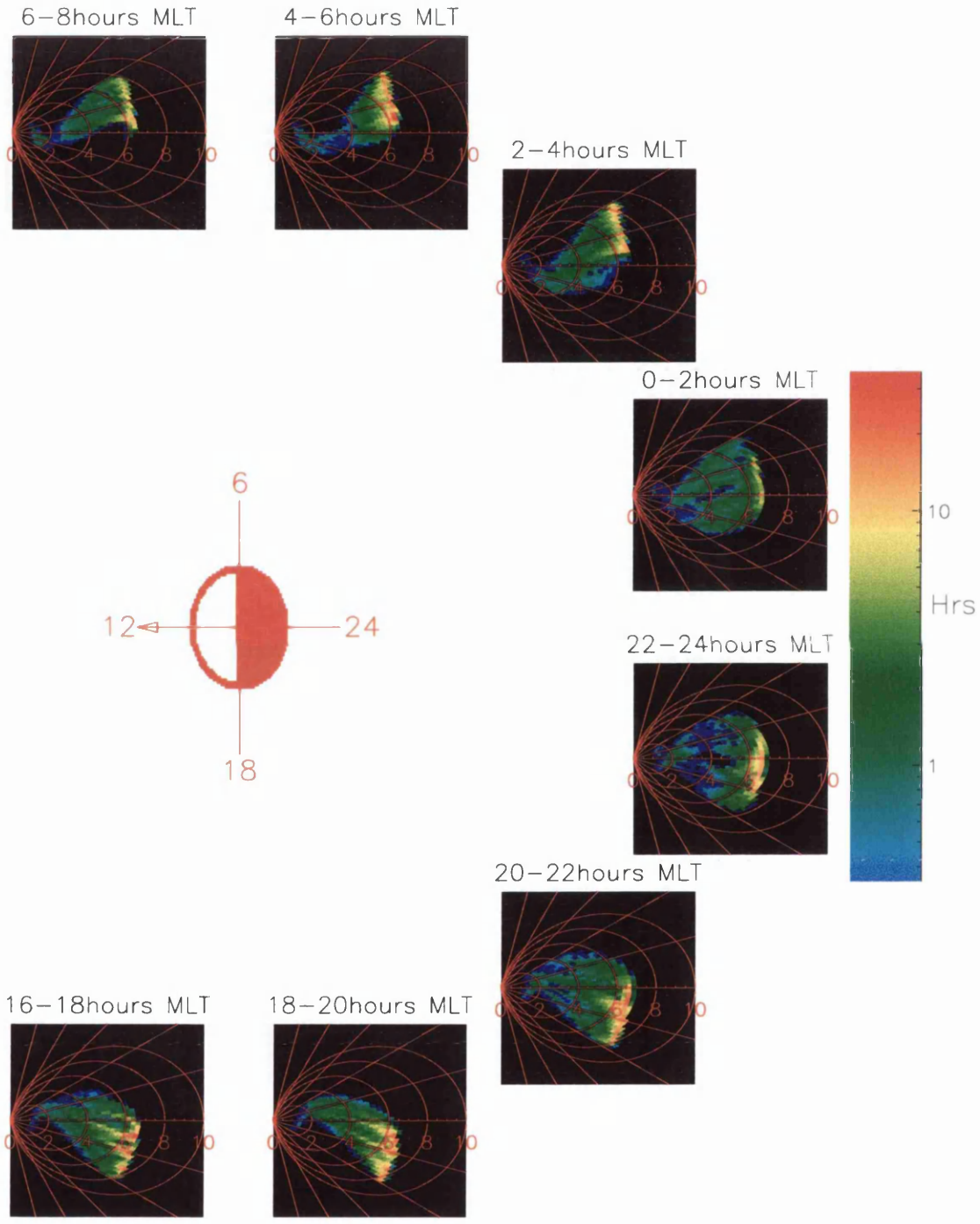

Figure 4.9: Operational time spent by CRRES over the full mission lifetime, in each 0.25L × 4° magnetic latitude bin summed over 2 hours MLT. Further explanation of the plot is given in the text.

The distribution of the observed FAEs is shown in Figures 4.10 and 4.11. These are of the same format as Figures 4.8 and 4.9, but in this case the purple colour indicates regions that have been sampled by CRRES, but where no FAEs were observed. The quantity displayed is the number of FAEs observed in each bin normalised to the time (in hours) that CRRES spent in each bin through its operational lifetime.

As can be seen from Figure 4.10 almost no FAEs are seen in the sampled L-range around noon (08:00 - 15:00 MLT). Away from noon FAEs are seen frequently on L-shells >6, with occurrence frequency generally increasing with L-shell. A few events are seen on L-shells between 4.5 and 6, though only one is seen inside L=4.5. As mentioned in Section 4.2.1 this is most likely due to the fact that no FAEs are seen within the plasmasphere. Although coverage around midnight is less on the higher L-shells there are definitely fewer events in this sector on L-shells for which al MLT are sampled. Peaks in the distribution are around 04:00 MLT and 19:30 MLT.

Looking closely at Figure 4.11 it seems that events are seen at different magnetic latitudes dependent on MLT. Events prior to 22:00 MLT are mainly seen south of the equator though this appears to be due to coverage limitations of higher L-shells. Around midnight most events are seen near the equator (22:00 MLT - 24:00 MLT especially). It is curious that while there is coverage at higher latitudes around midnight for L-shells around 7, few FAEs are seen. From 02:00 MLT - 08:00 MLT most events are seen away from the equator at northern latitudes, and again the lack of events does not arise as a product of a lack of observation time. It is clearer still from Figure 4.11 that the lack of observations of FAEs around midnight is not due to lack of coverage alone. Looking back to Figure 4.9 it can be seen that the coverage between L-values of 6 and 7 is substantial, and yet the frequency of FAE observations is much less than those at similar L-shells away from midnight.

Figures 4.12, 4.13 and 4.14 show the distribution of events of the dropout, sharp onset, and substorm types respectively, summed over all magnetic latitudes in the

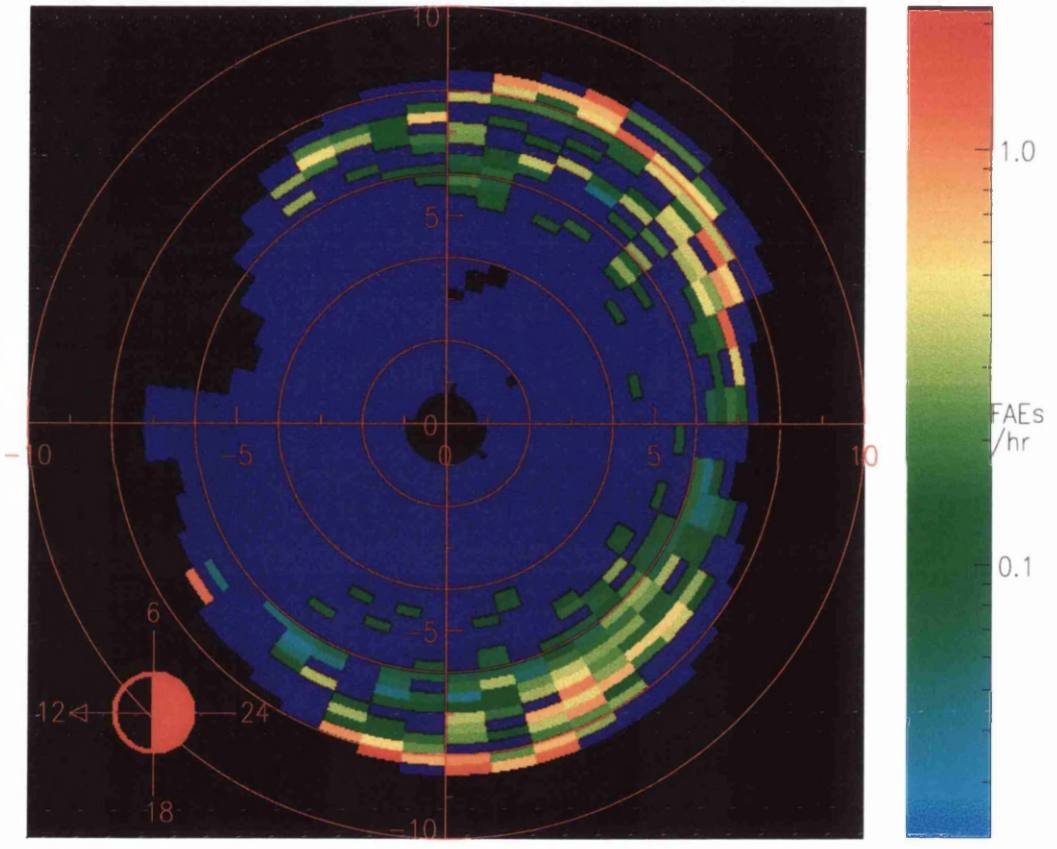

Figure 4.10: Number of FAEs seen by CRRES normalised to the observation time in each 0.25L × 30 minutes MLT bin summed over all magnetic latitudes. Further explanation of the plot is given in the text.

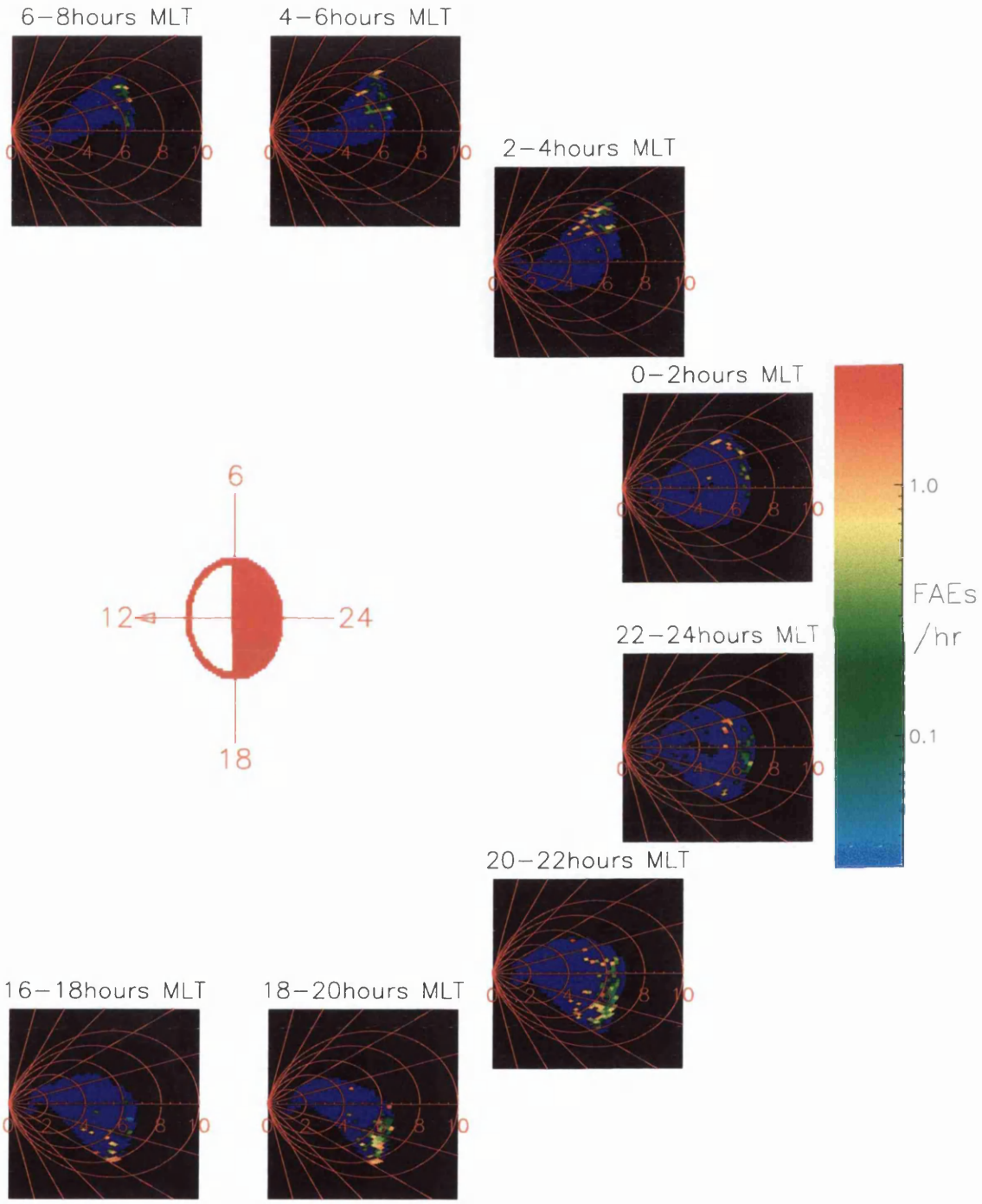

Figure 4.11: Number of FAEs seen by CRRES normalised to the observation time in each 0.25L × 4° magnetic latitude bin summed over 2 hours MLT. Further explanation of the plot is given in the text.

same format as the total distribution was shown in Figure 4.10.

The most obvious feature of Figures 4.12, 4.13 and 4.14 is that nearly all FAEs of the sharp onset type occur to the west of midnight. This supports the argument that they may well be connected to the westward traveling surge. The events of the dropout type and substorm type are both seen either side of midnight, though in the case of the dropout events none are seen within ± 1 hour MLT of midnight. The FAEs of the dropout type often occur on higher L-shells than those of the other two types. The distribution of the different types of event has not been shown over magnetic latitude, as in Figure 4.11, due to the fact that there are fewer events, leading to poor statistics, but generally the dropout types are seen further away from the magnetic equator than the other two types of FAE, though this is dominated by the sampling.

4.3 Association of FAEs with Substorms

Johnstone et al., 1994, suggested that one type of FAE (the substorm type) was associated with (not necessarily caused by) magnetospheric substorms, and a second type (the sharp onset type) was possibly related to the westward traveling surge, a feature of the auroral substorm. This section examines more closely the association between FAEs and substorms to try and establish a link.

A recent study by *Flowers*, 1998, has produced a list of substorm onset times for the CRRES epoch. From the study 187 substorms have been identified by looking for dipolarisation signatures in the magnetic field data provided by CRRES and the GOES 6 and GOES 7 spacecraft, combined with particle injection signatures using the LEPA and EPAS instruments on CRRES, and particle analysers on a number of LANL spacecraft. The spacecraft used to generate the list were all in a geosynchronous orbit, except for CRRES, which reached geosyncronous altitudes at apogee. *Borovsky et al.*, 1993a, found that the mean rate of substorm occurrence was 4.2 per

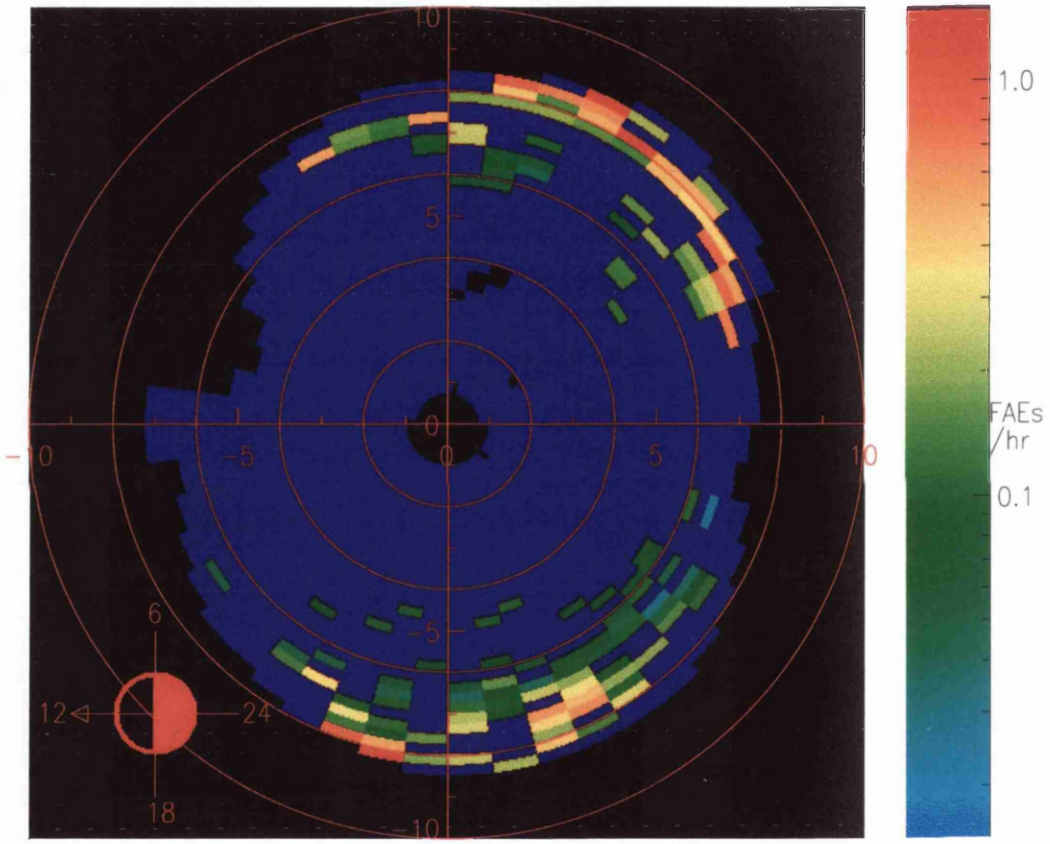

Figure 4.12: Number of FAEs of the 'Dropout' seen by CRRES normalised to the observation time in each 0.25L × 30 minutes MLT bin summed over all magnetic latitudes. Further explanation of the plot is given in the text.

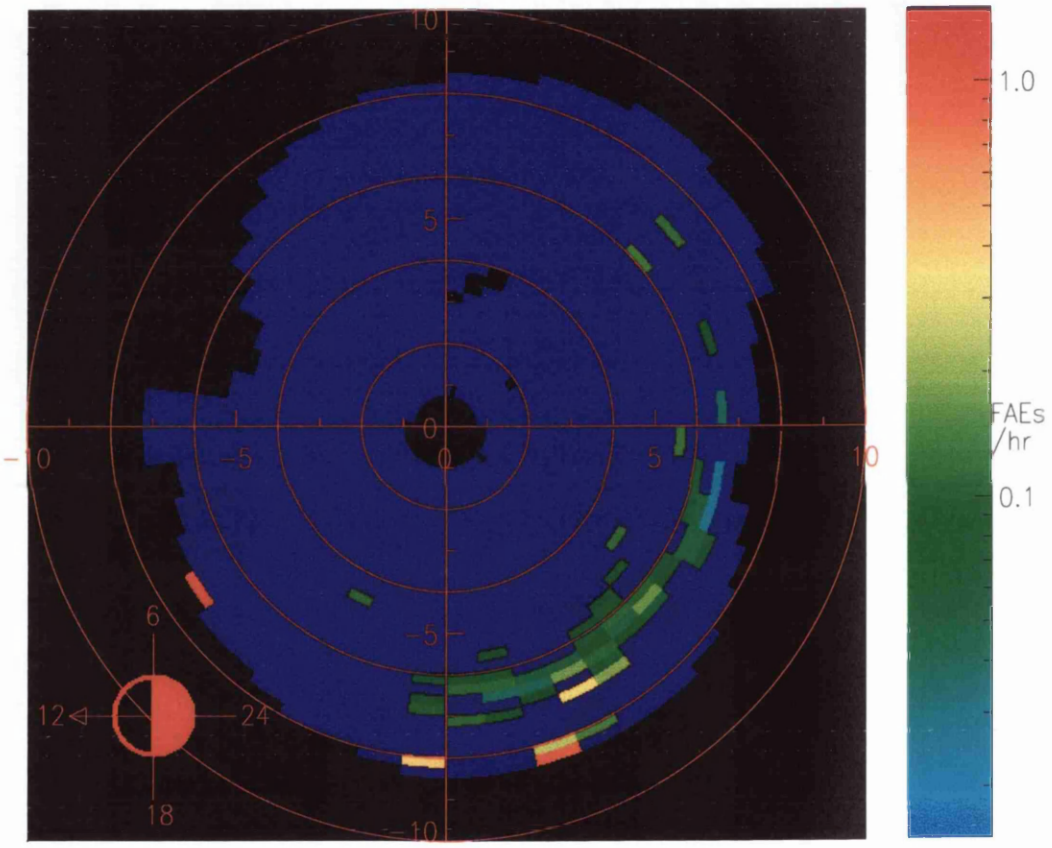

Figure 4.13: Number of FAEs of the 'sharp onset' type seen by CRRES normalised to the observation time in each 0.25L × 30 minutes MLT bin summed over all magnetic latitudes. Further explanation of the plot is given in the text.

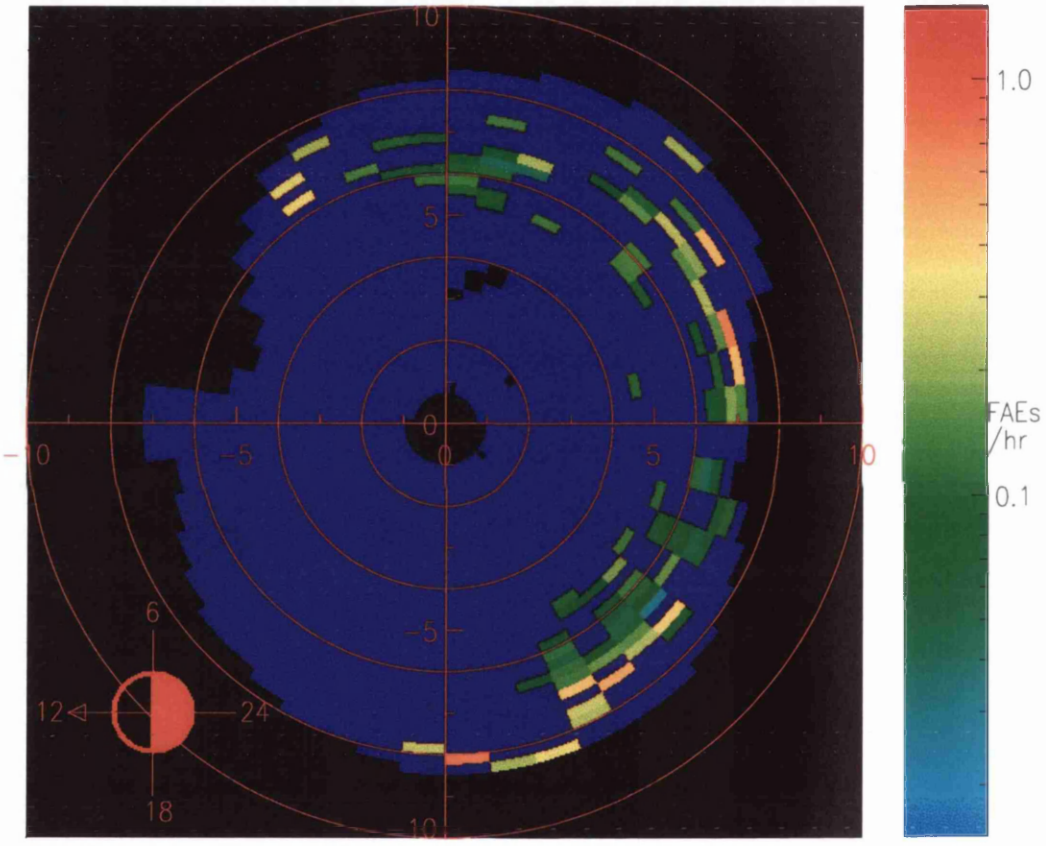

Figure 4.14: Number of FAEs of the 'substorm' type seen by CRRES normalised to the observation time in each 0.25L × 30 minutes MLT bin summed over all magnetic latitudes. Further explanation of the plot is given in the text.

day, and thus it is estimated that this list accounts for around 10% of substorms that occurred over the 15 month lifetime of CRRES. The *Flowers*, 1998, list of substorm onset times can be used to examine whether there is indeed a link between FAEs and substorms.

For 95 of the substorms on the list, over half, an FAE (though often more than one) is seen in the CRRES LEPA data on the same CRRES orbit. The timings of these FAEs relative to substorm onset time as established by *Flowers*, 1998, is shown in Figure 4.15. We define a time interval which refers to the closest temporal occurrence of an FAE, either prior to or following substorm onset, within a CRRES orbit (defined as perigee to perigee). There are two reasons why the closest temporal occurrence of an FAE either before or after substorm onset is used. Firstly the error involved in substorm onset time calculated by *Flowers*, 1998, is estimated to be around 10 to 20 minutes, with onsets more likely to have occurred prior to the calculated onset time. Substorm onsets might occur before the calculated onset time because a substorm onset can only be detected once the magnetic field and particle injection signatures have propagated to the spacecraft location. The second reason why the closest temporal occurrence of an FAE either before or after substorm onset is used is because it may be the case that the FAE is connected not to the listed substorm but to either the previous or following substorm.

There are 62 substorms for which an FAE is observed by CRRES within an hour of onset, 52 of these occur within 20 minutes. 62 substorms corresponds to $\frac{1}{3}$ of all substorms on the list and $\frac{2}{3}$ of those for which an FAE is seen during the same orbit. Considering that the mean time between FAEs observed by CRRES is of the order 1 day, this clearly shows a link between substorms and FAEs (further strengthened by the fact that often many FAEs are associated with the same injection event).

The distribution shown in Figure 4.15 has a secondary peak between 1 hour 50 minutes and 4 hours 30 minutes. Though this is small and thus far from smooth, it

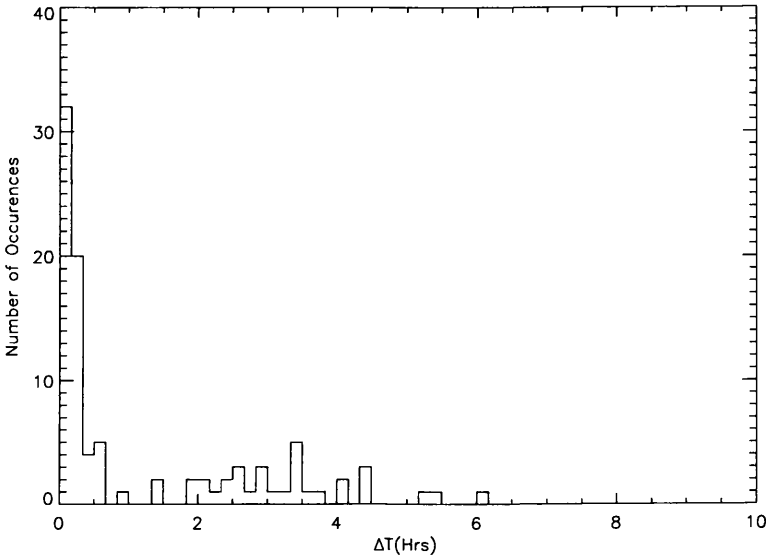

Figure 4.15: Histogram showing the distribution of times between substorm onset as identified by *Flowers*, 1998, and the closest temporal occurrence of an FAE as observed by CRRES.

is significant (of the 33 substorms not within 1 hour of substorm onset 23 of them lie within the 2 - 4 hour ΔT period). *Borovsky et al.*, 1993a, found that the distribution of substorm repeat times had a broad peak between 2 and 4 hours and that the modal time between substorm onset was 2.75 hours. The substorms found to be $\sim$2.75 hours apart, occurred when substorms were taking place in a cyclic fashion. It is not surprising therefore, that we see a peak in the time between substorm onset and FAE observation, between 2 and 4 hours, as these are likely to be related to a substorm onset either prior to or following the one determined by *Flowers*, 1994 (i.e. not one seen by *Flowers*, 1994).

We believe that the three different types of FAE described in Section 4.1.2 are essentially the same phenomena whose appearance is affected by the position of CRRES within the dynamic magnetosphere at the time of the FAEs, and the background electron population. One might then argue that not all the three types of event are

associated with substorms. Figure 4.16 shows the distribution from Figure 4.15 in terms of the different event types. All three distributions in Figure 4.16 are similar showing a strong peak near zero. The secondary peak seen in the distribution covering all types (Figure 4.15) cannot be seen clearly in any of the distributions shown in Figure 4.16 due to the Poisson noise associated with the fewer events. It seems that the different types of FAE share the temporal association with substorms.

The probability of CRRES observing an FAE within 1 hour of substorm onset during times when CRRES is on L-shells >5 is 51±6%. However, as has been shown, the distribution of the observed FAEs is not uniform over all MLT, and thus it would be expected that the probability of observing FAEs within 1 hour of substorm onset would also vary with MLT. The distribution of these probabilities is shown in Figure 4.17, with error bars calculated from Poisson statistics. It is worth noting at this point that due to the fact that CRRES was one of the satellites used to determine this list of substorms, the list favors those where CRRES is in a position to see dipolarisation and injection events. In fact over a third of the substorms on the list occur when CRRES is between 20:00 MLT and 24:00 MLT. However none of the substorms were identified with data from CRRES alone (if at all), and the usage of other spacecraft allows the calculations to be extended around all local time.

If we compare the probability distribution shown in Figure 4.17 to the rates of FAEs seen in the same region of space, Figure 4.18, it is clear that they follow roughly similar shapes (though in Figure 4.18 there is an asymmetry between the 12:00 - 24:00 sector and the 00:00 - 12:00 sector which is much weaker in Figure 4.17). It is not unexpected that the two distributions would be similar as the probability distribution (Figure 4.17) can be interpreted simply as a superposition of the distribution of FAE observation (Figure 4.18) on the distribution of spacecraft position at substorm onset (ideally uniform). However, it would be unreasonable to expect that if FAEs occurred both associated with substorms and independently, that the distribution around MLT

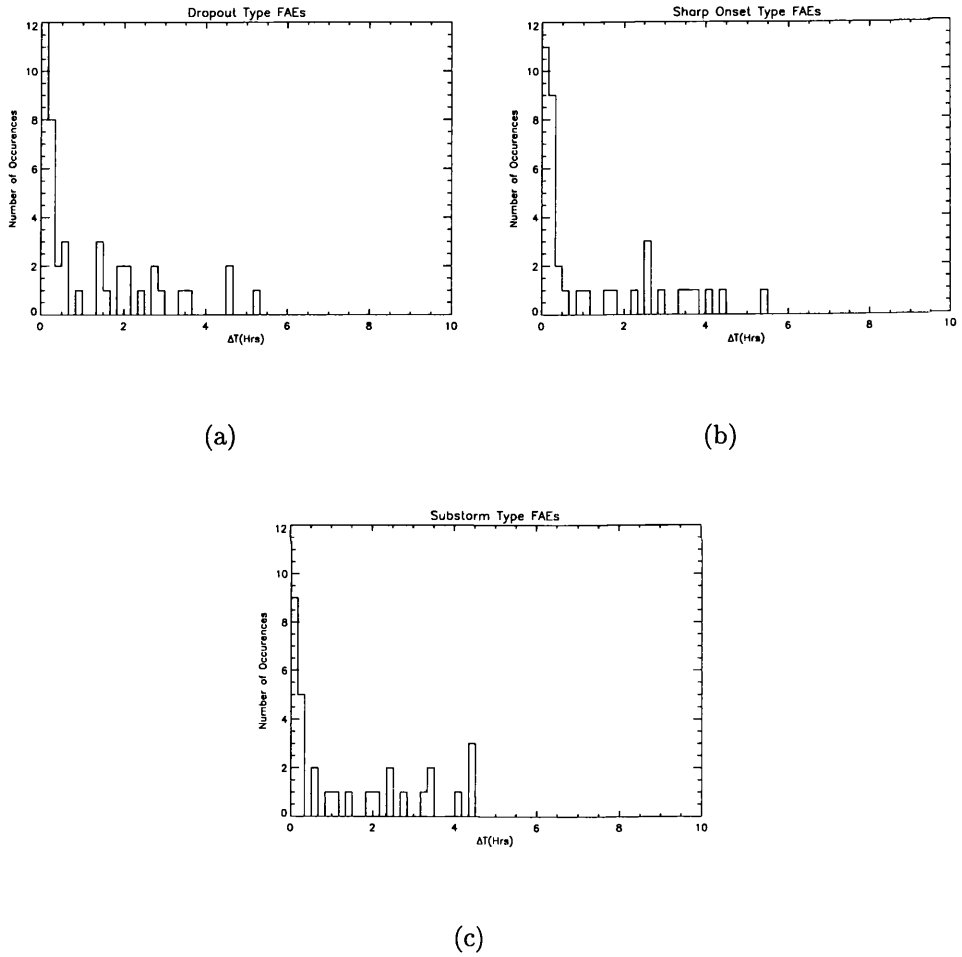

Figure 4.16: Histogram showing the distribution of times between substorm onset as identified by *Flowers*, 1998, and the closest temporal occurrence of an FAE as observed by CRRES for (a) FAEs of the dropout type, (b) FAEs of the sharp onset type, and (c) FAEs of the substorm type.

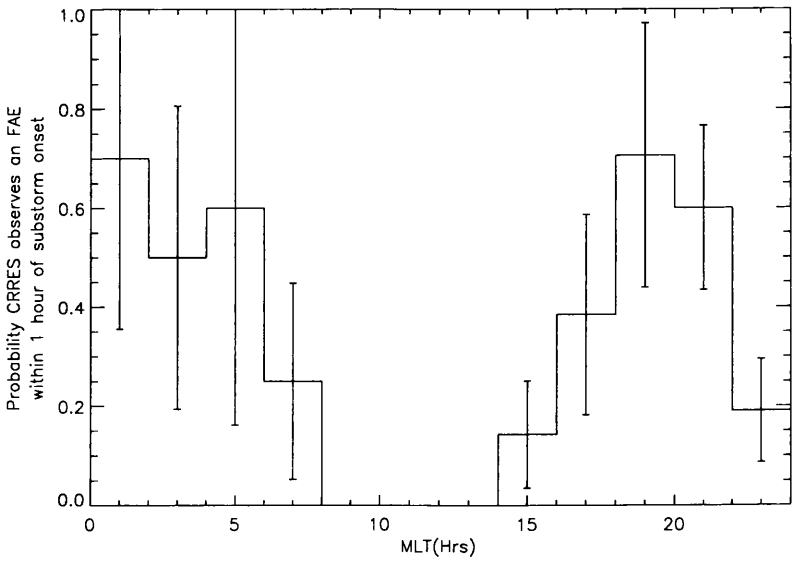

Figure 4.17: Histogram showing the probability of CRRES observing an FAE within 1 hour of substorm onset time (calculated by *Flowers*, 1998) as a function of MLT for times when CRRES is on L-shells > 5.

of the FAEs related to substorms and the independent events would be identical. If all FAEs were observed around times of substorm onset one would expect the same distribution to be seen in Figure 4.17 and Figure 4.18 (assuming that the FAEs seen within an hour of substorm onset are related to that substorm). The difference between the distributions can be illustrated by taking the ratio of the quantities shown in Figures 4.17 and 4.18 as is done in Figure 4.19.

In the case where all FAEs seen were associated with a substorm it would be expected that the distribution around MLT of the quantity shown in Figure 4.19 would be a constant. Ignoring MLTs from 08:00 to 14:00, where the coverage by CRRES was low, or nonexistent, the observations are consistent with a uniform distribution, with only one bin, either the 00:00 - 02:00 MLT bin or the 20:00 - 22:00 MLT bin, not lying within 1σ (and that bin is well within 2σ and so can be dismissed as a statistical anomaly). However the errors on the distribution are very large in some

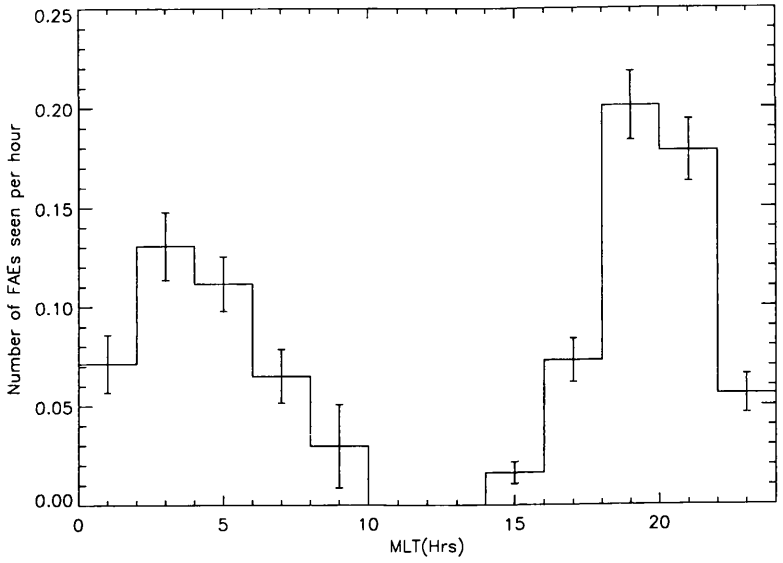

Figure 4.18: Histogram showing the number of FAEs CRRES sees per hour of observation in each 2 hour MLT bin while CRRES is on L-shells > 5.

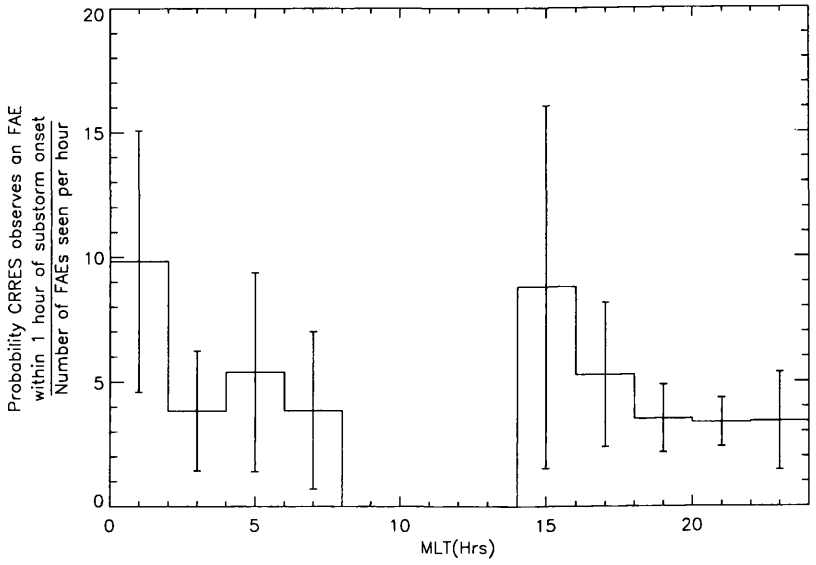

Figure 4.19: Histogram showing the ratio between the probability of CRRES observing an FAE within 1 hour of substorm onset and the number of FAEs CRRES sees per hour of observation as a function of MLT for times when CRRES is on L-shells > 5.

cases, and while it is consistent with a uniform distribution, it would also be consistent with many other distributions. So from this it cannot be declared that all FAEs are associated with substorms, although our observations are consistent with them being so.

To truly say that all FAEs are associated with substorms it is necessary to decide for each event whether or not a substorm is in progress. In order to investigate this the AE index has been studied for each event. However the AE index is not an ideal proxy for a substorm as FAEs are often seen near onset, a time when the auroral electrojet (and thus the AE index) may not have responded to the substorm, see Figure 4.20. In order to see if FAEs are related to substorms, the maximum 1 minute value for the AE index in the hour following the event is used. Figure 4.21 shows the distribution of the maximum AE index in the hour following an FAE. The average of this maximum AE index is 819 nT, and the majority of events occur when this index is high, reinforcing the argument that these events are substorm related. There are however a number of events at times of low AE index. 35 events (6.5%) are seen when the AE index does not go above 150 nT in the hour following the event.

It is possible that the FAEs seen at times of low AE may occur at times when the AE index is a poor measure of activity. The AE index is calculated from a number of magnetometers which lie at latitudes concurrent with an average auroral oval. The AE index may not show a substorm for two reasons. Firstly it may be that the auroral oval is not lying near it's average position, resulting in weaker magnetic signatures at the ground stations. These magnetic signatures in turn lead to an underestimation of the AE index. Secondly problems also occur due to a lack of data when the strongest region of the auroral electrojet lies over Asia. However, it seems that a small percentage of events are seen at quiet times, though these are the exception rather than the norm.

It should be stressed here that the main point is the fact that the majority of FAEs

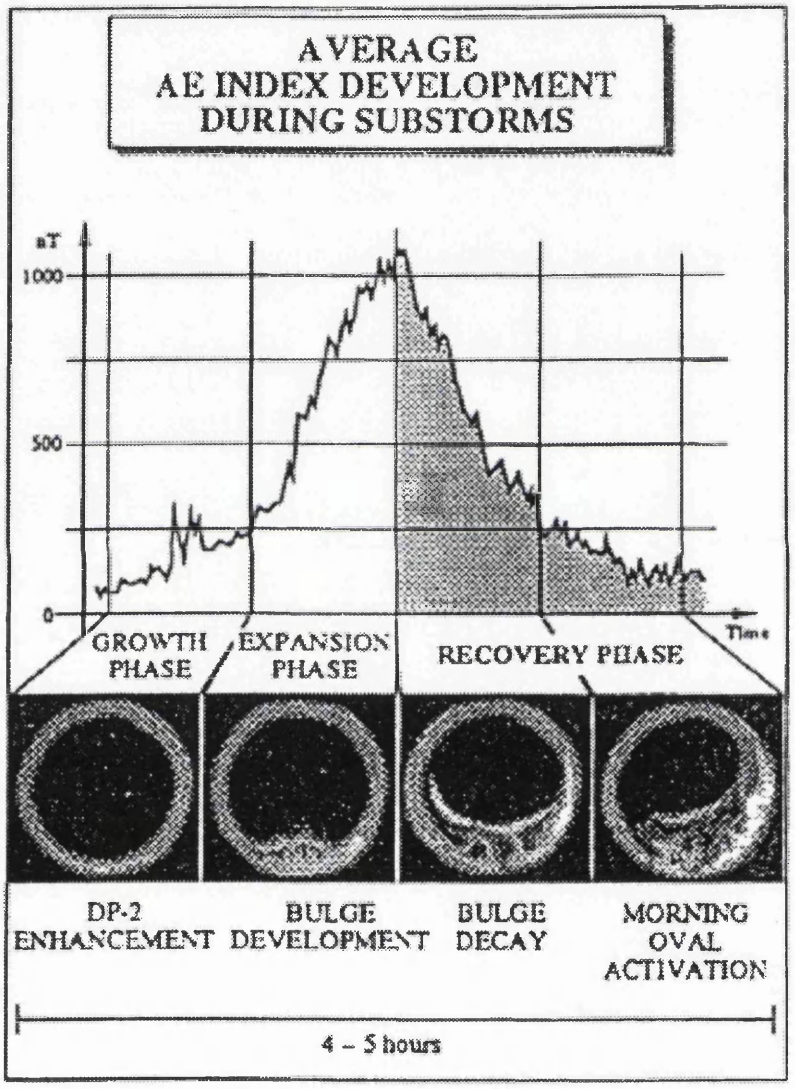

Figure 4.20: Average AE index development during substorms [*Koskinen*, 1994]. Onset is defined as the start of the expansion phase.

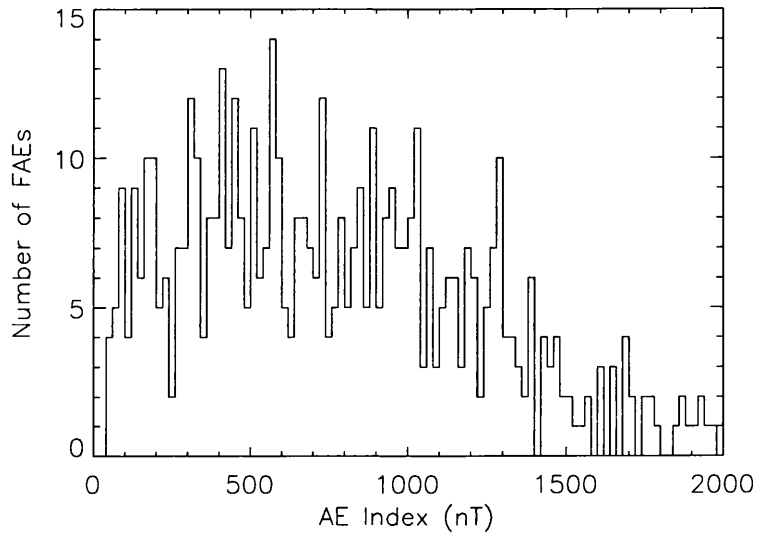

Figure 4.21: Histogram showing the distribution of the maximum AE index in the hour following an FAE.

are associated with substorms, and that those that are, are usually seen within 20 minutes of substorm onset. At certain MLTs (04:00-06:00 MLT and 18:00-20:00 MLT) the chance of CRRES observing an FAE within an hour of substorm onset is high enough to suggest that FAEs are present with every substorm, and as such may form an integral part of the substorm process. The possible role that they play will be discussed in Chapter 7.

4.4 AMPTE/CCE Observations [*Klumpar*, 1993].

As mentioned in Section 4.1.1, *Klumpar*, 1993, surveyed the location of counter-streaming electrons, out to 8.5 R_e, using data from the Hot Plasma Composition Experiment (HPCE) on the AMPTE/CCE satellite. The AMPTE/CCE spacecraft was spin-stabilized at 10 rpm, with its spin axis in the equatorial plane, and offset from the Earth-Sun line by about 20 degrees. The HPCE consists of 8 fixed energy

electron sensors, operating simultaneously, each with a 5° full width conical field of view. The sensors were mounted with the centers of their fields of view perpendicular to the spacecraft spin axis. This meant that the HPCE was not able to sample the electrons in the field aligned bin (0°-10° pitch angle) at all times, only when the magnetic field passed within 10° of the sensor's 5° field of view (cf. LEPA's 120° field of view).

To catorgorise the HPCE data an anisotropy index was found for each energy channel for a set of 6.4 minute intervals, by calculating the ratio between the average flux in the field aligned bin (0°-10° pitch angle) to the trapped bin (80°-90° pitch angle). Note that no account is taken of whether the electrons are traveling up or down the field line, i.e. electrons with pitch angles 170°-180° are binned with the 0°-10° pitch angle electrons, pitch angles 160°-170° are binned with pitch angles 10°-20° etc. However, this is of little importance as nearly all field aligned electrons seen in this region of the magnetosphere are counterstreaming. An anisotropy index $>$ 1.5, occurring in more than one of the eight energy channels, was taken to be an indication of counterstreaming electrons. Counterstreaming electrons will be seen in several neighbouring energy channels so an anisotropy index $>$1.5 in only one energy channel can be dismissed as a false signal.

Figure 4.22 shows the results of the AMPTE/CCE survey (note that noon is to the top of the figure). Comparing Figure 4.22 with Figure 4.10 there we can see similarities. Firstly the distributions in both figures increases with radial distance, with little inside L = 6. Secondly a minimum at midnight exists in both distributions. In Figure 4.22 the midnight minimum is not as wide as that seen in the CRRES data, however the agreement is generally good. Though there are fewer examples of counterstreaming electrons on the dayside compared to the nightside, in the AMPTE/CCE data, there are a significant number. This suggests that the lack of observations of FAEs on the dayside by CRRES is a result of limeted coverage.

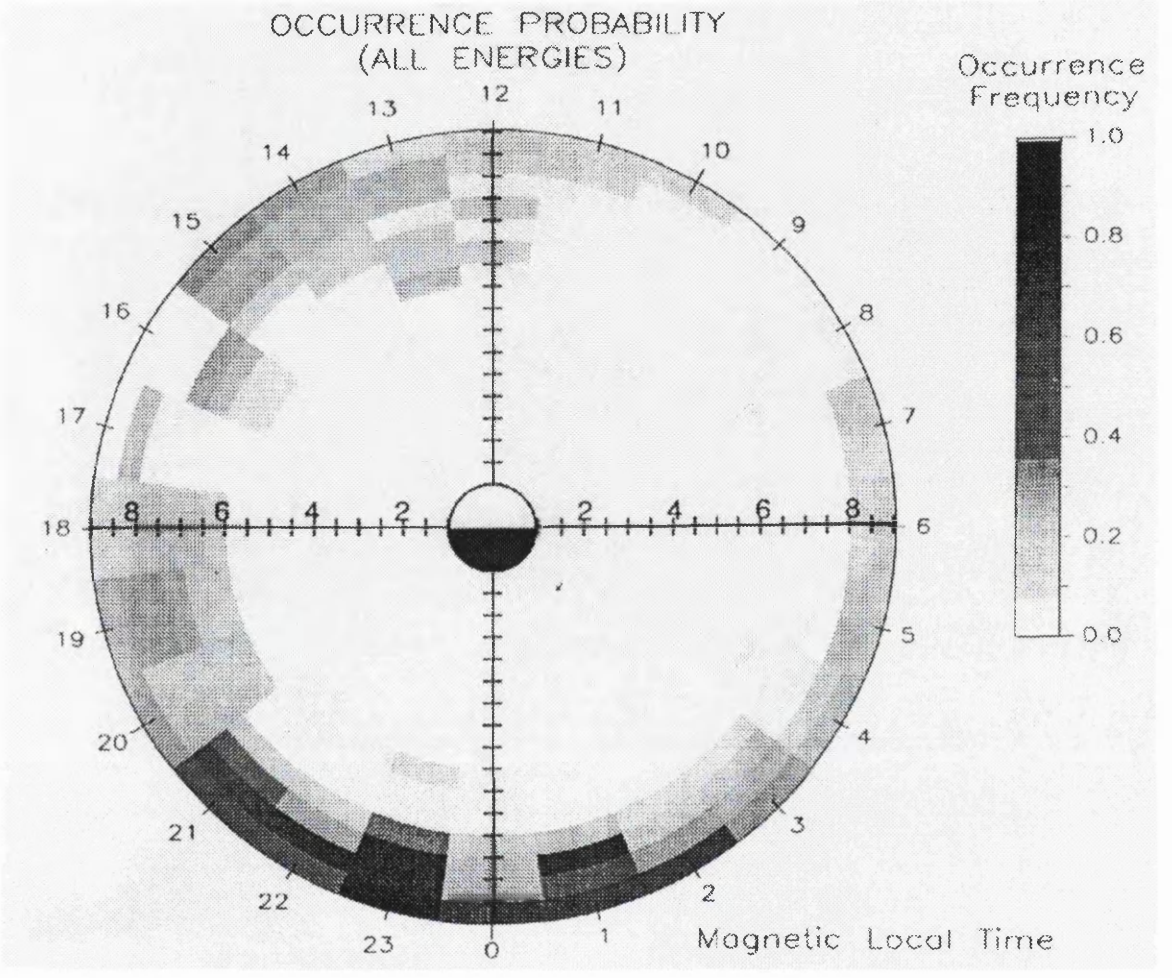

Figure 4.22: The probability of occurrence of the 6.4 minute average anisotropy index exceeding 1.5 in any two energy channels of the HPCE on the AMPTE/CCE. (Taken from *Klumpar*, 1993).

While the AMPTE/CCE survey in general has greater time coverage than CRRES, the exception is on the nightside where CCE has less observation time than CRRES has in that region.

The main discrepancy between the AMPTE/CCE survey and the CRRES results presented here, is the actual probability of observing field aligned electrons. In some parts of the magnetosphere the AMPTE/CCE survey suggest occurrence frequencies of >50% (clearly not consistent with the majority of FAEs being related to substorm

onset), compared to a maximum value of ~2 FAEs seen per hour in the CRRES observations. Considering the duration's of FAEs shown in Figure 4.5 (i.e. 92%<10 minutes), it is clear that the AMPTE/CCE observation frequencies are a factor of a few larger than the CRRES observation frequencies. One factor which may account for some of this discrepancy in the observed frequency of events is the way in which the anisotropy index is calculated. The events seen within the LEPA data set are such that 1 minute of counterstreaming electrons would produce an average anisotropy index >1.5 in a 6.4 minute bin. Events may well straddle two or more bins, e.g. a 5 minute event may result in two consecutive 6.4 minute bins having an average anisotropy index >1.5. This exaggeration, however, is not enough to account for the apparent discrepancy in the observed frequency of events. It is possible to explain this discrepancy, when consideration is given to the conditions when AMPTE/CCE sampled the magnetosphere for counterstreaming electrons.

Klumpar, 1993, calculated the probabilities of occurrences of counterstreaming electrons only considering times when the magnetic field was such that the HPCE would be able to observe them. This would be more likely to occur when the field was more dipole-like rather than in a stretched out configuration, i.e. after a dipolarisation or substorm onset. It turns out that the HPCE could only see the field aligned component of the electron distribution 38% of the time [*Klumpar*, 1993]. Thus the times when HPCE is able to see counterstreaming electrons, are also the times when counterstreaming electrons are most likely to be seen. Due to the 120° field of view, LEPA is able to observe the field aligned direction at nearly all times, and so the survey presented in Section 4.2.2 does not include the kind of overestimation made by *Klumpar*, 1993.

In addition to the fact that *Klumpar*, 1993, has overestimated the probability of counterstreaming electrons being observed in the magnetosphere by a factor of 2-3, the distribution of these probabilities is also invalid. The overestimation cannot be

assumed to be constant around local time, due to the fact that field lines around midnight are more likely to be stretched further away from a dipolar configuration than at other MLT. As there are no details given in the *Klumpar*, 1993, paper of what proportion of time HPCE was able to observe along the field line, in the different regions of the magnetosphere, the overestimation cannot be properly corrected for.

4.5 Summary

- FAEs are common on auroral field lines and previous observations have been well documented. LEPA provides, for the first time near the equator, good resolution in pitch angle and energy combined with full coverage in pitch angle, allowing the field aligned direction to be seen at nearly all times. FAEs are bursts of counterstreaming electrons, generally seen associated with injection events and following a restructuring of the geomagnetic field. They generally occur at the lower energy of the LEPA, with distributions peaked at 90° simultaneously occupying the higher energies. The events can be categorised into 3 types; Dropouts, Sharp Onsets, and Substorm. The three different types of event are thought to be related phenomena, with the differences in appearance arising as a result of the variable background electron populations and the position of the spacecraft relative to magnetospheric features (e.g. the westward traveling surge and particle injection region).

- The distribution of FAE durations compared to the distance away from the earth suggests that FAEs may be associated with azimuthally extended features of limited radial extent. The size of such features, when mapped down to the ionosphere, are of similar length scales to auroral arc systems.

- The distribution of FAEs through the magnetosphere has been presented, subject to sampling limitations . FAEs are seen on L-shells >4.5 with frequency

of observation increasing with L-shell. Very few FAEs are seen around noon (though this may be a sampling effect), with peaks in the distribution on the nightside either side of midnight.

- The association of FAEs with substorms has been demonstrated by looking at the relationship between the timings of FAEs and the onset times provided by *Flowers*, 1998. The observations are consistent with FAEs being purely a substorm related phenomena. The AE index agrees with this in general. It seems a small percentage of events occur during quiet times, however this may reflect limitations in the AE index leading to mistaken identification of quiet times, and there may have been substorms in progress during these 'quiet time' events. The probability of observing an FAE associated with a substorm is large (>60%) in the 04:00-06:00 MLT and 18:00-22:00 MLT sectors, and thus we have concluded that FAEs very likely form integral part of the substorm process.

- The previous survey of counterstreaming electrons by *Klumpar*, 1993, has been reviewed. Similarities exist between it and the results presented here. However, we have suggested that the probabilities of seeing an FAE determined by *Klumpar*, 1993, are overestimated due to a bias associated with the chosen sampling approach. We also suggest that without correcting for this overestimation the *Klumpar*, 1993, distribution is invalid.

Chapter 5

Acceleration of Field Aligned Electrons Part 1 - Electron Observations

Previous observations, made by *Lin et al.*, 1979 and confirmed by *Moore and Arnoldy*, 1982, have suggested that field aligned electrons (as described in Chapter 4) are scattered out of counterstreaming beams with a narrow spread of pitch angles to larger pitch angles. The scope of their observations was limited by the instrumentation used. In this chapter the evidence provided by the more capable LEPA experiment is examined and a more comprehensive description of the FAEs is made. For the first time the full details of the energy-pitch angle distributions associated with counterstreaming electrons in the equatorial regions of the magnetosphere have been measured. They are presented here. It will be clearly shown that pitch angle scattering does take place to larger pitch angles, and that it is usually accompanied by acceleration to higher energies. The acceleration of the electrons is a new feature, not seen in observations prior to the CRRES mission.

5.1 Previous Observations of the Acceleration of Field Aligned Electrons - *Lin et al.*, 1979

The only reported observations (until now) which have suggested that field aligned electrons are scattered out of counterstreaming beams to larger pitch angles in the region under study, are those made with the ATS 6 satellite [*Lin et al.*, 1979 and *Moore and Arnoldy*, 1982]. *Lin et al.*, 1979, studied three examples and found that the distribution functions could be approximated by a single Maxwellian prior to substorm onset, and by the superposition of two Maxwellians thereafter. It was found that when the distribution was described by two Maxwellians there was a high temperature ($\sim$3 keV) component seen at all pitch angles and a low temperature ($\sim$1 keV) beam component seen initially only at small pitch angles ($\leq 30°$). After some time passed, the low temperature component was also seen at large pitch angles. Three possibilities were suggested to explain the appearance of the low temperature component at large pitch angles;

- the low temperature electron distributions are organised within spatial structures in the magnetosphere, and they are observed to change due to the relative motion of the spacecraft and the structures,
- the large pitch angle low temperature ($\sim$1 keV) electrons are produced when electric and magnetic wave turbulence locally heat the cold ($\ll$1 keV) plasma,
- the source of the large pitch angle low temperature ($\sim$1kev) electrons is small pitch angle low temperature ($\sim$1kev) electrons (i.e. the electron beam). The beam particles are scattered to larger pitch angles by wave-particle interactions occurring near the equatorial plane.

The fact that there were three observations of the low temperature component appearing first at small pitch angles and later at larger pitch angles was taken to suggest

a causal relationship. The first explanation was considered unlikely as only coincidence could explain the causal relationship (i.e. it was not expected that the relative motion of the spacecraft through a spatial structure would introduce a bias towards seeing low temperature component at small pitch angles before seeing it a large pitch angles). The second case was also considered unlikely as it was expected that in the case of turbulent heating the temperature would increase with time and the density would remain constant, whereas the opposite was observed, i.e. the temperature remained unchanged and the density increased with time. The third explanation was considered reasonable as it was expected that the electron beam would be unstable to wave-particle interactions.

5.2 LEPA Observations of the Acceleration of Field Aligned Electrons

In this section we review some LEPA observations made at the time of FAEs. The acceleration of FAEs seen by LEPA was first reported by *Johnstone et al.*, 1996, who undertook an initial study of six events. Unfortunately the study was conducted prior to the discovery of the magnetic byte swapping error discussed in Section 3.4.2, and so the pitch angle energy distributions shown were invalid. In this study we have expanded the study throughout the lifetime of CRRES, having corrected for the magnetic byte swapping error.

5.2.1 Examples

In this chapter we are interested in the details of the pitch angle energy distributions. As discussed in Chapter 3 LEPA operates in two principal modes. The first returns electron observations for three planar distributions (the symmetry plane, loss cone and 90° distributions) at 8° by 5.625° resolution, and the second returns electron

observations for the full angular coverage distribution at 16° by 22.5° resolution. The resolution of the full angular coverage distribution is insufficient to reveal the level of detail required to see the scattering and acceleration features which are the subject of this chapter. The construction of pitch angle distributions from the symmetry plane, loss cone and 90° distributions can, however, provide the required resolution. LEPA was operated in the second mode for the majority of the time on and after Orbit 614, and occasionally prior to Orbit 614. As LEPA was not always in the first mode, and since there were also a few orbits where the data contains bad data records, only 158 of the 532 FAE seen in our survey of LEPA data are suitable for the detailed investigation of distributions. While there is a sufficient number of events to allow common features to be identified it must be noted that, due to the nature of the CRRES orbit, this subset of the events only covers MLT from 08:00 through midnight to 19:00 and is biased to high latitude post-midnight observations.

Orbit 77

Figure 5.1 shows a survey plot for Orbit 77. There are two FAEs on this orbit, the first at 13:47 UT and the second at 15:43 UT. Concentrating on the second event we can see that after a period of low fluxes, 15:00 - 15:40 UT, there is an injection of field aligned electrons, 15:43 - 15:50 UT with energies < 5 keV. At 15:45 UT fluxes with energies in the range 1-10 keV appear, peaked at 90°, growing in intensity over the next few minutes. After 15:50 UT increased fluxes remain in the 1-10 keV range, peaked at 90°. These fluxes gradually decrease with time, with the peak at 90° becoming more pronounced, in a manner consistent with pitch angle diffusion into the loss cone. At 16:20 UT there is an injection of higher energy, >10 keV, electrons.

Figure 5.2 shows a sequence of energy vs pitch angle plots, each averaged over 1 spin (30 seconds) including data from the symmetry plane, loss cone and 90° distributions. The axes for each plot are shown in Figure 5.3. The 158 plots cover the

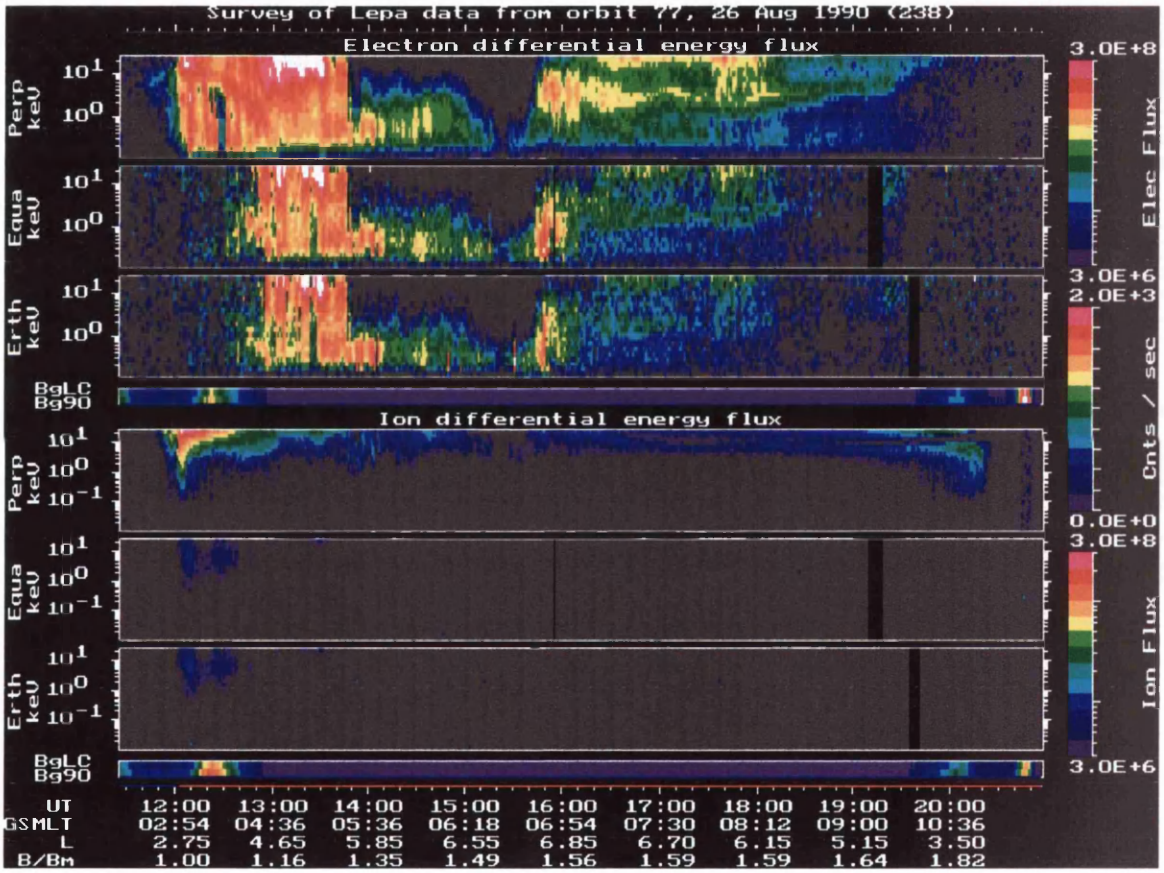

Figure 5.1: LEPA survey plot illustrating two FAEs on Orbit 77 at 13:47, and 15:43 UT. The form of the plot is described on Page 83.

period from 15:04 UT to 16:23 UT each marked with a time stamp above the plot. This time stamp has the year, followed by the day of year, then the UT is given in hours, minutes and seconds. The time stamp indicates the start time of the averaging. The time between successive plots is not always exactly 30 seconds; there are 2 reasons for this. Firstly, for the purposes of collecting distributions a spin is defined as starting when the magnetic field direction lies in the field of view of the detector, and ending when the magnetic field direction again lies in the field of view of the detector (i.e. from one loss cone distribution to the one after next, over which time two symmetry plane distributions are collected). The magnetic field direction is not absolutely constant (and as shall be shown later, it can be quite variable at the time of FAEs), and so a spin as defined here may vary in duration (and start time). The second reason is that occasional gaps in the data mean that a single distribution may occasionally be missing and so the time between successive plots may be around 1 minute. The colour scale of the plots has been allowed to saturate at higher fluxes in order to emphasise certain features.

The first signs of strong field aligned fluxes are seen briefly in the 3 plots starting 15:29:37 UT (row 6). Here strong field aligned fluxes are seen at 0° but not at 180° with energies 400 ± 200 eV. These then disappear and weak bidirectional fluxes, perhaps a residue, can be seen in both directions until the main event starts at 15:43:04 UT. The brief appearance of field aligned electrons can be seen in the earthward electron panel of the survey plot Figure 5.1.

In the main event electrons first appear near the loss cone, both parallel and antiparallel, at 400 ± 200 eV. These are then scattered to larger pitch angles. While being scattered over pitch angles 0° - 60° (and 180° - 120°) the electrons are also accelerated, typically reaching energies of 1 keV, with extremes of up to 10 keV. The scattering from 60° - 90° (and 120° - 90°) appears to take place in pitch angle alone, with little or no change in energy. After the loss cone electrons disappear, substantial

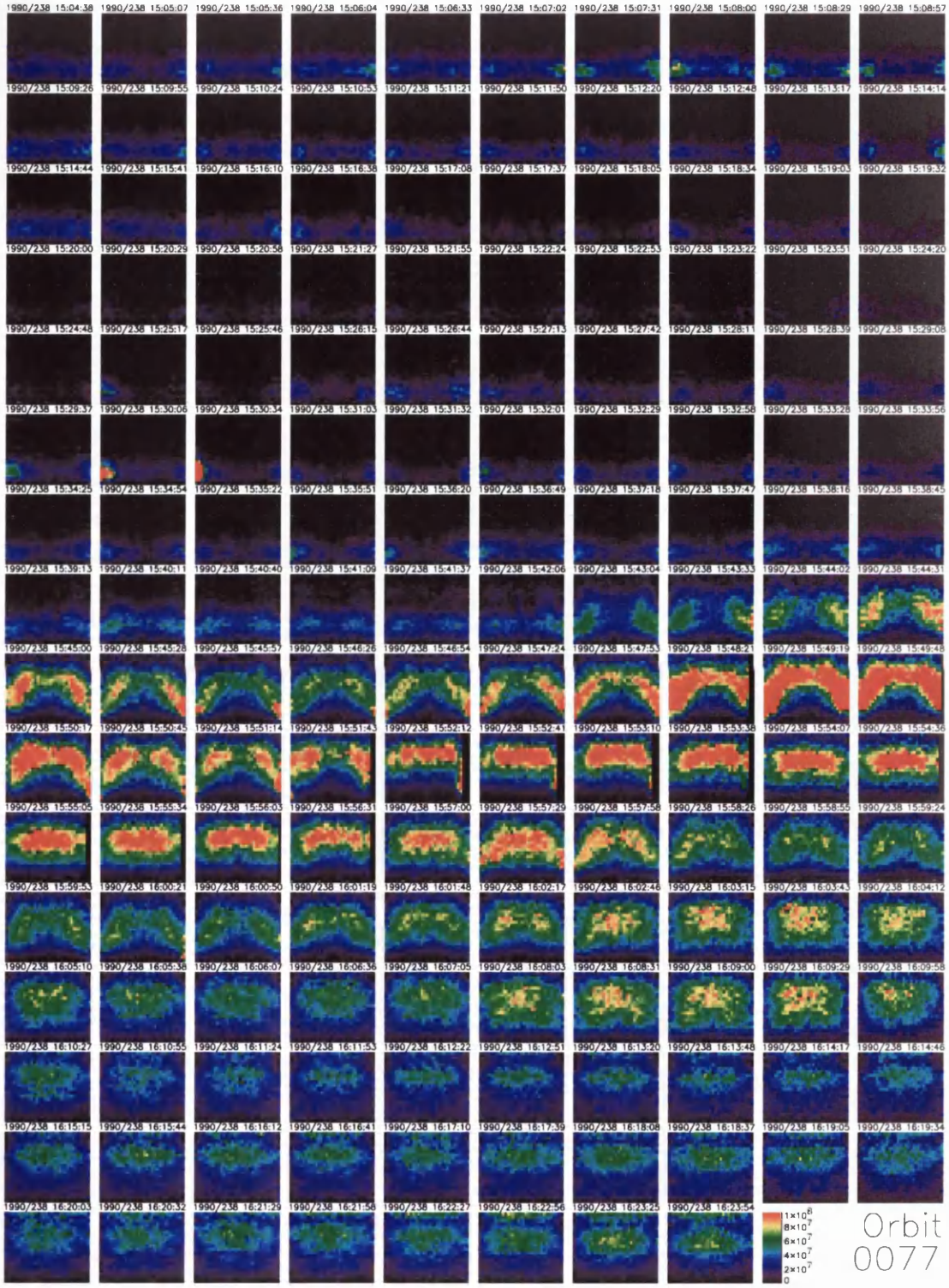

Figure 5.2: A series of pitch angle energy spectrograms illustrating an FAE on Orbit 77. The FAE lasts from 15:43 UT to 16:01 UT. The colour in each plot indicates the differential energy flux in $cm^{-2}s^{-1}ster^{-1}$ according to the colour scale in the lower right corner of the figure. Each spectrogram has the same axes, illustrated in Figure 5.3. Each panel is marked with a timestamp above it.

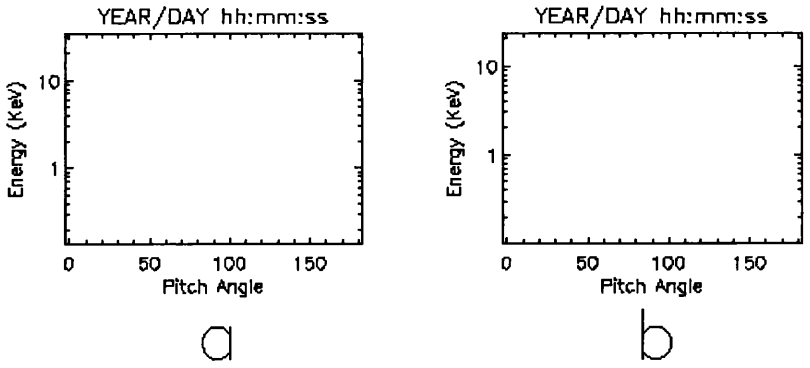

Figure 5.3: The axes used by spectrograms in Figures 5.2, 5.5, and 5.7. a) shows the axes used when LEPA is operating over the attenuated energy range, prior to and on Orbit 209, while b) shows the axes used when LEPA is operating over the unattenuated energy range, following Orbit 209.

fluxes remain above 1 keV. These slowly decrease, presumably through pitch angle diffusion into the loss cone, over the next 30 minutes.

A feature to note in Figure 5.2, is that the form of the distribution can change significantly between consecutive panels, which indicates that the processes affecting the electrons are very rapid with significant acceleration happening on time scales of a spin period or less. Although tempting, it may not always be appropriate to view Figure 5.2 as the sequential development of a distribution under an acceleration process. The fluxes of accelerated particles seem to increase with time during intervals such as 15:43 - 15:45 UT in Figure 5.2, however, this is not always the case and what is often seen (on other orbits) is that high fluxes of accelerated electrons appear within one spin period. So what we are seeing in each frame, is the result of an acceleration process on a field aligned distribution. It then follows that the electrons are scattered along paths indicated by the presence of strong electron fluxes, seen most clearly in the 15:49:48 panel (note that the colour scale is saturated). While the development of the acceleration process itself cannot be seen in Figure 5.2 in a flowing sequence, Figure 5.2 does still present the story of the distribution development on

longer timescales, though some of the panels may appear 'out of sequence'.

Orbit 264

A second event is shown in Figures 5.4 and 5.5, which are of the same form as Figures 5.1 and 5.2. This event has been included to show that different amounts of acceleration have been seen and that the path in pitch angle energy space can vary. For this orbit two brief events can be seen, at 10:30 UT and 10:50 UT, each with a duration of 2 minutes and existing in the earthward direction only. No acceleration is seen in these two unidirectional events. We do see some examples of unidirectional beams (on other orbits) which are scattered out of the loss cone, though these are always short lived (1 - 2 minutes duration). Following a period of low fluxes the main FAE of this orbit is seen at 11:20 UT and has a duration of 11 minutes. This event shows strong field aligned fluxes in both parallel and antiparallel directions. Following the event, fluxes in the loss cone disappear until a higher energy injection event is seen.

In Figure 5.5 the 10:50 UT event can be seen in 4 panels (10:49:46 - 10:51:12) with energies 300 $\pm$ 100 eV. These fluxes are only seen at 0° and are very field aligned, confined to the loss cone. The first signs of the main event can be seen in the panel marked 11:20:10, where again fluxes confined to the loss cone at 0° are seen. In the next panel (11:20:39) these fluxes cover almost the entire energy range of LEPA, still confined to the loss cone at 0°. The next panel shows the first signs of particles in the 180° loss cone, with the electrons at 0° again covering the usual energy range. The particles in the two loss cones are often seen at different energies in a single panel (e.g. panels 11:21:30, 11:23:30, 11:23:59, and 11:29:12). This may indicate that the two beams have separate sources and are not just mirroring trapped populations, though some component of a mirroring population is undoubtedly present in most panels. An alternative explanation is that within half a spin period CRRES moves from a

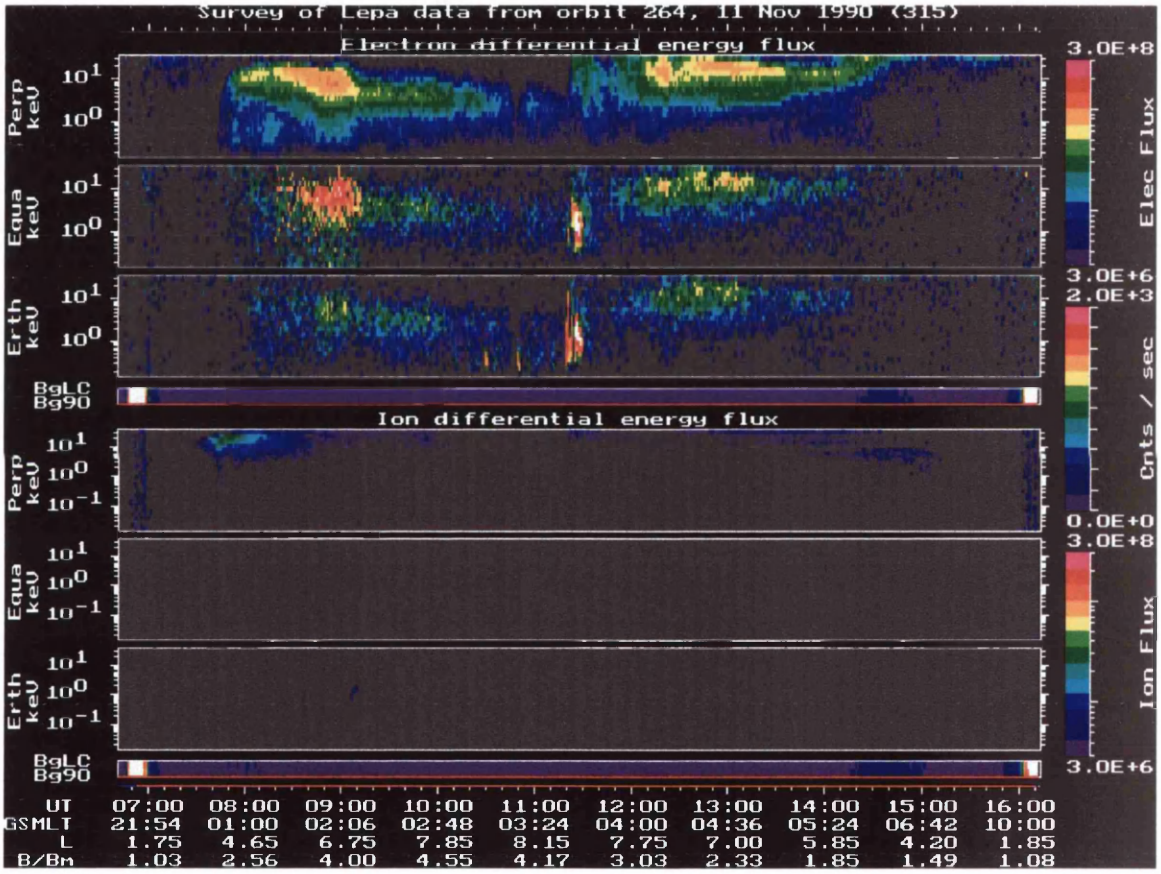

Figure 5.4: LEPA survey plot illustrating three FAEs on Orbit 264 at 10:30 UT, 10:50 UT, and 11:20 UT. The form of the plot is described on Page 83.

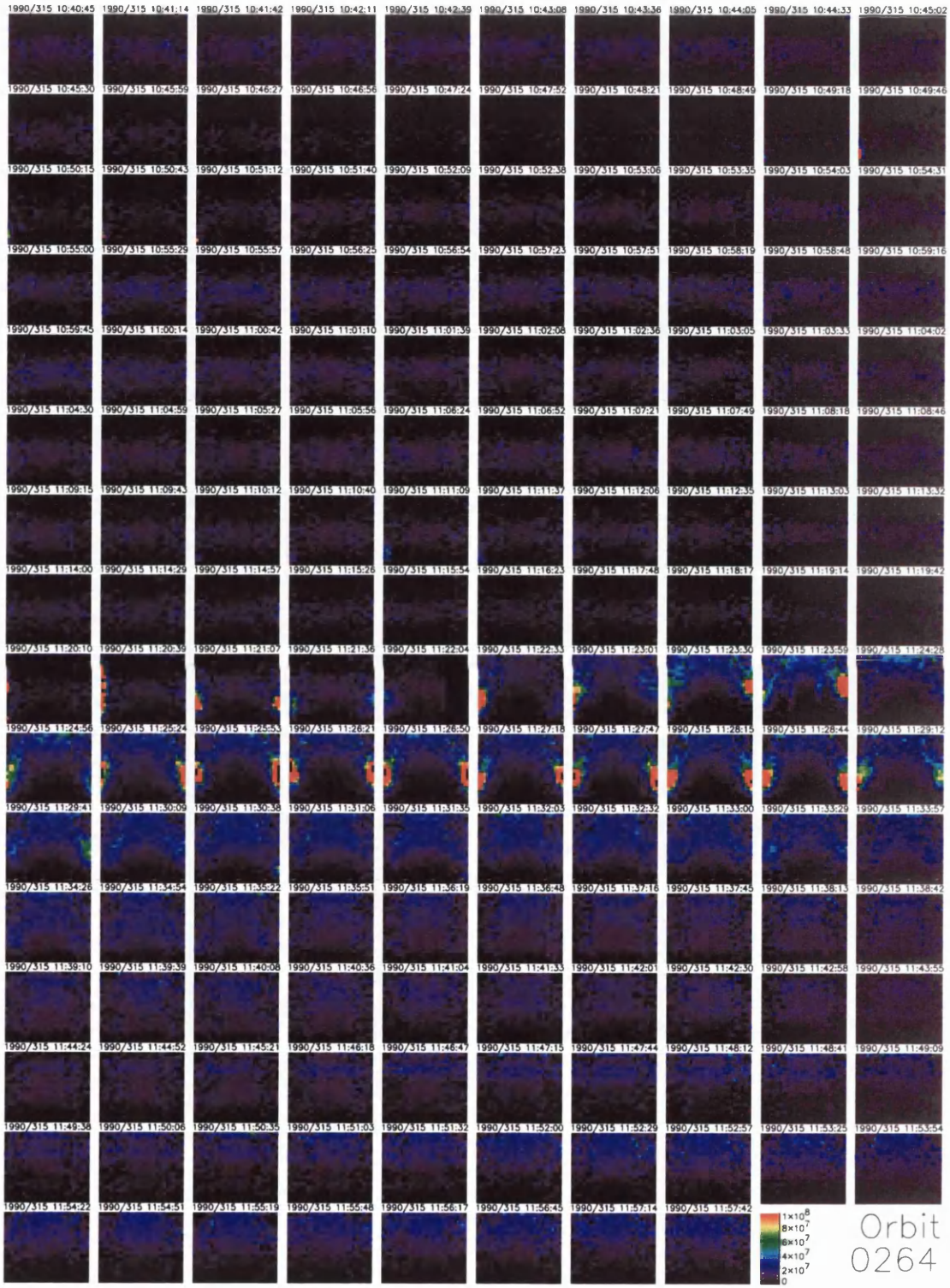

Figure 5.5: A series of pitch angle energy spectrograms illustrating two FAEs on Orbit 264 at 10:50 UT and 11:20 UT. The colour in each plot indicates the differential energy flux in $cm^{-2}s^{-1}ster^{-1}$ according to the colour scale in the lower right corner of the figure. Each spectrogram has the same axes, illustrated in Figure 5.3.

low energy beam to one with a higher energy and thus the two different energy beams will be seen in the same panel at 0° and 180°.

The scattering in this case is far weaker than that seen in the event on Orbit 77, but we again see pitch angle scattering in a similar form. Also the particles are accelerated to the highest energies detectable by LEPA (> 20 keV), and possibly above.

Orbit 69

In a few cases the field aligned electrons appear to be scattered out of the loss cone, but with very little or no change in energy. One such case occurs on Orbit 69. The survey plot for Orbit 69 is shown in Figure 5.6, and is of the same form as those previously shown. On this orbit there is a long duration (43 minutes) event at 8:12 UT followed by three FAEs seen almost exclusively in the earthward direction only (9:22 UT duration 3 minutes, 9:30 UT duration 29 minutes, and 10:12 UT duration 1 minute). The 8:12 UT event is complicated by a higher energy distribution (thought to be unrelated), making the scattering path (if present) hard to determine in the pitch angle vs energy plots (not shown), while in the other events very little scattering is seen. The main event we wish to discuss starts at 10:18 UT, and is initially in the earthward loss cone only, but soon is evident in both. At 10:24 UT fluxes are enhanced at 90° covering the same energy as the FAE. These 90° fluxes increasein intensity while the field aligned electrons are present ($\sim$ 23 minutes), then decreasein intensity while the energy increases over the next hour. The FAE is followed by a small injection of particles around 10 keV.

Two of the short duration events on this orbit can be seen in the first two rows of panels of the energy vs pitch angle plots in Figure 5.7, and a third at 10:12:27 just before the main event. The main event starts in the panel marked 10:16:46 as weaker fluxes, but grows to strong fluxes in the panel marked 10:18:12. The strong fluxes of

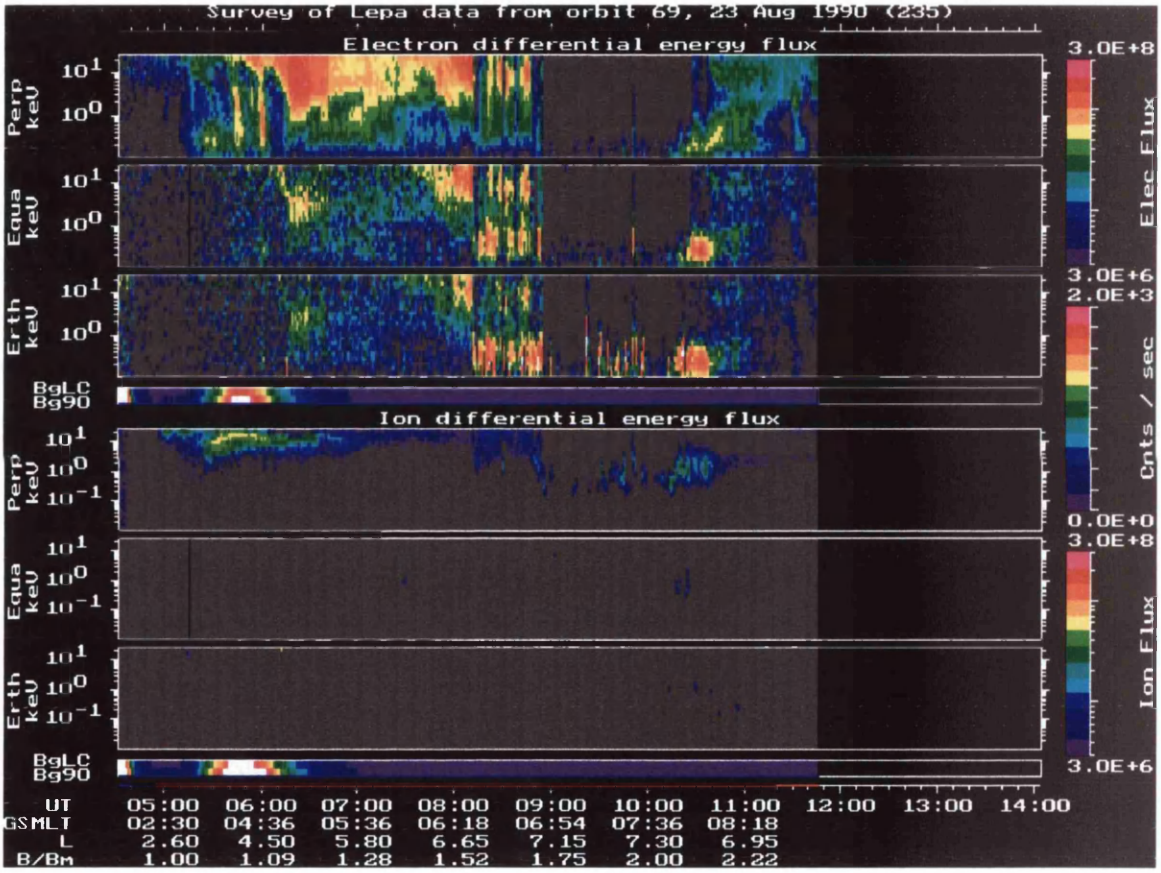

Figure 5.6: LEPA survey plot illustrating five FAEs on Orbit 69 at 8:12 UT, 9:22 UT, 9:30 UT, 10:12 UT and 10:18 UT. The form of the plot is described on Page 83.

counterstreaming electrons remain evident through to 10:38:52 (with the exception of the two panels marked 10:23:00 and 10:23:29. The main point to note here is simply that the diffusion that takes place is in pitch angle only, with no detectable change in energy. In the 10:21:34 UT and 10:24:56 UT panels high fluxes are seen accros most pitchangles, but only for half a spin, indicating that the scattering seen in this event is still a rapid process

Following the FAE the fluxes slowly decrease. A feature best seen in the 10:51:51 UT panel in Figure 5.7, is often seen following FAEs. The distribution of electron differential energy flux in energy-pitch angle space is similar to the diffusion curves for resonant interactions between electrons and whistler mode waves suggested by *Johnstone*, 1996, (Figure 5.8). The fact that the distribution of electron follows the *Johnstone*, 1996, curves supports our presumption that the decrease of fluxes following FAEs is due to pitch angle diffusion into the loss cone by whistler mode waves. The fact that the distribution does not always resemble the *Johnstone*, 1996, curves does not preclude the type of diffusion suggested by *Johnstone*, 1996, as the shape of the pitch angle distribution depends on the initial distribution shape and the time over which diffusion has been taking place. We shall return to this point in Section 6.2.1.

Though some events, such as the one illustrated in Figure 5.7 show no signs of acceleration the majority of the events lasting longer than a few minutes (and many of the shorter ones) display some signs of the type of acceleration seen in the first two examples given above. Of the 158 events for which the pitch angle data has been studied, 63% show signs of simultaneous acceleration and scattering of field aligned electrons, 3% show scattering with no acceleration, and 14% show no scattering at all. In 20% of events the situation is confused by higher energy electron populations and conclusions cannot be drawn regarding the scattering process. It appears that the acceleration of field aligned electrons is usual and events where no acceleration is seen are unusual. The scattered particles can typically be seen in the 'Perp' panel

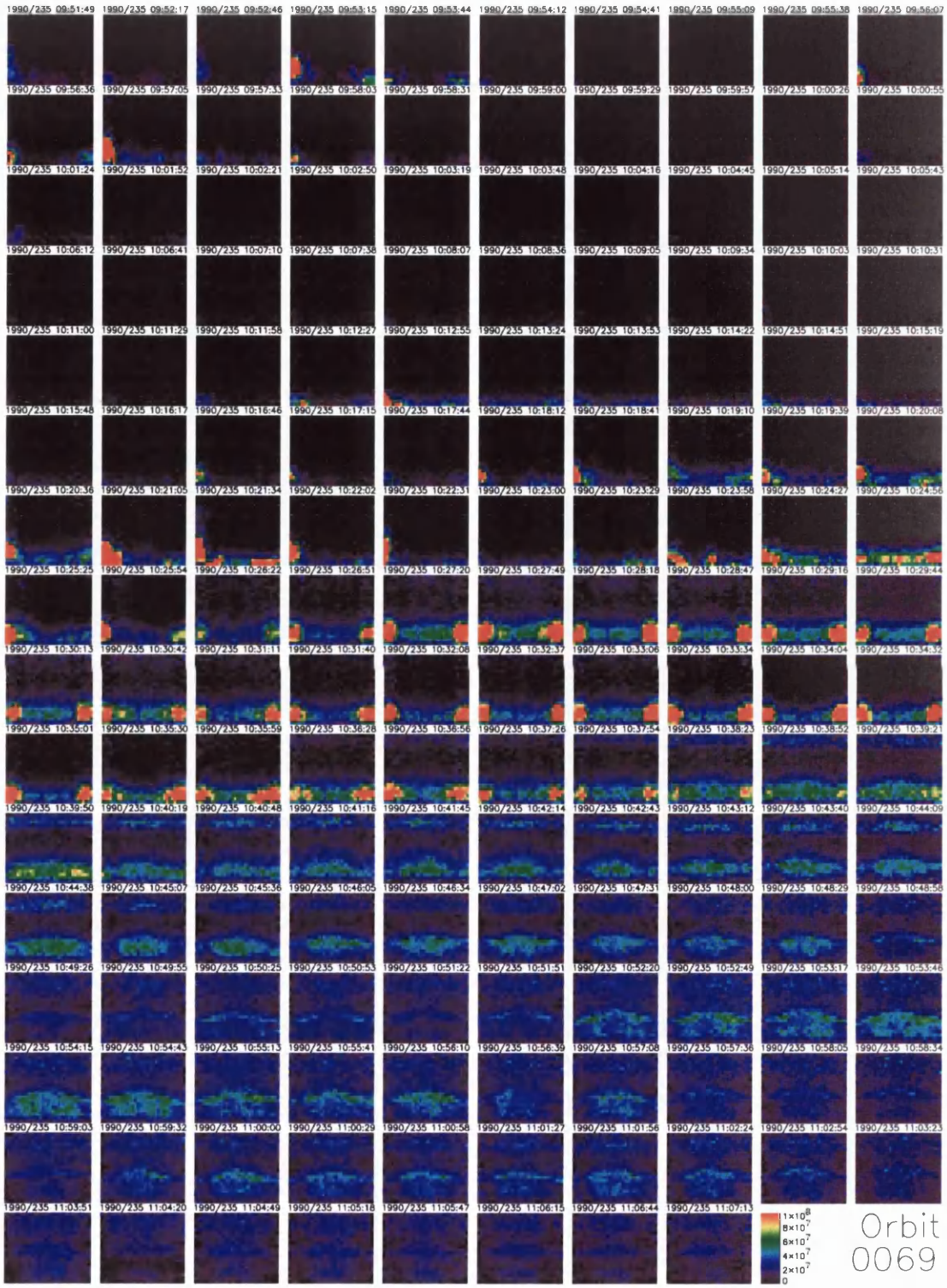

Figure 5.7: A series of pitch angle energy spectrograms illustrating three FAEs on Orbit 69. The first FAE is in progress at start of the time period shown and the second and third start at 10:12 UT and 10:18 UT respectively. The colour in each plot indicates the differential energy flux in $cm^{-2}s^{-1}ster^{-1}$ according to the colour scale in the lower right corner of the figure. Each spectrogram has the same axes, illustrated in Figure 5.3.

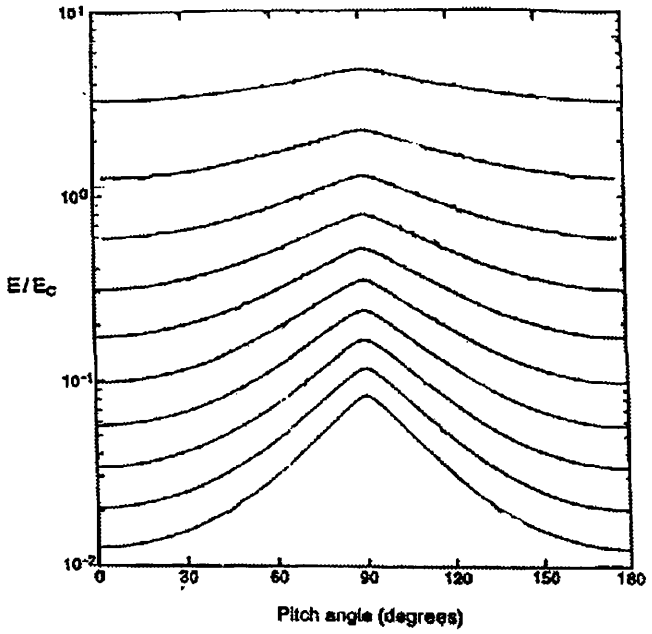

Figure 5.8: The characteristic diffusion curves for whistler mode waves suggested by *Johnstone*, 1996.

of the survey plots as fluxes which appear soon after the appearance of the field aligned fluxes. In the case of the highlighted events during Orbits 77 and 264 (where acceleration is seen) the 90° scattered fluxes are seen at higher energies than the field aligned fluxes, and in the case of the highlighted event during Orbit 69 (where no acceleration is seen) the 90° scattered fluxes are seen at the same energy as the field aligned fluxes. The 13:47 UT event in Orbit 77 (Figure 5.1 shows scattered 90° fluxes at slightly higher energies than the field aligned fluxes which is consistent with the small acceleration seen in the pitch angle vs energy plots (not shown).

All three examples shown here roughly follow the same form, with periods of low flux preceding the FAE, followed by an injection of high energy electrons after the event. While a number of the events have a similar form to these, others do not (see Chapter 4). These examples have been selected because at these times little else is occurring and the counterstreaming, accelerated and scattered electrons can be seen clearly. Many events occur during very active times, such as those shown in Figure 4.3. During active events, acceleration of the form illustrated above can be seen, however as other processes are happening simultaneously, the acceleration paths are not as clear as in the examples given here. No events of the dropout type have been used here because the duration of dropout type events tends to be short ($\leq$ 2 minutes), so only three or four panels would show relevant data.

The general ordering of the events, illustrated in Figure 5.9, is always the same. First we see the bidirectional field aligned beams (a) followed by the simultaneous acceleration and pitch angle scattering of electrons (b). We then see the scattering in pitch angle with no change in energy (c) and finally the beams disappear and the fluxes slowly diffuse into the loss cone (d). We do not always see the whole picture and may miss the beginning or end stages of the event, and sometimes the distribution can hop between stages, however, we do only ever see the overall process in this order suggesting that whatever is taking place is a one way process. The fact that we only

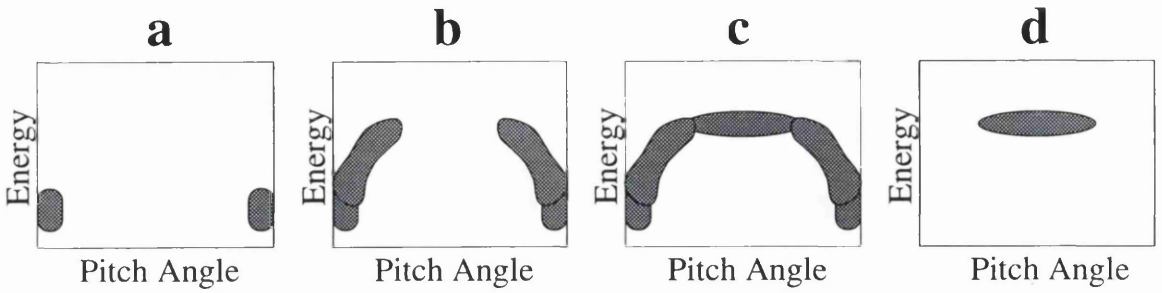

Figure 5.9: The general ordering of the process of acceleration/scattering of FAEs seen by CRRES. Each panel (a-d) represents a panel such as those in Figures 5.2, 5.5, and 5.7.

see the scattering process in the order shown in Figure 5.9, independent of whether the spacecraft is outbound or inbound, implies that what we see is not due to a consistent spatial organisation, but rather a temporal effect.

5.2.2 Acceleration Characteristics

A schematic view of the scattering path followed by electrons during FAEs is shown in Figure 5.10. Field aligned electrons are scattered up to pitch angles of around 60° while being accelerated (light shaded area), increasing the energy of the electrons by a factor of around 10 (though this can vary greatly). The electrons then appear to continue to be scattered to larger pitch angles, but with little or no change in energy (dark shaded area). It may be the case that the scattering and acceleration are independent processes, although we suggest that they are not. Our main reason for this suggestion is that a single, well defined, reasonably thin (comparable in width to the electron beam) scattering path is seen. One might expect a seperate scattering process to act at all energies and so we would expect to see a greater spread in the scattering path. Further reasons why we believe that the pitch angle scattering and the acceleration are caused by the same process shall become clear when we investigate a possible scattering mechanism. In this and the next chapter we will

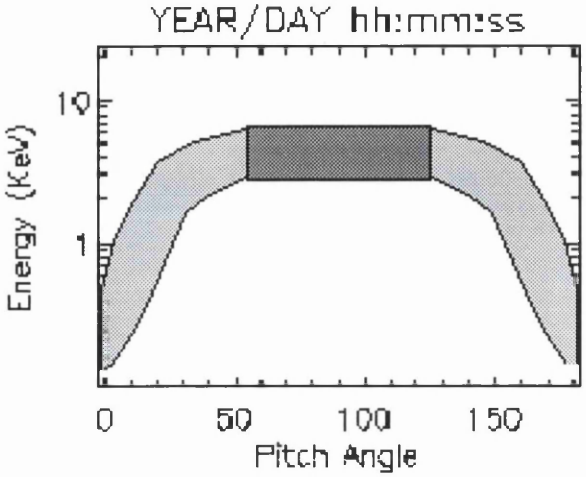

Figure 5.10: A schematic view of the scattering path followed by electrons during FAEs. The light shaded region indicates the path when electrons are scattered to larger pitch angles while being accelerated. The dark shaded region indicates the path at larger pitch angles where there is little or no change in energy.

primarily consider the part of the path when the electrons are accelerated.

Some further insight into the mechanism responsible for the acceleration can be gained from studying the distributions in velocity space using coordinates perpendicular and parallel to the magnetic field. We use the FAE during Orbit 77 as a typical example.

$v_\perp$ vs. $v_{||}$ Differential Energy Flux Plot

Figure 5.11 shows the data from 6 sequential panels of Figure 5.2 in $v_\perp$ vs. $v_{||}$ co-ordinates. The figure shows the distribution prior to and during the period of strongest acceleration (15:47 - 15:50 UT), with the accelerated fluxes increasing from the first to the fourth panel. Fluxes are slightly weaker in the fifth panel. In the sixth panel the loss cone is empty, and the fluxes are slightly decreased compared to those seen in the fifth panel. The electrons which appear in the loss cone have parallel velocities in the range 1×10^7 ms^{-1} $< v_{||} <$ 3×10^7 ms^{-1} (300 eV $<$ E $<$ 2.6 keV). The

electrons are accelerated both perpendicular and parallel to the magnetic field with an overall change in velocity of around 3-4$\times 10^7$ ms^{-1}. At higher energies it appears that the electrons are scattered to smaller parallel velocities, while still increasing in perpendicular velocity, in other words scattered in pitch angle with little or no change in total velocity.

$v_\perp$ vs. $v_{||}$ Phase Space Density Plot

Figure 5.12 shows the same data as in Figure 5.11, except this time it is presented in terms of phase space density. Note, that in this plot, the scale is logarithmic as opposed to the linear scale used previously, due to the larger variation in the values plotted. These plots are dominated by the fall off of the distribution function with increasing energy. It is hard to see the scattered electrons, though the counterstreaming beams of the FAE are still clearly seen. While the acceleration of these electrons seems small in terms of the distribution function, the fact that it is so clear when the distribution is seen in terms of differential energy flux, means that this process significantly affects the distribution of energy within the particle population.

The main feature to note from Figure 5.12, is that the distribution function decreases along the scattering path, identified from Figure 5.11, and indicated by the black lines. This is typical of a diffusion process, during which the net motion of a scattered particle population is from high phase space density regions to lower phase space density regions [*Thorne and Horne*, 1996]. We suggest the source of the scattering resulting in this diffusion process may be the wave-particle interactions with the waves observed simultaneously in-situ by the PWE instrument (further discussion in Chapter 6.

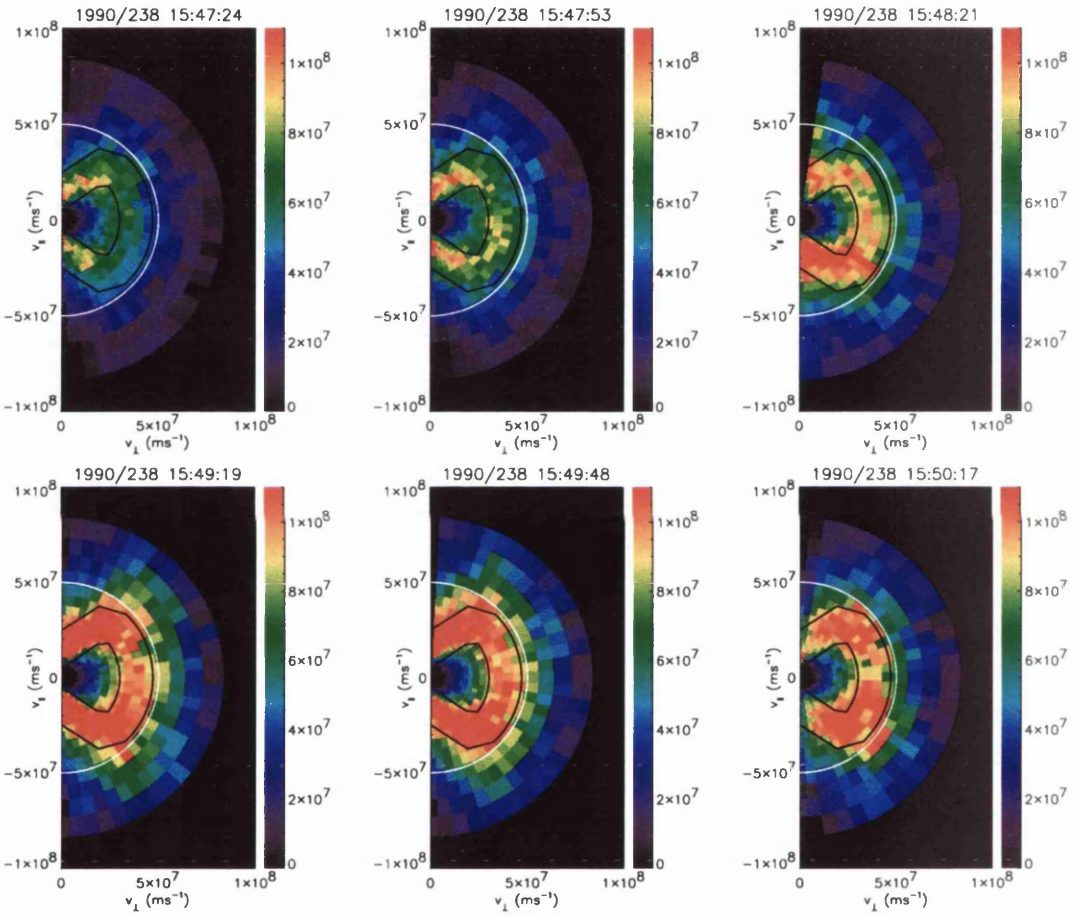

Figure 5.11: A sequence of plots in velocity space illustrating the 15:44 - 15:55 UT FAE in Orbit 77. The colour scale indicates the differential energy flux. The white line indicates a contour of constant speed, v=5×10^{7}ms^{-1}, and the black lines indicate the edges of the scattering path (identified by eye). Note, linear differential energy flux scale.

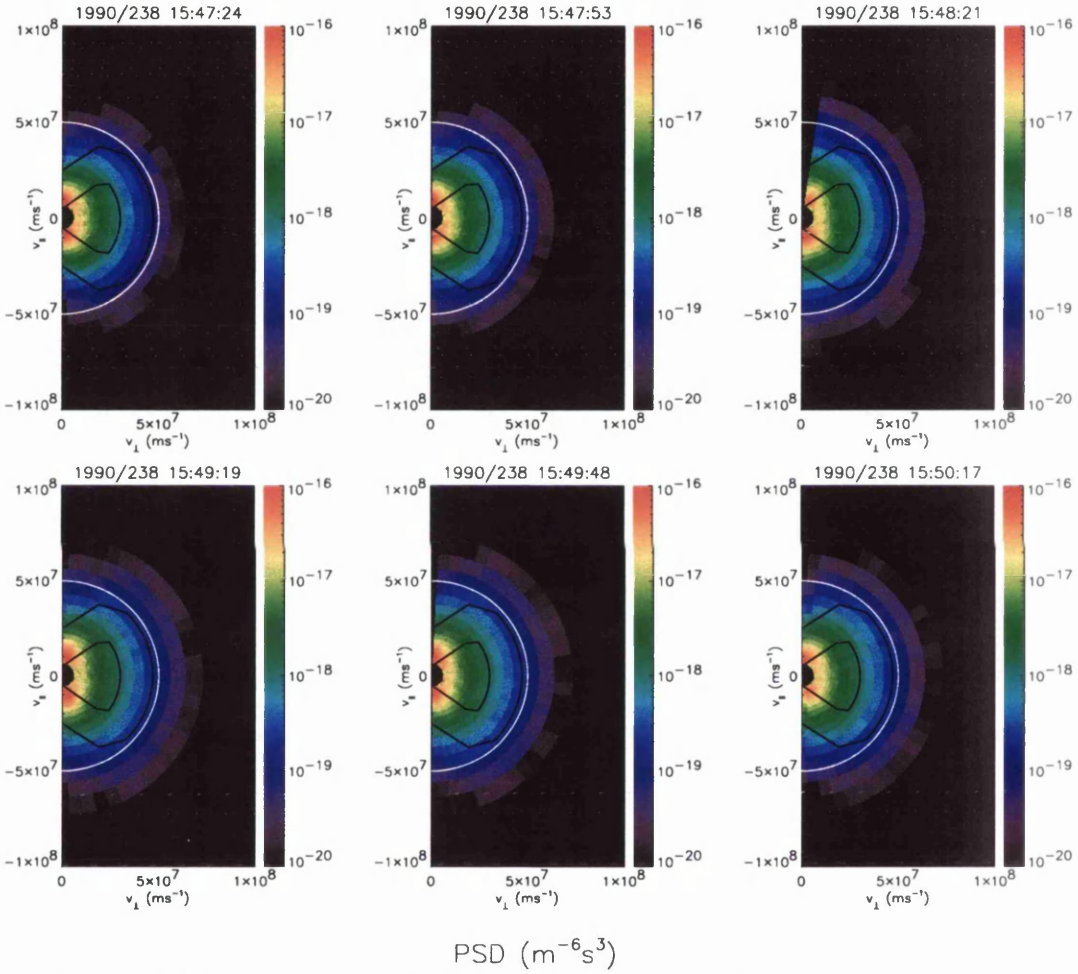

Figure 5.12: A sequence of plots in velocity space illustrating the 15:44 - 15:55 UT FAE in Orbit 77. The colour scale indicates the phase space density. The white line indicates a contour of constant speed, v=5×10^{7}ms^{-1}, and the black lines indicate the edges of the scattering path (identified by eye) from Figure 5.11. The counterstreaming beams can be seen in the scattering path at $v_\perp$ <1×10^{7}ms^{-1}. Note, logarithmic phase space density scale.

Phase Space Density vs. Pitch Angle Plot

Before going on to discuss the waves and their relationship with FAEs it is worthwhile introducing two further ways of viewing the data. Figure 5.13 illustrates the accelerated particles more clearly than in Figure 5.12. Figure 5.13 shows the same 6 panels of data, again in phase space density, but this time with each energy channel plotted as a line. The colour of the line identifies the energy it represents, as indicated by the key. The data has been smoothed by a 3×3 boxcar average, in pitch angle energy space, to increase the signal to noise ratio. In Figure 5.13, the field aligned electrons are seen as a peak at 0° and 180° at low energies (0.1 - 0.7 keV). Moving to higher energies the peak (which we interpret as the scattered electrons) is seen at increasing pitch angles (e.g. for 2.6 keV at 40° and 140° which rises from an initial value of $\leq 2\times10^{-19}m^{-6}s^{3}$ to $5\times10^{-19}m^{-6}s^{3}$). Above 3 keV the distribution is fairly isotropic except for minima towards the loss cones. Figure 5.13 illustrates that while the accelerated particles cannot clearly be seen in Figure 5.12 they are still important in terms of the particle distribution function. It can also be seen that the phase space density at higher energies increases at all pitch angles (e.g. illustrated by the shaded region between 4.4 keV and 5.9 keV) . The phase space density increase at high energies is due to the accumulation of energised electrons. The steady levels of phase space density at lower energies implies a persistent source of low energy electrons, replacing those which have been energised.

The source electrons are clearly evident in Figure 5.13, as the loss cone fluxes at low energies. In the third panel there is a minimum rather than a peak in the loss cone at 180°, and also at 0° in the final panel. Also, at 180° in the fourth panel and at 0° and 180° in the fifth panel, the fluxes in the loss cone, though still considerably higher than those at 90°, are not as high as seen in the other panels (usually above $2\times10^{-16}m^{-6}s^{3}$).

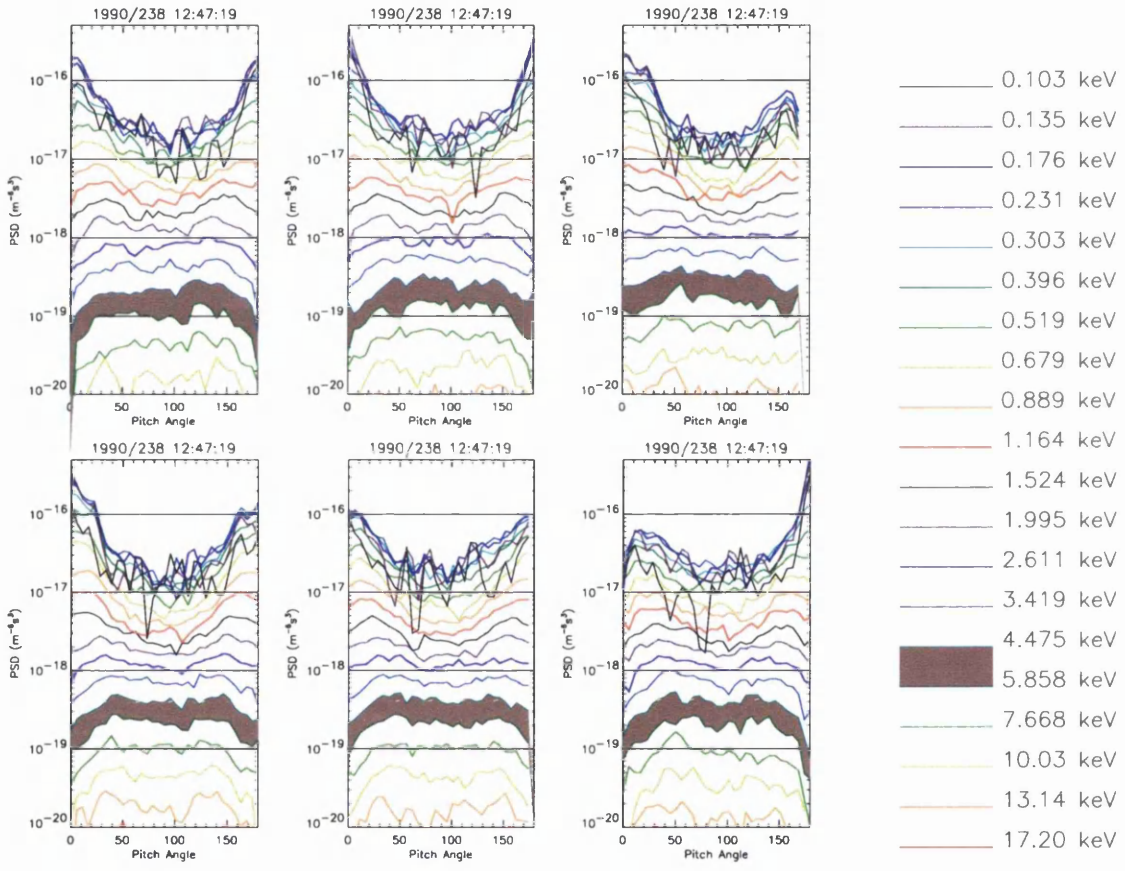

Figure 5.13: A sequence of plots of the phase space density as a function of pitch angle for each energy channel. The energy is indicated by the colour of the line.

Phase Space Density vs. Energy Plot

In all six panels of Figure 5.13, positive gradients in phase space density ($\frac{\partial f}{\partial v} > 0$) at low energies are seen across all pitch angles. The gradients in phase space density can be seen more clearly in Figure 5.14 where phase space density is shown as a function of energy averaged over 30° pitch angle bins. The $\frac{\partial f}{\partial v} > 0$ is most pronounced in the 0-30° bin and the 150-180° bin, corresponding to the electron beam. Such positive gradients are generally accepted as being unstable to wave growth. Particularly $\frac{\partial f}{\partial v_{\|}} > 0$ is unstable to wave growth via Landau resonance with parallel propagating waves. Unfortunately all examples of $\frac{\partial f}{\partial v} > 0$ occur at the extreme low end of the energy range seen by LEPA (i.e. near 0.1 keV). As will be seen later, there are other reasons for suspecting that the cold (< 100 eV) electrons, below the energy to which LEPA is sensitive, may have an effect on the acceleration process.

Variation of Scattering Path with Magnetic Latitude

As discussed in Section 2.2 an electron's pitch angle will change as it moves along a magnetic field line. If μ is conserved, the pitch angle is related to field strength simply by

$$\frac{\sin^2 \alpha_1}{B_1} = \frac{\sin^2 \alpha_2}{B_2}. \tag{5.1}$$

By using Equation 5.1 and assuming a dipole field geometry we can calculate how a particular pitch angle distribution will change with magnetic latitude. As an electron moves away from the equator along a field line there is an increase in field strength, causing the electron's pitch angle to increase towards 90°. Particles with equatorial pitch angles near 90° are effectively removed from the distribution at higher magnetic latitudes by magnetic mirroring.

The fact that we see a single clear scattering path implies that the scattering is taking place preferentially at a specific magnetic latitude. If the scattering were taking place across a wide range of latitudes we would expect, at least for observations

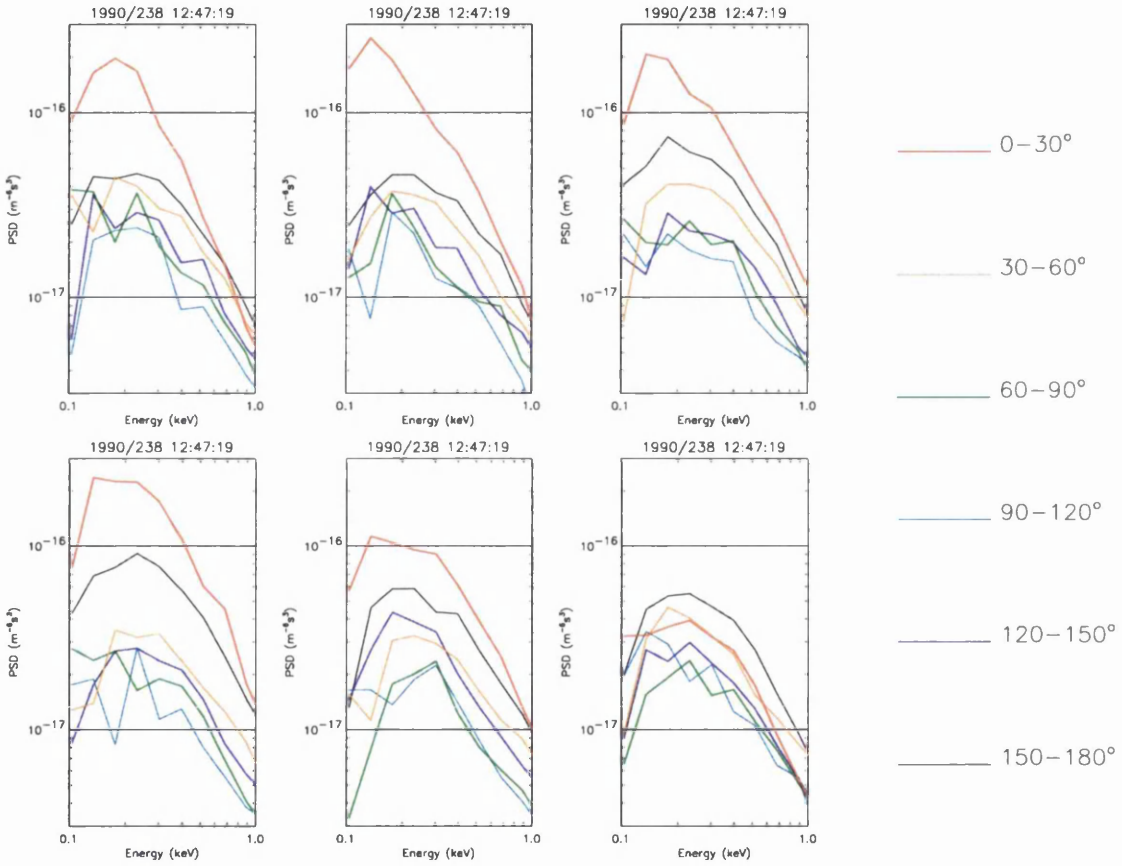

Figure 5.14: A sequence of plots of the phase space density as a function of energy averaged over 30° pitch angle bins. The pitch angles are indicated by the colour of the line.

near the magnetic equator, to see a large spread in the velocity space occupied by the scattered particles. By studying the shape of the scattering path at different magnetic lattitudes we can see if the observations are consistent with a repeatable scattering event at a particular lattitude.

In order to show how the pitch angle distribution varies with magnetic latitude, we define the angle θ as the angle between the magnetic field direction and the scattering path (acceleration leg) in velocity space (see Figure 5.15). Note, θ is not the same as pitch angle. We have identified θ for each 30 second distribution in each of the 158 events for which we have high resolution pitch angle data. Figure 5.16 shows every measurement of θ plotted according to magnetic latitude. The curves show the expected variation of θ with magnetic latitude (assuming adiabatic motion and a dipole field geometry) for various values of θ_0, where θ_0 is the value of θ at the magnetic equator. The curves shown are for a beam velocity, v_b, of $1.5\times10^7 \mathrm{ms}^{-1}$ and a change in velocity along the scattering path, Δv, of $3\times10^7 \mathrm{ms}^{-1}$. Changes of v_b and Δv have increasing effect on θ at larger latitudes, but over the range of values of v_b and Δv that we observe the difference is only a few degrees at 30° magnetic latitude (ie. over our observation range). It appears from the data that a wide range of values of θ are seen at all magnetic latitudes. Most of the observations a consistent with curves having θ_0 in the range $20° < \theta_0 < 70°$.

The wide range of θ_0 values seen implies that either the specific magnetic latitude at which scattering is taking place varies greatly between individual events or that the scattering path varies greatly between individual events. It could also be that both the scattering path and the magnetic latitude location of the scattering are highly variable from event to event.

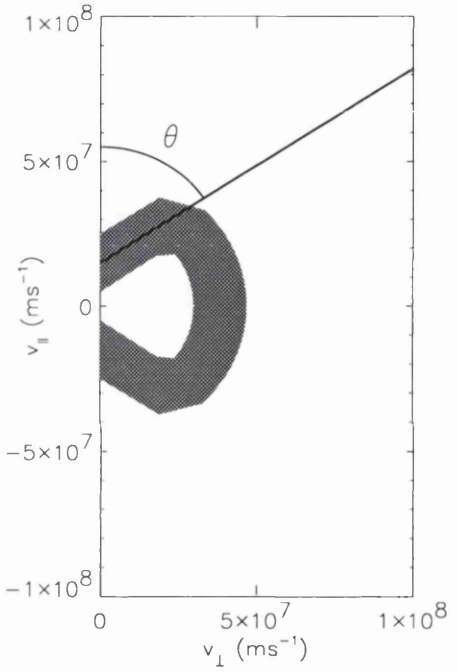

Figure 5.15: The angle θ is defined as the angle between the magnetic field direction and the acceleration leg of the scattering path (indicated by the shaded area in velocity space.

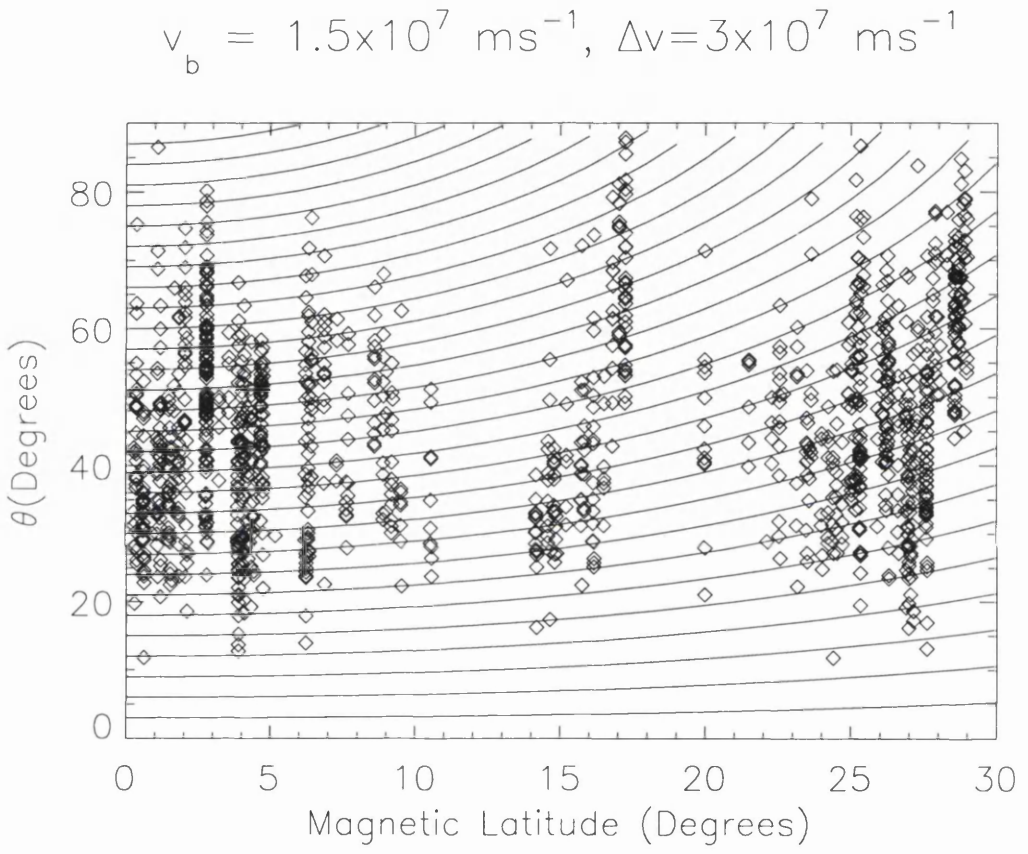

Figure 5.16: The change in θ as a function of magnetic latitude. Each diamond represents a single measurement of θ made during an FAE. The curves show the variation of θ as a function of magnetic latitude under adiabatic motion assuming a dipole field geometry for typical values of $v_b = 1.5\times10^7 \mathrm{ms}^{-1}$ and $\Delta v = 3\times10^7 \mathrm{ms}^{-1}$. Each curve is for a different value of θ_0, the value of θ at the equator.

5.3 Summary

- Previous observations of field aligned electrons being scattered out of the loss cone are limited to those made with the ATS-6 spacecraft. The lack of previous observations is presumably due to the lack of experimental data from the relavant region of space with sufficient pitch angle and energy coverage and resolution in previous missions. The LEPA data set allows the full details of the scattering to be seen, providing LEPA is operating in a mode where the three planar distributions are returned.

- The LEPA observations are reviewed and three examples are examined in detail to illustrate typical features. The field aligned electrons often appear to be accelerated and simultaneously scattered through limeted pitch angle range, out of the loss cone. This is seen to some degree on most of the FAEs in the LEPA data set, though a small number of events appear to be scattered in pitch angle with no signs of energisation. The acceleration path in velocity space is clearly identifiable with electrons being scattered both perpendicular and parallel to the magnetic field direction. The acceleration of field aligned electrons plays a significant role in the electron energy distribution. The acceleration path is along negative gradients in phase space density, consitent with aa diffusive scattering process.

- The pitch angle accelerated electrons are clearly evident when the distribution function is plotted as a function of pitch angle, over many of the energy channels. The source in the loss cone switches on and off through the events. This happens in both the upcoming and downgoing directions, though independently.

- We think that there is a unique magnetic latitude where the scattering occurs in a particular event. If this is not the case then we would expect to see a less clear cut scattering path in the observations.

- $\frac{\partial f}{\partial v} > 0$ is seen at low energies during FAEs. This is generally recognised as being unstable to wave growth, particularly $\frac{\partial f}{\partial v_{\|}} > 0$ which can generate parallel propagating waves via Landau resonance.

- To explain the observations we need to find a process which will produce the distinctive scattering path seen. Such a process must also be able to explain why no preferential θ_0 is observed.

Chapter 6

Acceleration of Field Aligned Electrons Part 2 - Investigation of Diffusion Process

In the last chapter we presented observations of the acceleration and pitch angle scattering of field aligned electrons during FAEs. In this chapter we try and gain some insight into the mechanism which may be causing the acceleration. The electron distributions are suggestive of a diffusive process producing the observed pitch angle scattering and acceleration, and here we investigate the possibility of the waves seen by the PWE on CRRES playing a role in the diffusive process.

6.1 Observational Study of Plasma Waves and the Acceleration of Field Aligned Electrons

6.1.1 Introduction to Plasma Wave Observations

Before studying the waves present at the time of FAEs it is helpful to compare the wave data from the PWE instrument and LEPA data from an 'ordinary' orbit, one when no FAEs are seen. Figure 6.1 shows the LEPA survey plot for Orbit 438. Here we can see low fluxes in the perpendicular direction over most of the orbit, with the fluxes in the parallel directions below the sensitivity of the instrument. Just prior to 23:00 UT there is a small injection event with fluxes strongly peaked at 90° (commonly known as a 'pancake distribution'). Figure 6.2 shows a survey plot for the PWE data for this orbit. The solidred line marked on the plot indicates the electron gyrofrequency, Ω_e (Equation 2.1) determined from the magnetometer data. The 5 dotted red lines follow harmonics of the Ω_e. The wave spectral intensity is indicated by the colour scale.

The signatures of a number of wave modes can be seen in Figure 6.2, (indicated by the letters 'a' to 'f') (see also Section 2.6). Initially CRRES is inside the plasmasphere and the strong emissions just below Ω_e (a) are characterised as 'plasmaspheric' hiss propagating in the whistler mode. This is again seen after 00:40 UT when CRRES reenters the plasmasphere. There is a line of strong emission (b) which runs across the entire plot between 17:15 UT and 01:45 UT, lying at the lower edge of the continuum emission. This line lies at the upper hybrid resonance frequency, Ω_{UHR} (Equation 2.8). UHR emission is often useful in determining ω_{pe}, and in turn the plasma density. In the frequencies above Ω_{UHR}, Auroral Kilometric Radiation (AKR) can be seen (c). When the spacecraft nears the equator, electrostatic Electron Cyclotron Harmonic (ECH) waves (d) are seen. ECH waves propagate at frequencies between the har-

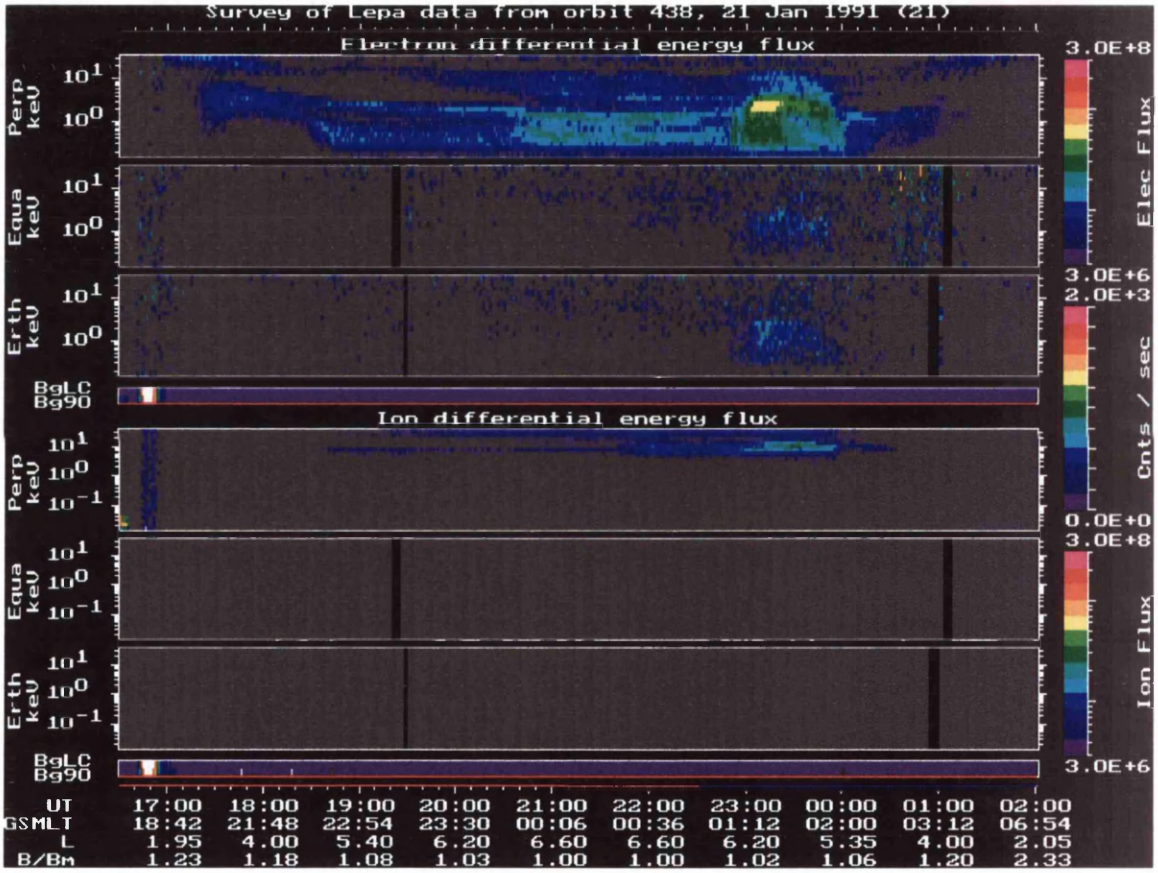

Figure 6.1: LEPA survey plot for Orbit 438. The form of the plot is described on Page 83.

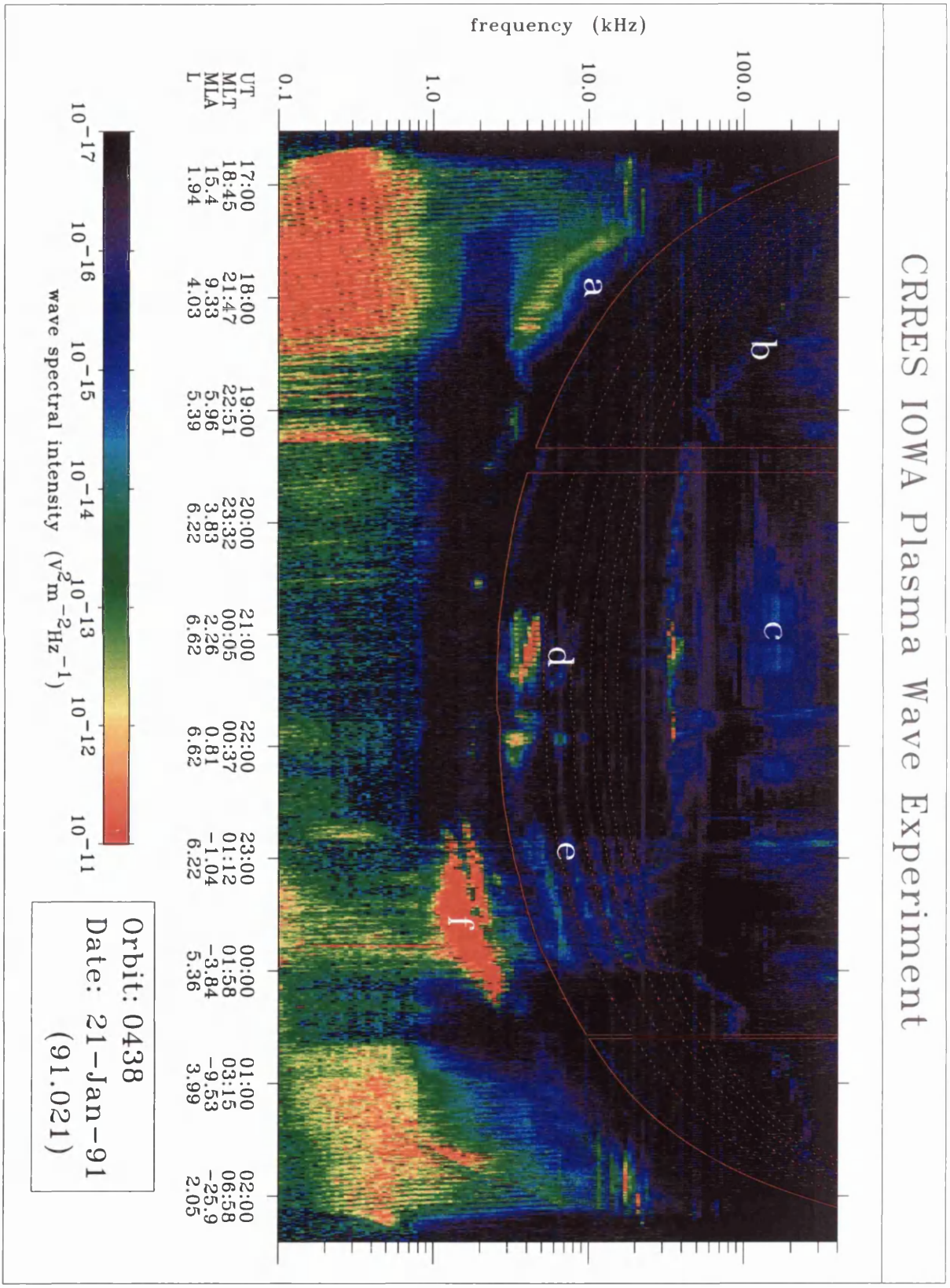

Figure 6.2: PWE survey plot for Orbit 438.

monics of Ω_e and is normally seen near the equator. ECH emission is again seen (e), enhanced in all bands up to Ω_{UHR}, coincident with the injection event around 23:00 UT seen in Figure 6.1. At the same time, strong whistler 'chorus' emissions can be seen below Ω_e (f). Further details of these emissions and others seen in the magnetosphere can be found in *Kurth and Gurnet*, 1991, and references therein.

6.1.2 Plasma Wave Observations Around the Time of FAEs

Figure 6.3 is a survey plot of the PWE data for Orbit 77. Comparing this to Figure 6.2 it is immediately clear that the wave activity during Orbit 77 presents a very different picture to that during Orbit 438. The first difference is that the wave activity is far greater during Orbit 77 with ECH and whistler mode emissions seen through the entire orbit. However, this is not surprising as the LEPA survey plot, Figure 5.1, shows far higher fluxes of electrons (predominantly at 90°) than that seen on Orbit 438. Through much of the plot the upper hybrid resonance frequency is hard to identify In fact it is fairly typical to be unable to determine Ω_{UHR} at times when the electron population seen by LEPA exhibits high fluxes which show lots of variation, and especially at times when FAEs are seen. The AKR is strong (and structured) throughout Orbit 77 indicating the presence of strong aurora. Strong AKR is not always seen during FAE orbits, but as it propagates from the aurora perpendicular to the magnetic field CRRES may not always be in a position to see it.

At the time of the FAE in Orbit 77 (15:43 to 16:00 UT) there is an increase in wave activity in both the whistler mode and the ECH mode. The emission is strong and it is not possible to distinguish between the different bands of ECH emission. At the time of the FAE it is especially hard to determine Ω_{UHR}, which, as will be shown in Section 6.2.1, leads to problems when calculating the theoretical diffusion curves. Figure 6.3 shows a fairly typical observation of the wave behavior during FAEs.

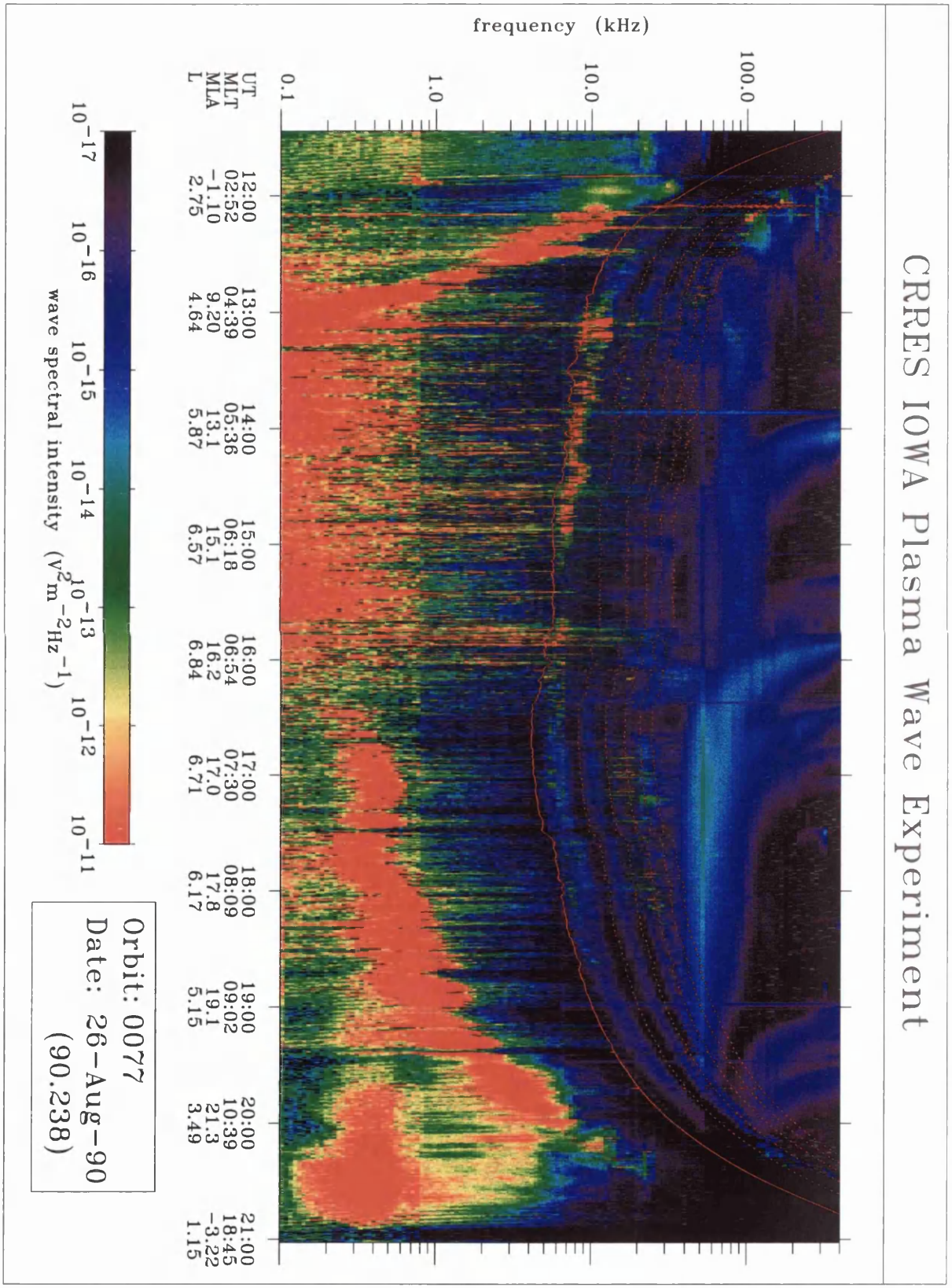

Figure 6.3: PWE survey plot for Orbit 77.

6.1.3 Comparison Between the Acceleration of Field Aligned Electrons and Wave Power

The first approach used to try to identify the wave mode responsible for the acceleration of field aligned electrons, was to try and find a statistical link between the wave power in the various modes observed during FAEs, and the acceleration seen in the electron distribution. In order to do this, a measure of the wave power in each mode has to be defined. The definition used here is the same as that used by *Meredith et al.*, 1999. Whistler mode emissions are, for the purposes of this statistical analysis, defined as those which lie in the range $0.1\Omega_e < \omega < \Omega_e$, while ECH emissions are those lying in the range $\Omega_e < \omega < 6\Omega_e$. A third class of emissions, denoted as hiss, is defined as those with frequencies less than $0.1\Omega_e$, and within the frequency range of the PWE (low frequency whistler mode waves).

The wave spectral intensity was integrated over the respective frequency range, to give a total intensity for each mode. This was done at 8 seconds resolution, the sampling resolution of the highest wave frequencies. The wave frequencies which were sampled at 16 seconds and 32 seconds were treated as two or four measurements of the same value respectively at 8 second intervals. These values for total intensity are then averaged over the 30 seconds used for the accumulation of each LEPA electron distribution. It is then possible to correlate the wave power in the various modes with intervals of interest in the evolution of the electron distributions.

The wave power sampled by the PWE may depend on the propagation direction of the measured waves relative to the spacecraft spin direction (due to the electric field sensor orientation). The difference between the spacecraft spin period and the PWE sampling periods leads to a beating effect, where different propagation directions are sampled on successive spins. A complete cycle, measuring all directions, takes 2, 4, or 8 minutes for sampling periods of 8, 16, and 32 seconds respectively. Generally, at the

time of FAEs the whistler and hiss frequency ranges are sampled at 32 seconds, and the ECH frequency range emission is mainly sampled at 16 seconds, though often the strongest ECH emissions lie at frequencies sampled at 32 seconds. If the wave power does not vary much between different propagation directions, or the propagation is such that the electric field perturbation has little variation in the spin plane[1] then this beating effect will be small.

We have split the FAEs into three categories, a) where both pitch angle scattering and acceleration are seen, b) where pitch angle scattering is seen but acceleration is not, and c) where no scattering is seen at all. Comparing the wave spectral intensities in the three modes between the three categories of FAEs has provided no insight into a wave mode which might be responsible for the acceleration. The wave spectral intensity in all three wave modes cover a large range (1×10^{-12} - 5×10^{-6} V^2m^{-2}) of values for all three categories of FAE. We have tried performing correlation calculations between the wave power and various features of the electron distribution, such as the gradient in phase space density along the acceleration leg of the scattering path, but have found no positive results.

Looking at Figure 6.4 gives some indication of the problems involved in the sort of analysis we have attempted. Figure 6.4 (note the different y-axis scales) shows the wave intensity as a function of time, for the three wave modes, plotted for the three FAEs looked at in Section 5.2, plus three others. Generally the 'whistler' and 'hiss' intensities follow a similar shape, which is not surprising as they represent waves propagating in the same mode. Viewing these six events, and indeed if many hundreds of events are viewed, no consistent picture emerges. Sometimes peaks are seen coincident with FAEs, such as for Orbit 264, but similar peaks are seen throughout active times. The only consistent feature in the wave data is that the FAEs occur at times when the wave activity is always reasonably high in all wave modes.

[1]It is in the spin plane that the PWE samples the electric field.

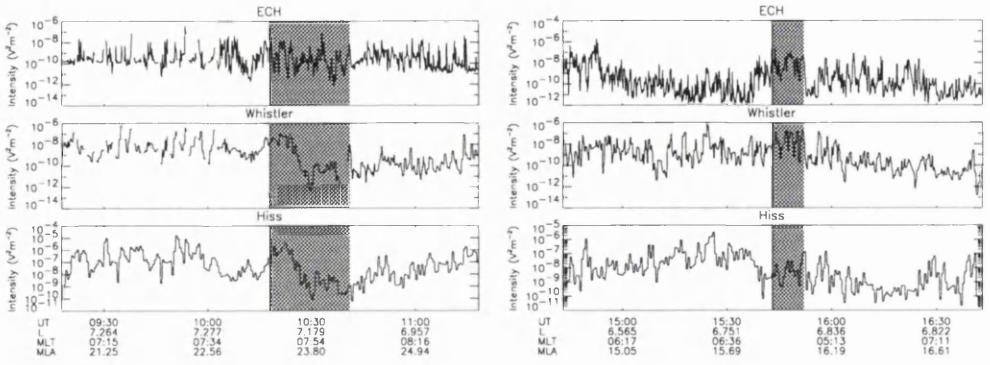

(a)

(b)

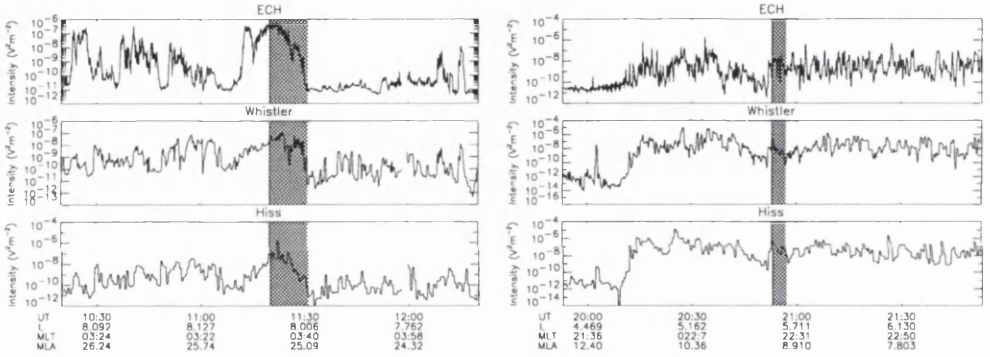

(c)

(d)

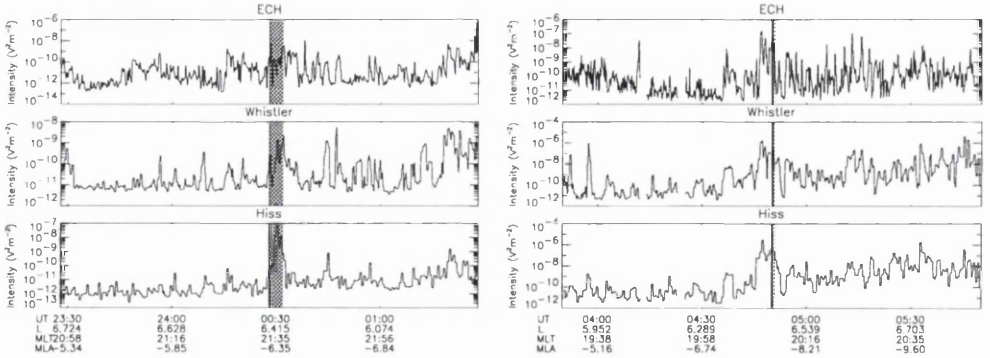

(e)

(f)

Figure 6.4: Six line plots showing the wave intensity as a function of time in three different wave modes around the time of FAEs in Orbits (a)69, (b)77, (c)264, (d)465, (e)670, and (f)678. The shaded areas indicates the times when field aligned electrons are seen.

The fact that no relationship is seen between wave power and the acceleration of field aligned electrons could be connected to the fact that these events occur during very active times. Very rarely are these events seen as the only particle population, and often electron populations at higher fluxes and energies are seen at the same time by LEPA. Various wave growth and damping mechanisms may be at work at the same time and it is unlikely that it will be possible to separate the acceleration of field aligned electrons from other processes which are at work, without a fuller understanding of the larger picture. Also the events are seen over a wide range of magnetic latitudes and as we have discussed (Section 5.2.2) we expect the scattering to take place at a particular magnetic latitude for each event. It is likely, therefore, that in many events the wave particle interactions responsible for the electron scattering are taking place away from CRRES. However, even by subdividing our events according to magnetic latitude no relationship between wave power and acceleration emerges.

It is unlikely that whistler mode waves and ECH mode waves will be of equal intensity in all directions of propagation, and in fact the waves will have different properties depending on the angle between their direction of propagation and the magnetic field direction. So it seems that the wave power sampling problem outlined above may have confused the analysis at its outset.

6.2 Theoretical Study of Plasma Waves and the Acceleration of Field Aligned Electrons Using the Cold Plasma Approximation

The second approach used to try to identify a wave mode which could be responsible for accelerating field aligned electrons is to compare the observed diffusion paths with theoretical resonant diffusion curves.

6.2.1 Theoretical Diffusion Curves [*Summers et al.*, 1998]

The nonrelativistic resonant diffusion curves have recently been derived, for whistler mode waves, by *Summers et al.*, 1998. These are the curves that electrons can diffuse along, under the influence of cyclotron resonant interactions with whistler mode waves. These paths can be expressed in $v_\perp$, $v_\parallel$, for right hand (R mode) waves, as

$$\frac{v_\perp}{c} = (f(x_c) - f(x))^{\frac{1}{2}}, \tag{6.1}$$

$$\frac{v_\parallel}{c} = g(x), \tag{6.2}$$

where x is the normalised wave frequency ω/Ω_e, x_c is defined for each curve by the boundary condition $v_\perp(x_c) = 0$, f and g are the functions

$$f(x) = \alpha\left(\frac{(1-x)}{x} + 2x - \ln x\right), \tag{6.3}$$

$$g(x) = -\left(\frac{\alpha}{x}\right)^{\frac{1}{2}}(1-x)^{\frac{3}{2}}, \tag{6.4}$$

and α is the dimensionless parameter given by

$$\alpha = \frac{\Omega_e^2}{\omega_{pe}^2} = \frac{B^2\epsilon_0}{n_e m_e}. \tag{6.5}$$

We are concentrating on the R mode waves with frequencies below Ω_e as the wave emission seen at frequencies above Ω_e is dominated by electrostatic waves (i.e. ECH). Using values typical for FAEs, an example of these diffusion curves is shown in Figure 6.5(a). Ω_e is determined from the magnetometer, and ω_{pe} from the upper hybrid resonance emissions seen in the PWE data. As already mentioned ω_{UHR} is hard to define at these times and so the derived ω_{pe} may vary considerably. It is hard to place a level of uncertainty on our derived value of ω_{pe} as the main problem is identifying the UHR emission. If we could identify a band of emission as the UHR emission we could estimate ω_{pe} to within a factor of two, however, the uncertainty involved in identifying the UHR emission means that ω_{pe} may vary from the true value by a factor of 10 or more.

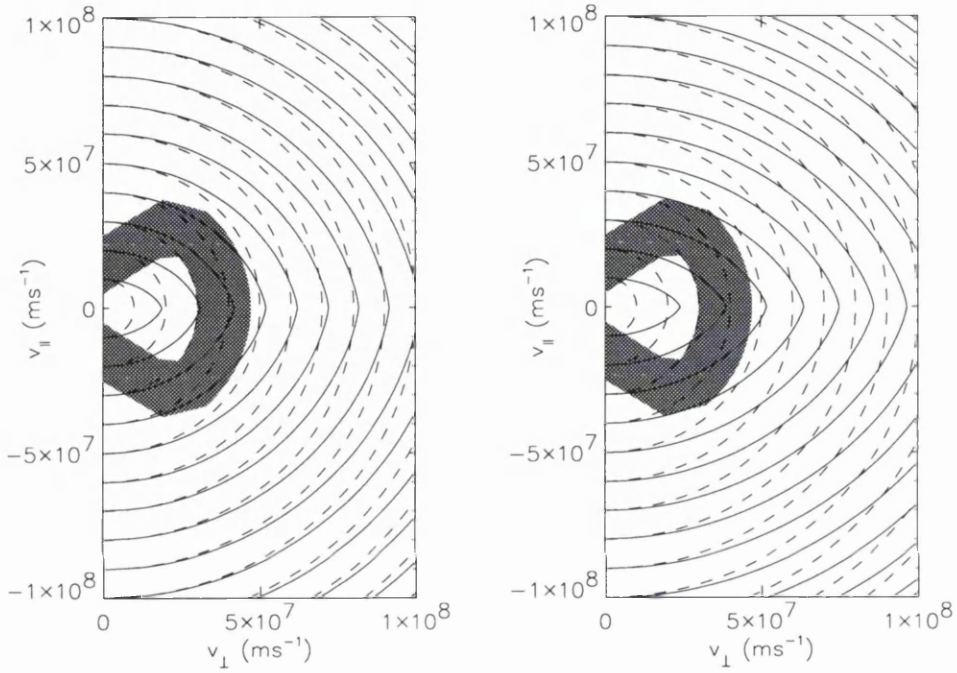

(a) (b)

Figure 6.5: Two examples of the resonant diffusion paths of electrons in velocity space, when being scattered by whistler mode waves according to *Summers et al.*, 1998, model. Each solid curve represents a diffusion path for a different value of x_c. The dashed lines show contours of constant speed. The shaded area shows the diffusion path of electrons seen at the time of the FAE during Orbit 77, as identified from Figure 5.11. The value of α used in (b) is five times that used in (a)

It is clear that the diffusion curves shown in Figure 6.5(a) do not follow the same shape as the diffusion paths seen in Figure 5.11 (shown as a shaded region in Figure 6.5). The shape of the diffusion curves depends on α; smaller values of α will produces more circular diffusion curves and larger values of α produce less circular curves. For comparison Figure 6.5(b) show the diffusion curves with α set at five times the value in Figure 6.5(a). For a given magnetic field strength, α is smaller for larger n_e. For any value of α it is always the case that as one moves along a diffusion curve so as to increase $v_\perp$ there is a decrease in $v_{||}$, and hence these curves cannot explain the acceleration leg of the scattering associated with FAEs.

6.2.2 Post-FAE Diffusion Into the Loss Cone

There are some features which are seen associated with FAEs which may perhaps be explained by the diffusion curves suggested by *Summers et al.*, 1998. In Section 5.2 we mentioned that in the interval following an FAE, as the electrons diffuse into the loss cone, features in the electron distribution are often seen which look similar to the diffusion curves for resonant interactions between electrons and whistler mode waves suggested by *Johnstone*, 1996. A mistake was made by *Johnstone*, 1996, in deriving these curves[2] (though the two sets of curves are similar in shape) so we will continue to use the resonant diffusion curves suggested by *Summers et al.*, 1998.

Figure 6.6 shows six panels from Figure 5.7 (Orbit 69) in velocity space (note that the axes cover a smaller range of velocities than in previous plots of this type). The white lines indicate circles of constant energy, and the black lines indicate diffusion curves of the form described by *Summers et al.*, 1998, which have been fitted by eye to

[2]The curves suggested by *Johnstone*, 1996, were calculated numerically using the integral form of the diffusion equation and assume that the phase velocity of the resonant wave remains constant. In fact the differential form of the diffusion equation (Equation 6.7) should be used [*Summers et al.*, 1998].

the data. The diffusion curves shown in Figure 6.6 follow the features of the electron distribution well. The value of α used in the diffusion curves in Figure 6.6 is $\frac{1}{16}$ of the value used in Figure 6.5(a). During Orbit 69 the UHR frequency suggests that n_e is around a factor of 100 too low to produce the curves shown in Figure 6.6, though again it is hard to determine which emission is the UHR emission.

6.2.3 Scattering Without Acceleration During FAEs

If we use similarly low values of α as that used in the Orbit 69 case (Section 6.2.2), we can produce resonant diffusion curves which fit the part of the scattering path where no acceleration is seen (within the energy resolution of LEPA) in our Orbit 77 example, Figure 6.7. However, in the part of the scattering path with no acceleration, electrons are only observed to diffuse towards pitch angles of 90° and not towards the loss cone. Since negative gradients in phase space density exist in both directions along the theoretical scattering path, it is not clear why the electrons are not seen to diffuse in both directions, if diffusion as described by *Summers et al.*, 1998, is taking place. Also the scattering path along which no acceleration is seen occurs at a particular energy (which varies between events) but covers a wide range of $v_{||}$. As the resonance responsible for the diffusion curves shown in Figure 6.5 depends only on $v_{||}$, there is no reason why pitch angle scattering should take place at a preferential energy according to the *Summers et al.*, 1998, model. In the case of Figure 6.6; electrons are only scattered over a small range of energies, but a broad band spectrum of whistler mode waves is invoked so that waves are available which are resonant with the range of v$_p$*arallel* needed to scatter electrons across all pitch angles.

6.2.4 Acceleration Region Location

It may be that the acceleration of the field aligned electrons takes place away from the magnetic equator. There are many observations at low altitudes of the acceleration of

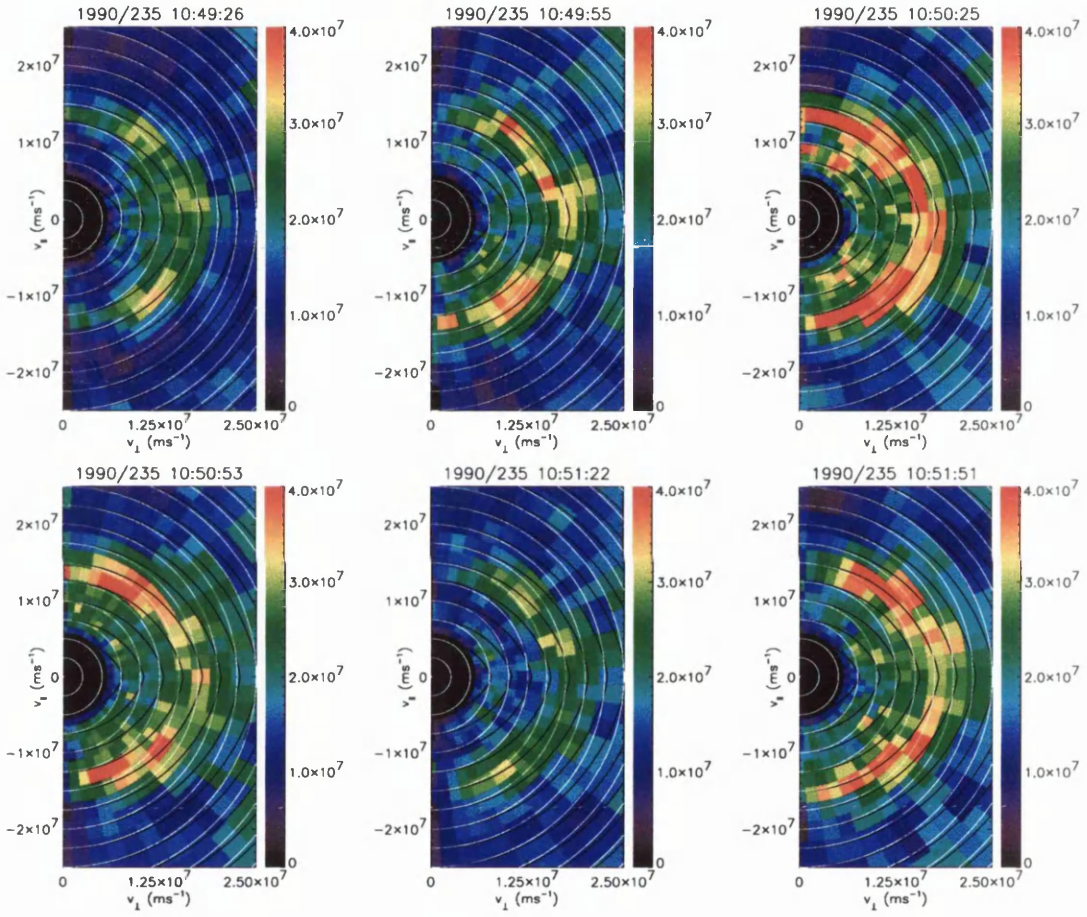

Figure 6.6: A sequence of plots in velocity space illustrating the period 10:49 - 10:51 UT following an FAE in Orbit 69. The colour scale indicates the differential energy flux. The white lines indicate contours of constant speed, v=5×10^{7}ms^{-1}, and the black lines indicate the theoretical resonant diffusion paths as suggested by *Summers et al.*, 1998, fitted by eye to the feature with fluxes 3 - 4 ×10^{7}cm^{-2}s^{-1}ster^{-1}. Note, linear differential energy flux scale.

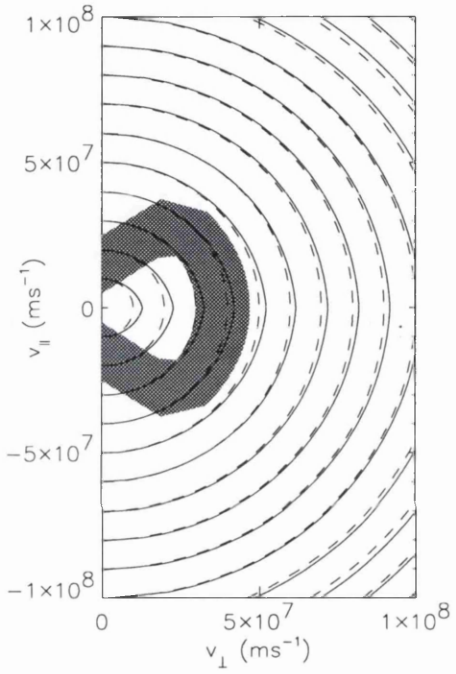

Figure 6.7: The resonant diffusion paths of electrons in velocity space as shown in Figure 6.6. Each solid curve represents a diffusion path for a different value of x_c. The dashed lines show contours of constant speed. The shaded area shows the diffusion path of electrons seen at the time of the FAE during Orbit 77, as identified from Figure 5.11. The diffusion curves could explain the part of the observed diffusion path where little or no energy change is seen.

particles perpendicular to the field direction, such as those made by *Pottelette et al.*, 1999, with the FAST spacecraft at 4300 km altitude. However, conservation of the first adiabatic invariant will result in the entire (0° - 180°) pitch angle distribution seen at 4300 km altitude being confined to a pitch angle range of only a few degrees near 0° and 180° (i.e. a beam) when seen near the equator. Thus no process at low altitudes ($\lesssim 1\ R_E$) can be used to explain the acceleration path seen in the LEPA data.

Figure 6.8 shows how particles which are spread out along a diffusion curve, formed at 28° magnetic latitude (similar to those shown in Figure 6.5) could, when seen nearer the magnetic equator, be redistributed in velocity space to produce a feature similar to the part of the scattering path where acceleration is seen during FAEs (assuming conservation of μ). Figure 5.16 suggests that if *Summers et al.*, 1998, type diffusion were taking place away from the equator, the diffusion would take place over a range of magnetic latitudes $> 10°$.

We might be able to explain the scattering path seen by suggesting that the acceleration leg of the scattering path is in fact a *Summers et al.*, 1998, type diffusion curve formed away from the equator, and that the non-acceleration leg of the scattering path takes place nearer the equator as described in Section 6.2.3. However, there are a number of problems with such a scenario (as well as those outlined in Section 6.2.3) namely that the non acceleration scattering is seen only towards 90° and only at one energy). Firstly we would expect, at least occasionally, to see features like that seen in the final panel of Figure 6.8 in our data set, but we do not. Secondly, current thinking suggests that the dominant wave particle interactions take place either near the magnetic equator, or at low altitudes, and we know of no reason for a preferential magnetic latitude away from the equator to become the dominant scattering region (though we cannot rule it out). Thirdly, in order to produce diffusion curves of such different shapes at two locations along a field line the plasma

density would have to change by a factor of 100 or more between the two locations.

6.3 Consequences of the Electron Beams on Resonant Diffusion

The theoretical diffusion paths suggested by *Summers et al.*, 1998, have been used successfully by *Meredith et al.*, 1999, to determine that whistler mode waves are the dominant mode in the formation of 'pancake' distributions outside of L=6. This result shows that the theory is sound and can provide a realistic interpretation of the processes at work. Pancake distributions are, however, very different from the field aligned distributions under investigation here. Pancake distributions are marginally stable distributions peaked at 90° pitch angle, formed as particles diffuse into the loss cone under the influence of wave-particle interactions, over timescales > 2 hours. It is possible, then, that the diffusion curves derived by *Summers et al.*, 1998, may not be valid when counterstreaming electron beam populations are present. Hence we examine the 'ingredients' used by *Summers et al.*, 1998, below.

6.3.1 'Ingredients' of *Summers et al.*, 1998, Diffusion Curves

The analysis by *Summers et al.*, 1998, combines the resonance condition,

$$\omega - kv_{||} = n\omega_{pe}, \tag{6.6}$$

where n is the integer order of resonance, taken to be 1, with the condition that in a reference frame moving with the phase velocity of the wave (the 'wave frame') the relativistic kinetic energy of the resonant particle is conserved, i.e.

$$v_{wave||}dv_{wave||} + v_{wave\perp}dv_{wave\perp} = 0. \tag{6.7}$$

(The subscript wave indicates the quantity is taken in the wave frame). While the kinetic energy of the resonant particle does not change in the wave frame, the wave

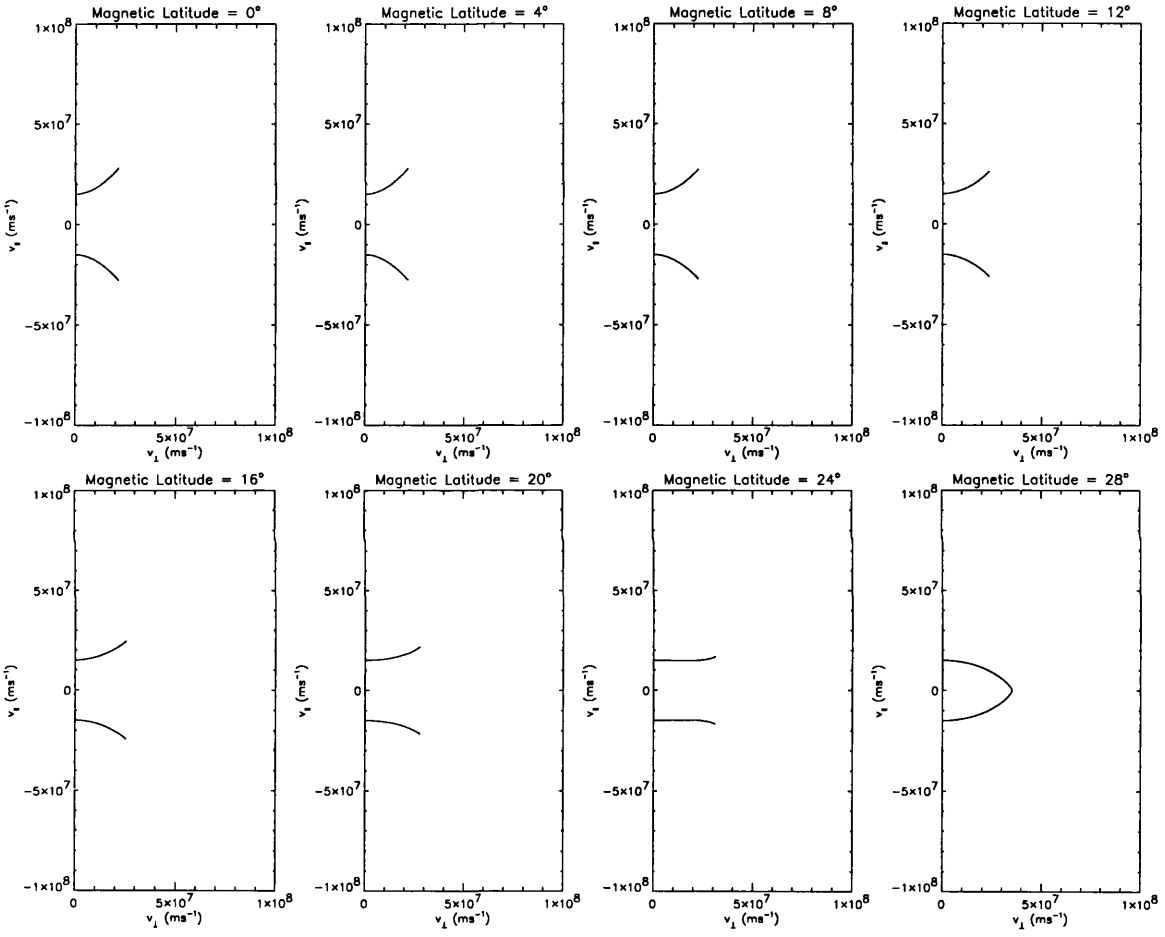

Figure 6.8: The appearance of a *Summers et al.*, 1998, type diffusion curve formed at 28° magnetic latitude seen at varying magnetic latitudes assuming conservation of μ and a dipole field geometry. Each curve is shown in velocity space with the same axes as Figures 5.11 and 5.12.

velocity may change during the interaction, and hence the kinetic energy of the resonant particle may change in the rest frame. From these two conditions the following equations for the R mode resonant diffusion curves were derived;

$$\frac{v_{\|}}{c} = -u\left(\frac{\omega_{pe}}{\omega} - 1\right), \tag{6.8}$$

$$\frac{v_{\perp}}{c} = \left(constant + 2\Omega_e \int \frac{u}{\omega} du\, u^2 \frac{\Omega_e^2}{\omega^2}\right)^{\frac{1}{2}}, \tag{6.9}$$

where u is the normalised phase velocity of the wave

$$u = \frac{u_{ph}}{c} = \frac{\omega}{ck}, \tag{6.10}$$

and is defined by the dispersion relation. The dispersion relation used by *Summers et al.*, 1998, is the standard cold plasma dispersion relation for parallel propagating electromagnetic waves;

$$n^2 = \frac{c^2k^2}{\omega^2} = 1 - \frac{\omega_{pe}^2}{\omega\left(\omega \pm \Omega_e\right)} - \frac{\omega_{pi}^2}{\omega\left(\omega \pm \Omega_i\right)}. \tag{6.11}$$

As Equations 6.6 and 6.7 are fundamental to resonant diffusion, any changes in the diffusion curves can only be made by using a different dispersion relation. In fact *Summers et al.*, 1998, suggest in their conclusions that their treatment should be extended to situations where the dispersion relation is more complex than the simple cold plasma approximation shown above.

6.3.2 Dispersion Relations

The angular frequency ω of an electromagnetic wave and its wave number k, are related simply by

$$n^2 = \frac{k^2c^2}{\omega^2} \tag{6.12}$$

where n is the refractive index, and c is the speed of light. In a vacuum n is constant and equal to unity, however, in a plasma the refractive index is not generally unity and tends to vary with frequency. The way in which n varies with ω is dependent on the properties and is described by the dispersion relation (e.g. Equation 6.11.

Dispersion Relation for Parallel Propagating Waves in a Cold Plasma

In the cold plasma approximation the plasma is treated as consisting of 2 populations, one of cold electrons, and the other of cold ions made up entirely of protons. The word 'cold' here implies that the temperature of the particles is low, such that their thermal velocities can be treated as zero. The plasma is also treated as being charge neutral, i.e. $N_e = N_i = N_0$ and having no net current, i.e. $\mathbf{v}_e = \mathbf{v}_i = 0$ (such particles cannot be seen by LEPA). A derivation of the cold plasma dispersion relation for parallel propagating waves is given in Appendix C.

The form of the dispersion relation is shown in Figure 6.9 for the case when $\omega_L > \Omega_e$, which as typically the case in the magnetosphere (including times when FAEs are observed). R mode waves with frequencies below Ω_e are generally known as whistler mode waves, and it is these waves which have been used to calculate the diffusion curves.

The background electron population (seen by LEPA) at the times of FAEs (i.e. ignoring the counterstreaming beams and the accelerated particles) is fairly isotropic. In the absence of the counterstreaming beams one would expect the cold plasma approximation to be valid. However, the counterstreaming beams are present and introduce strong anisotropies in the electron distribution, and so the cold plasma approximation may not be valid.

Dispersion Relation for Parallel Propagating Waves in a Cold Plasma with Counterstreaming Beams

In order to investigate wave-particle interactions for the field aligned events it is necessary to use a more realistic dispersion relation. Indeed, it is anisotropies within the particle distribution which will cause the waves to scatter particles, and the cold

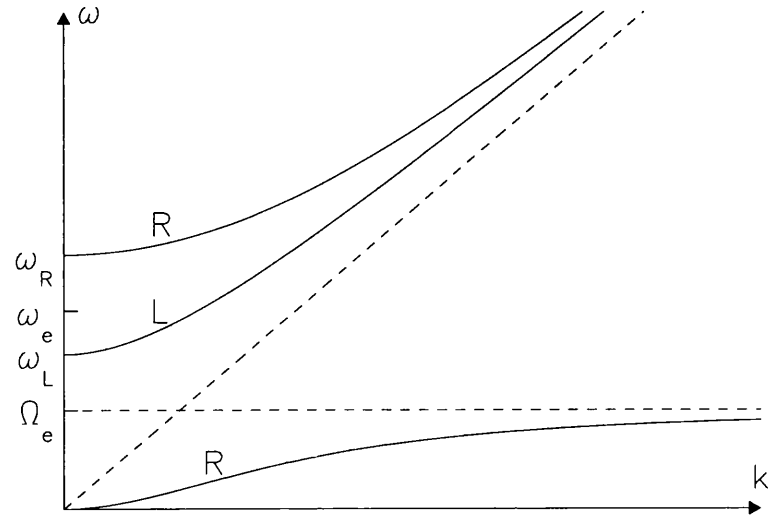

Figure 6.9: Dispersion diagram for parallel-propagating electromagnetic waves in a magnetised plasma for the case when $\omega_L > \Omega_e$. The lowest frequency branch (labeled R) corresponds to whistler mode waves and is the basis of the analysis in Section 6.2.

plasma approximation has none[3]. The background distribution at the time of the FAEs is generally fairly isotropic, and so it is the counterstreaming beams which are the main anisotropy in the distribution. *Gary*, 1993, suggested a form for a dispersion relation containing many cold components with velocities v_{0j} parallel to $\mathbf{B}$ in the limit $\Re(\omega) \gg \Im(\omega)$. Given in terms of the refractive index it is,

$$n^2 = 1 - \sum_j \frac{\omega_{pj}^2 (\omega - k_z v_{0j})}{\omega^2 (\omega - k_z v_{0j} \pm \Omega_j)}. \tag{6.13}$$

We apply this to the sort of distribution seen at the time of FAEs, treating the counterstreaming beams as further cold components.

In the case of a cold plasma with counterstreaming beams we will assume a cold background ion component (subscripted i) composed entirely of protons with zero

[3]Often, as in the case of 'pancake' distributions, the anisotropies in the hot electron population are treated as a perturbation on an isotropic cold population. The results presented later in this chapter suggest that this may not be a valid approach.

velocity, a cold background electron component (subscripted c) with zero velocity, and two beam components (subscripted b) of equal density and with velocities $\pm v$ along the field direction. Again this is a charge neutral plasma, and has no net current. This gives the dispersion relation as

$$n^2 = 1 - \frac{\omega_{pc}^2}{\omega\left(\omega \pm \Omega_e\right)} - \frac{\omega_{pi}^2}{\omega\left(\omega \pm \Omega_i\right)} - \frac{\omega_{pb}^2\left(\omega - k_z v\right)}{\omega^2\left(\omega - k_z v \pm \Omega_e\right)} - \frac{\omega_{pb}^2\left(\omega + k_z v\right)}{\omega^2\left(\omega + k_z v \pm \Omega_e\right)}. \quad (6.14)$$

Given that

$$N_e = N_c + 2N_b, \quad (6.15)$$

where N_e is the total electron density, the plasma frequency of the background electron component is given by,

$$\omega_{pc}^2 = \omega_{pe}^2 - 2\omega_{pb}^2. \quad (6.16)$$

Using Equation 6.16, Equation 6.14 can be rewritten as a new dispersion relation

$$n^2 = \underbrace{1 - \frac{\omega_{pe}^2}{\omega\left(\omega \pm \Omega_e\right)} - \frac{\omega_{pi}^2}{\omega\left(\omega \pm \Omega_i\right)}}_{\textit{Cold plasma approximation}} - \frac{2\omega_{pb}^2}{\omega\left(\omega \pm \Omega_e\right)} - \frac{\omega_{pb}^2\left(\omega - k_z v\right)}{\omega^2\left(\omega - k_z v \pm \Omega_e\right)} - \frac{\omega_{pb}^2\left(\omega + k_z v\right)}{\omega^2\left(\omega + k_z v \pm \Omega_e\right)}. \quad (6.17)$$

Here the first three terms on the right hand side of Equation 6.17 are those of the single electron component cold plasma dispersion relation (Equation 6.11), and three new terms have been introduced. Equation 6.17 presents some difficulties as k is present both on the left hand side (within n) and on the right hand side in the two beam terms. We have solved Equation 6.17 for u,

$$u = \sqrt{\frac{F(\omega)}{2G(\omega)}}, \quad (6.18)$$

where the forms of $F(\omega)$ and $G(\omega)$ are given in Appendix D.

This new dispersion relation for parallel propagating waves is shown by the solid lines in Figure 6.10, which also shows the single electron component cold plasma dispersion relation (as defined by Equation 6.11) as dashed lines. Plot (a) shows the dispersion relation for typical values during an FAE, $\Omega_e = 2 \times 10^4$ rad s^{-1},

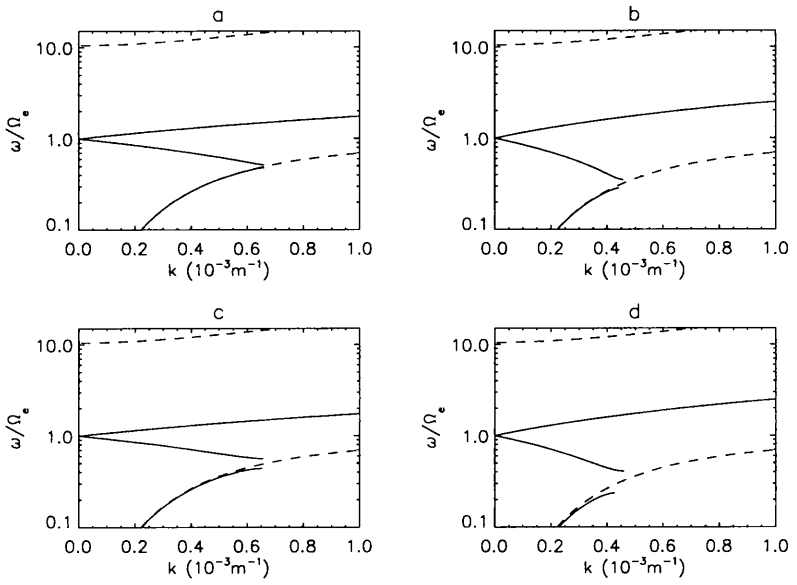

Figure 6.10: Dispersion diagram for parallel-propagating electromagnetic waves in a cold magnetised plasma with cold counterstreaming beams together with the single electron component cold plasma dispersion relation (dashed lines). Note, that in all plots there is a gap where the solution to the dispersion relation for a cold plasma with cold counterstreaming beams turns complex.

$\omega_{pe} = 2 \times 10^5$ rad s^{-1}, $\omega_{pb} = 1 \times 10^4$ rad s^{-1}, and $v = 1.5 \times 10^7$ ms^{-1}. Ω_e is calculated from the magnetometer, ω_{pe} is estimated from the upper hybrid resonance seen in the PWE data, and ω_{pb} and v are calculated from the LEPA data. The curve follows the single electron component cold plasma curve until it reaches a frequency $\omega = 0.48\Omega_e$. Here the solution becomes Complex, and has not been plotted. As ω increases the solution becomes Real again at $\omega = 0.52\Omega_e$, but k decreases reaching zero at $\omega = \Omega_e$. Currently it has only proved possible to solve Equation 6.18 for u and not for ω, and as what is required is a solution where u is Real and ω Complex, the nature of the diffusion curve is unknown in this Complex region. Even if a solution could be found, Equation 6.18 is only valid while the Imaginary part of ω is small compared with the Real part. This criterion may soon become invalid away from the Real regions.

The significance of the complex region can be seen in Figure 6.11. Figure 6.11

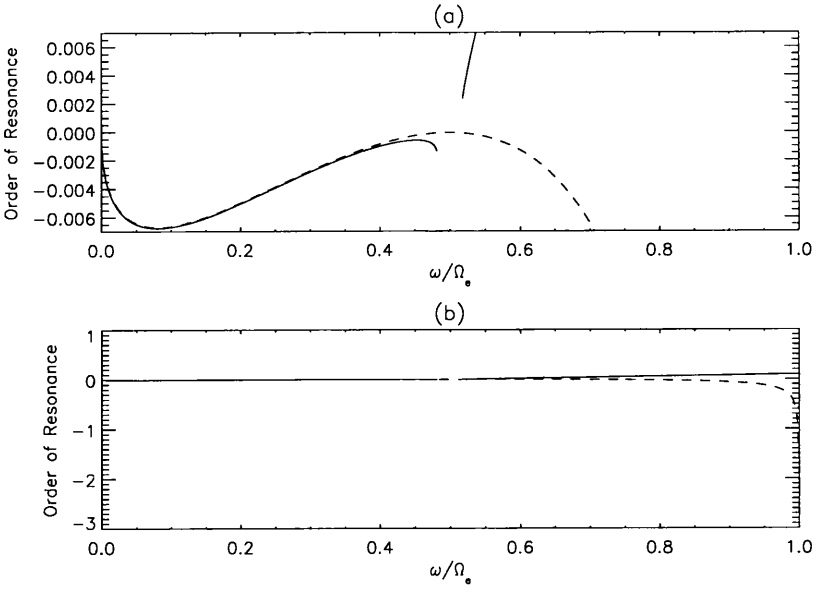

Figure 6.11: Dispersion diagram for parallel-propagating electromagnetic waves in a cold magnetised plasma with counterstreaming beams shown in terms of the order of cyclotron resonance with $v_{||} = v_b$ (solid line). The dashed line shows the single electron component cold plasma dispersion relation. Both plots show the same curves but with different y-axis scales.

shows the dispersion relation as a function of ω in terms of the order of cyclotron resonance with $v_{||} = v_b$. The dashed line shows the solution using the single component cold plasma approximation, and the solid line shows the solution for our new dispersion relation (again the complex region has not been plotted). We can see that in the cold plasma approximation the order of resonance tends to $-\infty$ as ω reaches Ω_e. It may be that using our new dispersion relation the order of resonance tends to $-\infty$ in the complex region, or it may simply reverse. In either case any cyclotron resonance with the beam must occur within the complex region. In fact the Landau resonance (effectively zeroth order cyclotron resonance) must also take place in this region.

When the dispersion relation turns Complex it indicates either wave growth or damping. The fact that our dispersion relation turns complex at frequencies resonant

with the beam velocity shows that it is the beam which is giving rise to the wave growth/damping. Without solving Equation 6.18 for ω, it is not possible to say whether wave growth or wave damping is taking place, though it does imply the transfer of energy between the wave and particle distributions. It would be expected that if the electrons are accelerated there would be a damping of the waves, as opposed to a growth.

Returning to Figure 6.10, plot (b) shows the curve calculated using the same values as used in plot (a) with the exception that v has been doubled, illustrating the effect the beam velocity has on the position of the Complex region (i.e. the frequency resonant with the beam is shifted down if the beam velocity increases). Plot (c) is calculated using the same values as plot (a) but ω_{pb} has been increased fourfold (corresponding to an increase of n_b by a factor of 16), causing a widening in the Complex region. This illustrates how the width of this Complex region in frequency space depends strongly on the ratio of the beam density to the cold plasma density. Plot (d) shows the dispersion curve with both increases in v and ω_{pb}.

It has already been noted (Section 6.1.2) that it is difficult to determine the cold plasma density at the time of FAEs, as the upper hybrid resonance emission is not clearly identifiable in the wave data and LEPA doesn't measure below 100 eV. The fact that the upper hybrid resonance is not clearly identifiable in the wave data may indicate that the dispersion relation in the single electron component cold plasma approximation is not valid. Normally the upper hybrid resonance emissions are seen at a frequency equal to Ω_e and ω_{pe} added in quadrature. However, at the time of FAEs there are three electron components, which may well affect the UHR emission.

The form of Equation 6.18 has not made it possible to analytically calculate velocity space diffusion curves, as Equation 6.9 requires the integration of u/ω with respect to u. At low frequencies our new dispersion relation approximates to the cold plasma dispersion relation, and so we would expect similar diffusion curves. All

we can really say with our current results is that the diffusion curves may well be different from those gained using the cold plasma relation.

Figure 6.12 shows the dispersion relation curve given by Equation 6.18 with $\omega_{pb} = 0$. The curve still reverses at a frequency resonant with the beam velocity as opposed to following the single electron component cold plasma approximation. It is interesting to note that the solution shown in Figure 6.12 does not allow cyclotron resonance with the beam particles, but Landau resonance is still possible. The reason that the solution is not the same as the single electron component cold plasma solution is due to the presence of v in Equation 6.18 (by setting v to infinity, the single electron component cold plasma approximation is achieved). The interesting point about the dispersion relation shown in Figure 6.12, is that no matter how low in density, between the frequency resonant with the beam velocity and Ω_e, $\frac{d\omega}{dk} < 0$ is obeyed (as opposed to the usual cold plasma dispersion relation where $\frac{d\omega}{dk} > 0$ at all frequencies). This leads to questions about how realistic Equation 6.18, and the approximation of the electron distribution actually is. The beams have been represented simply as a number of particles with $v_{||} = v$ and $v_{\perp} = 0$, whereas the reality of the situation has a distribution spread both parallel and perpendicular to the field. The fact that the solution turns Complex (which it does not do with $\omega_{pb} = 0$,) provides a certain amount of confidence that it represents reality.

The work in this section has purely been concerned with the interaction of electrons with parallel propagating right hand whistler mode waves. Ideally this treatment should be extended to a more realistic distribution function. It could also be extended to ECH waves and non parallel propagating waves. In reality much of this will prove difficult to perform analytically, but progress could be made numerically. One line of investigation may be to implement a ray tracing program such as the HOTRAY code described in *Horne*, 1989.

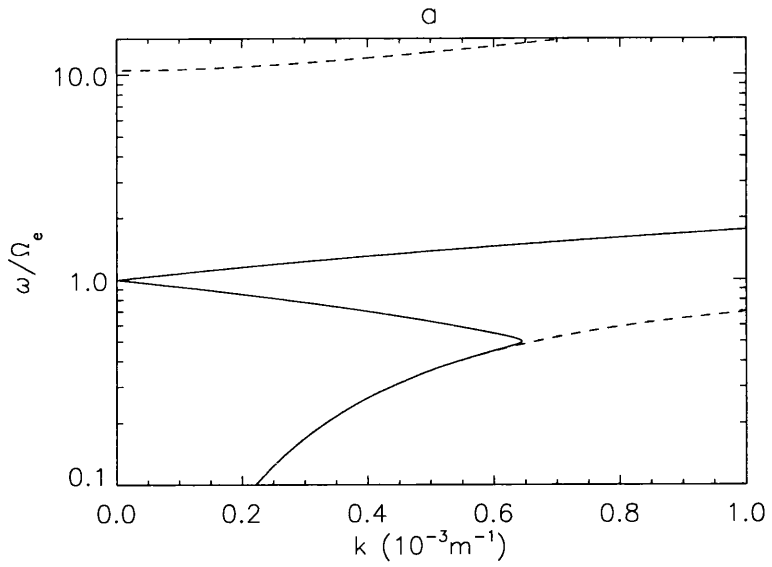

Figure 6.12: Dispersion diagram for parallel-propagating electromagnetic waves in a cold magnetised plasma with counterstreaming beams with $\omega_{pb} = 0$. Note that this dispersion relation remains Real throughout.

6.4 Summary

- We have suggested that the whistler mode waves or the ECH waves seen by the PWE on board CRRES may be responsible for the acceleration of field aligned electrons. At the times when FAEs are seen, the PWE detects strong broadband emission covering whistler and ECH frequencies. No clear correspondance between the wave power seen locally by the PWE and the acceleration of field aligned electrons has been seen, though this is thought to be due to sampling problems with the wave data and the fact that the generation of the observed waves is taking place via other mechanisms unrelated to the acceleration of field aligned electrons.

- The theoretical diffusion curves for resonant interactions between parallel propagating whistler mode waves and electrons suggested by *Summers et al.*, 1998,

have been examined. These cannot explain the scattering paths (light shaded region of Figure 5.10) seen associated with the acceleration of FAEs. It has been suggested that this may be because the approximation of a single electron component cold plasma is not a good description of the plasma at the time of FAEs.

- It may be possible to reconstruct the scattering path seen in the LEPA data with *Summers et al.*, 1998, type diffusion taking place away from the magnetic equator, producing the acceleration leg of the scattering path and a second region of *Summers et al.*, 1998, type diffusion taking near the magnetic equator producing the non-acceleration leg of the scattering path. However, features of the electron distribution (e.g. electrons are only scattered towards 90°) suggest that this is not happening.

- We have suggested a more realistic dispersion relation and partially analysed it. We have demonstrated that it behaves differently from the single electron component cold plasma approximation in a certain frequency range. The new dispersion relation has been shown to turn Complex near a frequency resonant with electrons of the beam velocity, which implies wave growth or damping, i.e. the transfer of energy between the wave population and the particle population can occur. The width of the Complex region depends on the ratio of the electron beam density to that of the cold population. It has not been possible to calculate full diffusion curves for our new dispersion relation, though it appears that the diffusion curves may be different from those proposed by *Summers et al.*, 1998.

- The investigation has shown that at the time of FAEs the dispersion relation is not dominated by the $v = 0$ cold plasma component. The nature of waves and hence the resonant diffusion paths may depend greatly on the presence of counterstreaming beams. The arguments presented here require further work

on the effect of a more realistic distribution function, and extension to other wave modes.

Chapter 7

The Source of FAEs and The Relation of FAEs to FACs

In this chapter we are looking at FAEs in relation to Field Aligned Currents) FACs. We present various forms of circumstantial evidence suggesting that FAEs and FACs are related, before looking at the magnetic field perturbations during FAEs and then attempting to measure the FAC density directly from the LEPA data.

7.1 Introduction

The work contained within this chapter has been motivated by a study of six substorm onsets carried out by *Maynard et al.*, 1996. The *Maynard et al.*, 1996, study used CRRES measurements of magnetic and electric fields, and LEPA electron data, in conjunction with ground based measurements. A summary of these six cases is shown in Table 7.1. FAEs (counterstreaming bursts) were observed during three of the substorms (Orbits 585, 497, and 445). *Maynard et al.*, 1996, made no attempt to place the FAEs in the context of the substorm model, except to mention some points regarding their source. *Maynard et al.*, 1996, suggests that the electron beams originate from electrons back-scattered from the ionosphere which were originally trapped

		Event					
No.	Observation	535	540	486	585	497	445
1	Relation to Harang	dusk	dawn	dusk	dusk	dusk	dusk
2	Onset to electrons (min)	8	5	8	14	5	5
3	Enhanced dawn-dusk E	yes	yes	yes	yes	yes	yes
4	Dusk-dawn E excursions	yes	yes	yes	yes	yes	yes
5	Trapped electron remnant	yes	yes	yes	yes	yes	yes
6	Pre-onset plasma sheet electrons	no	yes	no	no	yes	yes
7	Strong field-aligned currents	yes	yes	no	no	yes	no*
8	"Explosive growth phase"	no	yes	yes	no	weak	no
9	Counterstreaming bursts	no	no	no	yes	yes	yes
10	AKR†	pre G	throughout	at G	near G	at G‡	at G
11	Pseudobreakup	yes	no	no	no	no	yes§
12	Distance from onset		closest		greatest		

*Weaker field aligned currents were observed associated with the pseudo breakup at 16:00 UT
†Observations relative to ground onset (G) and CRRES injection (C)
‡AKR observed throughout with major intensification at later onset at Narssarssauq
§Pseudo-breakup related to first onset at 16:00 UT

Table 7.1: Summary of observations made by *Maynard et al.*, 1996, using CRRES measurements of magnetic and electric fields, and LEPA electron data in conjunction with ground based measurements.

beneath a field aligned potential drop prior to being released due to temporal and spatial changes.

Item 7 in Table 7.1 shows that three of the events, during Orbits 497, 540, and 535, investigated by *Maynard et al.*, 1996, displayed characteristics in B_D (see Section 3.5.2) which could be attributed to filamentary FACs [*Nagai*, 1982]. The other three events, during Orbits 445, 486, and 585, display weaker variations in B_D. In Orbit 486 and Orbit 445 events CRRES is very near the magnetic equator where FACs should vanish as should their magnetic signatures[1] [Vasyliunas, 1970]. The Orbit 585 event occurs when CRRES lies at 21:15 MLT, the earliest MLT of any of the 6 events, and the injected electrons are not seen until sometime after substorm

[1] A simple way of viewing this is that FACs are generally assumed to flow between the ionosphere and field perpendicular currents such as the cross-tail or ring current at low latitudes. It is not usual that FACs flow from one hemisphere to the other and so no net FAC should be seen at the equator.

onset.

Off the magnetic equator, large scale variations in B_D may be attributed to the Region 1 and Region 2 FACs [*Iijima and Potemra*, 1978]. Other smaller scale deviations have been attributed by *Maynard et al.*, 1996, to a filamentary current structure associated with the substorm current wedge. This is not to say that variations in the other components of the magnetic field will not have variations associated with FACs, but rather that variations in B_D are predominately caused by FACs whereas variations in B_V and B_H may have other causes. No connection between the filamentary FACs and the FAEs seen by *Maynard et al.*, 1996, was suggested, perhaps because only one of the six events exhibited evidence of both. However, *Mauk and Meng*, 1991, did suggest that counterstreaming electron beams, such as those seen by the ATS-6 satellite [*McIlwain*, 1975] may be connected to FACs. This is because only the most field aligned electrons seen in the equatorial regions may reach the ionosphere and carry a current into or out of it.

7.2 High Latitude Observations of Field Aligned Electron Beams

Before going on to discuss the CRRES observations of FAEs and their relation to the FAC systems it is useful to discuss the high latitude observations of field aligned electron beams which we believe to be the source of the FAEs observed by CRRES.

7.2.1 Older Studies

As mentioned in Section 4.1.1 a number of spacecraft at high latitudes have observed field aligned electron beams. The first documented satellite observations were made with the S3-3 satellite by *Sharp et al.*, 1980. The S3-3 observations were of counterstreaming beams in the keV range made at an altitude of $\sim$1 R_e. The coun-

terstreaming beams were usually around 10° wide and were seen at energies up to 7 keV. As with many of the later observations they were often seen around the time of upgoing ion conics. *Collin et al.*, 1982, went on to study the statistical nature of these events, which to our knowledge is the only published statistical analysis of field aligned electron beams at high latitudes. The S3-3 statistical survey is discussed in Section 7.2.4.

Suprathermal (< 500 eV) bursts of field aligned electrons were observed with the ISIS-2 satellite at 1400 km altitude by *Johnstone and Winningham*, 1982. The electron bursts were presented in the context of being the same phenomenon as the field aligned suprathermal bursts seen by sounding rockets [e.g. *Raitt and Sojka*, 1979]. It was concluded that the bursts were an integral part of the acceleration mechanism responsible for generating the electrons which produce discrete auroral arcs scince the two phenomena (bursts and discrete arcs) are both found in auroral regions, but never seen on the same field lines. *Klumpar and Heikkila*, 1982, suggested that the upward field aligned electron beams observed with ISIS-2 could be the carriers of the downward FAC seen in the same regions as the beams.

Lin et al., 1982, presented observations of counterstreaming electrons at altitudes of 2-3 R_E made with the DE-1 spacecraft. They suggested that two types of counterstreaming electrons exist, though it is unclear how the two types relate to observations of counterstreaming electrons near the geomagnetic equator. *Burch et al.*, 1983, showed that field aligned electron beams of energies 20-200 eV were common in the dayside magnetosphere and suggested that they are a primary source of dayside Region-1 Birkeland currents.

Simultaneous observations by the VIKING satellite [*Hultqvist et al.*, 1987, and *Hultqvist and Lundin*, 1987] of upwardly accelerated auroral electrons and ions of similar energies ($\sim$ 1 keV) at altitudes of around 13000 km led to the suggestion that the particles were accelerated by a time varying field aligned electric field component.

ELECTRONS		
Beams:	(1)	Bidirectional, broad-E
	(2)	Upgoing, narrow-E (due to $U_{\parallel}$).
	(3)	Upgoing, broad-E
	(4)	Downgoing, broad-E
	(5)	Downgoing, narrow-E (due to $U_{\parallel}$).
Conics:	(1)	Bidirectional, with loss-cone
	(2)	Upgoing, high-E
	(3)	Bidirectional, trapped (in $U_{\parallel}$).
POSITIVE IONS		
Beams:	(1)	Bidirectional, narrow-E
	(2)	Upgoing, narrow-E (due to $U_{\parallel}$).
Conics:	(1)	Bidirectional, narrow-E.
	(2)	Upgoing, broad-E.
	(3)	Upgoing, broad-E "tuning fork".
Abbreviations:		E = Energy.
		$U_{\parallel}$ = Field aligned potential drop.

Table 7.2: Classification Scheme for Beams and Conics suggested by *Lundin et al.*, 1987, based on observations made with the VIKING spacecraft.

The frequency of the electric field variations is such that the downward component of the electric field is seen as quasi-static by the electrons, producing the observed acceleration. The ions, however, experience the fluctuating field as a wave, prompting the formation of ion conics. *Lundin et al.*, 1987, used the VIKING data to show that there were in fact a variety of different types of energised auroral particles. It was suggested, therefore, that a number of different acceleration/heating processes must be responsible. *Lundin et al.*, 1987, suggested a new classification for these phenomena which is outlined in Table 7.2.

The Freja satellite has also observed upward-directed electron beams coincident with ion conics near 1700 km altitude [*Boehm et al.*, 1995]. One particularly intense event was seen with strong field aligned fluxes up to 2 keV, while many others have been seen in the 0.1-2 keV range. *Boehm et al.*, 1995, suggested that while electrostatic acceleration to 0.5-1 keV may take place, the more energetic electrons may have been further accelerated by ~1 kHz waves.

7.2.2 FAST Observations of Field Aligned Electron Beams

By far the best observations of field aligned electron beams at high latitudes made to date are those made with the FAST satellite [*Carlson et al.*, 1998b]. These observations hence provide the basis for what is currently our best understanding of the mechanism responsible for the formation of the field aligned electron beams.

Carlson et al., 1998b, states that the electron beams seen by FAST are undoubtedly the origin of the highly collimated counterstreaming beams observed deep in the magnetosphere, such as those seen by *Klumpar*, 1993, and that they may be used as a tracer to connect the downward current region into the outer magnetosphere. If correct it is reasonable to suppose that the FAEs seen by CRRES are also connected to the upgoing beams seen at high latitudes and to the FACs flowing in the magnetosphere.

The conclusion of the *Carlson et al.*, 1998b, study was that upgoing electron beams were accelerated by diverging electric field, quasi-static potential structures. These structures appear to have similar properties (except for the reversed polarity) to the converging electrostatic shocks thought to be responsible for accelerating the upgoing ion beams and the downgoing inverted V electrons which produce the auroral light. An optical signature of the diverging shocks when they occur within regions of diffuse

Diverging Electrostatic Shocks	Converging Electrostatic Shocks
Downward Current Region	Upward Current Region
Upgoing Field Aligned Electrons	Downgoing inverted V electrons
Ion heating transverse to **B** (ion conics)	Upgoing ion beams
Large amplitude ion cyclotron waves and D.C. turbulence	Large amplitude ion cyclotron waves and D.C. turbulence
Electrostatic solitary wave (ESW) and VLF saucer source region	AKR source region

Table 7.3: Signatures of regions of diverging and converging electrostatic shocks, after *Carlson et al.* 1997.

aurora is the 'black aurora'[2] since precipitation is suppressed [*Marklund et al.* 1984]. In a more general case they may be considered the 'inverse aurora'. This leads to a model of converging and diverging electrostatic shocks regulating the upward and downward current regions, each of which have a number of observational signatures. These signatures are listed in Table 7.3

In both regions the main carrier of the current is the electrons though due to the requirement to maintain quasi-neutrality, the location along the flux tube where the beams can be formed is controlled by the ion distribution. There is a seasonal dependence of the low altitude formation of shocks [*Bennett et al.*, 1983] and the upgoing electron and ion beams produced by the shocks [*Carlson et al.*, 1998b] (more beams and shocks are seen forming between 2000 km and 4000 km altitude in the winter than in the summer) which suggests that the ion scale height may regulate the formation of both types of beams.

[2]'Black aurora' refers to regions within an auroral arc where there is no auroral emissions, as opposed to the gaps between arcs.

An example of the beams seen by FAST are shown in Figure 7.1. The improvement in the quality of the FAST observations over previous missions is due to the nature of the instrumentation used, details of which can be found in *Carlson et al.*, 1998a, and references therein. The instrumentation includes two pairs of 'top-hat' analysers, to measure high resolution energy spectra of ions (3 eV - 25 keV) and electrons (4 eV - 30 keV) in 32 pitch angle bins every 78 ms, i.e. at very high time resolution. Each pair is mounted on opposite sides of the spacecraft with their 180° field of view lying in the spin plane. The spin axis of the spacecraft is such that the Earth's magnetic field direction is nearly always within 5° of the spin plane during auroral crossings. Deflection plates automatically steer the view direction to follow the magnetic field direction so that full 360° of pitch angle are measured every sweep independent of the direction of the spacecraft spin axis. The pitch angle and energy bins are contiguous to ensure that no fine angle or energy features are missed.

Figure 7.1 shows high time resolution FAST data from an active northern auroral crossing near magnetic midnight. The interpretation of the data which follows is that of *Carlson et al.*, 1998b. The first panel shows the spin axis component (nearly westward, -D in VDH coordinates) of perturbation of the magnetic field (ΔB_s). In the first half of the pass the slope of ΔB_s is negative indicating an upward FAC. In the second half the slope of ΔB_s reverses indicating a downward FAC. The direction of the currents matches the statistical Region 1 and Region 2 current systems expected near midnight (illustrated in Figure 2.11).

The next five panels show the electron data. The second and fourth panels show the energy spectrum for the upgoing and downgoing electron fluxes respectively, and the third panel shows the pitch angle spectrogram with 0° pitch angle corresponding to downgoing fluxes. The fifth and sixth panels show the total upgoing and downgoing electron flux and energy flux respectively. The upward FAC region (19:06:00 - 19:07:10 UT) is dominated by the broad region of downgoing inverted V electron pre-

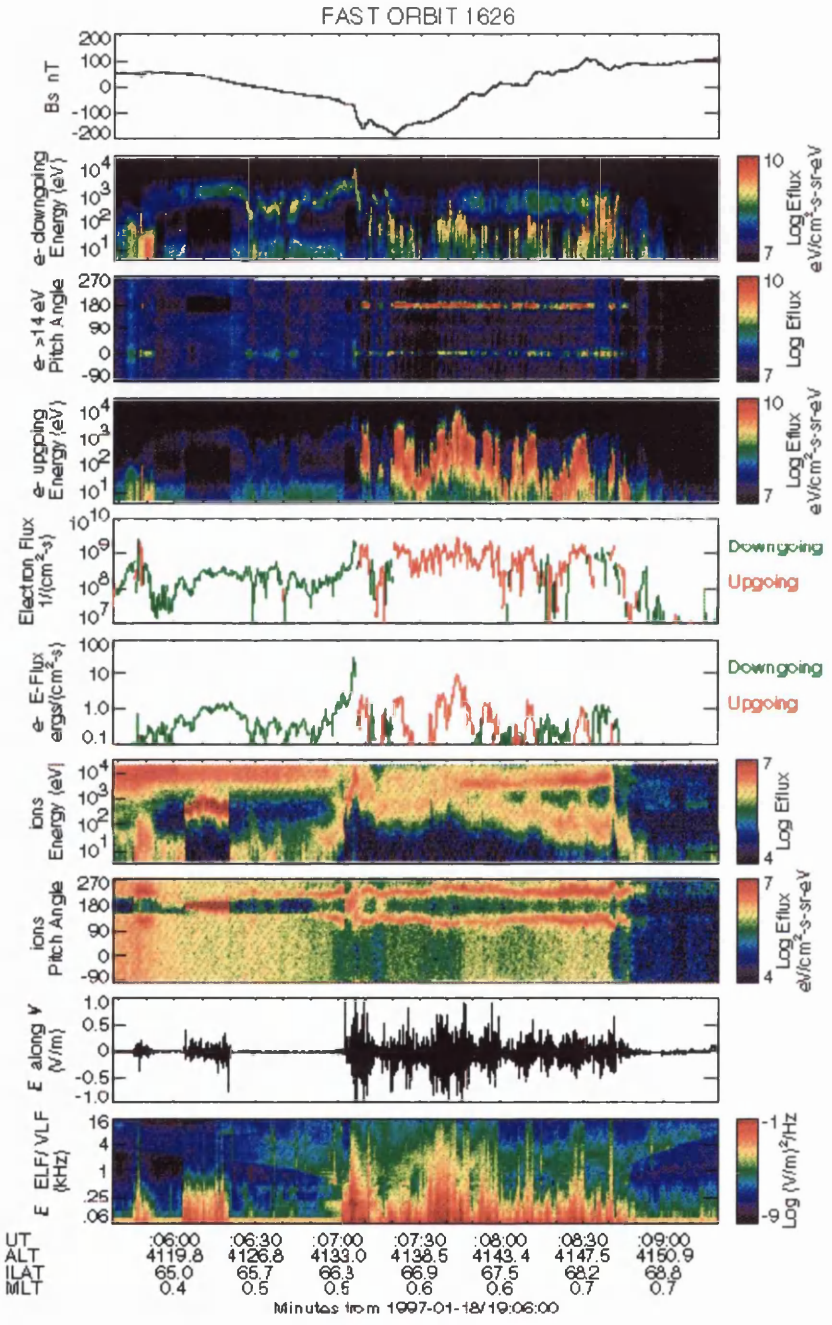

Figure 7.1: FAST observations of an auroral crossing near magnetic midnight that has nearly equal width regions of upward and downward Birkeland currents. Panels, starting from top: (a) The spin axis component (nearly westward) of the magnetic field. A positive (negative) slope indicates downward (upward) current. (b ,c, d) Electron energy flux spectrograms versus energy and pitch angle. Fluxes near 180° are upgoing. (e, f) Total electron particle flux and energy flux, colour coded for upgoing (green), and downgoing (red). (g, h) Ion energy flux spectrograms versus energy and pitch angle. The energy spectrogram is for all pitch angles. (i) The DC electric field signal perpendicular to B and parallel to the spacecraft velocity. (j) Power spectral density of low frequency E-field.

cipitation with an energy peak near 1 keV. The fluxes of 2-3 $\times$ 10^8 cm^2s^{-1} seen in the inverted V represent a moderate intensity aurora and only appear low in comparison to the very high fluxes seen in the downward current region.

The region of downward current (located between 19:07:20 UT and the polar cap boundary at ~19:09:00 UT) is characterized by very field aligned electrons both in the upward and downward directions though clearly dominated by the upgoing fluxes (which have peak differential energy fluxes ranging between 10^{10} and 10^{11} $cm^{-2}ster^{-1}s^{-1}$). The net electron fluxes in the downward current region are 2-3 times larger than those seen in the upward current region. The electron beams cover a large energy range extending from around 4 eV up to an abrupt cut off around 1 keV.

The ion population (illustrated in the seventh and eighth panels) shows some distinct differences between the regions of upward and downward current. In the region of upward current the ion population is dominated by the steady drizzle of plasma sheet ions except between 19:06:02 UT and 19:06:20 UT where the spacecraft crosses an upward ion beam. The presence of the ion beam suggests that the electrostatic shock potential responsible for the ion acceleration dipped below the spacecraft altitude in this region. The electric field component perpendicular to the field direction and aligned with the spacecraft velocity is shown in the ninth panel. The electric field is turbulent within the beam, but the positive spike inbound, and the negative spike outbound are the signature of a crossing of a convergent electrostatic shock. A second upward ion beam is seen at 19:07:03. The energy spread of the ion beams is moderate compared to that seen in the electron beams. The ion beams seen by FAST have been studied further by *McFadden et al.*, 1998, *Moebius et al.*, 1998, and *Ergun et al.*, 1998.

In the downward current region the ion population consists of weak ion precipitation as well as upgoing ion conics (seen as two symmetric traces that straddle the loss cone at 180° in the seventh panel of Figure 7.1). The two ion populations can be

seen in the energy spectrogram (the eighth panel of Figure 7.1). The upper trace at a fairly steady energy around 5 keV is that of the plasma sheet ions, and the lower energy trace is that of the ion conics, with energies varying between 10 eV and several keV. There is a distinct low energy cutoff of the ion conic energy spectrum which is a unique property of the conics which accompany upward electron beams. The cutoff energy of the ion conics follows the general trend of the energy of the electron beams. The electric fields which accompany the electron beams have very intense (0.1 - 1 Vm^{-1}) low frequency fluctuations. When isolated electron beams are seen by FAST, the electric fields have clear signatures of diverging electrostatic shocks.

7.2.3 Comparison of FAST and CRRES Observations

There are some differences between the electron beams seen at high latitudes and those seen by CRRES. The electron beams seen by FAST often cover a larger energy range than those seen by CRRES. The upper limit of the beam energy is similar between those seen by CRRES and FAST but the beams seen by FAST usually extending to lower energies than those seen by CRRES. However, due to the problems with detecting electrons covered by the low energy channels on LEPA (see Section 3.4.2) the extent to which this difference is real and significant is hard to gauge.

The second difference between the beams seen by CRRES and those seen at high latitudes concerns the width of the beam. Most of the reported observations of field aligned electron beams made at high latitudes (over a range of altitudes) cover roughly the same pitch angle range as those seen by CRRES ($\sim$ 10 - 15°). However, conserving total energy and the first adiabatic invariant we would expect that the same beams, seen nearer the equator would be much narrower ($\sim$ 0.01°) since the magnetic field is weaker there then nearer the poles. A certain amount of spread may have been introduced into the CRRES/LEPA data in the construction of the pitch angle energy arrays (see Section 3.4), but it is hard to understand how this could account for the

full width of the beam seen at CRRES. It is more likely that a very narrow beam would be unstable to wave particle interactions and thus spread through pitch angle.

The final difference is that the differential energy fluxes seen in the upgoing electron beams in the FAST data, are often an order of magnitude or more greater than those seen by CRRES. We suggest two possible explanations to account for the difference in the beam fluxes seen by CRRES and FAST. Firstly, FAST sees vastly different fluxes in the up and downgoing beam populations whereas CRRES sees fairly equal fluxes. It may be that CRRES observes an average population of beams originating in both hemispheres or of a trapped population undergoing bounce motion. The second, and possibly more important effect concerns the width of the beam. Liouville's theorem states that while moving under adiabatic motion the phase space density of a population of particles remains constant as it moves along a field line. Under these conditions the beam would occupy only very small pitch angles ($\lesssim 0.01°$) and the phase space density would be the same as is seen at low altitudes. If, however, the beams are indeed spread through pitch angle (as they appear to be) the amount of velocity space occupied by the beams would increase and the observed discrepancy in observed phase space density might be accounted for.

Before the link between the FAEs seen by CRRES and the electron beams seen at high latitudes can be solidified the differences detailed above need to be explained. As mentioned in Section 7.2, *Lundin et al.*, 1987, showed that there were various types of electron beam populations at high latitudes. How these beam populations and their different properties relate to the FAEs seen by CRRES also needs further investigation. Nevertheless, it does appear likely that these are the same phenomenon seen at different locations on a flux tube.

7.2.4 Distribution of High Latitude Observations of Electron Beams

Unfortunately, at this time no work has been published regarding the spatial distribution of the occurrence of the upgoing beams seen by FAST or the timing of them relative to substorms, though some work on their statistical nature is in progress [private communication *Carlson*, 1999]. The upgoing electron beams at higher latitudes are present for a wide range of geomagnetic activity, but their extent and intensity are certainly related to the level of geomagnetic activity [private communication *Carlson*, 1999].

The only known statistical survey regarding the distribution of field aligned electron beams at high latitudes is that made by *Collin et al.*, 1982, using data from the S3-3 satellite. Figure 7.2 shows the frequency of observing an electron beam (upgoing, downgoing, and counterstreaming beams are all included), firstly as a function of invariant latitude and secondly as a function of MLT. The distribution as a function of MLT is not very similar to the distribution of FAEs seen by CRRES (Figure 4.18) except for the fact that there is a double peaked structure in both distributions.

It is hard to compare Figure 7.2(b) directly with Figure 4.18 as the information in Figure 7.2(b) is summed over all invariant latitudes, some of which lie outside the field lines sampled by CRRES. Figure 7.3 shows the distribution of electron beams seen by S3-3 in terms of both MLT and invariant latitude. Problems arise with the statistical quality of the data when it is presented in this format. However, the diurnal variation is clear. The mean invariant latitude of beam occurrence is 76° (corresponding to an L-value of $\sim$ 17 in a dipole model) in the late morning sector, decreasing to 71° (corresponding to an L-value of $\sim$ 9.5 in a dipole model) in the pre-midnight sector. The variation of latitude in the occurrence of electron beams corresponds quite well to the *Feldstein et al.*, 1969, statistical auroral oval [*Collin et*

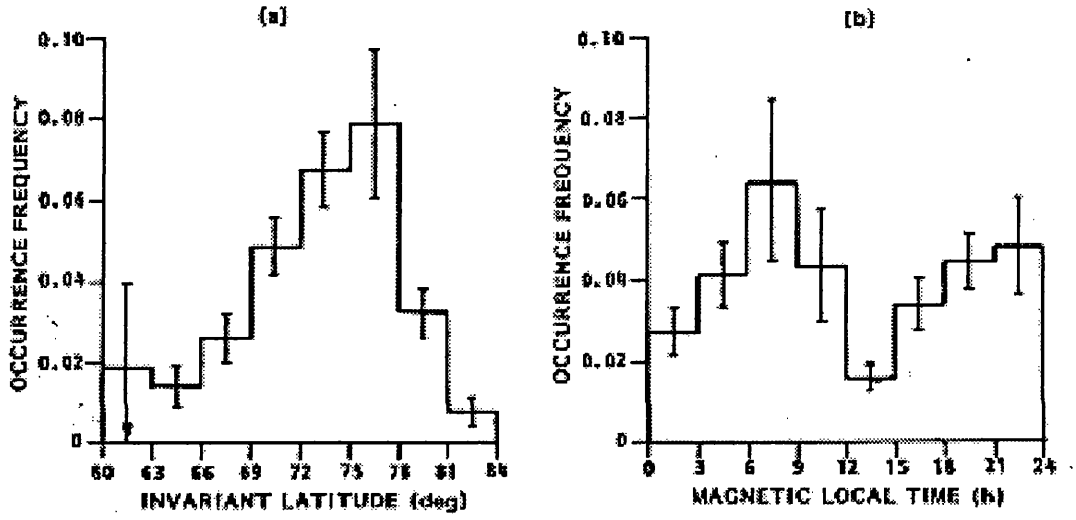

Figure 7.2: The frequency of occurrence of an electron beam within one satellite spin period as a function of (a) invariant latitude averaged over all magnetic local times and (b) magnetic local time averaged over invariant latitude, observed with the S3-3 satellite. The frequencies are also averaged over the altitude range of 3000-8000 km and do not distinguish between the directions of the beams [*Collin et al.*, 1982].

al., 1982] (see Figure 7.3). As we think these electron beams are the carriers of FACs it is not unexpected to see them in regions corresponding to the auroral oval, where the FACs are thought to originate.

The distribution shown in Figure 7.3 may also explain why CRRES observed very few FAEs on the dayside. The electron beams on the dayside are seen at higher invariant latitudes and thus will appear on higher L-shells. As CRRES spends very little time on an L-shell > 6 (corresponding to an invariant latitude of $\sim 66°$) between 09:00 MLT and 14:00 MLT it is not surprising that no FAEs were seen in this region (whereas FAEs have been seen on L-shells <6 on the nightside).

If, as seems likely, the FAEs seen by CRRES are composed of the same particles seen as beams at high altitudes it follows that they play a significant role in carrying FACs. Many of the studies outlined above relate upwardly accelerated beams to the Region 1 and Region 2 currents flowing out of the ionosphere. Other FACs which FAEs could play a role in are those associated with the current wedge and those associated with traveling convection vortices (TCVs). The latter, however, is a dayside phenomenon [*Zhu et al.*, 1997] and as most FAEs seen by CRRES are on the nightside, TCVs will be ignored.

7.3 FAEs and FACs

7.3.1 AE index

The AE index has been used in Section 4.3 as an indication of substorm activity. However, as it is an index of the current flowing in the auroral electrojet, it is logical to examine it in the context of a possible relationship between FAEs and the magnetospheric current systems. As the auroral electrojets connect regions of FAC we can in turn use the AE index as an indicator of the FACs flowing into and out of the auroral current system. By plotting the distribution of AE index at the time of FAEs

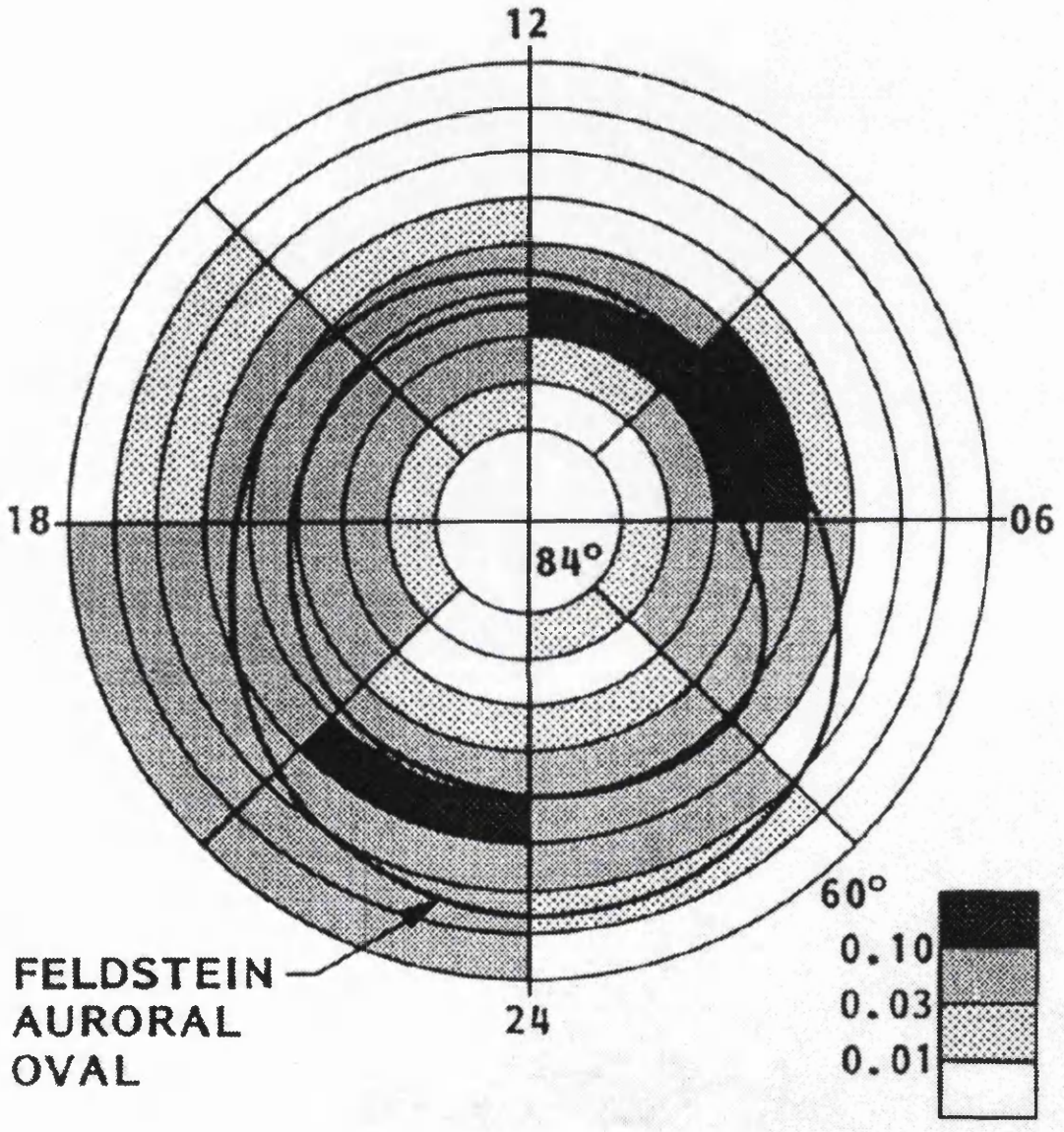

Figure 7.3: The frequency of occurrence of an electron beam within one satellite spin period as a function of invariant latitude, and magnetic local time, observed with the S3-3 satellite. The frequencies are averaged over altitudes between 3000 and 8000 km. The auroral oval [*Feldstein et al.*, 1969] is shown for comparison [*Collin et al.*, 1982].

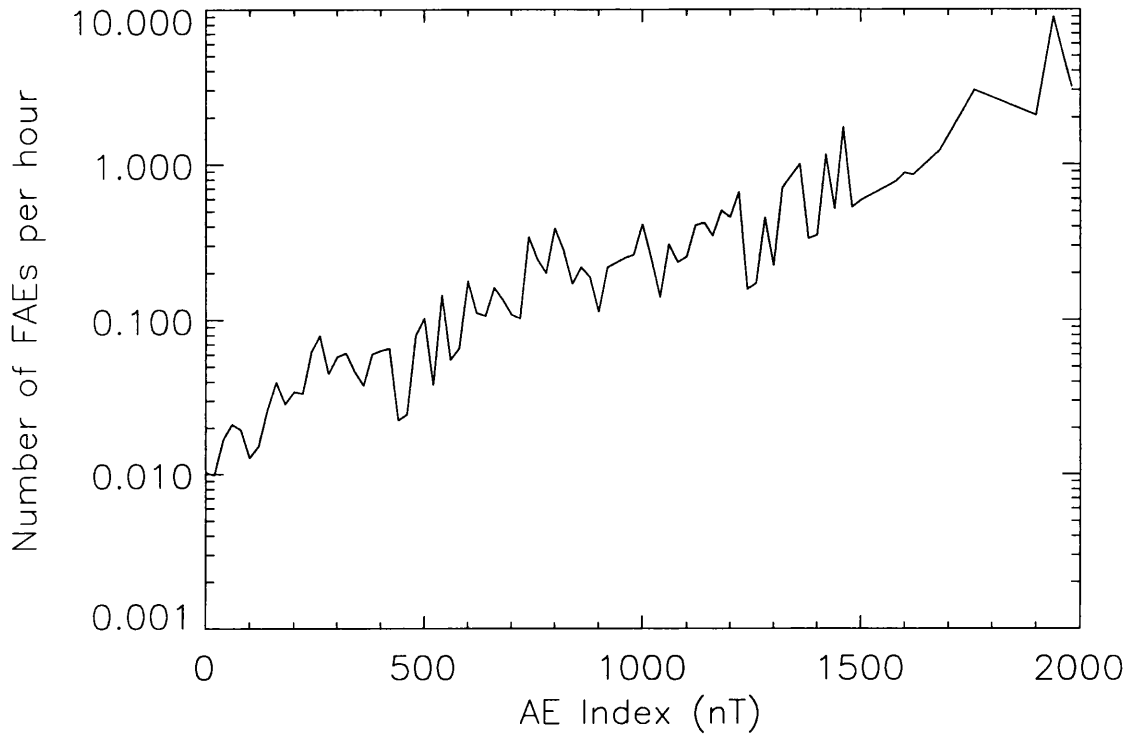

Figure 7.4: The distribution of AE index at the time of FAEs normalised to the distribution of the AE index throughout the lifetime of CRRES.

(as opposed to the maximum in the hour following as used in Section 4.3) normalised to the distribution of the AE index throughout the lifetime of CRRES a clear relation emerges, shown in Figure 7.4. As the AE index increases the frequency of FAEs seen by CRRES also increases. The Spearmans Rank Correlation coefficient between AE index and the frequency of FAEs seen is 0.88 with a significance of 1×10^{-25}, confirming the strong link in a statistical sense.

A correlation would be expected due to the fact that FAEs are seen during periods of high substorm activity within the magnetosphere, times when the auroral electrojet is typically enhanced. However, the strong correlation here indicates a more direct relationship, and so is very supportive of the hypothesis that FAEs are carriers of

significant FAC. The correlation continues to times of low (<150 nT) AE index, supporting the relation between FAEs and the auroral current system, rather than specifically being substorm related.

The relation between the FAE occurrence rate and the AE index is not linear (note logarithmic scale on the x-axis of Figure 7.4), with far more FAEs are observed at times of high AE index. The probable explanation for this is that as auroral activity increases so does the auroral oval width. This in turn means that the region of space near the magnetospheric equator which maps down to the aurora increases. Assuming that the FAEs are seen on auroral field lines it makes sense that the probability of seeing them will increase, as the region of space the auroral field lines occupy increases.

7.3.2 Distribution of Nightside FACs

Nakai et al., 1997, measured the statistical nature of FACs in the magnetotail during geomagnetically disturbed periods (shown in Figure 7.5) using ISEE 1 magnetic field data for 1978-1987. In order to examine the link between FAEs and FACs we have compared the results shown in Figure 7.5 with the distribution of FAEs seen by CRRES. It is hard to make a direct comparison as our CRRES observations extend only a little past $6R_E$ downtail (c.f. the distances of 5 - 15 R_E shown in Figure 7.5), however, there are some consistent features between the two distributions and we can assume that the FACs shown in Figure 7.5 are an extension of the FACs flowing nearer the Earth. The main point to note is that in the postmidnight sector the FACs flow at higher latitudes, whereas in the pre-midnight sector the FAC is stronger in the equatorial regions. Similar features can be seen in the distribution of FAEs, Figure 4.11. There also appears to be more current flowing in the pre-midnight sector than the postmidnight sector, similarly more FAEs are seen before midnight than after it (Figure 4.10).

Another feature shared by the FAC distribution measured by *Nakai et al.*, 1997,

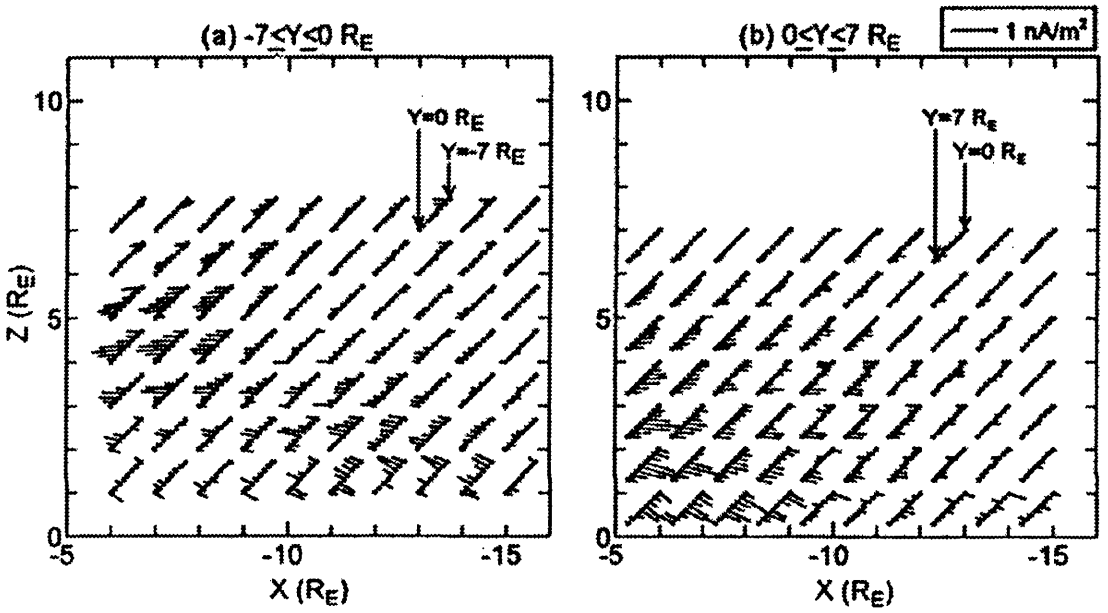

Figure 7.5: (a) The vector diagram of field aligned currents for disturbed periods in the post midnight sector. The origins for the points at y=0 are plotted with dots on the XZ plane, while those for the points at y<0 are displaced right and upward from their original position in the XZ plane; the dot at the far lower left (or upper right) of each array denotes the point at y=0 (or y=-7)R_E. (b) Same as (a), except for the pre-midnight sector. The dot at the far lower left (or upper right) of each array denotes the point at y=7 (or y=0)R_E. [*Nakai et al.*, 1997]

and the distribution of FAEs is a minimum around midnight. As the currents presented in Figure 7.5 are the average currents seen, it might be expected that the lack of current around midnight may be due to an averaging of positive and negative currents either side of midnight. As the current reversal region is not expected to always lie exactly at midnight, when averaged over long periods of time the current near midnight may appear small. However, the lack of FAEs around midnight suggests that the smaller current may in fact be real.

While the comparison of Figure 7.5 and the distribution of FAEs is not proof of FAEs being the carrier of FACs it is further evidence to strengthen the link.

7.4 Magnetic Field Measurements

The points discussed in Sections 7.2 and 7.3 are circumstantial evidence of the link between FAEs and FACs. Here we present the CRRES magnetometer data and use it to look for more direct evidence that FAEs are related to FACs.

Figure 7.6 shows the three components of the magnetic field in VDH co-ordinates measured around the time of the three FAEs discussed in Section 5.2 (Orbits 69, 77, and 264) and the three FAEs identified by *Maynard et al.*, 1996, (Orbits 445, 497, and 585). The magnetic field data shown here has had the Olson Pfitzer 85 model field [*Pfitzer et al.*, 1988] subtracted from it so as to highlight any changes in the field. A study by *Jordan et al.*, 1992, concluded that the Olson Pfitzer 85 model field showed the best agreement with the CRRES magnetometer data compared to other field models widely available at the time.

The six selected events shown in Figure 7.6 are fairly representative of the sort of magnetic field variations around the time of FAEs. However, little in the way of consistent features emerges concerning the large scale behavior of the magnetic field prior to and following an FAE. This is not surprising as FAEs usually occur around

the time of substorm onset, and are only one of many processes taking place which may affect the magnetic field configuration. One feature which is evident is that the H component of ΔB often changes from relatively large negative values to near zero. This change is due to a combination of the dipolarisation, which often occurs prior to FAEs, and the slow response of the model field to sudden changes in the global field topology.

The perturbations in the D component of the magnetic field during Orbits 69, 77, 264, and 497, all show significant short time scale ($\sim$ 15 minutes) variations when the FAEs are seen. These variations in B_D are indicative of filamentary FACs. There is a significant departure in B_D from the model just prior to the FAE during Orbit 585 but little variation during the event itself. Only the event on Orbit 445 shows no departure from the model in B_D. However, as mentioned in Section 7.1 this event occurs very close to the geomagnetic equator and so any FAC or B_D variations associated with the event would not be seen. The fact that the variations are not confined to the times when the FAEs are seen is to be expected as the magnetic field perturbation produced by a current will be seen outside of the current region as well as inside it.

Figure 7.7 shows the root mean squared ΔB_D averaged over the lifetime of each FAE, plotted against magnetic latitude. We can clearly see that the magnetic field signatures associated with FACs decrease as magnetic latitude decreases and reach zero at the equator. We interpret this as the FACs decreasing as they move towards the equator and merge with the ring current and cross-tail currents.

7.5 Estimating FAC Densities from LEPA data

As magnetic field perturbations measured by a single point spacecraft cannot be used to define a unique current configuration, and are not affected only by the local

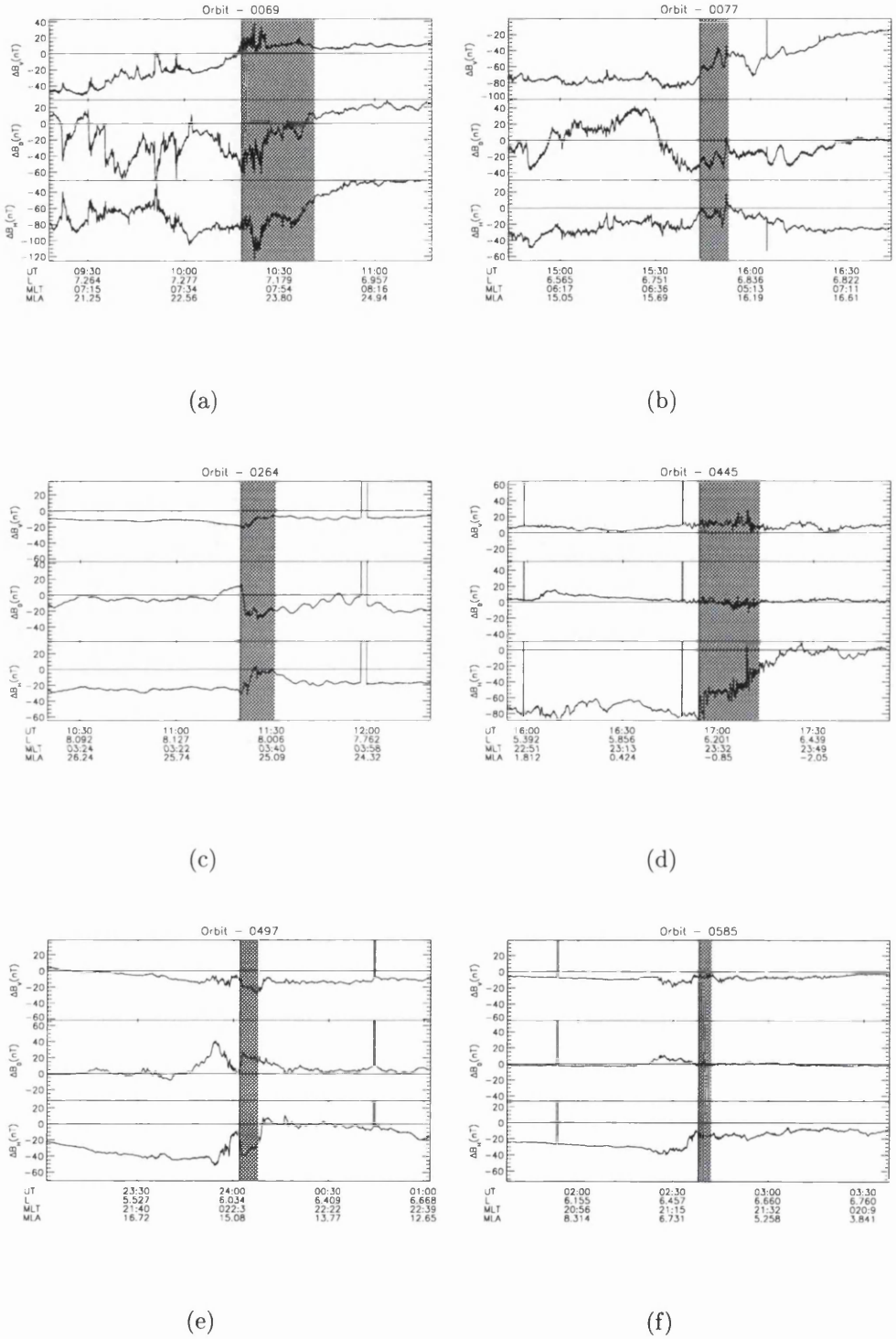

(a) (b)

(c) (d)

(e) (f)

Figure 7.6: 6 plots showing $\Delta\mathbf{B}$ in VDH co-ordinates around the time of FAEs in Orbits (a)69, (b)77, (c)264, (d)445, (e)497, and (f)585. The shaded areas indicate the durations of the FAEs.

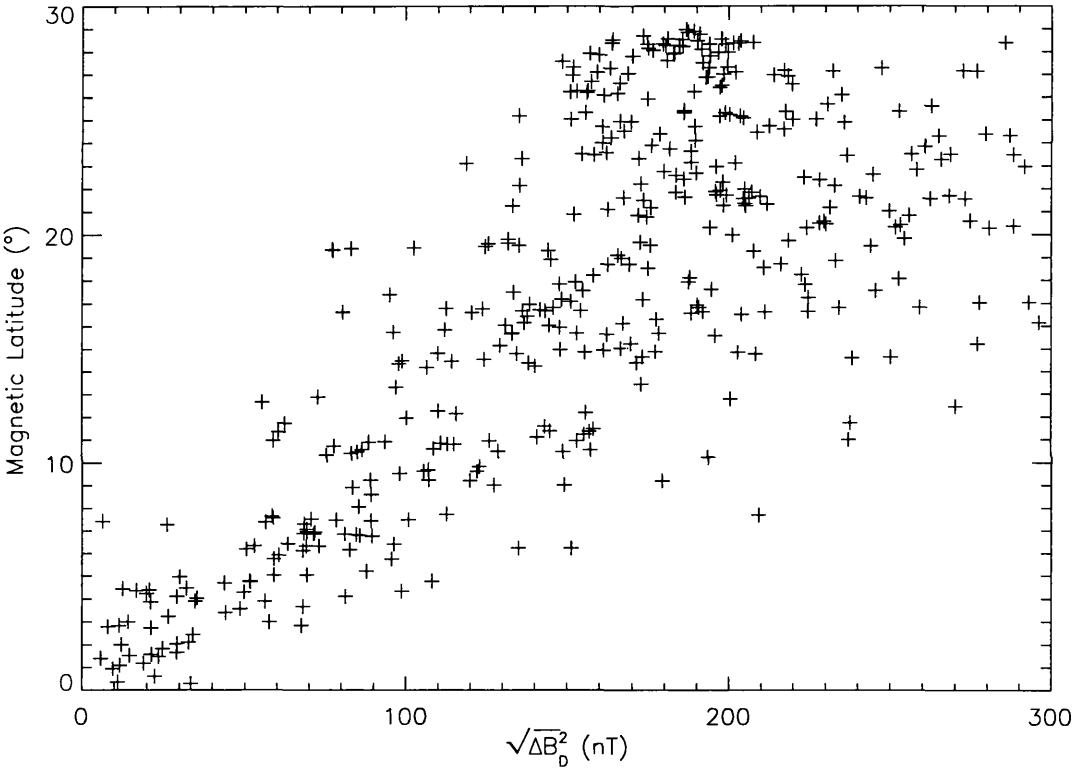

Figure 7.7: Root mean squared ΔB_D averaged over FAE lifetimes, plotted against magnetic latitude. Each cross represents a different FAE.

currents (i.e. the magnetic field is perturbed outside of the current region), an attempt has been made here to measure, directly, the field aligned component of the current density due to the electrons within the energy range of LEPA. This section describes the technique and its limitations by applying it to a situation in which we know what FACs should be present. The FAC densities are essentially estimated by subtracting the upgoing electron distribution from the downgoing one and calculating the net current in the field aligned direction. Note the ions are assumed to be much slower than the electrons and thus to make no contribution to the FAC. Due to the reduced pitch angle resolution provided with the 'full angular coverage' distribution, the FAC densities can only be estimated when LEPA is operating in a mode where it returns the three planar distributions. It is also possible to calculate the error in this current estimate from Poisson errors, which can be used quite effectively to show when the current estimates are significant. What we are estimating is the current density due to the electrons in the energy range detected by LEPA, any current carried by < 100 eV electrons will not be included.

In order to verify the technique, the FAC densities associated with some of the pancake distributions studied by *Meredith et al.*, 1999., have been estimated. It is thought that pancake distributions are formed as electrons diffuse into the loss cone through wave-particle interactions with either ECH or whistler mode waves in the equatorial regions of the magnetosphere. The result is a quasi-stable distribution peaked at 90°, with contours in the distribution function lying along the diffusion curves. As electrons are continually scattered into the loss cone and then lost to the atmosphere there is a net flow of electrons towards the Earth, i.e. the downgoing loss cone is full, and the upcoming one is empty, and hence a net current flows out of the ionosphere towards the equator.

It must be remembered that the distribution from which the current density is estimated is not collected simultaneously. In the case of pancake distributions this

fact will probably have little or no consequence as the electron distribution is changing sufficiently slowly that differences on the time scale of a spin are minimal. Also, the peak of the electron distribution occurs around a pitch angle of 90°. The near 90° pitch angles will be collected as a combination of the 90° distribution and the symmetry plane distribution. As it is the parts of the symmetry plane distribution near 90° that will be used, and these are taken at nearly the same time, the distribution will have had very little time to evolve during the time that the highest fluxes are measured. In the case of FAEs the majority of electrons occupy pitch angles near to 0° and 180°. The two sets of pitch angle data, near 0° and 180°, are composed mainly of the two loss cone distributions, which are taken around 15 seconds apart. The peak fluxes may also be contained within some of the symmetry plane distribution (see Section 3.4.2). If so, the parts of the symmetry plane distribution used will also be taken nearly 15 seconds apart. The fact that the 0° pitch angle electrons are measured some time apart from the 180° pitch angle electrons, combined with the fact that an FAE distribution is often changing on time scales of the order of a spin (30 seconds), means that some component of the calculated current density may be due to a change in the electron flux within 15 seconds. Thus, a continually decreasing (or increasing) flux may be interpreted as a steady net current. It is hard to gauge the scale of this effect as it is virtually impossible to separate any difference in upcoming and downgoing fluxes from a temporal change in the fluxes.

Figure 7.8 shows a LEPA survey plot for Orbit 426. This plot shows a fairly steady electron distribution, peaked at 90° throughout the orbit, with an injection at 23:50 UT. The electron fluxes then decrease, forming a quasi-stable pancake distribution. Around 02:40 UT the electron fluxes disappear as CRRES enters the plasmasphere. CRRES crosses the magnetic equator at 02:17 UT from north to south. It is thus expected that prior to 02:17 UT there will be a negative current measured, and following 02:17 UT there will be a positive one. It was difficult to find an ex-

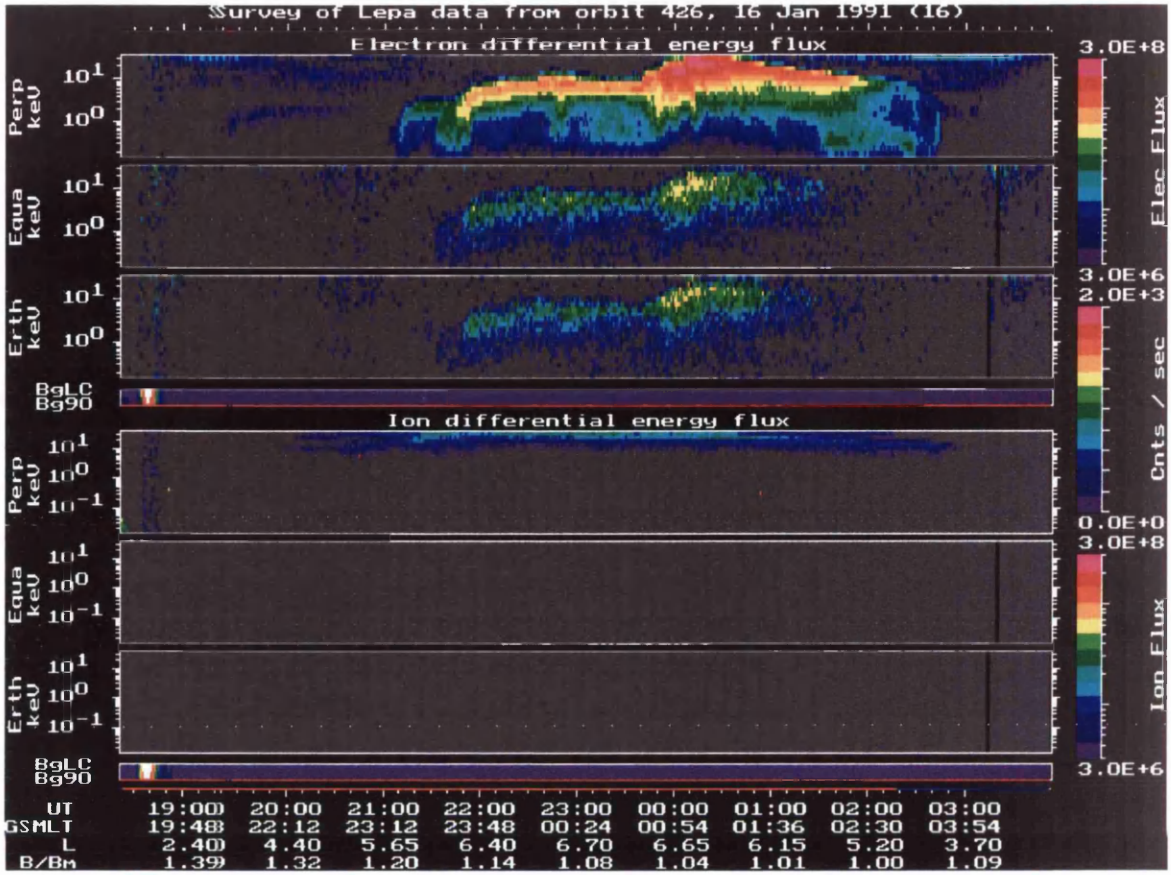

Figure 7.8: LEPA survey plot illustrating an electron pancake distribution on Orbit 426. The form of the plot is described on Page 83

ample where considerable fluxes of electrons have been injected, had enough time to reach a quasi-stable distribution, CRRES crosses the equator, remains outside of the plasmasphere, and no further injections take place, though by studying a number of examples we have still managed to verify the technique.

Figure 7.9 shows the FAC density estimated from LEPA data for this orbit between 01:00 UT and 03:00 UT. The dashed line shows an envelope of 1σ errors calculated from Poisson statistics around a curve smoothed by a 9 point boxcar average. It is clear that these calculated errors reasonably accurately reflect the random fluctuations in the current density measurements. In fact 57% of the values lie within this envelope compared to 68.3% that would be expected statistically if all variations from the

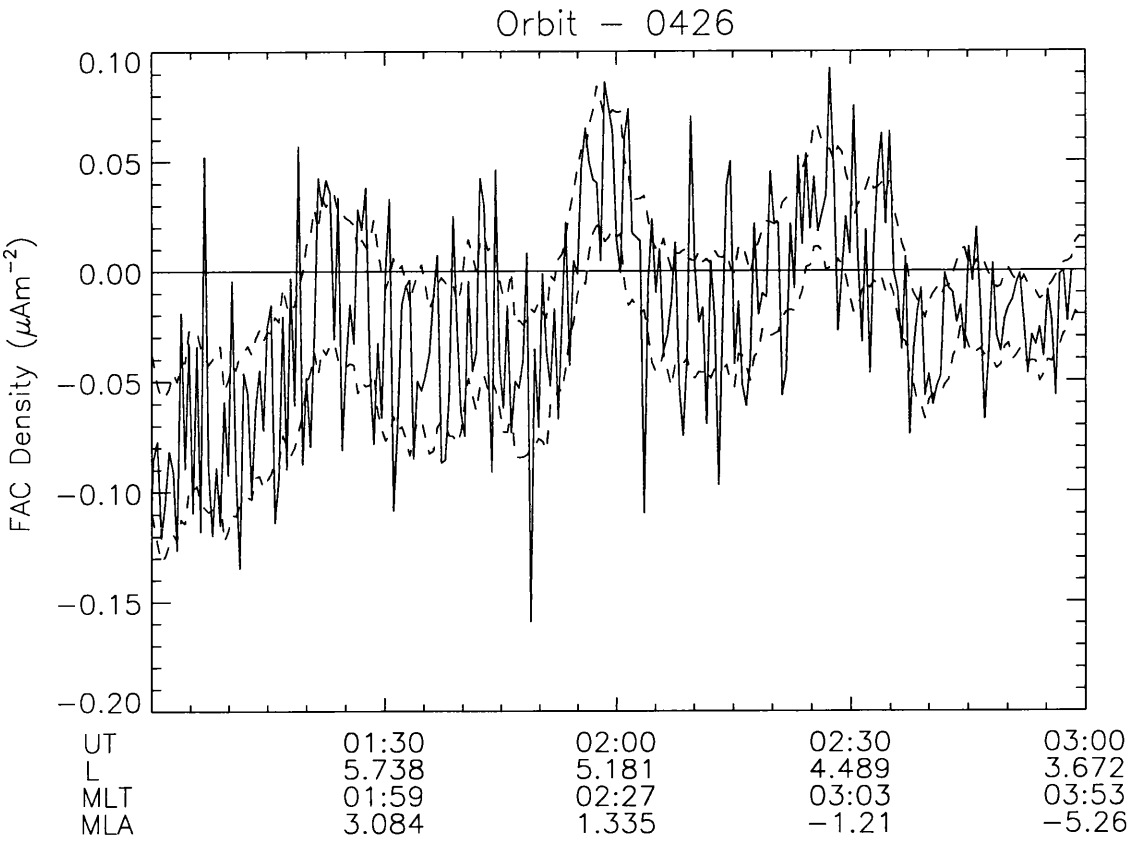

Figure 7.9: The field aligned current density estimated from the LEPA data for an equatorial crossing on Orbit 426. The equatorial crossing occurs at 02:17 UT. The dashed line shows an envelope of 1σ Poisson errors around a 9 point smoothed curve.

smoothed curve were due to Poisson errors.

Figure 7.10 shows the curve in Figure 7.9 smoothed by a 9 point boxcar average. Here we can see an initially negative current density, which decreases reaching zero near the equatorial crossing. Following the equatorial crossing the current density remains near zero presumably due to CRRES moving to lower L values and entering the plasmasphere around 02:40 UT.

The most evident feature in Figure 7.10 is a quasi-periodic signal in the estimated FAC density. This appears to be an instrumental effect. The vertical lines in Figure 7.10 indicate when the magnetic field direction moved from one coarse zone to

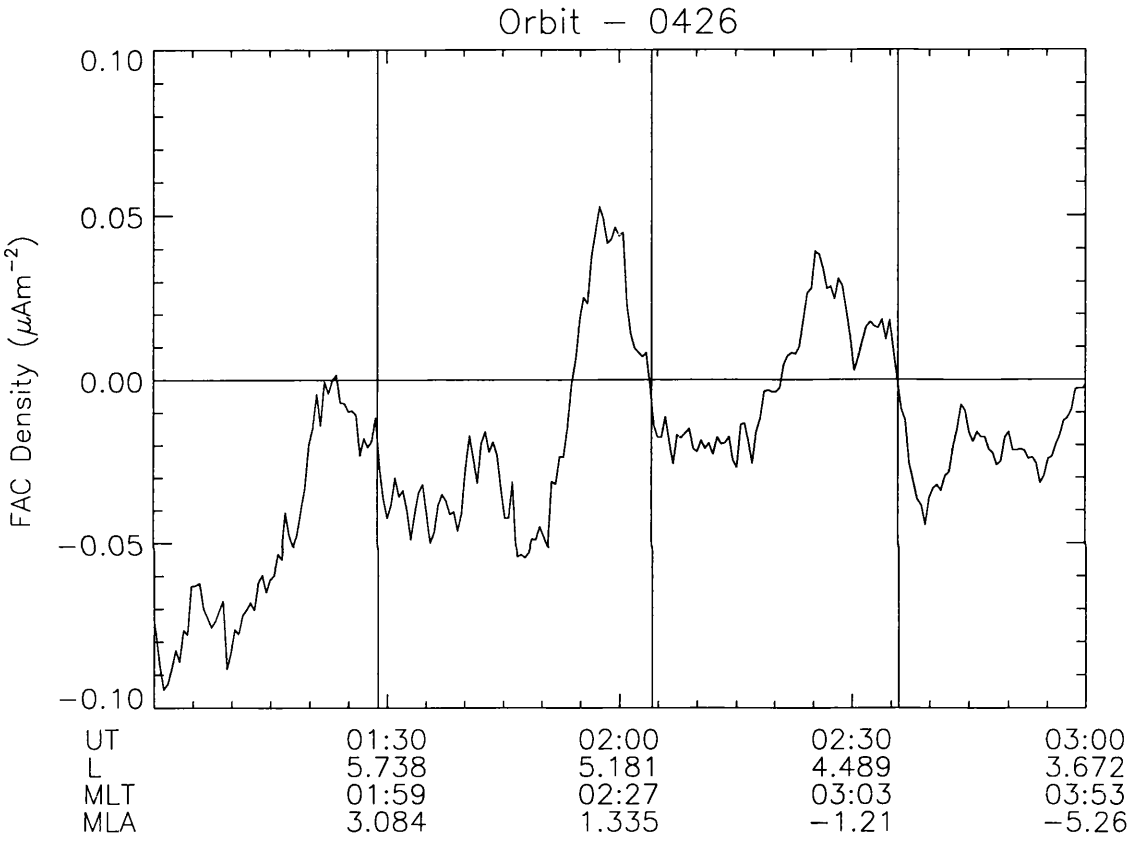

Figure 7.10: The field aligned current density estimated from the LEPA data, smoothed using a 9 point boxcar average, for an equatorial crossing on Orbit 426. The equatorial crossing occurs at 02:17 UT. Entry into the plasmasphere occurs at 02:40 UT The vertical lines indicate when the magnetic field direction moved from coarse zone to an adjacent one.

an adjacent one. During this time period the magnetic field changes in a smooth way. It seems that somehow (though we do not know how) the electron distribution collected, and in turn the estimated FAC density, depends on where the magnetic field direction lies within a detector coarse zone anode. The order of magnitude of the quasi-periodic effect is around $0.05\mu\text{Am}^{-2}$.

We have studied further examples of equatorial crossings with pancake distributions and suggest that the FAC densities associated with pancake distributions are measurable through this technique, or at least the direction can be confirmed. There are a number of considerations that must be borne in mind when examining this data. These are summarised below;

- Random fluctuations associated with Poisson errors are present.
- Variations in the estimated current densities occur due to the relative position of the magnetic field within the detector zone it lies within.
- The distribution from which the current density is calculated is not measured instantaneously, but is built up over a spin (30 seconds). Therefore, more quickly varying currents will not be well measured. The exact way in which the distribution is collected depends on the orientation of the magnetic field with respect to the spacecraft (see Section 3.4.2)

The three points listed above may have different significance when we apply our FAC density estimation technique to FAEs. We have shown above that the Poisson errors in the estimated FAC density can be calculated reasonably accurately for a pancake distribution and we expect the same to be true during an FAE. During an FAE the magnetic field direction does not change smoothly and may change by a few degrees in a spin. We therefore do not expect the variations in the estimated current density that occur due to the relative position of the magnetic field within the detector zones to always take on a quasi-periodic form. The best we can say is

that the fluxes during an FAE are similar to those seen in Figure 7.10 and that we would expect the variations of the estimated FAC density due to this effect to be of the same order ($0.05\mu\text{Am}^{-2}$). The third point, as mentioned above, may seriously affect our estimation of FAC densities at the time of FAEs due to the temporal variability seen in FAEs.

7.6 Estimated FACs at the time of FAEs

Figure 7.11 shows the FAC density estimated from the LEPA data around the time of the six FAEs for which the magnetic field data is shown in Figure 7.6. The shaded areas indicate the times when FAEs are seen. The dashed line shows an envelope of 1σ errors calculated from Poisson statistics around a curve smoothed by a 9 point boxcar average. As a guide to the significance of these current density values, they can be compared to values found by *Nakai et al.*, 1997, shown in Figure 7.5. The average FAC densities were found by *Nakai et al.*, 1997, to be of the order 1 nAm^{-2}, which is 2 orders of magnitude smaller than the typical current densities seen in our estimates around the time of FAEs.

As in Figure 7.9 (pancake case) the Poisson noise calculations explain most high frequency, low amplitude fluctuations throughout the plots in Figure 7.11 (FAEs). Comparing the six events two consistent features emerge. Firstly four of the events (during Orbits 69, 77, 497, and 585) show some amount of net current (i.e. the Poisson noise envelope does not include zero) during or following the event. The Orbit 445 event occurs near the magnetic equator and so would not be expected to show any net current. Only the Orbit 264 event shows no net current when we might expect to see some. Secondly, with the possible exception of Orbit 77 which has some large oscillations throughout, oscillations are seen in the estimated FAC density which are larger than the spread expected due to Poisson noise. These large oscillations are

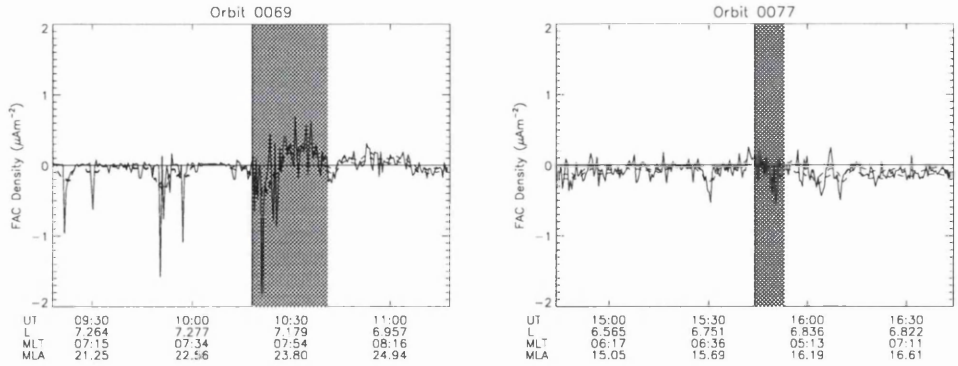

(a)

(b)

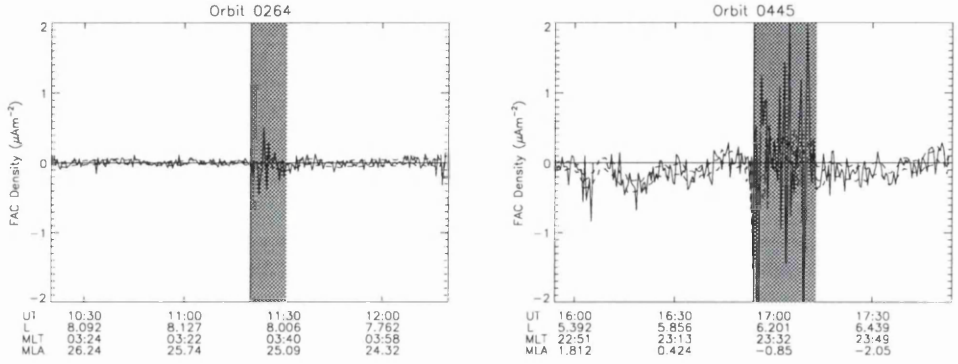

(c)

(d)

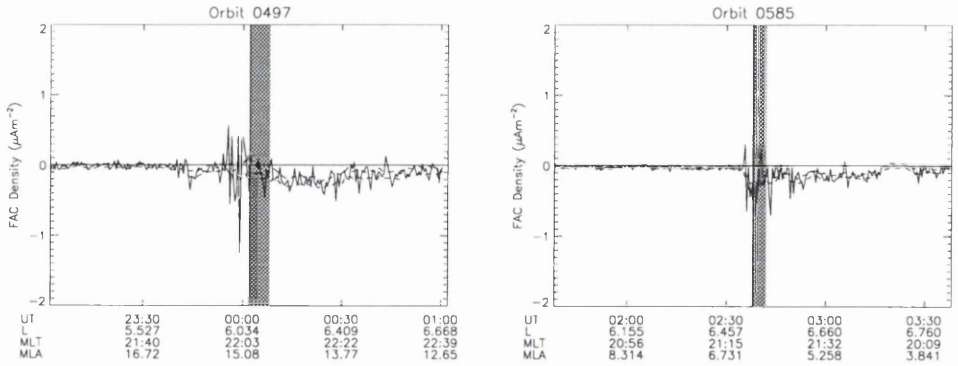

(e)

(f)

Figure 7.11: Six plots showing the FAC density calculated from the LEPA data around the time of FAEs in Orbits (a)69, (b)77, (c)264, (d)445, (e)497, and (f)585. The shaded areas indicate the durations of the FAEs. All 6 plots are of the same form as Figure 7.9

seen immediately the FAEs start on Orbit 69, 264 and 445, and just prior to the start of the FAE on Orbits 497 and 585 .

While it is hard to directly compare the estimated FAC density with the magnetic field variations, we would expect that the estimated FAC density would show a similar dependence on magnetic latitude. Figure 7.12 shows the estimated FAC density averaged over the duration of each FAE plotted against magnetic latitude. The clear relation seen in Figure 7.7, where ΔB_D increased as magnetic latitude increased, cannot be seen in Figure 7.12. In fact, if anything the opposite is true with the strongest estimated currents seen nearer the equator. From this we conclude that our current density estimation is not measuring the true current density at the time of FAEs. The fact that the strongest estimated current densities are not seen during the FAEs (see Figure 7.9 indicates that currents are not due to the electron beams. Instead, we suggest that these are a manifestation of the steady overall decrease in electron fluxes following the initial injection.

As we do not generally believe that our estimated FAC density at the time of FAEs represents the true FAC density, there is little reason to suspect that the large amplitude high frequency oscillatory FAC density seen in our estimate is real. Similar frequency oscillations are, however, often seen in the magnetic field data. We have performed a more detailed analysis of these oscillations by filtering the estimated FAC density and the magnetic field data data for periods in the range 30 -100 seconds (not presented here), and found that it is hard to relate the oscillations in the estimated FAC density to those in the magnetic field or either type of oscillation to the presence of an FAE.

While the FAC density estimations from LEPA data suffer from uncertainties due to temporal resolution, other current and future missions may have suitable temporal resolution to overcome these. Ideally measurements should be made of the upgoing and downgoing populations simultaneously as has been done on a number of low

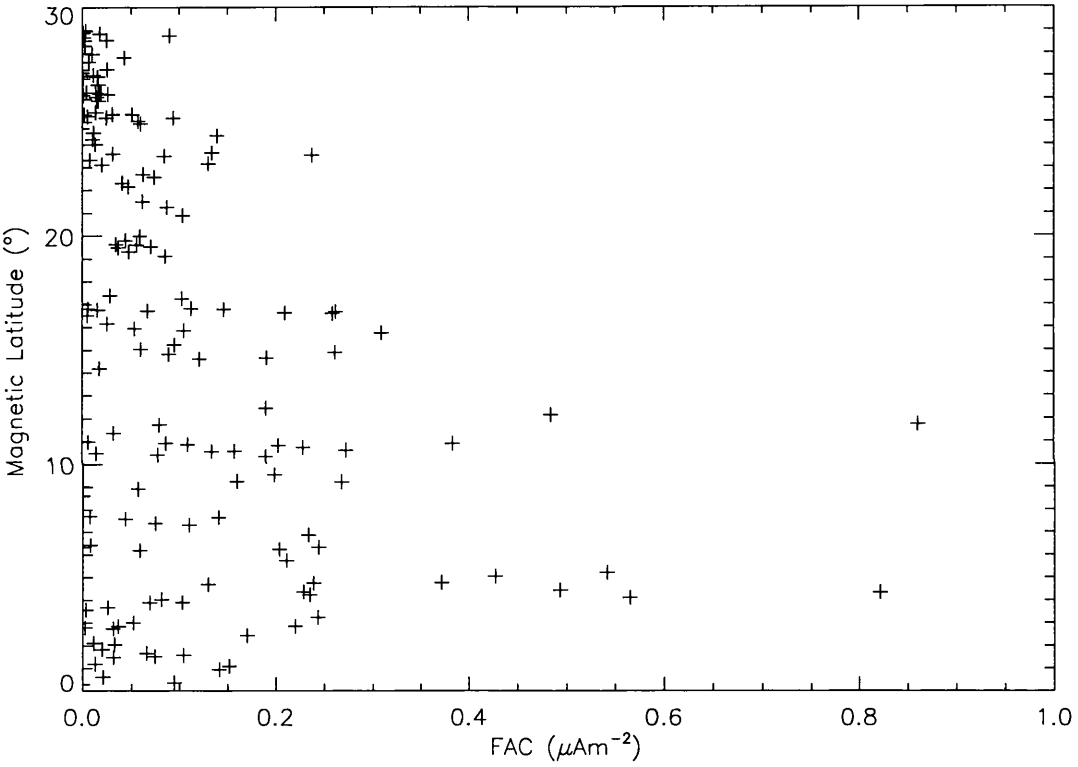

Figure 7.12: Current density estimated from LEPA data averaged over FAE lifetimes, and plotted against magnetic latitude. Each cross represents a different FAE.

altitude spacecraft. It is hoped that the Plasma Electron And Current Experiment (PEACE) [*Johnstone et al.*, 1997] to be flown on the Cluster II mission will be able to do this, and that the data may resolve some of the arguments presented here.

7.7 Summary

- Observations of field aligned electron distributions at high latitudes have been made by a number of spacecraft, over a wide range of altitudes (1700 km - $2R_E$). The beams are seen either upgoing, downgoing or counterstreaming and over a variety of energies. Often the electron beams are coincident with ion conics. Authors generally relate the electron beams to the Region 1 and Region 2 FACs.

- Detailed observations by the FAST spacecraft suggest that the upgoing electron beams are accelerated by diverging quasi-static electrostatic shocks related to the inverse aurora. We have suggested that these low altitude electron beam observations represent the source of the FAEs detailed in this thesis, and that the FAEs carry current in the FAC systems within the magnetosphere.

- The strong correlation between AE index and the occurrence rate of FAEs strengthens the link between FAEs and the magnetospheric current system. The relation is not however linear, with the occurrence rate of FAEs increasing roughly exponentially with AE index. We have suggested that this may be related to an increase in the width of the auroral zone at times of high AE index, volume of the magnetospher in which FAEs are present, and increasing the probability of observing FAEs.

- There are similarities between the distribution of FAEs seen by CRRES and the average FACs seen on the nightside, again strengthening the link between

FAEs and FACs.

- The ability to estimate FAC density from the LEPA data set has been demonstrated by applying the technique to a 'pancake' distribution seen around the time of an equatorial crossing. The example also demonstrated that the calculated Poisson errors reasonably explain the high frequency low amplitude random fluctuations seen in the estimated current density. A periodic signature in the calculated FAC revealed that there is a problem with the technique associated with relative position of the magnetic field direction within a detector anode.

- Our current density estimates at the time of FAEs are not consistent with the magnetic field data. The perturbations in the magnetic field due to FACs increase with increasing magnetic latitude, whereas this is not seen in our estimated FAC density. We conclude that due to the nature of the electron distribution (i.e. it is peaked at 0° and 180° pitch angle and varies rapidly) we cannot apply our FAC density estimate at the time of FAEs.

- Variations consistent with filamentary FACs (such as may exist within the substorm current wedge) are often seen in the D component of the magnetic field around the time of FAEs.

Chapter 8

Conclusions and Future Work

8.1 Conclusions

The FAEs presented here are undoubtedly the same phenomenon as those seen by a number of previous missions (such as ATS-6 and AMPTE/CCE) to the equatorial regions of the magnetosphere. We believe that the LEPA instrumentation has produced the best resolution observations yet of these results in terms of pitch angle and energy, and enabled us to make the most reliable survey of the distribution of events (within the sampling limitations imposed by the orbit of CRRES) to date. The results presented here represent the most complete survey of FAEs made with the LEPA data set. Also this thesis contains the first pitch angle distributions at the time of FAEs produced with a proper correction for the the onboard processing error described in Section 3.4.2. We have built up a picture of the FAEs and their possible role within the magnetospheric system and so we propose a model as follows.

We believe that the FAEs are the equatorial manifestation of the field aligned beams of electrons, such as those seen by the FAST satellite, which occur at high latitudes in association with aurorae. These beams are thought to ionospheric in origin, and accelerated by diverging electrostatic shocks associated with inverse aurora.

The high latitude beams are carriers of significant field aligned current away from the auroral region. The relation between FAEs and auroral features is supported by the facts that FAEs are seen on auroral field lines. Furthermore the distribution of FAE durations with orbital radius are consistent with FAEs having a limited radial extent which, when mapped to the ionosphere, corresponds to features of similar size to auroral arc systems (0.3-3km). Multiple FAEs are consistent with CRRES crossing field lines mapping to multiple arcs.

We have shown that FAEs are predominantly a substorm related phenomenon and as such we suggest that they form part of the substorm current wedge and the Region-1 and Region-2 current systems. The substorm current is only seen during substorms, and the Region-1 and Region-2 currents are enhanced during substorms. The connection between FAEs and FACs is supported by the high correlation between the observation frequency of FAEs and the AE index, which is a direct indication of the current flowing in the auroral electrojet. The correlation between AE index and the observation frequency of FAEs extends to low (< 150 nT) values of the AE index, which we take as an indication that FAEs are related to quiet time FACs as well as FACs seen at substorm times. The connection with the substorm current wedge is supported by the the fact that signatures in the magnetic field perturbations at the time of FAEs often suggest filamentary FACs, which *Maynard et al.*, 1996, suggested form part of the substorm current wedge.

We have attempted to directly measure the FAC density at the time of FAEs directly from the LEPA electron data. While the indications are that this technique can provide meaningful results when the electron distribution changes slowly compared the sampling period, we do not find that this is so during the active times when FAEs are seen.

We have presented observations of electrons being scattered out of the field aligned beam, by what seems to be a wave-particle interaction. At the same time as being

scattered to larger pitch angles the electrons are accelerated, typically resulting in an increase of energy by a factor of around ten, though the amount of energisation is highly variable. The pitch angle scattering and energisation of electrons appears to be common, with only a few events where scattering takes place with no energisation, or no scattering takes place at all.

We suggest that the scattering and acceleration of field aligned electrons may be caused by either the whistler mode or ECH mode waves seen by the PWE at the time of FAEs. The wave intensity seen by the PWE is always high in the whistler and ECH frequency bands at the time of FAEs, probably due to the high electron fluxes also seen around the time of FAEs. Comparisons between wave power and the acceleration seen in the FAEs give no insight into a responsible wave mode, though the short lifetime of FAEs and the low sampling frequency of wave power severely hinders this sort of analysis.

The scattering path of electrons seen at the time of energised FAEs cannot be described by the theoretical diffusion curves suggested by *Summers et al.*, 1998, for resonant interaction with whistler mode waves, unless the scattering were to take place in a region around 20° - 40° away from the geomagnetic equator. However, other features of the observations do not support the idea that diffusion along *Summers et al.*, 1998, type curves taking is place at mid-latitudes.

We suggest that the single electron component cold plasma dispersion relation, which is the basis of the diffusion curves suggested by *Summers et al.*, 1998, is not valid at the time of FAEs. We have suggested a more realistic dispersion relation which includes two cold beam components, and demonstrated that it is significantly different from the cold plasma approximation near to and above a frequency resonant with the electron beams. Our dispersion relation turns Complex at frequencies which are close to resonance with the electron beams implying a transfer of energy between the waves and the beam electrons. It is possible that this transfer of energy could

be responsible for the acceleration of the field aligned electrons. While we have not been able to calculate the diffusion paths relating to our new dispersion relation, we expect them to be different from those calculated using the cold plasma dispersion relation.

8.2 Future Work

In this thesis we have made a number of proposals regarding the nature of FAEs, some of which are better supported than others. In some cases, avenues of investigation are currently open e.g. the connection we have made between FAEs and substorms could be investigated further by studying the magnetic field signatures at the footpoints of the field lines FAEs are observed on. In most cases, however, we await results from current or future missions, or advances in the relevant theory.

Results from the FAST and Astrid-2 satellites should, in the near future, provide spatial and temporal occurrence distributions of the field aligned beams at high altitudes. These distributions can then be compared to the distributions of FAEs seen be CRRES and will help to clarify the link between the two phenomena. Missions such as Cluster II may provide observations of FAEs at mid latitudes, providing the missing link between the high altitude beams and the equatorial FAEs. Future missions may also be able to make better measurements of the FAC density direct from the electron population again increasing our understanding.

Perhaps the area we have touched upon which provides the most scope for future work is that of the resonant diffusion curves. The immediate step is to try and solve the dispersion relation suggested in Section 6.3.2 for ω, which will allow us to apply the solution to the relevant diffusion curve equations (for both $v_\perp$ and $v_\parallel$). More importantly we will have a solution for the dispersion relation in the complex region and will be able to produce diffusion curves in this region. Further progress may

be made by developing more realistic dispersion relations taking into account the thermal spread in the various component populations. At this time diffusion curves have only been calculated for parallel propagating whistler mode waves. The analysis needs to be extended to oblique propagating whistler mode waves, and to the more complicated problem of the ECH waves.

8.3 Final Word

The ionosphere has in the past been thought of, by many researchers, simply as having a passive role in substorm dynamics and it is only now with the advent of very high time and spatial resolution measurements made by a new generation of spacecraft (such as FAST and Astrid-2) that this view is being questioned. Recent studies [e.g. *Newell*, 1998] are indicating that aurora are suppressed by sunlight as the conductivity in the ionosphere changes, and in retrospect it is not surprising that the current systems flowing in the magnetosphere should change also.

So it seems that the upwardly accelerated electron beams (which we now believe to be the source of the FAEs seen by CRRES) may play an important role linking the ionosphere to the magnetosphere by the way of FACs. It is only by studying and understanding these beams and the associated FAEs, throughout the magnetosphere, that their true role in the magnetospheric system can be discovered.

Appendix A

LEPA energy channels

Channel Number	Low Energy Bound (keV)	High Energy Bound (keV)	Channel Number	Low Energy Bound (keV)	High Energy Bound (keV)
00	28.47	21.69	15	0.48	0.37
01	21.69	16.53	16	0.37	0.28
02	16.53	12.59	17	0.28	0.21
03	12.59	9.60	18	0.21	0.163
04	9.60	7.31	19	0.163	0.124
05	7.31	5.57	20	0.124	0.094
06	5.57	4.25	21	0.094	0.072
07	4.25	3.24	22	0.072	0.055
08	3.24	2.47	23	0.055	0.042
09	2.47	1.88	24	0.042	0.032
10	1.88	1.43	25	0.032	0.024
11	1.43	1.09	26	0.024	0.018
12	1.09	0.83	27	0.018	0.014
13	0.83	0.63	28	0.014	0.011
14	0.63	0.48	29	0.011	0.008

Table A.1: LEPA energy channels when operated over the unattenuated range. (Note, Lepa was not sensitive in the lowest 10 energy channels.)

Channel Number	Low Energy Bound (keV)	High Energy Bound (keV)	Channel Number	Low Energy Bound (keV)	High Energy Bound (keV)
00	19.68	15.03	15	0.35	0.26
01	15.03	11.49	16	0.26	0.20
02	11.49	8.77	17	0.20	0.155
03	8.77	6.70	18	0.155	0.118
04	6.70	5.12	19	0.118	0.090
05	5.12	3.91	20	0.090	0.069
06	3.91	2.99	21	0.069	0.053
07	2.99	2.28	22	0.053	0.040
08	2.28	1.74	23	0.040	0.031
09	1.74	1.33	24	0.031	0.023
10	1.33	1.02	25	0.023	0.018
11	1.02	0.78	26	0.018	0.014
12	0.78	0.59	27	0.014	0.010
13	0.59	0.45	28	0.010	0.0080
14	0.45	0.35	29	0.0080	0.0061

Table A.2: LEPA energy channels when operated over the attenuated range. (Note, Lepa was not sensitive in the lowest 10 energy channels.)

Appendix B

List of FAEs

Orbit Number	UT	L-shell (R_E)	MLT	Magnetic Latitude (°)	Duration (Mins)	Type
0066	02:38	6.20	06:00	2.7368	07	Substorm
0067	11:00	5.70	05:00	15.366	04	Substorm
0067	11:13	5.96	05:00	16.162	01	Dropout
0067	11:56	6.65	06:00	18.295	05	Dropout
0067	12:17	6.90	06:00	19.133	02	Substorm
0067	14:06	7.36	07:00	22.258	25	Substorm
0067	15:08	6.96	08:00	23.637	08	Substorm
0069	08:12	6.78	06:00	17.380	43	Dropout
0069	08:59	7.14	06:00	19.794	01	Dropout
0069	09:22	7.24	07:00	20.884	03	Dropout
0069	09:30	7.26	07:00	21.251	29	Dropout
0069	10:12	7.24	07:00	23.113	01	Dropout
0069	10:18	7.23	07:00	23.318	23	Dropout
0070	18:10	6.24	06:00	6.9480	07	Substorm
0070	19:31	6.36	07:00	8.3667	01	Substorm
0070	19:34	6.36	07:00	8.4128	04	Substorm
0071	03:42	6.17	06:00	5.7357	02	Other
0076	07:59	6.38	08:00	19.107	13	Substorm
0077	13:47	5.65	05:00	12.450	18	Other
0077	15:44	6.80	06:00	15.944	09	Substorm
0087	17:22	6.10	05:00	7.9170	05	Substorm
0088	02:07	5.31	05:00	2.4410	06	Substorm
0106	12:53	7.02	05:00	20.586	02	Dropout

Table B.1 : List of FAEs as observed by the LEPA on CRRES

Orbit Number	UT	L-shell (R_E)	MLT	Magnetic Latitude (°)	Duration (Mins)	Type
0106	12:58	7.07	05:00	20.711	08	Dropout
0106	13:22	7.25	06:00	21.241	01	Dropout
0106	13:29	7.28	06:00	21.375	01	Dropout
0106	13:47	7.35	06:00	21.684	05	Dropout
0106	14:19	7.37	06:00	22.133	03	Dropout
0106	15:13	7.14	07:00	22.708	04	Other
0106	15:38	6.90	07:00	22.944	02	Other
0116	14:00	5.27	04:00	11.569	02	Substorm
0125	08:12	7.26	05:00	23.057	03	Substorm
0133	14:46	6.41	05:00	15.650	09	Dropout
0133	15:09	6.60	05:00	16.039	03	Dropout
0133	15:39	6.76	05:00	16.366	01	Dropout
0133	15:51	6.80	05:00	16.453	03	Dropout
0133	15:59	6.82	05:00	16.500	07	Dropout
0142	08:55	7.92	05:00	26.231	08	Other
0169	09:22	7.36	04:00	25.677	08	Other
0175	23:00	6.33	05:00	7.3933	02	Substorm
0175	23:18	6.24	05:00	7.5771	04	Substorm
0176	09:17	7.94	05:00	28.325	01	Dropout
0176	09:50	7.61	06:00	28.558	03	Other
0184	13:19	6.61	03:00	19.306	02	Other
0184	13:34	6.77	04:00	19.479	02	Other
0184	13:41	6.84	04:00	19.535	02	Other
0184	13:54	6.94	04:00	19.606	01	Other
0184	14:01	6.98	04:00	19.626	03	Other
0185	22:37	5.56	03:00	6.1884	06	Other
0185	01:19	6.53	05:00	10.971	11	Substorm
0185	01:39	6.47	05:00	11.356	13	Substorm
0185	02:02	6.35	05:00	11.727	01	Substorm
0185	02:58	5.78	06:00	12.148	04	Substorm
0186	07:20	4.81	02:00	21.693	03	Dropout
0186	07:34	5.34	02:00	22.877	02	Dropout
0186	07:41	5.58	02:00	23.376	02	Dropout
0186	08:08	6.43	03:00	24.890	06	Dropout
0186	09:25	7.96	04:00	27.271	05	Dropout
0186	09:53	8.23	04:00	27.727	02	Dropout
0190	01:36	6.63	04:00	12.720	07	Other
0190	01:47	6.66	04:00	13.033	02	Other
0191	11:39	8.10	04:00	26.518	06	Dropout
0198	07:54	8.09	04:00	27.752	06	Dropout
0198	08:10	8.25	04:00	28.059	14	Dropout
0198	08:30	8.38	04:00	28.380	09	Dropout

Table B.1 continued : List of FAEs as observed by the LEPA on CRRES

Orbit Number	UT	L-shell (R_E)	MLT	Magnetic Latitude (°)	Duration (Mins)	Type
0198	08:42	8.43	04:00	28.541	04	Dropout
0198	08:56	8.46	04:00	28.702	05	Dropout
0198	09:14	8.45	04:00	28.863	03	Dropout
0198	09:26	8.42	05:00	28.943	03	Dropout
0198	09:34	8.38	05:00	28.983	05	Dropout
0198	09:55	8.25	05:00	29.042	02	Dropout
0198	10:02	8.20	05:00	29.045	03	Dropout
0198	10:07	8.15	05:00	29.042	06	Dropout
0208	08:45	6.06	02:00	24.706	02	Substorm
0208	09:14	6.88	03:00	25.840	04	Dropout
0208	09:56	7.70	03:00	26.738	09	Substorm
0208	10:16	7.96	03:00	26.963	03	Dropout
0208	10:22	8.02	03:00	27.010	05	Dropout
0208	10:32	8.10	03:00	27.070	02	Dropout
0208	10:37	8.13	04:00	27.092	01	Dropout
0218	11:47	6.19	02:00	20.896	02	Sharp Onset
0219	00:08	6.58	04:00	10.335	02	Substorm
0219	00:14	6.57	04:00	10.410	03	Substorm
0219	00:19	6.56	04:00	10.469	04	Substorm
0219	00:28	6.54	04:00	10.568	09	Substorm
0219	00:45	6.47	04:00	10.727	01	Substorm
0219	01:27	6.18	05:00	10.918	01	Substorm
0219	01:40	6.05	05:00	10.899	05	Substorm
0219	01:49	5.95	05:00	10.859	03	Substorm
0219	01:55	5.88	05:00	10.815	08	Substorm
0219	02:13	5.62	05:00	10.604	07	Substorm
0234	01:12	5.55	02:00	16.810	03	Substorm
0234	01:19	5.71	02:00	17.034	02	Substorm
0234	01:26	5.85	02:00	17.250	15	Substorm
0237	09:07	8.70	03:00	28.971	03	Dropout
0237	09:24	8.66	04:00	28.895	04	Dropout
0237	09:31	8.63	04:00	28.850	02	Dropout
0237	09:42	8.57	04:00	28.765	01	Dropout
0237	09:50	8.51	04:00	28.692	04	Dropout
0237	10:01	8.41	04:00	28.574	18	Dropout
0237	10:42	7.93	04:00	27.962	01	Dropout
0237	10:50	7.81	05:00	27.809	02	Dropout
0259	07:36	6.82	02:00	27.886	04	Dropout
0259	07:45	7.08	02:00	28.060	02	Substorm
0259	08:02	7.52	02:00	28.291	01	Substorm
0261	04:00	7.10	02:00	25.170	01	Substorm

Table B.1 continued : List of FAEs as observed by the LEPA on CRRES

Orbit Number	UT	L-shell (R_E)	MLT	Magnetic Latitude (°)	Duration (Mins)	Type
0261	04:05	7.19	02:00	25.248	01	Substorm
0261	04:10	7.27	02:00	25.322	01	Other
0261	04:17	7.38	02:00	25.422	02	Other
0261	05:18	7.98	03:00	26.084	03	Dropout
0261	05:31	8.03	03:00	26.173	01	Dropout
0261	05:37	8.04	03:00	26.206	05	Dropout
0261	05:55	8.04	03:00	26.280	01	Dropout
0261	06:00	8.04	03:00	26.292	05	Dropout
0264	10:30	8.09	03:00	26.245	02	Dropout
0264	10:50	8.13	03:00	25.929	02	Dropout
0264	11:20	8.06	03:00	25.327	11	Dropout
0276	11:30	7.09	04:00	24.395	04	Dropout
0276	11:49	6.71	04:00	23.638	02	Dropout
0276	12:00	6.48	04:00	23.159	05	Dropout
0276	12:10	6.25	05:00	22.695	01	Dropout
0276	12:18	6.05	05:00	22.300	01	Dropout
0276	12:21	5.98	05:00	22.146	01	Dropout
0278	03:37	7.15	02:00	24.925	02	Dropout
0279	13:53	6.59	02:00	16.154	07	Dropout
0279	14:09	6.71	02:00	15.847	02	Dropout
0279	14:14	6.74	02:00	15.741	04	Dropout
0279	15:13	6.82	03:00	14.188	06	Dropout
0281	08:41	7.09	01:00	27.151	02	Dropout
0281	09:02	7.53	02:00	27.143	02	Dropout
0281	09:24	7.86	02:00	26.983	05	Dropout
0281	09:32	7.96	02:00	26.894	03	Dropout
0281	09:51	8.12	02:00	26.626	06	Dropout
0283	04:10	6.65	01:00	27.141	03	Dropout
0283	04:23	6.98	01:00	27.278	02	Dropout
0283	05:25	8.09	02:00	27.612	25	Dropout
0298	10:22	8.13	03:00	25.187	05	Dropout
0300	04:37	7.73	02:00	27.044	07	Dropout
0300	05:12	8.13	02:00	26.970	06	Dropout
0302	00:44	6.79	02:00	16.623	03	Substorm
0302	01:45	7.06	02:00	16.780	23	Sharp Onset
0302	02:13	7.02	03:00	16.760	06	Substorm
0302	02:26	6.96	03:00	16.720	04	Substorm
0302	02:35	6.92	03:00	16.677	03	Substorm
0302	02:47	6.84	03:00	16.599	02	Substorm
0304	18:32	4.53	00:00	7.6982	05	Substorm
0305	07:29	8.52	03:00	27.292	03	Substorm

Table B.1 continued : List of FAEs as observed by the LEPA on CRRES

Orbit Number	UT	L-shell (R_E)	MLT	Magnetic Latitude (°)	Duration (Mins)	Type
0312	03:24	7.51	02:00	23.585	02	Substorm
0312	03:49	7.66	02:00	23.527	02	Substorm
0320	09:36	7.36	01:00	24.722	02	Dropout
0320	09:44	7.44	01:00	24.526	04	Dropout
0320	09:55	7.54	01:00	24.235	03	Dropout
0320	10:03	7.59	02:00	24.009	02	Dropout
0320	10:20	7.67	02:00	23.492	04	Dropout
0322	07:07	8.32	02:00	26.237	04	Dropout
0322	07:43	7.98	03:00	25.328	03	Dropout
0322	07:53	7.86	03:00	25.038	04	Dropout
0325	10:44	6.79	01:00	21.506	01	Substorm
0414	02:10	6.66	01:00	11.139	03	Sharp Onset
0417	03:47	6.09	22:00	26.600	03	Sharp Onset
0417	05:03	7.13	14:00	23.473	01	Sharp Onset
0417	05:09	7.17	00:00	23.233	11	Substorm
0422	07:43	7.19	00:00	18.061	02	Substorm
0422	07:51	7.17	00:00	17.651	04	Substorm
0422	07:59	7.15	01:00	17.237	01	Dropout
0422	08:12	7.09	01:00	16.551	03	Dropout
0422	08:19	7.06	01:00	16.175	02	Substorm
0422	08:31	6.98	01:00	15.520	02	Substorm
0425	11:18	5.72	23:00	10.450	03	Sharp Onset
0429	05:28	7.08	01:00	16.909	04	Substorm
0431	22:35	6.09	23:00	12.838	03	Sharp Onset
0444	08:10	6.92	00:00	14.806	05	Substorm
0445	16:05	5.47	22:00	1.5727	09	Substorm
0445	16:54	6.14	23:00	-0.608	19	Substorm
0461	08:45	6.62	00:00	9.5356	04	Substorm
0461	08:55	6.54	00:00	8.9162	05	Substorm
0461	09:15	6.35	01:00	7.6503	03	Substorm
0464	11:48	6.06	23:00	3.8977	06	Substorm
0465	20:53	5.59	22:00	9.2143	04	Substorm
0465	23:46	6.67	00:00	4.4317	05	Substorm
0465	23:54	6.64	00:00	4.2348	04	Substorm
0481	11:56	6.46	23:00	0.2813	07	Substorm
0481	13:03	6.59	00:00	-3.892	20	Sharp Onset
0482	22:18	6.70	23:00	2.8342	01	Substorm
0482	22:20	6.70	23:00	2.7878	48	Substorm
0482	23:30	6.54	19:00	1.0891	08	Substorm
0482	23:55	6.35	00:00	0.3582	11	Substorm
0484	17:00	6.31	22:00	-4.361	06	Sharp Onset

Table B.1 continued : List of FAEs as observed by the LEPA on CRRES

Orbit Number	UT	L-shell (R_E)	MLT	Magnetic Latitude (°)	Duration (Mins)	Type
0484	17:50	6.63	23:00	-6.328	07	Substorm
0490	02:11	5.34	21:00	22.563	07	Sharp Onset
0494	20:39	6.70	23:00	-3.235	02	Sharp Onset
0497	23:57	5.98	22:00	15.228	03	Substorm
0497	00:01	6.04	22:00	15.033	04	Substorm
0533	19:11	6.42	22:00	-4.025	11	Substorm
0533	19:33	6.60	22:00	-4.691	12	Substorm
0533	20:41	6.76	22:00	-6.429	10	Substorm
0543	21:27	6.41	21:00	2.1037	07	Sharp Onset
0543	21:36	6.49	21:00	1.8283	08	Sharp Onset
0543	21:48	6.58	22:00	1.4833	04	Sharp Onset
0545	16:27	5.85	21:00	-6.869	07	Substorm
0545	16:36	5.99	21:00	-7.309	02	Substorm
0545	17:06	6.38	21:00	-8.605	09	Substorm
0546	03:28	6.73	22:00	9.2438	03	Sharp Onset
0547	12:40	6.30	21:00	-9.022	01	Dropout
0550	17:32	5.77	21:00	-4.749	03	Dropout
0551	02:47	5.48	20:00	14.601	03	Substorm
0551	06:09	6.60	22:00	2.8462	04	Sharp Onset
0553	01:23	6.79	22:00	4.1006	09	Substorm
0560	20:38	6.39	21:00	-0.943	01	Substorm
0560	20:46	6.46	21:00	-1.185	10	Substorm
0577	18:48	5.53	20:00	-1.665	07	Sharp Onset
0577	19:32	6.20	21:00	-3.568	03	Sharp Onset
0585	02:38	6.52	21:00	6.3311	04	Sharp Onset
0586	11:28	5.76	20:00	-10.55	06	Sharp Onset
0589	18:20	6.74	21:00	-10.98	04	Other
0589	18:35	6.83	21:00	-11.36	01	Other
0589	18:42	6.86	21:00	-11.53	04	Other
0589	19:04	6.93	21:00	-12.02	02	Other
0590	03:23	6.24	21:00	6.2286	13	Sharp Onset
0590	03:41	6.41	21:00	5.2101	01	Sharp Onset
0590	03:44	6.44	21:00	5.0438	01	Sharp Onset
0590	03:49	6.48	21:00	4.7685	06	Sharp Onset
0590	03:57	6.54	21:00	4.3326	02	Sharp Onset
0592	21:52	5.17	20:00	8.0253	03	Substorm
0592	21:57	5.26	20:00	7.6724	04	Substorm
0592	22:01	5.34	20:00	7.4035	05	Dropout
0592	22:23	5.72	20:00	6.1029	01	Dropout
0592	22:27	5.78	20:00	5.8942	03	Substorm
0593	08:48	6.12	20:00	-6.648	03	Sharp Onset
0594	20:54	6.82	22:00	-9.887	05	Substorm

Table B.1 continued : List of FAEs as observed by the LEPA on CRRES

Orbit Number	UT	L-shell (R_E)	MLT	Magnetic Latitude (°)	Duration (Mins)	Type
0594	21:02	6.79	22:00	-10.04	04	Substorm
0594	21:35	6.57	22:00	-10.72	02	Dropout
0596	12:39	4.25	19:00	-7.817	03	Other
0604	21:35	6.56	21:00	-2.039	13	Substorm
0607	00:53	4.67	19:00	11.735	01	Dropout
0608	12:02	6.18	20:00	-14.64	01	Substorm
0608	12:06	6.25	20:00	-14.88	01	Substorm
0609	22:08	6.20	20:00	1.5204	06	Sharp Onset
0609	00:50	6.53	22:00	-2.996	03	Substorm
0609	01:14	6.30	22:00	-3.670	02	Substorm
0613	13:26	6.47	20:00	-16.52	03	Sharp Onset
0613	13:32	6.56	20:00	-16.81	04	Sharp Onset
0613	14:49	7.37	21:00	-19.98	04	Substorm
0614	22:49	5.85	20:00	4.5244	03	Sharp Onset
0614	02:23	6.27	22:00	-2.769	03	Sharp Onset
0615	10:09	6.93	21:00	-14.39	05	Dropout
0623	16:30	6.94	20:00	-16.66	10	Substorm
0625	14:51	7.21	22:00	-25.37	05	Substorm
0628	18:48	7.09	21:00	-15.64	03	Dropout
0628	19:19	7.01	21:00	-16.13	03	Other
0628	19:30	6.95	21:00	-16.30	03	Dropout
0628	19:50	6.80	22:00	-16.63	03	Sharp Onset
0640	18:20	6.82	22:00	-22.62	03	Sharp Onset
0645	19:54	6.18	22:00	-20.41	04	Dropout
0645	20:02	6.02	22:00	-20.59	02	Dropout
0649	08:39	7.01	21:00	-14.96	03	Dropout
0651	04:00	6.61	20:00	-3.406	06	Dropout
0662	17:29	7.39	21:00	-21.61	03	Other
0662	17:56	7.21	21:00	-21.93	02	Other
0662	18:01	7.16	21:00	-21.99	02	Other
0666	07:41	6.94	20:00	-14.23	04	Substorm
0666	07:54	6.99	20:00	-14.86	03	Substorm
0666	08:00	7.01	21:00	-15.15	01	Substorm
0668	03:32	6.67	20:00	-4.774	02	Dropout
0670	00:28	6.43	21:00	-6.318	04	Substorm
0671	07:01	5.98	19:00	-12.19	07	Other
0671	08:32	7.08	20:00	-17.07	01	Other
0671	08:34	7.09	20:00	-17.17	07	Other
0671	08:42	7.15	20:00	-17.55	02	Other
0671	08:48	7.19	20:00	-17.83	03	Other
0671	09:26	7.35	21:00	-19.53	01	Other

Table B.1 continued : List of FAEs as observed by the LEPA on CRRES

Orbit Number	UT	L-shell (R_E)	MLT	Magnetic Latitude (°)	Duration (Mins)	Type
0671	09:29	7.36	21:00	-19.66	04	Other
0672	17:56	6.79	20:00	-14.79	05	Substorm
0673	04:05	6.57	20:00	-5.749	03	Other
0673	05:00	6.69	21:00	-8.070	04	Dropout
0675	23:01	6.30	19:00	-1.994	02	Dropout
0675	23:37	6.56	20:00	-3.000	05	Substorm
0675	00:32	6.69	20:00	-4.294	01	Sharp Onset
0675	00:36	6.69	20:00	-4.382	02	Other
0675	00:40	6.68	20:00	-4.468	03	Other
0676	09:04	6.98	20:00	-18.71	12	Substorm
0677	19:18	6.76	20:00	-11.96	04	Sharp Onset
0678	04:50	6.46	20:00	-7.734	01	Sharp Onset
0679	14:05	6.84	19:00	-21.27	03	Substorm
0679	14:18	7.01	19:00	-21.66	03	Substorm
0679	14:26	7.11	19:00	-21.88	02	Substorm
0679	14:49	7.36	20:00	-22.43	06	Substorm
0679	17:08	7.33	21:00	-24.30	04	Dropout
0679	17:17	7.22	21:00	-24.38	02	Dropout
0680	02:44	6.36	21:00	-5.923	03	Sharp Onset
0680	02:53	6.28	21:00	-6.125	03	Other
0681	10:14	7.25	20:00	-21.63	03	Dropout
0683	05:19	6.16	19:00	-9.247	02	Substorm
0683	05:26	6.24	19:00	-9.619	02	Substorm
0683	05:30	6.29	19:00	-9.829	04	Substorm
0684	15:09	6.67	19:00	-19.50	02	Substorm
0685	02:01	6.56	20:00	-3.868	03	Sharp Onset
0685	02:08	6.59	20:00	-4.105	01	Sharp Onset
0685	02:34	6.65	20:00	-4.955	03	Sharp Onset
0685	04:03	6.24	21:00	-7.484	06	Sharp Onset
0688	08:12	7.19	20:00	-17.93	02	Substorm
0688	08:19	7.21	20:00	-18.22	07	Substorm
0688	08:31	7.23	20:00	-18.70	02	Substorm
0688	08:38	7.23	21:00	-18.97	01	Substorm
0710	09:07	7.38	20:00	-21.74	01	Dropout
0710	09:11	7.36	20:00	-21.85	06	Dropout
0710	09:32	7.23	21:00	-22.39	02	Substorm
0710	09:37	7.19	21:00	-22.50	02	Substorm
0710	09:54	7.00	21:00	-22.84	02	Substorm
0711	15:26	5.66	18:00	-15.58	08	Sharp Onset
0712	05:22	6.25	21:00	-11.24	02	Substorm
0712	05:29	6.17	21:00	-11.36	04	Substorm

Table B.1 continued : List of FAEs as observed by the LEPA on CRRES

Orbit Number	UT	L-shell (R_E)	MLT	Magnetic Latitude (°)	Duration (Mins)	Type
0712	05:36	6.08	21:00	-11.48	03	Substorm
0713	11:17	6.31	18:00	-22.96	02	Dropout
0713	11:24	6.46	18:00	-23.28	03	Dropout
0713	11:38	6.73	19:00	-23.84	05	Dropout
0713	11:51	6.96	19:00	-24.32	07	Dropout
0719	00:59	6.59	20:00	-6.232	11	Sharp Onset
0732	07:43	7.30	19:00	-20.77	02	Dropout
0732	07:55	7.39	19:00	-21.17	03	Dropout
0733	18:16	7.07	20:00	-17.48	03	Dropout
0733	19:23	6.74	20:00	-16.95	08	Substorm
0733	19:38	6.58	20:00	-16.81	06	Substorm
0733	19:50	6.44	21:00	-16.69	03	Substorm
0735	13:30	8.01	19:00	-27.01	04	Dropout
0735	12:42	7.67	19:00	-26.42	01	Dropout
0735	12:48	7.73	19:00	-26.52	04	Dropout
0736	21:51	6.04	18:00	-5.036	08	Sharp Onset
0736	00:19	6.51	20:00	-6.946	01	Dropout
0736	00:24	6.48	20:00	-6.974	04	Sharp Onset
0738	18:50	6.85	19:00	-14.47	04	Dropout
0738	18:55	6.86	19:00	-14.45	05	Dropout
0739	02:55	5.78	18:00	-9.017	09	Dropout
0739	04:59	6.77	19:00	-13.43	01	Substorm
0739	05:54	6.72	20:00	-14.85	04	Substorm
0749	07:55	7.31	20:00	-21.26	03	Substorm
0749	08:00	7.30	20:00	-21.36	04	Substorm
0749	08:11	7.26	20:00	-21.57	04	Substorm
0754	07:23	7.25	19:00	-21.85	03	Dropout
0754	07:35	7.36	19:00	-22.22	06	Dropout
0754	07:48	7.47	19:00	-22.59	02	Dropout
0754	07:54	7.51	19:00	-22.76	03	Dropout
0754	08:02	7.56	19:00	-22.97	03	Dropout
0754	08:08	7.59	19:00	-23.12	06	Dropout
0754	08:34	7.68	19:00	-23.74	05	Dropout
0754	09:13	7.63	20:00	-24.46	05	Dropout
0754	10:26	6.80	21:00	-24.89	07	Other
0754	10:58	6.03	21:00	-24.39	04	Dropout
0754	11:06	5.79	21:00	-24.16	03	Dropout
0754	11:11	5.63	21:00	-23.98	07	Dropout
0755	16:17	6.36	18:00	-16.92	04	Dropout
0755	17:23	6.90	19:00	-17.16	03	Sharp Onset
0756	04:38	6.64	20:00	-12.78	03	Substorm

Table B.1 continued : List of FAEs as observed by the LEPA on CRRES

Orbit Number	UT	L-shell (R_E)	MLT	Magnetic Latitude (°)	Duration (Mins)	Type
0759	10:27	7.89	20:00	-26.86	01	Dropout
0759	10:36	7.83	20:00	-26.93	01	Dropout
0760	17:36	6.35	18:00	-13.96	07	Sharp Onset
0760	21:43	5.49	21:00	-11.43	04	Substorm
0760	22:03	5.05	21:00	-10.93	04	Substorm
0761	06:34	6.51	20:00	-16.57	07	Dropout
0761	06:43	6.41	20:00	-16.62	03	Dropout
0761	07:02	6.16	20:00	-16.64	04	Other
0762	15:11	7.67	19:00	-24.94	04	Dropout
0765	19:50	6.64	19:00	-10.80	03	Substorm
0765	20:41	6.72	19:00	-10.49	03	Substorm
0766	04:02	5.76	17:00	-14.63	04	Dropout
0766	04:17	6.02	18:00	-15.21	01	Sharp Onset
0766	04:43	6.40	18:00	-16.16	07	Sharp Onset
0766	04:52	6.52	18:00	-16.46	04	Sharp Onset
0766	05:09	6.71	18:00	-17.02	02	Dropout
0766	07:20	7.20	20:00	-20.30	02	Sharp Onset
0766	07:24	7.19	20:00	-20.36	02	Sharp Onset
0767	14:34	6.74	18:00	-21.56	03	Dropout
0767	14:38	6.79	18:00	-21.59	03	Dropout
0767	14:47	6.90	18:00	-21.66	01	Dropout
0767	14:52	6.95	18:00	-21.69	07	Dropout
0767	15:14	7.14	18:00	-21.72	06	Dropout
0767	15:45	7.31	19:00	-21.60	02	Dropout
0767	15:50	7.33	19:00	-21.56	11	Dropout
0767	16:14	7.37	19:00	-21.33	10	Dropout
0767	16:27	7.36	19:00	-21.18	10	Dropout
0767	16:39	7.34	19:00	-21.02	07	Dropout
0767	16:52	7.30	19:00	-20.83	07	Dropout
0767	17:08	7.23	19:00	-20.57	03	Dropout
0767	17:13	7.20	19:00	-20.49	03	Dropout
0767	17:20	7.15	19:00	-20.37	01	Dropout
0767	17:25	7.11	19:00	-20.28	06	Dropout
0767	18:18	6.54	20:00	-19.22	01	Dropout
0768	02:18	6.62	19:00	-9.203	16	Other
0768	02:46	6.61	19:00	-9.630	03	Substorm
0768	02:51	6.60	19:00	-9.697	04	Substorm
0768	04:05	6.12	20:00	-10.23	09	Sharp Onset
0769	12:13	8.25	19:00	-28.37	05	Substorm
0771	08:12	7.82	19:00	-24.10	02	Dropout
0771	11:00	6.12	21:00	-24.50	05	Dropout

Table B.1 continued : List of FAEs as observed by the LEPA on CRRES

Orbit Number	UT	L-shell (R_E)	MLT	Magnetic Latitude (°)	Duration (Mins)	Type
0774	14:53	7.82	19:00	-25.37	03	Substorm
0774	15:07	7.75	19:00	-25.17	05	Substorm
0774	15:17	7.68	19:00	-25.02	02	Substorm
0774	15:34	7.54	19:00	-24.74	04	Substorm
0774	15:42	7.46	20:00	-24.60	01	Substorm
0775	00:54	6.61	19:00	-7.455	02	Sharp Onset
0775	01:01	6.60	19:00	-7.490	01	Sharp Onset
0775	01:08	6.58	19:00	-7.519	02	Sharp Onset
0777	18:53	6.26	18:00	-10.47	06	Sharp Onset
0778	10:04	4.76	21:00	-19.33	05	Sharp Onset
0779	13:40	5.24	16:00	-18.53	05	Dropout
0779	14:14	6.04	17:00	-19.82	03	Sharp Onset
0779	14:43	6.54	17:00	-20.32	09	Sharp Onset
0779	15:25	7.02	18:00	-20.46	07	Sharp Onset
0779	17:25	7.21	19:00	-18.91	02	Sharp Onset
0779	17:35	7.15	19:00	-18.70	03	Sharp Onset
0779	17:42	7.11	19:00	-18.56	13	Sharp Onset
0779	17:56	7.01	19:00	-18.25	04	Sharp Onset
0779	18:02	6.96	19:00	-18.11	07	Other
0779	18:10	6.89	19:00	-17.93	01	Other
0779	18:15	6.84	19:00	-17.81	05	Dropout
0779	18:26	6.73	20:00	-17.54	09	Dropout
0780	23:47	4.72	17:00	-5.761	09	Dropout
0780	03:00	6.75	19:00	-10.96	07	Dropout
0780	03:09	6.75	19:00	-11.11	10	Dropout
0780	03:27	6.73	19:00	-11.37	06	Dropout
0780	03:44	6.69	19:00	-11.59	03	Dropout
0781	14:33	7.64	19:00	-26.57	10	Dropout
0781	14:57	7.30	20:00	-26.10	05	Dropout
0782	22:09	6.46	18:00	-6.896	04	Sharp Onset
0782	23:48	6.62	19:00	-7.078	06	Sharp Onset
0782	00:35	6.38	19:00	-6.863	02	Sharp Onset
0782	00:38	6.36	19:00	-6.840	02	Dropout
0782	00:42	6.33	20:00	-6.807	01	Dropout
0782	00:46	6.29	20:00	-6.772	02	Dropout
0783	09:35	8.23	19:00	-27.01	06	Dropout
0783	09:45	8.23	19:00	-27.10	14	Sharp Onset
0783	10:18	8.13	19:00	-27.31	10	Sharp Onset
0783	12:11	6.25	20:00	-26.02	29	Other
0785	06:58	7.07	19:00	-19.33	01	Substorm
0785	07:02	7.04	19:00	-19.36	01	Substorm
0785	07:07	7.00	19:00	-19.39	02	Substorm

Table B.1 continued : List of FAEs as observed by the LEPA on CRRES

Orbit Number	UT	L-shell (R_E)	MLT	Magnetic Latitude (°)	Duration (Mins)	Type
0785	07:13	6.94	20:00	-19.43	03	Substorm
0785	08:38	5.48	21:00	-18.33	30	Substorm
0786	12:15	4.50	16:00	-18.97	05	Sharp Onset
0786	17:58	6.52	20:00	-18.85	07	Sharp Onset
0786	18:24	6.07	20:00	-18.07	03	Dropout
0795	11:28	8.33	18:00	-28.52	10	Dropout
0795	12:05	8.34	19:00	-28.38	01	Sharp Onset
0795	12:11	8.32	19:00	-28.34	03	Sharp Onset
0795	12:20	8.29	19:00	-28.26	12	Sharp Onset
0795	12:40	8.17	19:00	-28.06	05	Sharp Onset
0796	22:23	6.68	19:00	-7.424	01	Other
0796	22:38	6.65	19:00	-7.280	03	Other
0799	04:42	7.04	18:00	-16.03	08	Sharp Onset
0806	05:25	6.75	19:00	-15.67	04	Dropout
0806	05:32	6.70	19:00	-15.69	01	Sharp Onset
0806	05:38	6.65	19:00	-15.70	02	Sharp Onset
0806	05:50	6.54	19:00	-15.69	01	Sharp Onset
0809	09:34	7.97	17:00	-28.32	01	Substorm
0809	09:39	8.02	18:00	-28.36	02	Substorm
0809	09:57	8.17	18:00	-28.46	01	Substorm
0809	10:02	8.21	18:00	-28.49	01	Substorm
0809	10:27	8.33	18:00	-28.53	02	Substorm
0816	11:33	8.14	19:00	-27.93	01	Dropout
0816	11:38	8.11	19:00	-27.86	03	Dropout
0826	19:01	6.37	19:00	-12.26	04	Sharp Onset
0830	09:35	8.21	17:00	-28.33	02	Other
0830	09:55	8.28	18:00	-28.27	04	Other
0830	10:06	8.30	18:00	-28.22	02	Other
0830	10:18	8.30	18:00	-28.14	05	Other
0830	10:26	8.29	18:00	-28.08	01	Other
0830	10:33	8.28	18:00	-28.02	01	Other
0830	10:40	8.26	18:00	-27.95	03	Other
0830	10:53	8.20	18:00	-27.80	04	Other
0832	04:44	6.63	17:00	-21.49	07	Dropout
0832	04:52	6.76	17:00	-21.63	08	Dropout
0832	05:04	6.93	17:00	-21.83	05	Dropout
0832	08:28	7.29	19:00	-23.21	08	Other
0846	07:34	7.68	18:00	-23.52	03	Other
0846	07:42	7.65	18:00	-23.50	03	Other
0846	07:46	7.63	18:00	-23.48	03	Other
0846	07:53	7.58	18:00	-23.45	01	Other

Table B.1 continued : List of FAEs as observed by the LEPA on CRRES

Orbit Number	UT	L-shell (R_E)	MLT	Magnetic Latitude (°)	Duration (Mins)	Type
0846	09:48	5.80	19:00	-20.85	03	Substorm
0847	18:44	6.46	18:00	-10.95	03	Other
0851	09:04	7.92	17:00	-28.32	07	Dropout
0851	09:32	8.09	17:00	-28.15	05	Dropout
0851	10:23	8.16	17:00	-27.57	08	Dropout
0851	10:39	8.12	18:00	-27.31	04	Dropout
0855	03:03	6.90	17:00	-14.35	02	Sharp Onset
0855	03:07	6.91	17:00	-14.37	05	Sharp Onset
0856	10:52	6.04	15:00	-25.60	01	Other
0856	10:54	6.08	15:00	-25.62	08	Other
0856	11:04	6.30	15:00	-25.69	44	Other
0856	11:57	7.14	16:00	-25.38	17	Dropout
0856	12:15	7.32	16:00	-25.09	02	Dropout
0856	12:18	7.34	16:00	-25.03	06	Dropout
0856	12:25	7.40	16:00	-24.90	02	Dropout
0856	12:34	7.46	17:00	-24.71	32	Dropout
0856	13:08	7.59	17:00	-23.88	08	Dropout
0856	13:28	7.60	17:00	-23.32	34	Dropout
0856	14:05	7.51	17:00	-22.14	03	Dropout
0856	14:34	7.33	18:00	-21.11	02	Dropout
0856	14:41	7.28	18:00	-20.84	04	Dropout
0856	14:55	7.15	18:00	-20.30	03	Dropout
0856	15:09	7.00	18:00	-19.73	04	Dropout
0856	15:20	6.87	18:00	-19.27	12	Other
0856	15:37	6.64	18:00	-18.53	07	Dropout
0856	15:57	6.33	18:00	-17.60	03	Dropout
0856	16:13	6.05	19:00	-16.82	04	Dropout
0858	07:46	6.78	15:00	-28.35	05	Dropout
0858	07:53	6.92	16:00	-28.38	05	Dropout
0858	08:34	7.58	16:00	-28.40	17	Dropout
0858	09:01	7.86	16:00	-28.27	02	Dropout
0858	09:07	7.91	16:00	-28.23	04	Dropout
0858	09:23	8.01	17:00	-28.10	11	Dropout
0858	09:40	8.08	17:00	-27.93	08	Dropout
0858	09:51	8.11	17:00	-27.79	12	Dropout
0858	10:11	8.12	17:00	-27.51	04	Sharp Onset
0858	10:31	8.09	17:00	-27.18	05	Sharp Onset
0859	20:32	6.69	17:00	-6.736	05	Sharp Onset
0872	09:07	7.82	16:00	-27.98	03	Dropout
0872	09:14	7.87	16:00	-27.89	23	Dropout
0872	09:54	8.01	17:00	-27.28	02	Other

Table B.1 continued : List of FAEs as observed by the LEPA on CRRES

Orbit Number	UT	L-shell (R_E)	MLT	Magnetic Latitude (°)	Duration (Mins)	Type
0872	10:04	8.02	17:00	-27.10	02	Dropout
0872	10:24	7.99	17:00	-26.69	04	Dropout
0904	06:58	4.95	18:00	-11.00	06	Dropout
0906	01:35	6.42	17:00	-6.163	08	Dropout
0926	14:19	6.86	16:00	-14.53	03	Dropout
0926	14:44	6.84	16:00	-13.31	04	Dropout
0926	14:57	6.81	16:00	-12.65	03	Dropout
0946	06:49	6.21	17:00	-14.77	04	Other
0974	06:21	6.82	15:00	-16.43	05	Dropout
0974	06:34	6.72	15:00	-16.04	01	Dropout
0974	07:06	6.41	16:00	-14.94	05	Dropout
0978	00:15	6.10	16:00	1.3976	12	Other
0991	12:02	6.62	14:00	-12.88	03	Dropout
1044	09:20	5.45	15:00	-6.410	05	Dropout

Table B.1 continued : List of FAEs as observed by the LEPA on CRRES

Appendix C

Dispersion Relation for a Cold Plasma

The discussion given here follows that of *Goertz and Strangeway*, 1995. A more rigorous discussion can be found in *Gary*, 1993. In the cold plasma approximation the plasma is treated as consisting of 2 populations, one of cold electrons, and the other of cold ions made up entirely of protons. The word 'cold' here implies that the thermal energy of the particles is low, such that their thermal velocities can be treated as zero. The plasma is also treated as being charge neutral, i.e. $N_e = N_i = N_0$ and having no net current, i.e. $\mathbf{v}_e = \mathbf{v}_i = 0$. Initially, here, the protons will be assumed to have infinite mass, thus immobile (a suitable assumption for high frequency waves).

In order to find a dispersion relation a wave solution needs to be applied to the relevant conservation and Maxwell's equations. The wave solution is given by,

$$\mathbf{B} = \mathbf{B}_0 + \mathbf{B}_1 \tag{C.1}$$

$$\mathbf{E} = \mathbf{E}_1 \tag{C.2}$$

$$\mathbf{u} = \mathbf{u}_{e1}. \tag{C.3}$$

Where the quantities subscripted with 0 are the background unperturbed quantities (note $\mathbf{E}_0 = 0$ and $\mathbf{u}_{e0} = 0$), and those subscripted with 1 are the perturbations of

these quantities given by,

$$B_{x1}(x,t) = \tilde{B}_x \exp(-iwt + ikx) \quad \text{(C.4)}$$

$$E_{x1}(x,t) = \tilde{E}_x \exp(-iwt + ikx) \quad \text{(C.5)}$$

$$u_{ex1}(x,t) = \tilde{u}_{ex} \exp(-iwt + ikx), \quad \text{(C.6)}$$

and similar relations in the y and z directions. The quantities denoted with a tilde indicate a Complex amplitude of the perturbation.

It is convenient to choose a coordinate system such that the unperturbed magnetic field lies along the z axis, i.e. $\mathbf{B}_0 = B_0\hat{\mathbf{z}}$. Substituting C.1-C.3, with $\mathbf{k} = k\hat{\mathbf{z}}$, into the momentum equation,

$$m_e n_e \left(\frac{\partial \mathbf{u}_e}{\partial t} + \mathbf{u}_e \cdot \nabla \mathbf{u}_e\right) + e n_0 \left(\mathbf{E} + \mathbf{u}_e \times \mathbf{B}\right) = 0, \quad \text{(C.7)}$$

and 2 of Maxwell's equations,

$$\nabla \times \mathbf{E} = -\frac{\partial \mathbf{B}}{\partial t}, \quad \text{(C.8)}$$

$$\nabla \times \mathbf{Bx} = \mu_0 \mathbf{j} + \mu_0 \epsilon_0 \frac{\partial \mathbf{E}}{\partial t}, \quad \text{(C.9)}$$

(C.10)

produces a complete set of equations, which in their linearised form are;

$$-i\omega m_e \tilde{\mathbf{u}}_e + e\tilde{\mathbf{E}} + e\tilde{\mathbf{u}}_e \times \mathbf{B}_0 = 0 \quad \text{(C.11)}$$

$$\mathbf{k} \times \tilde{\mathbf{E}} - \omega \tilde{\mathbf{B}} = 0 \quad \text{(C.12)}$$

$$i\mathbf{k} \times \tilde{\mathbf{B}} + \mu_0 n_0 e \tilde{\mathbf{u}}_e + \frac{i\omega}{c^2}\tilde{\mathbf{E}} = 0. \quad \text{(C.13)}$$

A solution must have $\tilde{\mathbf{u}}_e$, $\tilde{\mathbf{E}}$, and $\tilde{\mathbf{B}}$ all in the x-y plane (perpendicular to $\mathbf{B}_0$), and so the relations between the six unknowns ($\tilde{u}_{ex}$,$\tilde{u}_{ey}$,$\tilde{E}_x$,$\tilde{E}_y$,$\tilde{B}_x$,$\tilde{B}_y$) are given by

$$k\tilde{E}_y = -\omega \tilde{B}_x \quad \text{(C.14)}$$

$$k\tilde{E}_x = \omega \tilde{B}_y \quad \text{(C.15)}$$

$$ik\tilde{B}_y = \mu_0 n_0 e\tilde{u}_{ex} + \frac{i\omega}{c^2}\tilde{E}_x \quad \text{(C.16)}$$

$$ik\tilde{B}_x = -\mu_0 n_0 e\tilde{u}_{ey} - \frac{i\omega}{c^2}\tilde{E}_y \quad \text{(C.17)}$$

$$i\omega m_e \tilde{u}_{ex} = e\tilde{E}_x + eB_0\tilde{u}_{ey} \quad \text{(C.18)}$$

$$i\omega m_e \tilde{u}_{ey} = e\tilde{E}_y + eB_0\tilde{u}_{ex}. \quad \text{(C.19)}$$

Which can be reduced to two equations

$$\left(1 - \frac{(\omega^2 - k^2c^2)}{\omega_{pe}^2}\right)\tilde{E}_x + \left(i\frac{(\omega^2 - k^2c^2)\,\Omega_e}{\omega_{pe}^2}\right)\tilde{E}_y = 0 \quad \text{(C.20)}$$

$$\left(-i\frac{(\omega^2 - k^2c^2)\,\Omega_e}{\omega_{pe}^2}\right)\tilde{E}_x + \left(1 - \frac{(\omega^2 - k^2c^2)}{\omega_{pe}^2}\right)\tilde{E}_y = 0, \quad \text{(C.21)}$$

from which the dispersion relation can be found. Given in terms of the refractive index it is

$$n^2 = \frac{c^2k^2}{\omega^2} = 1 - \frac{\omega_{pe}^2}{\omega\,(\omega \pm \Omega_e)}. \quad \text{(C.22)}$$

The plus sign in Equation C.22 refers to a right handed wave (the R mode wave), and the minus sign to a left handed wave (the L mode wave). From this dispersion relation it can be seen that the R mode will propagate at all frequencies where $\omega > \Omega_e$, and for $\omega < \Omega_e$ only above a cutoff frequency ω_R, given by

$$\omega_R = \frac{\Omega_e}{2} + \sqrt{\omega_{pe}^2 + \frac{\Omega_e^2}{4}} \quad \text{(C.23)}$$

The L mode, however, propagates only above a cutoff frequency ω_L, given by

$$\omega_L = -\frac{\Omega_e}{2} + \sqrt{\omega_{pe}^2 + \frac{\Omega_e^2}{4}} \quad \text{(C.24)}$$

R mode waves with frequencies below Ω_e are generally known as whistler mode waves (see Figure 6.9).

If the proton mass is not assumed to be infinite, Equation C.22 becomes [*Gary*, 1993]

$$n^2 = \frac{c^2k^2}{\omega^2} = 1 - \frac{\omega_{pe}^2}{\omega\,(\omega \pm \Omega_e)} - \frac{\omega_{pi}^2}{\omega\,(\omega \pm \Omega_i)}. \quad \text{(C.25)}$$

From this expression we can see that there is a resonance for the R mode at $\omega = \Omega_e$ and for the L mode at $\omega = \Omega_i$, and that the ion term has little effect except near the ion gyrofrequency.

Appendix D

Dispersion Relation for a Cold Plasma with Counterstreaming Beams

$$
\begin{aligned}
u &= \sqrt{\frac{F(\omega)}{2G(\omega)}} \\
F(\omega) &= -\omega^5 - c^{-2}v^2\omega^5 + \Omega_e^3\omega(\Omega_i+\omega) - 3\Omega_e^2\omega^2(\Omega_i+\omega) + c^{-2}v^2\omega^3\omega_{pe}^2 \\
&\quad -\Omega_i(\omega^4 + c^{-2}v^2\omega^4 - c^{-2}v^2\omega^2\omega_{pe}^2) + c^{-2}v^2\omega^3\omega_{pi}^2 \\
&\quad +\Omega_e\omega(3\Omega_i\omega^2 + c^{-2}v^2\omega^2\Omega_i + 3\omega^3 + c^{-2}v^2\omega^3 - 2c^{-2}v^2\omega_{pb}^2\Omega_i \\
&\quad -2c^{-2}v^2\omega\omega_{pb}^2 - c^{-2}v^2\omega\omega_{pi}^2) \\
&\quad + \Big(\omega^2\Big(-4c^{-2}v^2\omega(\Omega_e-\omega)^3(\Omega_i+\omega)\Big(\Omega_i(\omega_{pe}^2-\omega^2) + \Omega_e(\Omega_i\omega+\omega^2-\omega_{pi}^2) \\
&\quad +\omega(\omega_{pi}^2+\omega_{pb}^2-\omega^2)\Big) + \Big(\Omega_e^3(\Omega_i+\omega) - 3\Omega_e^2\omega(\Omega_i+\omega) \\
&\quad +\Omega_e(3\Omega_i\omega^2 + c^{-2}v^2\omega^2\Omega_i + 3\omega^3 \\
&\quad +c^{-2}v^2\omega^3 - 2c^{-2}v^2\omega_{pb}^2\Omega_i - 2c^{-2}v^2\omega_{pb}^2\omega - c^{-2}v^2\omega_{pi}^2\omega) \\
&\quad -\omega(\Omega_i(\omega^2 + c^{-2}v^2\omega^2 - c^{-2}v^2\omega_{pe}^2) \\
&\quad +\omega(\omega^2 + c^{-2}v^2\omega^2 - c^{-2}v^2\omega_{pe}^2 - c^{-2}v^2\omega_{pi}^2))\Big)^2\Big)\Big)^{\frac{1}{2}} \\
G(\omega) &= (\Omega_e-\omega)^2(\Omega_i(\omega_{pe}^2-\omega^2) + \Omega_e(\Omega_i\omega+\omega^2-\omega_{pi}^2) + \omega(\omega_{pe}^2+\omega_{pi}^2-\omega^2))
\end{aligned}
$$

Acknowledgements

Firstly I would like to pay tribute to the memory of my supervisor, Professor Alan Johnstone. It is fair to say that it was the prospect of having Alan as a supervisor which played a very strong part in my choice to come to MSSL. I would like to thank him for all his help and guidance over the years and not least his faith, I hope you now have found the answer.

Secondly I would like to thank all those who have been members of the space plasma group during my time at MSSL for their support. Particular thanks goes to Andrew Fazakerly who stepped in in Alan's absence and helped me through the writing up process. Special thanks also to Nigel Meredith, and Ian Krauklis for their useful discussions and input, Mark Birdseye for his help with the CRRES UDF software, and Nick Flowers for keeping my computer alive (well almost).

I would like to thank all my friends among the staff and students, past and present, at MSSL for making the last four years what they were. Paul, Jim, Steve, Encarni, Kerry, Mat, Geraint, Eva, Matt, Sarah, Ady, Saqib, Kate, Jenny, Joe, Mike, Neale, Jenni, Roger, and others too numerous to mention I thank you all. Most of all though I would like to thank Lee and Neil for making the Naz, Gaz, Laz years something very special.

My final thanks goes to my parents and family, without whom's continual support (both moral and financial), encouragement, and understanding, I would not have made it this far.

I am grateful for the PPARC studentship which has allowed me to undertake this Ph.D.

References

Akasofu, S. I., The Development of the Auroral Substorm, *Planet. Space. Sci.*, **12**, 273-282, 1964.

Anderson, R. R., D. A. Gurnett, and D. L. Odem, CRRES Plasma Wave Experiment, *J. Spacecraft and Rockets*, **29**, 570-573, 1992.

Arnoldy, R. L., Fine Structure and Pitch Angle Dependence of Synchronous Orbit Electron Injections, *J. Geophys. Res.*, **91**, 13411-13421, 1986.

Baker, D. N., S. J. Bame, W. C. Feldman, J. T. Gosling, R. D. Zwickl, J. A. Slavin, E. J. Smith, Strong Electron Bidirectional Anisotropies in the Distant Tail: ISEE 3 Observations of Polar Rain, *J. Geophys. Res.*, **91**, 5637-5662, 1986.

Baker, D. N., S. J. Bame, J. T. Gosling, M. S. Gussenhoven, Observations of Polar Rain at Low and High Altitudes, *J. Geophys. Res.*, **92**, 13547-13560, 1987.

Baker, D. N., A. Nashida, T. Mukai, T. Yamamoto, Y. Saito, Y. Matsuno, S. Kokubun, T. I. Pulkkinen, Observations of Bidirectional Electrons in the Distant Tail Lobes: GEOTAIL Results, *Geophys. Res. Lett*, **24**, 959-962, 1997.

Baumjohann, W., and R. A. Treumann, *Basic Space Plasma Physics*, Imperial College Press, 1996.

Bennet, E. L., M. Temerin, and F. S. Mozer, The Distribution of Auroral Electrostatic Shocks below 8000-km Altitude, *J. Geophys. Res.*, **88**, 7107-7120, 1983.

Boehm, M. H., J. Clemmons, J. E. Wahlund, A. Eriksson, L. Eliasson, L. Blomberg, P. Kitner, H. Hofner, Observations of an Upward-Directed Electron Beam With the Perpendicular Temperature of the Cold Ionosphere, *Geophys. Res. Lett*, **22**, 2103-2106, 1995.

Borg, H., L. A. Holmgren, B. Hultqvist, F. Cambou, H. Reme, A. Bahnsen, Some Early Results of the keV Plasma Experiment on GEOS-1, *Space Sci. Rev.*, **22**, 511-535, 1978.

Borovsky, J. B., R. J. Nemzek, and R. D. Belian, The Occurrence Rate of Magnetospheric Substorm Onsets: Random and Periodic Substorms, *J. Geophys. Res.*, **98**, 3807-3813, 1993a.

Borovsky, J. B., Auroral Arc Thicknesses as Predicted by Various Theories, *J. Geophys. Res.*, **98**, 6101-6138, 1993b.

Burch, J. L., P. H. Reiff, M. Sugiura, Upward Electron Beams Measured by DE-1: A Primary Source of Dayside Region-1 Birkeland Currents, *Geophys. Res. Lett*, **10**, 753-756, 1983.

Carlson, C. W., J. P. McFadden, R. E. Ergun, F. S. Mozer, M. Temerin, D. M. Klumpar, E. G. Shelley, W. K. Peterson, E. Moebius, L. M. Kistler, C. Cattell, R. Elphic, R. Strangeway, R. Pfaff, Magnetic Field-Aligned Particle Fluxes Observed from the FAST Satellite (abstract), in *IAGA 1997 Abstract Book*, pp 357-358, 1997.

Carlson, C. W., R. F. Pfaff, and J.G. Watzin, The Fast Auroral SnapshoT (FAST) Mission, *Geophys. Res. Lett*, **25**, 2013-2016, 1998a.

Carlson, C. W., J. P. McFadden, R. E. Ergun, M. Temerin, W. Peria, F. S. Mozer, D. M. Klumpar, E. G. Shelley, W. K. Peterson, E. Moebius, R. Elphic, R. Strangeway, C. Cattell, R. Pfaff, FAST Observations in the Downward Auroral Current Region: Energetic Upgoing Electron Beams, Parallel Potential Drops, and Ion Heating, *Geophys. Res. Lett*, **25**, 2017-2020, 1998b.

Coates, A. J., A. D Johnstone, S. J. Kellock, M. F. Smith, T. Booker, and J. D. Winningham, A Space-borne Plasma Analyzer for Three-dimensional Measurements of the Velocity Distribution, *IEEE Trans. Nucl. Sci.* **32**, 139-144, 1985.

Collin, H. L., R. D. Sharp, E. G. Shelley, The Occurrence and Characteristics of Electron Beams Over the Polar Regions, *J. Geophys. Res.*, **87**, 7504-7511, 1982.

Cowley, S. W. H., The Magnetosphere and its Interaction With the Solar Wind and with the Ionosphere, in *The Behavior of Systems in the Space Plasma Environment*, edited by R. N. DeWitt, D. Duston, and A. K. Hyder, pp. 147-181, Kluwer Academic Publishers, 1993.

Dungey, J. W., Interplanetary Field and the Auroral Zones, *Phys. Rev. Lett.*, **40**, 47-48, 1961.

Eather, R. H., *Majestic Lights*, p31,American Geophysical Union, 1980.

Ergun, R. E., C. W. Carlson, J. P. McFadden, F. S. Mozer, G. T. Delory, W. Peria, C. C. Chaston, M. Temerin, R. Elphic, R. Strangeway, R. Pfaff, C. A. Cattell, D. Klumpar, E. Shelley, W. Peterson, E. Moebius, L. Kistler, FAST Satellite Observations of Electric Field Structures in the Auroral Zone, *Geophys. Res. Lett*, **25**, 2025-2028, 1998.

Feldstein, Y. I., S. I. Isaev, and A. I. Lebedinsley, The Phenomonology and Morphology of Aurorae, in *Annals of the IQSY*, vol. 4, pp. 311-368, MIT Press, Cambridge, Mass., 1969.

Flowers, N. J., An Investigation of Substorm Particle Injections Associated With Magnetospheric Substorms, *Ph.D. Thesis*, University College London, 1998.

Gary, S. P., *Theory of Space Plasma Microinstabilities*, Cambridge University Press, 1993.

Goertz, C. K., and R. J. Strangeway, Plasma Waves, in *Introduction to Space Physics*, edited by Kivelson, M. G., and C. T. Russell, pp. 27-57, Cambridge University Press, 1995.

Hada, T., A. Nishida, T. Teraswa, E. W. Hones, Jr., Bi-Directional Electron Pitch Angle Anisotropy in the Plasma Sheet, *J. Geophys. Res.*, **86**, 11211-11224, 1981.

Hardy, D. A., D. M. Walton, A. D. Johnstone, M. F. Smith, M. P. Gough, A. Huber, J. Pantazis, and R. Burkhardt, Low Energy Plasma Analyzer, *IEEE Trans. Nucl. Sci.*, **40**, 246-251, 1993.

Horne, R. B., Path-Integrated Growth of Electrostatic Waves: The Generation of Terrestrial Myriametric Radiation, *J. Geophys. Res.*, **94**, 8895-8909, 1989.

Horne, R. B., P. J. Christiansen, M. P. Gough, Weak Electrostatic Waves Near the Upper Hybrid Frequency: A Comparison Between Theory and Experiment, *J. Geophys. Res.*, **92**, 3243-3259, 1987.

Hughes, W. J., The Magnetopause, Magnetotail and Magnetic Reconnection, in *Introduction to Space Physics*, edited by Kivelson, M. G., and C. T. Russell, pp. 227-287, Cambridge University Press, 1995.

Hultqvist, B., R. Lundin, Parallel Electric Fields Accelerating Ions and Electrons in the Same Direction, *Astrophys. Space Sci.*, **144**, 149-154, 1988.

Hultqvist, B., R. Lundin, K. Stasiewicz, L. Block, P. A. Lindqvist, G. Gustafsson, H. Koskinen, A. Bahnsen, T. A. Potemra, L. J. Zanetti, Simultaneous Observation of Upward Moving Field-Aligned Energetic Electrons and Ions on Auroral Zone Field Lines, *J. Geophys. Res.*, **93**, 9765-9776, 1988.

Iijima, T., and T. A. Potemra, Field-Aligned Currents in the Dayside Cusp Observed by Triad, *J. Geophys. Res.*, **81**, 5971-5979, 1976.

Johnstone A. D., J. D. Winningham, Satellite Observations of Suprathermal Electron Bursts, *J. Geophys. Res.*, **87**, 2321-2329, 1982.

Johnstone A. D., A. J. Coates, B. Wilken, W. Studemann, W. Weiss, R. C. Irelli, V. Formisano, H. Borg, S. Olsen, J. D. Winningham, D. A. Bryant, S. J. Kellock, The Giotto Three-dimensional Positive Ion Analyser, *Physics (E)* **20**, 795-805, 1987.

Johnstone A. D., N. J. Flowers and R. Liu, Observations in the Equatorial Region of the Field Aligned Electron and Ion Distributions in the Energy Range 100 eV to 5 keV Associated with Substorm Onsets, in *Proceedings of the Second International Conference on Substorms, Fairbanks, Alaska, USA.*, Geophysical Institute, 1994.

Johnstone A. D., Pitch Angle Diffusion of Low Energy Electrons and Positive Ions in The Inner Magnetosphere: A Review of Observations and Theory, *Adv. Space Res.*, **17**, 1089-1098, 1996.

Johnstone A. D., S. Szita, N. J. Flowers, and N. P. Meredith, Observations of Particle Injection From CRRES, in *Proceedings of the Third International Conference on Substorms, Versailles, France.*, ESA, 1996.

Johnstone A. D., S. Burge, P. J. Carter, A. J. Coates, A. J. Coker, A. N. Fazakerley, M. Grande, R. A. Gowen, C. Gurgiolo, B. K. Hancock, B. Narheim, A. Preece, P. H. Sheather, J. D. Winningham, and R. D. Woodliffe, PEACE: A Plasma Electron And Current Experiment, *Space Sci. Rev.*, **79**, 351-398, 1997.

Johnson, M. H., and J. K. Ball, Combined Release and Radiation Effects Satellite (CRRES): Spacecraft and Mission, *J. Spacecraft and Rockets*, **29**, 556-563, 1992.

Jordan, C. E., J. N. Bass, M. S. Gussenhoven, H. J. Singer, and R. V. Hilmer, Comparison of Magnetospheric Magnetic Field Models With CRRES Observations During the August 26, 1990, Storm, *J. Geophys. Res.*, **97**, 16907-16920, 1992.

Kennel, C. F., F. L. Scarf, R. W. Fredricks, J. H. McGehee, and F. V. Coroniti, VLF Electric Field Observations in the Magnetosphere, *J. Geophys. Res.*, **75**, 6136-6152, 1970.

Kennel, C. F., and M. Ashour-Abdalla, Electrostatic Waves and the Strong Diffusion of Magnetospheric Electrons, in *Magnetospheric Plasma Physics*, edited by A. Nashida, pp 245-344, Center for Academic Publications, Tokyo, Japan, 1982.

Kivelson, M. G., Physics of Space Plasmas, in *Introduction to Space Physics*, edited by Kivelson, M. G., and C. T. Russell, pp. 27-57, Cambridge University Press, 1995.

Klumpar, D. M., W. J. Heikkila, Electrons in the Ionospheric Source Cone: Evidence for Runaway Electrons as Carriers of Downward Birkeland Currents, *Geophys. Res. Lett*, **9**, 873-876, 1982.

Klumpar, D. M., Statistical Distributions of the Auroral Electron Albedo in the Magnetosphere, *Geophys. Monogr. Ser.* Vol. **80**, edited by Lysak, R. L., pp. 163-171, AGU, Washington, DC, 1993.

Klumpar, D. M., J. M. Quinn, and E. G. Shelley, Counterstreaming electrons at the magnetic equator near 9 R_E, *Geophys. Res. Lett*, **15**, 1295-1298, 1998

Knecht, D. J., and B. M. Shuman, The Geomagnetic Field, in *Handbook of Geophysics and the Space Environment*, edited by A. S. Jursa, pp. 4.1-4.37, Airforce Geophysics Lab., United States Air Force, 1985.

Koskinen, H., Magnetospheric Substorms, *Alpbach Summer School*, 1994.

Kremser, G., A. Korth, S. L. Ullaland, S. Perraut, A. Roux, A. Pedersen, R. Schmidt, P. Tanskanen, Field-Aligned Beams of Energetic Electrons (16 keV $\leq$ E $\leq$ 80 keV) Observed at Geosynchronous Orbit at Substorm Onsets, *J. Geophys. Res.*, **93**, 14453-14464, 1988.

Kurth, S. W., and D. A. Gurnett, Plasma Waves in Planetary Magnetospheres, *J. Geophys. Res.*, **96**, 18977-18991, 1991.

Lin, C. S., G. K. Parks, S. DeForest, and C. E. McIlwain, Temperature Characteristics of Electron Beams and Ambient Particles, *J. Geophys. Res.*, **84**, 2651-2654, 1979.

Lin, C. S., J. L. Burch, J. D. Winningham, J. D. Menietti, R. A. Hoffman, DE-1 Observations of Counterstreaming Electrons at High Altitudes, *Geophys. Res. Lett*, **9**, 925-928,1982.

Lundin, R., L. Eliasson, B. Hultqvist, K. Stasiewicz, Plasma Energization on Auroral Field Lines as Observed by the VIKING Spacecraft, *Geophys. Res. Lett*, **14**, 443-446, 1987.

Lyons, L. R., and D. J. Williams, Quantitative Aspects of Magnetospheric Physics, p173, D. Reidel Publishing Co., Dordrecht, Holland, 1984.

Mauk, B. H., and C. I. Meng, The Aurora and Middle Magnetospheric Processes, in *Auroral Physics*, edited by C.-I. Meng, M. J. Rycroft, and L. A. Frank, p. 223, Cambridge Univ. Press, New York, 1991.

Maynard, N. C., W. J. Burke, E. M. Basinska, G. M. Erickson, W. J. Hughes, H. J. Singer, A. G. Yahnin, D. A. Hardy, F. S. Mozer, Dynamics of the Inner Magnetosphere Near Times of Substorm Onsets *J. Geophys. Res.*, **101**, 7705-7736, 1996.

McFadden, J. P., C. W. Carlson, R. E. Ergun, F. S. Mozer, M. Temerin, W. Peria, D. M. Klumpar, E. G. Shelley, W. K. Peterson, E. Moebius, L. Kistler, R. Elphic, R. Strangeway, C. Cattell, R. Pfaff, Spatial Structure and Gradients of Ion Beams Observed by FAST, *Geophys. Res. Lett*, **25**, 2021-2024, 1998.

McIlwain C. E., Coordinates for Mapping the Distributions of Magnetically Trapped Particles, *J. Geophys. Res.*, **66**, 2651-2654, 1961.

McIlwain C. E., Auroral Beams Near the Magnetic Equator, in *The Physics of Hot Plasmas in the Magnetosphere*, edited by B. Hultquist and L. Stenflow, p91, Plenum, New York, 1975. McPherron, R. L., Magnetospheric Dynamics, in *Introduction to Space Physics*, edited by Kivelson, M. G., and C. T. Russell, pp. 400-458, Cambridge University Press, 1995.

McPherron, R. L., C. T. Russell, and M. P. Aubry, Satellite Studies of Magnetospheric Substorms on August 15, 1968 - 9. Phenomenological Model For Substorms, *J. Geophys. Res.*, **78**, 3131-3149, 1973.

Meredith, N. P., A. D. Johnstone, S. Szita, R. B. Horne, and R. R. Anderson, 'Pancake' Electron Distributions in the Outer Radiation Belts, *J. Geophys. Res.*, in press 1999.

Mobius, E., L. Tang, L. M. Kistler, M. Popecki, E. J. Lund, D. Klumpar, W. Peterson, E. G. Shelley, B. Klecker, D. Hovestadt, C. W. Carlson, R. E. Ergun, J. P. McFadden, F. Mozer, M. Temerin, C. Cattell, R. Elphic, R. Strangeway, R. Pfaff, Species Dependent Energies in Upward Directed Ion Beams Over Auroral Arcs as Observed with FAST TEAMS, *Geophys. Res. Lett*, **25**, 2029-2032, 1998.

Moore, T. E., and R. L. Arnoldy, Plasma Pitch Angle Distributions Near the Substorm Injection Front, *J. Geophys. Res.*, **87**, 4405-4417, 1982.

Nagai, T., Observed Magnetic Substorm Onset Signatures at Synchronous Altitude, *J. Geophys. Res.*, **87**, 265-270, 1982.

Nakai, H., Y. Kamide, and C. T. Russell, Statistical Nature of the Magnetotail Current in the Near-Earth Region, *J. Geophys. Res.*, **102**, 9573-9586, 1997.

Newell, P. T., New Findings about Aurora Confirm Importance of Ionosphere in Space Weather, *EOS Trans.*, **79** 625, 1998.

Parks, G. K., C. S. Lin, B. H. Mauk, S. DeForest, and C. E. McIlwain, Characteristics of Magnetospheric Particle Injection Deduced From Events Observed on August 18, 1974, *J. Geophys. Res.*, **82**, 5208-5214, 1977.

Parks, G. K., *Physics of Space Plasmas, An Introduction*, Addison-Wesley Publishing Company, 1991.

Pfitzer, K. A., W. P. Olson, and T. Mogstad, A Time Dependent Source Driven Magnetospheric Field Model (abstract), *Eos Trans. AGU*, **69**, 426, 1988.

Primdahl, F., A. Bahnsen, M. Ejiri, P.Hoeg, G. Marklund, B. N. Maehlum, J. K. Olesen, E. Ungstrup, L. J. Zanetti, Rocket-borne and Groundbased Observations of Coincident Field-Aligned Currents, Electron Beams, and Plasma Density Enhancements in the Afternoon Auroral Oval, *Plan. Space Sci.*, **32**, 561-583, 1984.

Raitt, W. J., and J. J. Sojka, Field-Aligned Suprathermal Electron Fluxes Below 270 km in the Auroral Zone, *Planet. Space Sci*, **25**, 5-13, 1977.

Richardson, J. D., J. F. Fennel, D. R. Croley, Jr., Observations of Field-Aligned Ion and Electron Beams from SCATHA (P78-2), *J. Geophys. Res.*, **86**, 10105-10110, 1981.

Sharp, R. D., E. G. Shelley, R. G. Johnson, A. G. Ghielmetti, Counterstreaming Electron Beams at Altitudes of $\sim$1 R_e Over the Auroral Zone, *J. Geophys. Res.*, **85**, 92-100, 1980.

Singer, H. J., and W. P. Sullivan, P. Anderson, F. Mozer, P. Harvey, J. Wygant, W. McNeil, Fluxgate Magnetometer Instrument on the CRRES, *J. Spacecraft and Rockets*, **29**, 599-601, 1992.

Summers, D., R. M. Thorne, and F. Xiao, Relativistic Theory of Wave-Particle Resonant Diffusion with Application to Electron Acceleration in the Magnetosphere, *J. Geophys. Res.*, **103**, 20487-20500, 1998.

Thorne, R. M., and R. B. Horne, Whistler Absorption and Electron Heating Near the Plasmapause, *J. Geophys. Res.*, **101**, 4917-4928, 1996.

Vasyliunas, V. M., Mathematical Models of Magnetospheric Convection and its Coupling to the Ionosphere, in *Particles and Fields in the Magnetosphere*, edited by B. McCormac, p. 60, D. Reidel, Hingham, Mass., 1970.

Walt, M., and W. M. MacDonald, The Influence of the Earth's Atmosphere on Geomagnetically Trapped Particles. *Rev. Geophys., 2*, 543-577, 1964.

Wolf, R. A., Magnetospheric Configuration, in *Introduction to Space Physics*, edited by Kivelson, M. G., and C. T. Russell, pp. 27-57, Cambridge University Press, 1995.

Wygant, J. R., P. R. Harvey, F. S. Mozer, N. Maynard, H. Singer, M. Smiddy, W. Sullivan, and P. Anderson, The CRRES Electric Field/Langmuir Probe Instrument, *J. Spacecraft and Rockets*, **29**, 601-603, 1992.

Zhu, L., P. Gifford, J. J. Sojka, and W. Schunk, Model Study of Ground Magnetic Signatures of Traveling Convection Vortices, *J. Geophys. Res.*, **102**, 7449-7459, 1997.